

DOMAIN PATTERNS AND DYNAMICS
IN THE MAGNETOELECTRIC SWITCHING
OF SPIN-SPIRAL MULTIFERROICS

Dissertation

zur

Erlangung des Doktorgrades (Dr. rer. nat.)

der

Mathematisch-Naturwissenschaftlichen Fakultät

der

Rheinischen Friedrich-Wilhelms-Universität Bonn

vorgelegt von

Tim Hoffmann

aus

Köln

Bonn, 2012

Angefertigt mit Genehmigung der Mathematisch-Naturwissenschaftlichen Fakultät der Rheinischen Friedrich-Wilhelms-Universität Bonn

1. Gutachter: Prof. Dr. Manfred Fiebig
2. Gutachter: Prof. Dr. Karl Maier

Tag der Promotion: 16.11.2012

Erscheinungsjahr: 2013

Abstract

The magnetoelectric effect has attracted tremendous attention in the past decade because it is highly interesting for applications. In particular, magnetoelectric switching allows to switch a magnetic order by an electric field. This effect may be used in novel memory devices and is potentially very energy efficient.

Also from the physics point of view, magnetoelectric switching is a fascinating topic. It is based on a complex interdependence of the electric and magnetic order in the material. Their coupling is intrinsically strong in magnetically-induced ferroelectrics, among which spin-spiral multiferroics are most prominent. Here, the ferroelectric polarization is formed as a consequence of a complex spiral magnetic order. Due to this inherent coupling spin-spiral multiferroics are promising materials for reliable magnetoelectric switching.

Even though the switching speed is crucial for applications, its timescale has been unknown up to now. Moreover, hardly any work was devoted to the dynamic aspects of the actual switching process so far.

In the present work, we investigate the magnetoelectric switching properties of two selected spin-spiral multiferroics, MnWO_4 and CuO using optical Second Harmonic Generation (SHG). Since ferroic switching processes are generally governed by the nucleation and grow of domain, a major focus is set on the determination and analysis of the domains structures in static, quasi-static and dynamic conditions. For this purpose, an electrical-pump–optical-probe method was developed, which allows to reconstruct the evolution of the three-dimensional domain pattern with high temporal and spatial resolution.

For the first time, we determined the actual magnetoelectric switching time. The observed time scale on the order of milliseconds is surprisingly slow. High domain wall mobilities and the dependence on the applied electric field strength suggest, that the reason for the slow switching lies in the low ferroelectric polarization of spin-spiral multiferroics. This is backed by energy considerations.

This work provides valuable insights in two important areas of magnetoelectric switching. First, it intensely discusses the domain structures, which govern the switching process. Second, it yields pioneering work on the dynamics of the switching process. The method developed here paves the way for a systematic analysis of the yet largely unexplored field of magnetoelectric switching dynamics.

Contents

Abstract	v
Introduction	1
1 Physical background	5
1.1 Ferroics	6
1.2 Multiferroics	15
1.3 The magnetoelectric effect	18
1.4 Spin-spiral multiferroics	21
1.5 Application aspects	23
2 Experimental method	25
2.1 Second harmonic generation (SHG)	25
2.2 Experimental setups	36
3 Investigated materials	43
3.1 MnWO_4	43
3.2 CuO	54
4 MnWO_4	57
4.1 General domain structures and properties	57
4.2 Static magnetoelectric effects	68
4.3 Dynamics of magnetoelectric switching	77
4.4 Influence of growth method	94
4.5 Discussion of magnetoelectric switching	94
5 Cupric Oxide – CuO	99

5.1 Symmetry analysis	99
5.2 Experimental details	100
5.3 Characterization by SHG	101
5.4 Domains	105
5.5 Static magnetoelectric effects	106
5.6 Summary	107
Conclusion and Outlook	109
A Supplementary measurements	113
A.1 Temperature dependence	113
A.2 Signals for the generation of domain contrast	117
A.3 Spectral shifts	118
B Optical pump-probe measurements on MnWO₄	123
B.1 Experimental setup	124
B.2 800 nm pumping	124
B.3 Pump beam absorption	125
B.4 400 nm pumping	127
C MnWO₄ thin film	131
D Developed software	135
D.1 Image handling	135
D.2 Measurement program – Infinity	140
E List of measurements	145
Bibliography	147
Publications and presentations	163

Introduction

Today's information technology would be unthinkable without the possibility to efficiently store large amounts of data. Here, non-volatile memory media are of particular interest because they do not lose the information when not powered. This allows devices to be switched off completely without the need for permanent power supply via power cables or batteries. Furthermore, non-volatile memory reduces the power consumption during device operation because it does not require energy to continuously refresh its state. This is especially important for mobile devices.

Presently, most persistent data storage devices exploit the physics of ferroic order, in which the material has two stable states. Naturally these two states can be used to encode a bit. Since they are stable, ideally this information will persist forever. The most common approach uses ferromagnetic media in form of hard disk drives and magnetic tapes for large scale backup systems. Alternative schemes using a ferroelectric polarization instead of a magnetization have been developed (FeRAM) [1, 2], but possess only a small market share in niche applications [3].

Ferroic materials belong to the group of strongly correlated electron systems. These materials cannot be described any more by one electron interacting with an average background of all the other electrons. Instead, spin, charge and orbital degrees of freedom of all electrons may interact in a complex way. This results in interesting new phenomena like high-temperature superconductivity [4], giant magnetoresistance (GMR) [5, 6] and colossal magnetoresistance (CMR) [7, 8].

Not only are these effects highly interesting from a physics point of view, some of them significantly contributed to applications. The storage medium in a hard disk drive, a thin magnetic film, is the same since the early days of computer technology approximately 50 years ago. Over the years, its composition has been optimized, but the tremendous success of hard discs is based on improvements of the read-write head. Here, major discoveries in the field of strongly correlated electron systems, like the GMR effect and exchange bias [9, 10] have significantly increased the sensitivity of the sensor, which allows for higher data densities and, related to that, higher read and write speed [11].

The idea to remove any mechanical moving parts, which are prone to failure and limit access time, lead to the development of magnetic random access memory (MRAM) [12, 13]. It can be viewed as an array of magnetic cells, each provided with a read-and-write unit. Aside from GMR also other strongly correlated effects like the tunneling magnetoresistance (TMR) [14] may be used for readout [15–17]. One of the technical disadvantages of MRAM is the need for

high currents and thus high power during the writing process. In contrast the aforementioned FeRAM is very power efficient, but has certain issues with data retention and, depending on the implementation, a destructive readout. Trying to unite the advantages of both systems, one would need a material that can be written electrically, but stores information magnetically. In the field of ferroics this is known as *magnetoelectric effect* [18], in which magnetic properties are influenced by electric fields, or conversely electric properties by magnetic fields. More precisely, the influence should result in *magnetoelectric switching*, i.e. a reversal of the magnetic order as a result of the applied field.

Magnetoelectric effects have been primarily observed in materials that possess both a ferroelectric and a magnetic order, so called *multiferroics* [19–25]. Most research so far was dedicated to finding new materials and mechanisms that allow for the coexistence of both orders [26, 27]. Moreover, just having both orders present does not necessarily imply a strong coupling, and thus the possibility for magnetoelectric switching. Spin-spiral induced ferroelectricity was found to be one way out [28, 29]. Here, the magnetic order creates the ferroelectric polarization, which guarantees a strong coupling. An obstacle is the low ordering temperature of most spin-spiral multiferroics (typically < 40 K) [30–33], which hampers their use in applications. The recent discovery of spin-spiral induced ferroelectricity in materials like CuO and hexaferrites proves that this effect is not necessarily a low-temperature phenomenon and can occur at higher temperatures up to room temperature. While the ultimate material is yet to be found, these developments give hope that suitable materials exist.

Apart from further search for suitable materials, more knowledge is required on the magnetoelectric properties of the materials already known today. Despite being known since the 1960s and intensive research during the past decade, many important aspects of magnetoelectric switching are still unknown. From ferroelectrics and ferromagnets we know that domains and domain wall motion plays a crucial role in the switching of ferroics. Up to now there are only some results on static domain structures in multiferroics [34–38]. More generally, reports on the dynamics in multiferroics are scarce. While direct AC response has been measured in magnetostrictive-piezoelectric compounds at microwave frequencies [18], time domain measurements had insufficient temporal resolution [39, 40]. Collective excitations of the electric and magnetic system, so-called electromagnons, were studied using terahertz waves [41]. Furthermore optical pump-probe experiments give insight into the ultrafast recovery of the multiferroic order after optical pumping [42, 43] and on the dynamics of phase transitions [44]. However, no experiments have been performed so far, in which magnetoelectric switching was temporally resolved. In particular, the switching time, one of the most important parameters for applications, is yet unknown. Furthermore, nothing is known about the domain dynamics during magnetoelectric switching.

It is the aim of this thesis to investigate these aspects of magnetoelectric switching. For the first time, we directly measure the actual switching speed in the time domain and its dependence on external parameters like temperature and applied field strength. Since domains play a major role in ferroic switching, particular emphasis is put on the domain patterns during equilibrium and non-equilibrium states of the switching process. Two model compounds were chosen for the investigation. MnWO_4 is a well known representative for classical low-temperature spin-spiral induced multiferroicity [45]. On the other hand, with an ordering

temperature of 230 K, CuO belongs to the novel high-temperature multiferroics [46].

We apply the method of *Optical Second Harmonic Generation* (SHG) as measurement technique to study multiferroics [47]. Since this technique is symmetry based, it allows for the measurement of any ferroic order, including antiferromagnetic spin spirals. Often it is even possible to distinguish between different ferroic orders in the material, which allows to probe the magnetic and the electric subsystem separately in a magnetoelectric switching process. As an optical technique, SHG allows imaging down to the optical diffraction limit ($\approx 1 \mu\text{m}$). This is important for the observations of domains, whose evolution govern the magnetoelectric switching process. Finally, laser pulses can be made very short in time, allowing for a high temporal resolution in time-resolved measurements of the magnetoelectric switching. Both temporal and spatial resolution can be combined to obtain the evolution of the complete domain pattern.

This work is structured in the following way:

Chapter 1 introduces the physics of multiferroics and of the magnetoelectric effect. In particular, we focus on magnetically induced ferroelectricity in spin-spiral materials, which guarantee a strong coupling between the electric and magnetic order.

Chapter 2 explains the basic principles of the experimental method (SHG). A number of techniques and setups were developed in the course of this work. They allow the measurement of different static and dynamic aspects of the magnetoelectric effect and are detailed also in that chapter.

Chapter 3 is dedicated to the materials under investigation, MnWO_4 and CuO. It summarizes previous results on their multiferroic and magnetoelectric properties.

Chapter 4 contains the experimental results on MnWO_4 . Static as well as dynamic magnetoelectric properties are discussed. Aside from integral measurements like hysteresis loops and overall switching speed, special emphasis is put on the structure of the domain pattern and its temporal evolution during magnetoelectric switching. Furthermore we determine the influence of external parameters like temperature and electric field strength on the switching speed.

Chapter 5 presents the measurements on CuO. Since no SHG measurements have been performed on CuO before, in the first part of the chapter, fundamental characterizing measurements like polarization and spectral dependencies are presented. That way, signals coupling to the multiferroic order were identified and used for temperature measurements and domain images. Also we provide first results on the influence of external electric fields.

Chapter 1

Physical background

It is commonly known that the magnetization in ferromagnetic materials can be switched by magnetic fields. Likewise, ferroelectrics can be switched by electric fields. This is a general feature of ferroic materials. By definition a ferroic order has to be switchable by its conjugate field. But what about crosswise effects? Indeed, it is possible to reverse a ferroelectric polarization by a magnetic field and to reverse a magnetization by an electric field in some materials. These processes are called *magnetolectric switching*. In a more general definition this includes also the switching of an antiferromagnetic order using electric fields. The present work investigates the latter process in detail.

How does magnetolectric switching work? Electric dipoles align in an electric field and magnetic moments align in a magnetic field. However, fields other than the conjugate field do not have a direct influence. Thus, a magnetolectric effect is mediated via the order, which is conjugate to the field and a coupling between the electric and the magnetic system. If we manipulate a magnetic state with an electric field, the actual physics splits up into two parts: A change of the electric polarization in the material and the magnetic system reacting to that change:

$$\text{Electric Field} \rightarrow \text{Electric Polarization} \overset{\text{ME Coupling}}{\leftrightarrow} \text{Magnetic Order} \quad .$$

Therefore, at the core of every magnetolectric effect there is the *magnetolectric coupling*, i.e. a coupling between charges and magnetic moments in the material. This definition of the magnetolectric effect is phenomenological. As a consequence, the coupling can be caused by a large variety of physical mechanisms.

If reliable magnetolectric switching is desired, one needs a rigid coupling mechanism. The magnetic order should be one-to-one correlated to the electric polarization to guarantee its reversal. This is true only for some coupling mechanisms. Among them, magnetically induced ferroelectricity in spin-spiral multiferroics is the most prominent one. Here, polarization forms as a consequence of a spiral magnetic order. The sign of the magnetically induced ferroelectric polarization directly depends on the helicity of the spin spiral. Because of this magnetolectric coupling, the helicity of the spin spiral can be switched using an electric field.

This chapter introduces the background information necessary to understand magnetoelectric switching in spin spiral multiferroics. First, we discuss basic features of ferroic orders including their switching properties. As a second step, properties of multiferroics, particularly magnetically induced ferroelectrics with spiral spin order, are summarized. Special emphasis is put on the magnetoelectric coupling mechanism in this class of materials. An additional section puts the magnetoelectric switching in a broader context of the magnetoelectric effect. Finally, we briefly discuss application aspects.

1.1 Ferroics

The term "ferroics" was first introduced around 1970 to summarize ferromagnetic, ferroelectric and ferroelastic materials [48, 49], when people noted that all of these material classes have conceptually similar properties. They all possess different energetically equivalent orientation states, i.e. directions of magnetization, ferroelectric polarization or strain respectively. Furthermore, it is possible to switch between these orientation states by applying an external field.

Before giving a rigorous definition of ferroics, we describe their basic features at the example of ferroelectricity in the perovskite structure (figure 1.1). In the high temperature phase, the cation is located in the center of the cube, resulting in an inversion symmetric structure (a). Below a *critical temperature* T_C it is energetically favorable for the central cation to bind to one of the anions. Assume for simplicity that it can only bind to the top or bottom anion and, consequently, it will move up (b) or down (c). The shift of the ion results in a net electric polarization \mathcal{P} , which is the *order parameter* in this case. By definition, an order parameter is a quantity which is zero above the phase transition and finite below. If the ion has moved up, the polarization will be positive. Conversely, a downward shift results in a negative polarization. Both states are energetically equivalent, but have a different sign (or, in general, phase) of the order parameter. Since both states are equally probable, there can be regions with polarization pointing up and other regions with polarizations pointing down in a larger crystal. These regions of a constant orientation of the order parameter are called *domains*. The lost inversion symmetry at the phase transition results in a lower symmetry of the new phase.. The lost symmetry operation transforms the different domain states into each other: applying the inversion to a polarization pointing up, results in a polarization pointing down. It is possible to switch between the domain states by applying an external electric field along the polarization axis. This energetically favors one orientation of the polarization over the other. If the field is stronger than a critical value, the *coercive field* E_C , it will enforce the reversal of the polarization.

After giving an intuitive idea of a ferroic phase transition, we now introduce the formal definition [50]:

"A ferroic phase transition is a phase transition that is non-disruptive and changes the point-group symmetry."

The non-disruption criterion means that change from one phase to the other can be described by a continuous transformation. For the perovskite example above, this transformation is the

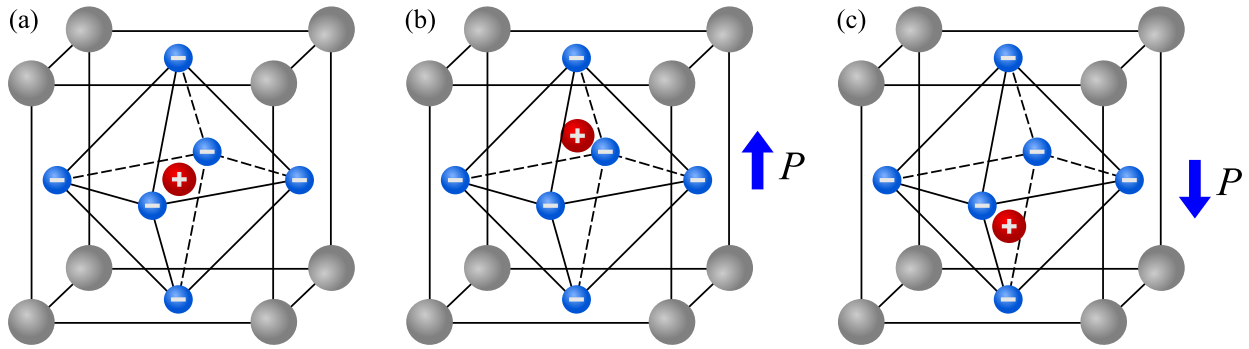


Figure 1.1 – Illustration of a ferroelectric phase transition at the example of a perovskite structure.

(a) Above the phase transition temperature T_C , the cation (marked red) is centered. There is no net polarization because the centers of the positive and the negative charge distributions coincide.

(b), (c) Below T_C , the ion off-centers, giving rise to a finite polarization \mathcal{P} , which is the order parameter. There are different energetically equivalent orientations of the order parameter, which results in the existence of domains. It is possible to switch between these different stable configuration by applying an external field along the direction of \mathcal{P} .

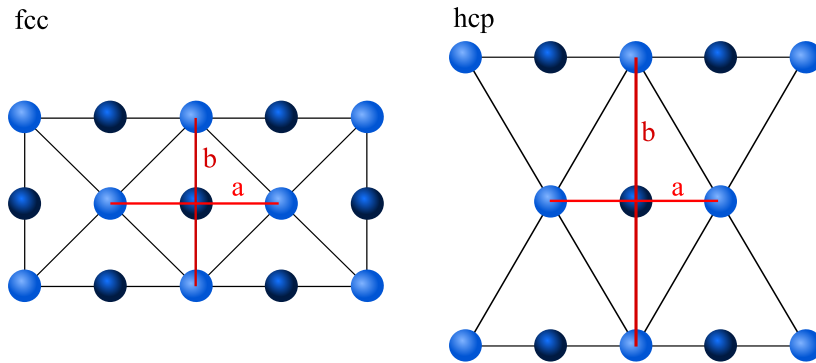


Figure 1.2 – Example of a disruptive phase transition. Depicted are views on fcc and hcp crystal structures along the c axis. Darker circles represent atoms that are shifted half a unit cell, i.e. located at $c = 1/2$. In a fcc \rightarrow hcp phase transition the ratio $\frac{b}{a}$ has to change discontinuously from 1 to $\sqrt{3}$. No values in between are possible.

shift of the central atom, which can be continuously increased from zero. An example of a disruptive phase transition is the change from a fcc to a bcc lattice (figure 1.2). The ratio of the distances $\frac{b}{a}$ has to change discontinuously from 1 to $\sqrt{3}$ because crystal structures with values in between are not possible.

The non-disruption criterion is necessary but not sufficient for a ferroic phase transition. Additionally, a change of point-group symmetry is required.

1.1.1 Landau theory

Landau theory can be used to describe ferroic phase transitions [51–53].¹ It formulates the free energy as a polynomial of the order parameter. Taking the simplest form for a ferroelectric

¹Aside from *Landau theory*, also other terms are found in the literature. Sometimes the theory is named Landau-Ginzburg theory. Shortly after Landau, Devonshire independently developed a physically equivalent theory. Therefore, also the name Landau-Devonshire theory is found, and also Landau-Ginzburg-Devonshire theory. For brevity we will only use Landau theory in the following.

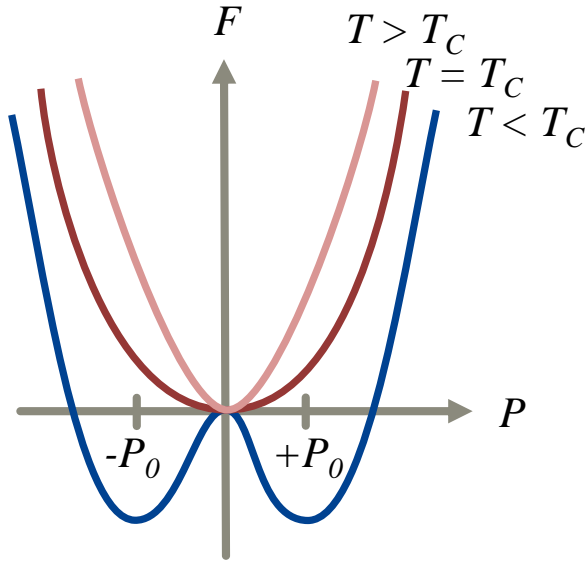


Figure 1.3 – Free energy potential of a ferroelectric phase transition as described by Landau theory (equation (1.1)). There is only one minimum for temperatures higher than the phase transition temperature T_C . It is located at $\mathcal{P} = 0$, implying that the material is paraelectric. Below the phase transition ($T < T_C$), the shape of the potential changes to a double-well structure. Its minima at $\pm P_0$ constitute the equilibrium polarization values. Since they are equal in energy, the ground state is degenerate and the material will realize either one with equal probability.

material, the free energy reads

$$F = \frac{\alpha}{2}\mathcal{P}^2 + \frac{\beta}{4}\mathcal{P}^4 \quad , \quad (1.1)$$

where the electric polarization \mathcal{P} is the order parameter. α and β are the coefficients of the polynomial. The simplest approximation for introducing a temperature dependence is a linear scaling of the coefficient $\alpha = a(T - T_C)$, where T_C is the critical temperature and $a > 0$. In the form of Equation (1.1), β has to be positive for stability. Otherwise, increasing \mathcal{P} would infinitely decrease the free energy. Figure 1.3 shows the the shape of F above and below T_C . Equilibrium values of \mathcal{P} correspond to minima of the free energy. Since α is positive for $T > T_C$, only one minimum exists at $\mathcal{P} = 0$, implying that the material is paraelectric. In contrast, two minima at $\mathcal{P}_0 = \pm\sqrt{-\frac{\alpha}{\beta}}$ emerge, when lowering the temperature below T_C . They represent the two possible orientations of the spontaneous polarization.

The temperature dependence of the equilibrium polarization magnitude directly follows from the one of $\alpha(T)$: $|\mathcal{P}_0(T)| \propto \sqrt{T_C - T}$. Because the polarization sets in continuously at T_C , this phase transition is of *second order*. With a modified free energy, also *first order* phase transitions are possible, in which the order parameter itself changes discontinuously.

The above example illustrated Landau theory for a ferroelectric system. However, Landau theory is a general concept that applies to all kinds of ferroic order. It does not depend on the physical realization of the order parameter. Of course, different systems may require other coefficients and different additional terms in the free energy (equation (1.1)). In a strict sense, the expansion of the free energy in terms of the order parameter is only valid for an infinitesimal region below the phase transition. However, Landau theory has proven to qualitatively and sometimes quantitatively describe many systems [53].

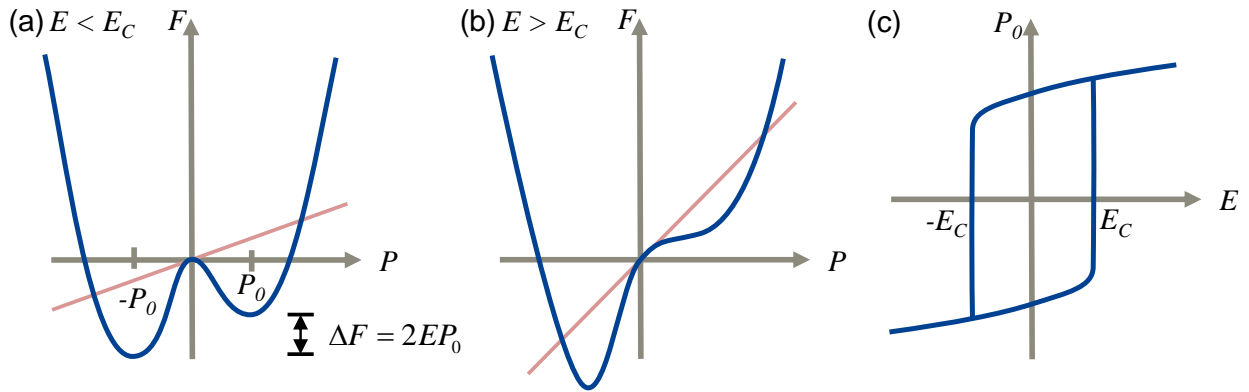


Figure 1.4 – Influence of an electric field on the free energy potential in Landau theory. The red line depicts the energy term EP .

(a) A weak electric field rises the energy of one minimum and decreases the one of the other. However, the upper minimum is still meta stable, so that a material in that state would not switch yet.

(b) If the electric field exceeds the coercive field, the former upper energy minimum vanishes. Therefore, the material has to switch to the only one remaining minimum.

(c) The electric field dependence of the polarization exhibits a hysteresis.

Landau theory of switching

Landau theory can be extended to describe the switching of the order parameter by an external field. For the example of a ferroelectric the electric field E has to be incorporated into equation (1.1):

$$F = \frac{\alpha}{2}\mathcal{P}^2 + \frac{\beta}{4}\mathcal{P}^4 - E\mathcal{P} \quad . \quad (1.2)$$

This results in a deformation of the free energy (figure 1.4 (a)). One of the minima is raised by an amount EP , while the other one is lowered by the same amount, creating a preferred orientation for the polarization. Assume that the material is in state $+P_0$ and we apply a negative field. Then $-P_0$ becomes the global minimum. However, as long as the field is weak, the material cannot overcome the barrier between the two states. This results in a hysteresis, i.e. the direction of the polarization depends on the history of the sample in low or zero electric field. Only when the field strength exceeds a critical value, the coercive field E_C , switching is induced (figure 1.4 (b)).

The local minima in the Landau potential describe possible ground states of the system. If the electric field is changed slowly, also the minima will move slowly and the system will progress through a series of ground states. Therefore, a quasi-static hysteresis loop can be calculated directly from Landau theory (figure 1.4 (c)).

The coercive field E_C is the critical field strength required to reverse the polarization direction. It turns out that measured coercive fields are smaller than the ones predicted by Landau theory [54]. This can be explained by the fact that Landau theory is a mean field theory, in which all dipoles in the sample have to switch at the same time. Usually, this does not happen in a real crystal. Instead, domains nucleate at defects and grow by domain wall motion [55,

56]. The energy to switch the polarization may be significantly lowered at a defect. This corresponds to a locally lowered energy barrier in the Landau picture. It can be incorporated into Landau theory by discretizing the sample volume and minimizing the free energy for every volume element [57, 58]. Then, an additional coupling term can be introduced to account for domain wall costs. The increased accuracy of the model is paid for by the fact that these coupled equations can only be solved numerically. Since we will use Landau theory only for a qualitative interpretation, we will stick to the mean field version for explanations.

Switching Dynamics

The Landau free energy describes the energy potential of the system. Aside from defining the ground states as its minima, the potential also determines the dynamics in non-equilibrium situations. This is described by the Landau-Khalatnikov equation [58, 59]:

$$\gamma \frac{\partial \mathcal{P}}{\partial t} = - \frac{dF}{d\mathcal{P}} \quad , \quad (1.3)$$

where γ is a viscosity coefficient containing the material properties. It states that the rate of change of the polarization directly scales with the curvature of the free energy. Because of the minus sign, the polarization moves towards the next local minimum. The solution of this differential equation describes the temporal evolution of the polarization $\mathcal{P}(t)$ also in non-equilibrium states. In particular, it contains the switching time of the process.

Even for the relatively simple case of equation (1.2), the Landau-Khalatnikov equation can only be solved numerically. Nevertheless, one observation can already be deduced without exactly solving it. Let the system be in state $+\mathcal{P}_0$. If a negative electric field larger than the coercive field is applied instantaneously, the free energy possess only one minimum at $-\mathcal{P}_0$ (c.f. figure 1.4 (b)). From there it rises monotonically to $+\mathcal{P}_0$. The slope $\frac{dF}{d\mathcal{P}}$ will be the larger, the higher the applied field is. It follows immediately from equation (1.3) that the switching time will decrease with increasing electric field.

Also this equation is just a mean field approximation, which does not contain the influence of domain wall motion.

1.1.2 Types of ferroics

There are four types of ferroic orders: ferromagnetism, ferroelectricity, ferroelasticity and ferrotoroidicity. Ferromagnetism and ferroelectricity have already been introduced above. Ferroelasticity describes the spontaneous strain in a material, which may be influenced by external stress fields. Finally, as a recent development, ferrotoroidicity has been recognized as a fourth type of ferroic order [60, 61]. The order parameter is the toroidal moment, which arises in magnetic vortex structures.

The different types of ferroic order can be distinguished by their symmetry behavior under space inversion ($\mathbf{r} \rightarrow -\mathbf{r}$) inversion and time reversal ($t \rightarrow -t$). In the context of ferroics, time reversal means the reversal of magnetic moments. This equivalence can be visualized by

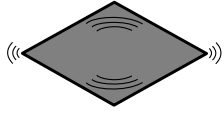
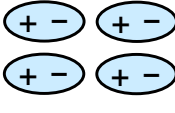
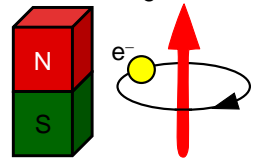
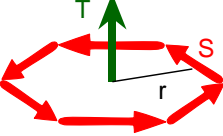
Time \ Space	Invariant	Change
Invariant	Ferroelastic 	Ferroelectric 
Change	Ferromagnetic 	Ferrotoroidic 

Figure 1.5 – Each primary ferroic order possesses a different symmetry under space inversion and time reversal. In particular, ferromagnetic structures are invariant under space inversion. However, the spatial arrangement of the spins itself can break the space inversion symmetry. This is a necessary requirement for magnetically induced ferroelectricity and is realized in spin spirals, for example. [60]

considering a magnetic moment generated from orbital angular momentum. In a classical picture the electron can be considered on a circular orbit. The orbital angular momentum $L = r \times p$ and hence the magnetic moment is an axial vector. Upon time reversal the electron will circle the other way round. This reverses the sign of the momentum and consequently also the magnetic moment. In contrast, being an axial vector, the magnetic moment does not reverse under space inversion.

Each of the four ferroic orders has a different symmetry behavior (figure 1.5). In particular, ferroelectricity requires a broken space inversion symmetry. While a single magnetic moment is inversion symmetric, the spatial distribution of magnetic moments in the material can break the inversion symmetry, resulting in magnetically induced ferroelectricity. This is for example the case in spin spirals, as will be detailed in section 1.4.

Because spin spirals are antiferromagnetic and induce a ferroelectric polarization, we will focus on these two orders in the following.

1.1.3 Antiferromagnets

Antiferromagnets are magnetic materials, in which the orientation of the magnetic moments is distributed in such a way that they cancel completely. Thus, there is no net magnetization. In contrast to paramagnetism, which does not exhibit a magnetization either, an antiferromagnetic state is ordered.

The simplest form of an antiferromagnet is formed by aligning adjacent magnetic moments antiparallel (figure 1.6 (a)). Also spin spirals are antiferromagnetic because the continuous rotation of the spins averages out to zero net magnetic moment (figure 1.6 (b)).

Antiferromagnets are not ferroic because there is no macroscopic physical quantity that corresponds to the order parameter. Consequently, there exists no conjugate field that could be used to switch between the different degenerate energy minima. Apart from this, the above mechanism of spontaneous symmetry breaking and the properties following from that also

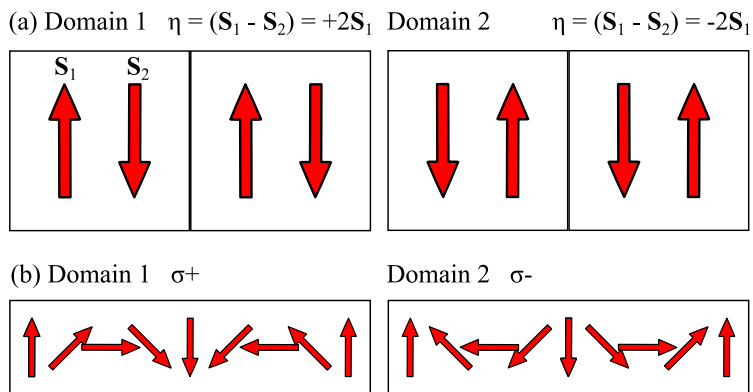


Figure 1.6 – Illustration of antiferromagnetic domains

(a) Simple Heisenberg-Antiferromagnet. Displayed are the two possible domain states. The order parameter is defined as a linear combination of spins in the unit cell $\eta = S_1 - S_2$. Therefore, its sign marks the domain state.

(b) Transversal spin spiral. The domains differ in the sense of rotation of the spins.

apply to antiferromagnets. Even though the sum off all magnetic moments is zero, one can define the order parameter as certain linear combination of the magnetic moments in the unit cell (figure 1.6). Consequently there are also domains in antiferromagnets, as will be detailed in the next section.

1.1.4 Domains

Domains represent regions of uniform order parameter orientation. Switching in ferroics usually does not happen homogeneously but by nucleation and growth of reverse domains until the other single domain state is reached. Therefore, it is essential to understand the domains of a ferroic material when investigating its switching properties. After illustrating typical aspects of domains at the example of ferromagnetic domains [62], the concepts explained here are transferred to ferroelectrics and antiferromagnets. There is little knowledge on domains in magnetoelectric switching. Since magnetoelectric switching is ferroelectric switching with a coupled magnetic order, at least we will introduce typical domain aspects of ferroelectric switching. These are later compared to our experimental findings on magnetoelectric switching.

Ferromagnetic domains

In a ferromagnet the exchange interaction enforces a parallel alignment of the magnetic moments. This leads to a macroscopic magnetization, which is the order parameter. It points into different directions in adjacent domains. The adjacent domains are separated by a domain wall, which costs energy due to a not fully satisfied exchange interaction inside the wall. This disfavors domain walls and results in macroscopic domain sizes. On the other hand, a fully aligned ferromagnet has a stray field, which itself contains energy. Domains can be formed to reduce this stray field, leading to a lowered magnetization. Therefore, this field is also called demagnetizing field. As a result the ground state may be multi-domain. The actual domain size results from a competition between the energy of the demagnetizing field and the domain wall energy.

The orientation of the domain walls in the material depends on the microscopic physics. Exchange paths along different crystallographic directions may not be equally large. Since

every domain wall costs exchange energy, it is favorable to align a wall normal to the direction of weakest exchange.

Domain walls themselves are usually not atomically sharp. For example in 180° domains the magnetic moment continuously rotates by 180° . The actual width of the the wall is determined by a competition between exchange energy and anisotropy energy. Typical ferromagnetic wall widths are on the order of a few ten nanometers [63]. Furthermore, the rotation vector can either be normal to the domain wall (Bloch wall) or it can lie in the plane of the wall (Néel wall).

The application of an external magnetic field energetically favors the one domain state over the other. Consequently the material tries to enlarge domains of this orientation at the expense of the other one. This is achieved by the movement of domain walls.

Defects in the material can hinder the free motion of domain walls [63]. A wall can be pinned to a defect because the local magnetic or crystal structure is modified at a defect. It can be energetically favorable to incorporate the defect into the wall. The pinning can be overcome in higher external magnetic fields, as soon as the field energy of the domain configuration outweighs the energy gain of the pinning. As a result, pinning increases the remanence and the coercive field.

Antiferromagnetic domains

Like in a ferromagnet, antiferromagnetic domain walls cost energy because of not completely satisfied exchange interactions. But in contrast to ferromagnets there is no equivalence to a demagnetizing field. From the point of view of a global minimum of the free energy, antiferromagnets should be single domain. However, it is experimentally found that also antiferromagnets are usually in a multi-domain state. The reason is found in the emergence of the order at the phase transition. When crossing the critical temperature, the material has to choose one of the degenerate ground states. Different regions may choose different orientations of the order parameter, resulting in a multi-domain state. Furthermore, pinning can hinder the expansion of nucleated domains, which enforces the independent choice in spatially separated regions.

Since the demagnetizing field favors small domains, its absence causes antiferromagnetic domains to be larger than ferromagnetic ones.

Because the net magnetic moment of an antiferromagnet is zero, it cannot be switched by an external magnetic field. However, a number of indirect methods like optical excitation or spin polarized tunnel currents have been used to manipulate antiferromagnetic structures [64–66].

Ferroelectric domains

The fundamental types of competing energies in ferroelectrics are the same as in ferromagnets: Domain wall energy, depolarizing field and energy of the domains in the external field. Consequently, some main aspects of ferroelectric and ferromagnetic domains are similar. The ground state is typically multi-domain and results from competition between domain wall

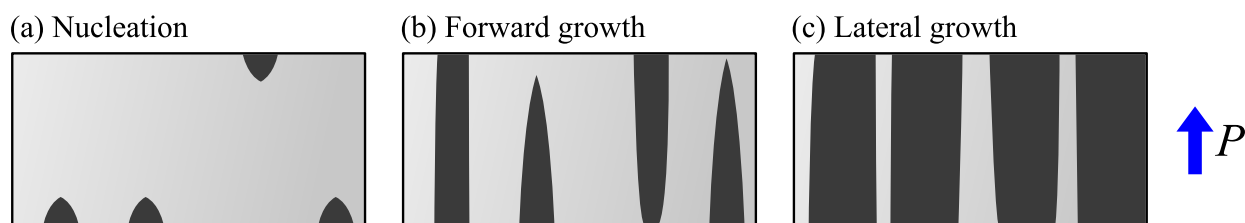


Figure 1.7 – Ferroelectric switching is a three-stage process. First reverse domains nucleate. These grow forward along the polarization direction, followed by a slower lateral growth perpendicular to the polarization direction.

energy and depolarizing field. Ferroelectrics can be switched by an external electric field. The switching process usually consists of the nucleation of the reversed domains and their growth by domain wall motion. Here, too, pinning of the domain walls at defects can influence the hysteresis loop [67, 68].

Due to the dipolar character of the polarization and its coupling via the long-range Coulomb interaction, there is a strong anisotropy of the energy cost of domain walls. This often leads to the formation of stripe domain patterns.

Domain walls

Domain walls are the transition regions between different domains. They are not atomically sharp, but possess a certain width, in which the order is gradually adapted from one state to the other. Typical domain wall widths in ferromagnets are on the order of 100 unit cells, which results from a competition between exchange energy and anisotropy energy [62]. In contrast, domain walls in simple Heisenberg antiferromagnets extend only across very few unit cells [69]. The same is true for ferroelectric domain walls [70]. One thus might draw the conclusion that domain walls in spin-spiral multiferroics should also be very narrow. However, a high domain wall relaxation rate obtained from frequency dependent giant magneto-capacitance measurements as well as simulations suggest wider domain walls of approximately 20 unit cells [71].

Switching of ferroelectric domains

After application of an electric field, switching in ferroelectrics occurs in a three-stage process (figure 1.7) [72]:

1. Nucleation of reverse domains
2. Forward growth along the polarization direction
3. Lateral growth perpendicular to the polarization direction

Depending on the nucleation rate and the domain wall velocity, this switching can be either nucleation-limited or growth limited. Both types exhibit different dynamics figure 1.8 [73].

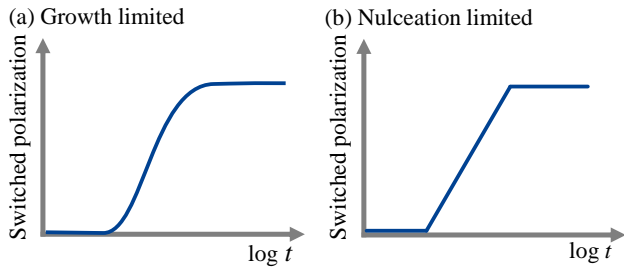


Figure 1.8 – Dependence of the temporal evolution of switched polarization on the type of the switching process [73].

(a) In growth-limit switching, the domain walls move at a constant velocity, resulting in a linear or quadratical time-dependence of the switched polarization.

(b) Nucleation-limited switching assumes independent domain nucleation, with an exponential distribution of the switching times.

Nucleation-limited switching (NLS) assumes that domains nucleate independently of each other in the sample [74]. This is a statistical process in which the times at which switching occurs are often exponentially distributed, leading to an exponential switching curve.

In the growth-limited switching, the nucleation of reverse domains is considered instantaneous after applying the field. The limiting factor in this process is the growth of the domains via domain wall motion. This process is modeled in the Kolmogorov-Avrami-Ishibasi (KAI) model [75]. Here, the domain wall velocity only depends on the magnitude of the applied electric field, but not on domain size or shape.

Both switching types are experimentally observed in various materials, however, there appears to be a tendency that switching in bulk materials is growth limited while switching of thin-films is rather nucleation limited [76].

Even though the domains and dynamics in ferroelectric switching have been investigated for more than 50 years, many aspects are still to be understood [73]. Therefore it continues to be an active area of research [77].

1.2 Multiferroics

Multiferroics are by definition materials that exhibit more than one ferroic order in the same phase [78]. Though originally not included, antiferroic orders are nowadays also included in this definition. Therefore, a ferroelectric antiferromagnet is a multiferroic. While any combination of (anti-)ferroic orders is possible in principle, most multiferroics investigated nowadays are ferroelectric (anti-)ferromagnets and often when people speak of multiferroics they only mean this group of multiferroics [79]. This convention is also adopted in the rest of the present work.

The large interest in multiferroics [18, 27, 79–81] is based on the fact that their ferroic orders may interact and thus can exhibit fundamentally new physics and possibilities for applications. Most prominent is the magnetoelectric effect, in which a magnetic order can be influenced by an electric field or, conversely, an electric order by a magnetic field (section 1.3).

Even when disregarding the coupling between magnetic and electric order, it is not trivial to unite both phases in one material. The reason is that the most common mechanisms of ferroelectricity and magnetism are mutually exclusive [26]. On the one hand, the conventional mechanism of displacive ferroelectricity, like e.g. for BaTiO_3 as discussed in figure 1.1, requires

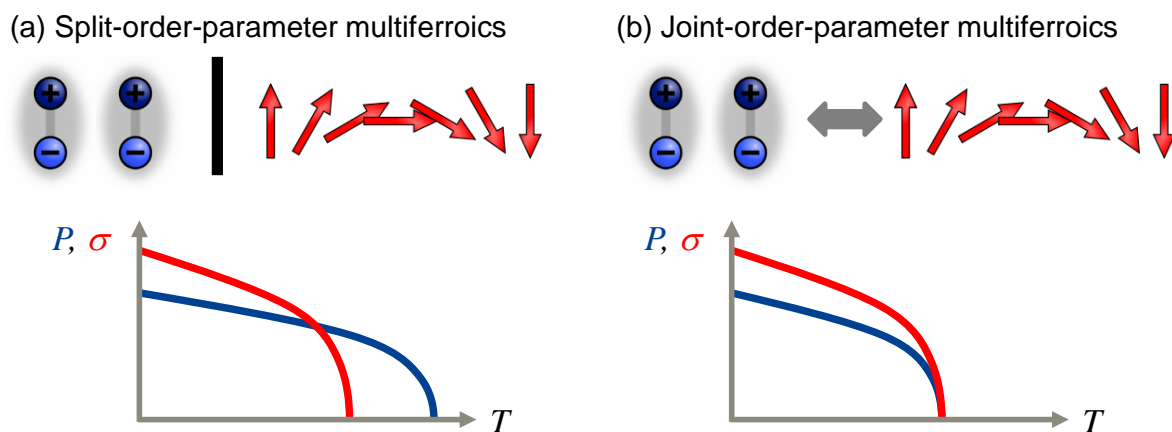


Figure 1.9 – Schematic illustration of the types of multiferroics.

(a) The electric and magnetic order in *split-order-parameter multiferroics* are not directly related to each other. They set in at different temperatures and are usually not coupled.

(b) Both orders have a common cause in *joint-order-parameter multiferroics*. Therefore, they appear simultaneously and exhibit a magnetoelectric coupling. Note that the image is a simplification because there can be more than one magnetic order parameter and the polarization might set in simultaneous only with one of them.

empty electron $3d$ shells. On the other hand, the magnetic moments in transition metal elements arise from partially filled $3d$ shells. Therefore, significant research went into the identification of alternative mechanisms that provide ferroelectricity and are compatible with partial filled $3d$ shells.

One distinguishes two classes of these mechanisms. The first one is compatible with the magnetic order, but is not related to it. The materials belonging to this class are termed *split-order-parameter multiferroics* [38, 82] or *Type I* [81] multiferroics. In contrast, the magnetic order is directly responsible for the emergence of ferroelectricity in *joint-order-parameter multiferroics* or *Type II* multiferroics. Sometimes these materials are also called magnetically induced ferroelectrics. Considering the coupling of the ferroic orders, the two classes exhibit fundamentally different physics, as will be detailed in the following.

1.2.1 Split-order-parameter multiferroics

Magnetic and electric order in split-order-parameter multiferroics are not inherently related to each other. For example, different atoms in the unit cell may be responsible for the existence of each order. They just happen to be simultaneously present in a material, but are triggered by different physical mechanisms. This is also reflected by the fact that the orders usually set in at different temperatures (figure 1.9 (a)).

Mechanisms that generate ferroelectricity in split-order-parameter multiferroics are the existence of lone-pairs, geometrical ferroelectricity and charge order [27].

If a magnetoelectric coupling exists at all, it is usually weak because the orders are not related. Typical coupling mechanisms involve stress (i.e. indirect coupling via piezoelectricity

and magnetostriction) or clamping of domain walls. Examples for split-order-parameter multiferroics are BiFeO_3 [83, 84] and the hexagonal manganites RMnO_3 ($R = \text{Sc, Y, Dy, Ho, Er, Tm, Yb, Lu}$) [85, 86].

1.2.2 Joint-order-parameter multiferroics

The ferroelectric order in joint-order-parameter multiferroics is created by specific types of magnetic order. As soon as such a magnetic order sets in, the ferroelectric polarization arises. Therefore, both orders appear jointly at the same temperature (figure 1.9 (b)).

It follows from symmetry considerations that the magnetic order itself already has to break space inversion to allow for a ferroelectric polarization (figure 1.5). Certain spiral spin structures fulfill this requirement, in particular cycloidal spin spirals. Inversion translates a right-handed spiral to a left handed spiral and is thus not a symmetry operation of the magnetic state. The details of spin spirals are explained in the dedicated section 1.4. There are also other non-centrosymmetric structures, which give rise to magnetically induced ferroelectricity. One example is a certain up-up-down-down collinear antiferromagnetic arrangement ($\uparrow\uparrow\downarrow\downarrow$) found in orthorhombic HoMnO_3 [87] and in the RMn_2O_5 series ($R = \text{Y, Tb, Er, ...}$) [88, 89].

Because one order generates the other, there is an intrinsically strong coupling between them. For spin spirals, this results in a one-to-one correlation between the polarization direction and the helicity of the spin spirals. The microscopic coupling mechanism will be explained in the dedicated section 1.4. If the polarization is reversed, also the helicity of the spin spiral has to change. This reflects the strong magnetoelectric coupling in spin-spiral multiferroics. Hence, this class of multiferroics is particularly promising in terms of magnetoelectric switching.

1.2.3 Proper and improper ferroic order

There is a fundamental difference, between an order parameter driving the phase transition and one which is just a secondary byproduct of another phase transition. An order parameter that is driving the phase transition is called *proper*. Examples are conventional displacive ferroelectrics and magnetic orders. An order parameter that arises only as the consequence of a proper order parameter is called *improper* [53, 90].

The temperature scaling $(T_C - T)^\beta$ is fundamentally different for proper and improper order. While a proper order parameter has an exponent of $\beta = \frac{1}{2}$ (c.f. section 1.1.1), an improper order parameter has an exponent of $\beta = 1$. Therefore, they are easily distinguishable in a temperature dependent measurement.

In spin-spiral multiferroics, the improper polarization arises from the coupling of two magnetic order parameters (equation (3.2) and (3.4)). However, for the case of MnWO_4 and most other spin-spiral multiferroics, the magnetic order parameters are activated in two successive phase transitions. It is common that the first order parameter does not critically scale with the temperature any more at the second phase transition [91, 92]. It is said to be *frozen*. Therefore, the polarization scales exactly like the second proper magnetic order parameter. Even though the magnetic system is still driving the phase transition, the temperature dependence

of the polarization looks like the one of proper ferroelectric. Such a situation is also called *pseudo-proper*.

1.3 The magnetoelectric effect

The term magnetoelectric effect is used with slightly different meanings in the literature. Historically it was first used for the *linear magnetoelectric effect*, in which a ferroelectric polarization is induced via an applied magnetic field, or vice versa, a magnetization is induced by an electric field with a linear dependence [18]. It was then found, that the induced quantity can also scale nonlinearly with the applied field. Therefore, the most common definition of the magnetoelectric effect is the induction of an electric polarization (magnetization) by an external magnetic (electric) field. This definition contains only induced quantities and thus does not directly relate to the switching of a spontaneous order. Switching is only implicitly included because induced and spontaneous order are usually not independent, switching is implicitly included. To explicitly include magnetoelectric switching, we use a slightly more general definition, which relaxes the requirement of an induced polarization or magnetization: In the most general sense, a magnetoelectric effect can be defined as an influence of a magnetic field on an electric polarization or conversely an influence of an electric field on a magnetic order, including antiferromagnetic order. This influence may either be the creation of a new order or the modification of an existing one. This broad definition also properly covers the case of electric-field-induced switching of a spin spiral, which is the focus of the present work.

The above definition is phenomenological, i.e. it only describes the effect, not the mechanism behind it. The basic scheme is always the same: Thus each magnetoelectric effect is two-step process. The field modifies its conjugate electric or magnetic system. If both systems are coupled, the other system may then react, too. It is this *magnetoelectric coupling* that is at the core of every magnetoelectric effect. There is a large variety of such coupling mechanisms. For example they can exist in the bulk or only at domain walls or interfaces. Also the coupling can be rigid, as in the the case of spin spirals (section 1.4) or indirect via strain.

Types of magnetoelectric effects

Often, the general term "magnetoelectric effect" is used also for the special case of a *linear magnetoelectric effect*. It describes a polarization \mathcal{P} induced by a magnetic field \mathbf{H} , or vice versa, a magnetization \mathbf{M} induced by an electric field \mathbf{E} [18]:

$$\mathcal{P}_{\text{ind.}} = \hat{\alpha}\mathbf{H} \quad \text{or} \quad \mathbf{M}_{\text{ind.}} = \hat{\alpha}\mathbf{E} \quad . \quad (1.4)$$

Here, $\hat{\alpha}$ is the magnetoelectric tensor. Other dependencies like the *nonlinear magnetoelectric effects*, such as $\mathcal{P} \propto \mathbf{H}^2$, $\mathbf{M} \propto \mathbf{E}^2$, and a bilinear coupling $\mathbf{M} \propto \mathbf{E}\mathbf{H}$ are possible as well. Some applications, like magnetoelectric sensors, ideally require a linear magnetoelectric effect. However, in the case of magnetoelectric switching, the response to an applied field is more complex because the switched electric or magnetic order exhibits a hysteresis.

1.3. The magnetoelectric effect

Electric-field-induced switching of a spin spiral is a magnetoelectric effect that does not rely neither on a linearly nor on a nonlinearly induced magnetization. Instead, the Dzyaloshinskii-Moriya interaction provides a direct link (section 1.4).

Relation between magnetoelectrics and multiferroics

There is no strict relation between multiferroic materials and magnetoelectric materials [79]. Magnetoelectric materials can be multiferroic or not, likewise multiferroics sometimes exhibit a magnetoelectric effect, but sometimes they do not.

Because the linear magnetoelectric coefficient is bounded by the product of electric and magnetic susceptibility, it can only be large in ferroelectric or ferromagnetic materials [93]. Therefore, a particularly strong linear magnetoelectric effect is possible in multiferroics. However, this rigorous limitation does not apply to other types of magnetoelectric effects. In the extreme case it can be sufficient to have an electrically and magnetically polarizable material. As long as there is a coupling between the electric and magnetic system, a magnetoelectric effect can exist in non-multiferroics. On the other hand, the simultaneous presence of electric and magnetic order does not necessarily imply a coupling between them. In this case, the material is not magnetoelectric.

In summary, magnetoelectrics require an electrically and magnetically polarizable material and a coupling between the electric and magnetic systems. In contrast, multiferroics require the electric and magnetic system to be ordered. Both concepts are not strictly related. However, the ordered systems are a subset of the polarizable systems, which is a prerequisite for the magnetoelectric effect. Therefore, even if it is not strictly required, many magnetoelectrics are multiferroic.

Toy model of magnetoelectric switching

In this section, we will introduce a toy model that describes the interplay between electric field and the electric and magnetic subsystems in magnetoelectric switching (figure 1.10). Since we will use this model later to describe the magnetoelectric switching in MnWO_4 , we choose spin spiral states for the magnetic system.

Each system has two extremal values. The fields $\pm E$ are assumed to be larger than the coercive fields. The maximal polarizations $\pm \mathcal{P}$ correspond to electric single domain states. Likewise the extremal values of the magnetic system represent single domain states of the magnetic helicity domains. Intermediate states in the magnetic and electric system can be interpreted as multi-domain states. The interactions between the systems are symbolized by springs. This reflects the fact that the violation of the interaction is in principle possible, but it will cost energy. While orientation dependent energy of an electric dipole in an electric field constitutes the interaction between electric field and electric system, the magnetoelectric interaction between electric and magnetic field is given by the Dzyaloshinskii-Moriya interaction as described in the next section (equation (1.5)).

This model is a strong simplification. Nevertheless, it nicely illustrates two main points of

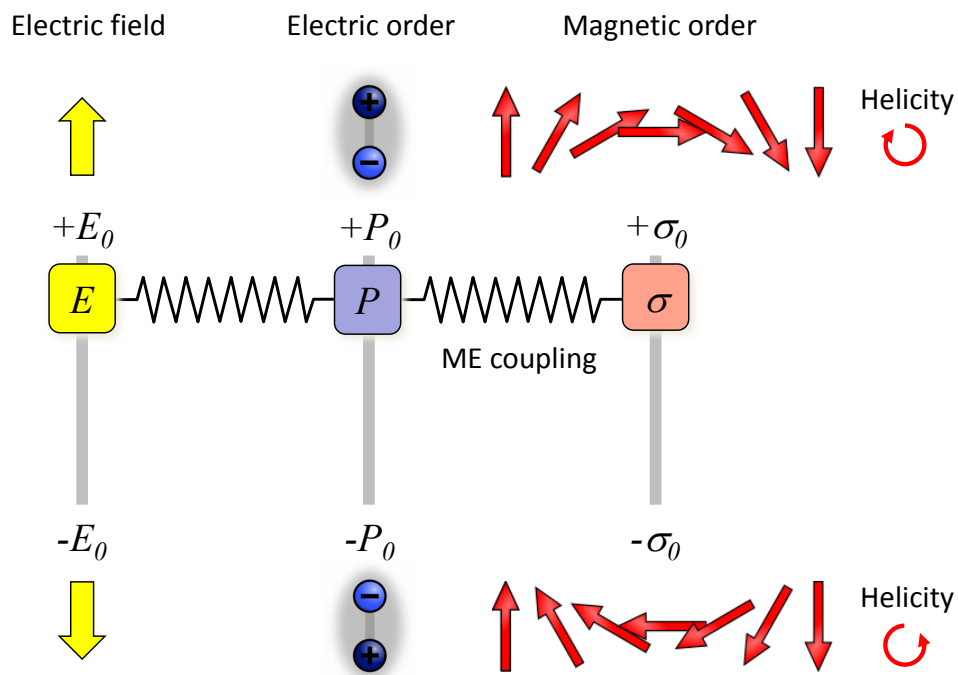


Figure 1.10 – Toy model for magnetoelectric switching in spin-spiral multiferroics.

The model depicts the systems involved in the magnetoelectric switching and their couplings. Each system has two extremal states. For the electric field these are the field values $\pm E_0$ which are larger than the coercive field. The extremal values of the polarization $\pm P_0$ and the magnetic helicity $\pm \sigma_0$ correspond to single-domain states. Intermediate values represent multi-domain states. The coupling between the systems guarantees their alignment. Non-alignment leads to increased energy, which may be seen as a spring under tension in the model.

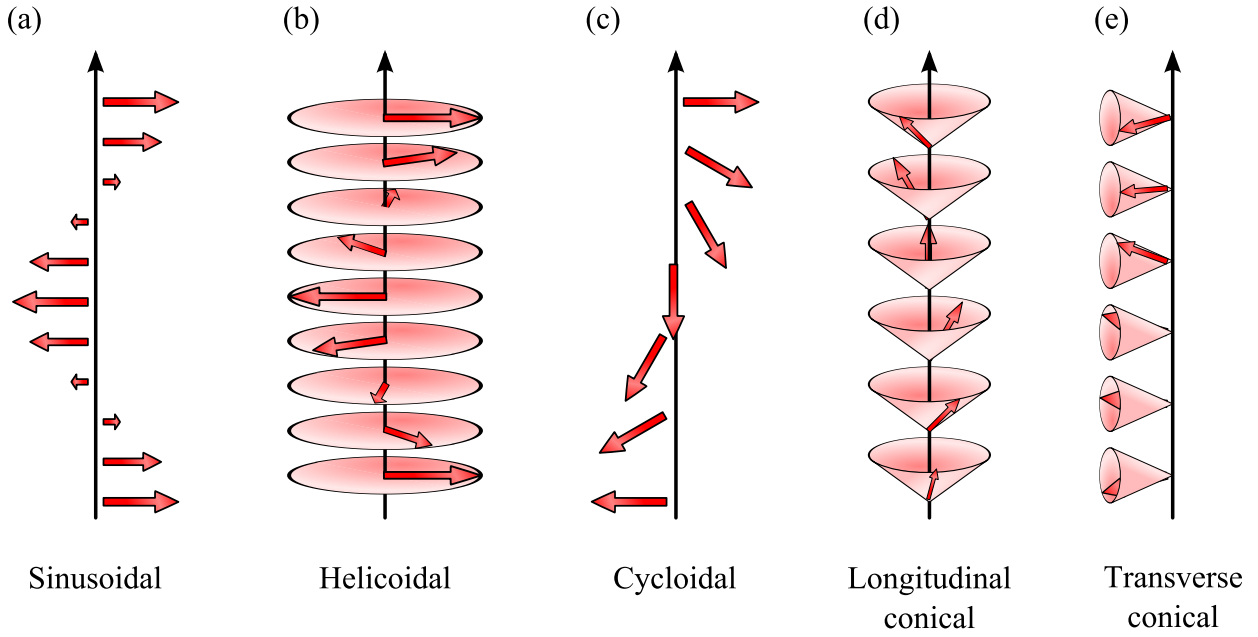


Figure 1.11 – Schematic picture of different modulated magnetic structures.

(a) sinusoidal change of the magnitude of the magnetic moments along the propagation axis.

(b), (c) The magnitude remains constant in helicoidal and cycloidal spin spirals. In the former case the rotation axis coincides with the propagation axis, while they are perpendicular in the latter case. (d), (e) In longitudinal and transverse conical spin spirals, the spins rotate not in a plane but on a cone, leading to a macroscopic magnetization.

magnetolectric switching. First, there is no direct effect of the electric field on the magnetic system. It only couples to the electric system, which mediates a change to the magnetic system via the magnetolectric interaction. Second, it allows to break the couplings, but this costs additional energy.

1.4 Spin-spiral multiferroics

Spin-spiral structures can result from *magnetic frustration*. This is a situation in which no spin arrangement exists that simultaneously fulfills all exchange paths. As a result, a compromise spin structure is obtained, which only partially fulfills these paths. Spin-spiral structures are formed for certain geometric arrangements of the spins and relative strengths of the exchange paths. Different spiral arrangements are possible (figure 1.11), among which only some can induce ferroelectricity.

The best known mechanism for the generation of a ferroelectric polarization by a spin spiral is based on the Dzyaloshinskii-Moriya interaction (DMI). This is an antisymmetric contribution to the Hamiltonian due to spin-orbit coupling [94]

$$\mathcal{H}_{\text{DMI}} = \frac{1}{2} \sum_{i,j} \mathbf{D}_{ij} \cdot (\mathbf{S}_i \times \mathbf{S}_j) \quad , \quad (1.5)$$

where \mathbf{S}_i and \mathbf{S}_j are neighboring spins and \mathbf{D}_{ij} is the *Moriya vector*. It can be expressed as

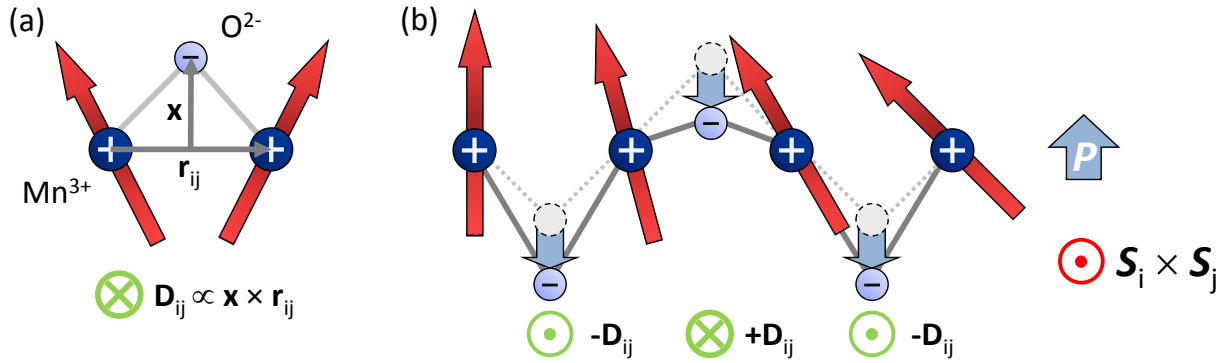


Figure 1.12 – Microscopic mechanism of the Dzyaloshinskii-Moriya interaction.

(a) The superexchange interaction between neighboring spins depends on their bond angle and thus on the displacement \mathbf{x} of the oxygen ions. The energy of the Dzyaloshinskii-Moriya interaction can be minimized for fixed bond angles of an existing spin spiral by adjusting the oxygen displacement.

(b) The Moriya vector $\mathbf{D}_{ij} \propto \mathbf{x} \times \mathbf{r}_{ij}$ alternates in sign in zig-zag chains. This leads to a homogeneous shift of the negative ions with respect to the positive ions which finally induces a polarization. Since the DMI depends on the helicity $\mathbf{S}_i \times \mathbf{S}_j$ of the spin-spiral, there is a one-to-one correlation between the helicity of the spiral and the sign of the induced polarization.

$\mathbf{D}_{ij} \propto \mathbf{x} \times \mathbf{r}_{ij}$. Here, \mathbf{r}_{ij} is the vector connecting the spins \mathbf{S}_i and \mathbf{S}_j and x is the displacement of an intermediate oxygen ion from the connection line which mediates the superexchange between the spins (figure 1.12 (a)).

If we assume that the positions of the magnetic ions and of the oxygen ion are fixed, this uniquely determines the bond angle, which in turn determines the type of exchange interaction between the spins. This is summarized in the Goodenough-Kanamori-Anderson (GKA) rules [95]. If the bond angle is 180° , an antiferromagnetic alignment is preferred. In contrast, ferromagnetic order results at 90° bond angle. Any angle in between will result in a non-collinear alignment. Therefore, through the DMI the displacement \mathbf{x} of the oxygen ions determines the spin angle and leads to the formation of a spin spiral.

Magnetically induced ferroelectricity in spin spirals works exactly the other way round. It is therefore also called the *inverse Dzyaloshinskii-Moriya interaction* [96]. If a spin spiral is present and the oxygen atoms are not fixed, the displacement \mathbf{x} can be changed to minimize the Dzyaloshinskii-Moriya energy term. If $\mathbf{x} > 0$, its absolute value is decreased, while it is increased for $\mathbf{x} < 0$.

In zig-zag chains, like depicted in figure 1.12 (b), this results in a shift of all oxygen ions in the same direction. Since they are all negatively charged and the spin carrying ions (e.g. Mn^{3+} or Cu^{2+}) carry a positive charge, this results in a shift of the negative center of charge with respect to the positive one. Hence, a macroscopic electric polarization \mathcal{P} emerges. It is perpendicular to the spin propagation axis \mathbf{r}_{ij} and in particular perpendicular to the helicity $\mathbf{S}_i \times \mathbf{S}_j$. Therefore, we can write:

$$\mathcal{P} \propto \mathbf{e}_{ij} \times \mathbf{S}_i \times \mathbf{S}_j \quad . \quad (1.6)$$

This equation shows the direct one-to-one correlation between the polarization direction and the helicity of the spin spiral.

1.5. Application aspects

Typical sizes of a magnetically induced ferroelectric polarization are on the order of 10 nC/cm^2 [97], which is three orders of magnitude smaller than polarization values of $\approx 10 \text{ }\mu\text{C/cm}^2$ observed in classical displacive ferroelectrics.

The DMI is only one possible microscopic mechanism that leads to the magnetoelectric coupling in spin spirals, but the relation 1.6 can be derived more generally in Landau theory [29]. It is a fundamental property following from symmetry. Consequently, also other microscopic mechanisms can exist that generate a spontaneous polarization from a spin spiral. Indeed that is the case for the *spin current* mechanism. A so-called *spin supercurrent* is a quantum mechanical effect that arises from virtual hopping of electrons, e.g. across a Mn–O–Mn bond and taking into account the spin of the electrons. In that sense it is the spin-polarized equivalent of double-exchange or superexchange. It is described in the Katsura-Nagaosa-Balatsky model (KNB model) [28, 98]. Because the effect is based on virtual hopping of the electrons, the ions remain fixed. The ferroelectric polarization result purely from a shift of the electrons [87].

The experimental distinction between electronic and ionic polarizations is non-trivial in spin-spiral multiferroics. The small polarization of $\approx 10 \text{ nC/cm}^2$ corresponds to an ionic shift of approximately 10^{-3} \AA . This is at the resolution limit of methods that can measure the crystal structure, like neutron scattering and X-ray diffraction. Often, it is unclear whether the ions or the electrons induced the polarization [89, 99, 100]. Both effects are supported by theoretical calculations and they may even be present simultaneously [87, 101]. Future dynamic magnetoelectric switching experiments may contribute to clarify this question because the electronic and ionic system can have different dynamic properties.

1.5 Application aspects

Even though this work focuses on the fundamental physics of magnetoelectric switching, we briefly discuss the application aspects. Both directions of the magnetoelectric effect have different uses. The effect of changing the electric polarization by a magnetic field can be used in a magnetic field sensor. The polarization results in surface charges, which can be directly measured as a voltage. For this application, the material should ideally not possess any hysteresis because otherwise the measured value would depend not only on the current magnetic field, but also on its history.

Conversely, persistent data storage applications require a hysteresis. Here, the information of one bit is encoded into two different states at zero field. These states can be written by field pulses of different signs. In particular, the inverse direction of the magnetoelectric effect is highly desirable for memory devices. It combines the advantages of ferroelectric and ferromagnetic memories. While an electric field for writing can be easily generated by a voltage, generating a magnetic field requires a current through a coil. The current results in significantly higher power consumption of magnetic writing compared to electric writing. Considering the readout process, FeRAM has the disadvantage that its readout process is destructive. After readout the information is not stored in the cell any longer and needs to be rewritten if it should be saved further. On the other hand, determining a magnetization can

be performed easily and efficiently by the GMR effect, as it is currently used for example in read heads of hard disk drives.

At first view, using an antiferromagnet seems to make a readout of the magnetic state impossible. There is no macroscopic magnetization, to which the readout process can couple. Nevertheless, there may be multiple ways to solve this problem. First, a ferrimagnetic material could be used. Here, the microscopic interaction is still antiferromagnetic, which allows for a coupling between ferroelectricity and the magnetic system. Because magnetic moments do not cancel completely, a net magnetization remains. Specifically considering spiral spin structures, such a scenario is realized in conical spin spirals [23]. Alternatively there are other ways to access the state of an antiferromagnet. One possibility would be to couple a ferromagnet to the antiferromagnet via exchange bias [102]. Even non-magnetic readout schemes are conceivable as the use of the SHG technique in this work proves.

Chapter 2

Experimental method

This chapter introduces the experimental method of Optical Second Harmonic Generation (SHG) used for the following experiments on magnetoelectric switching. The first part is dedicated to the physics of SHG. It particularly focuses on the application of SHG for measurements on (multi-)ferroics including their domain topology. The second part of this chapter describes the actual experimental setups developed for static and dynamic magnetoelectric switching experiments.

2.1 Second harmonic generation (SHG)

Optical Second Harmonic Generation (SHG) is a nonlinear optical effect which doubles the frequency of light when passing through matter. This effect was first predicted in the 1930s [103]. It could not be observed experimentally at that time because it requires light intensities larger than 10^{10} W/m², which could not be achieved with light sources available at that time. This changed thirty years later with the development of the laser [104], so that just one year afterwards the first SHG was generated in an experiment [105].

SHG is used as measurement technique in solid state physics [106, 107] and biology [108]. In the present work we use SHG to study multiferroics [47].

2.1.1 General introduction to SHG

In a photonic picture, SHG can be viewed as simultaneous absorption of two photons at frequency ω and emission of one photon at the doubled frequency 2ω (figure 2.1). The energy of the two photons lifts an electron from the ground state $|g\rangle$ to an excited state $|e\rangle$, which has an energy $E_{|e\rangle} = E_{|g\rangle} + 2\hbar\omega$. The electron returns to the ground state by emitting a single photon with an energy of $2\hbar\omega$.

In this picture, it is immediately clear that the efficiency of the process strongly depends on the energy levels of the material and the wavelength of the incident light. Because of the simultaneous absorption of two photons, the selection rules from linear optics do not

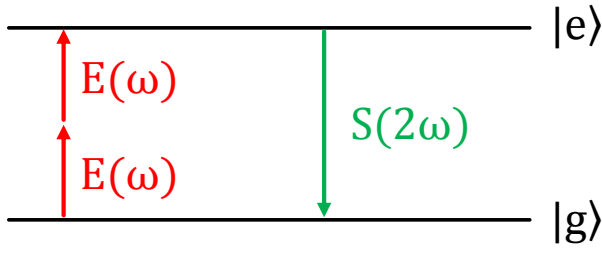


Figure 2.1 – Photonic picture of the SHG process. An electron is excited from its ground state $|g\rangle$ to an excited state $|e\rangle$ by simultaneous absorption of two photons at frequency ω . It returns to the ground state by emission of one photon with frequency 2ω .

apply. It is possible to calculate the spectra of SHG [109, 110]. However this is rarely done. Those calculations are quite complicated because the details of the band structure and their excitation have to be considered. As we will see below, the spectral features are less important for measurements on ferroic materials. Therefore, we will regard the frequency of the incident light as a free parameter and tune it to a value, at which the SHG process is efficient and we obtain a maximal SHG intensity.

Thinking of light in terms of waves, SHG results from an anharmonic oscillation of the electrons. Usually, the polarization \mathbf{P} induced in matter by an electric field \mathbf{E} is described by $\mathbf{P} = \varepsilon_0 \hat{\chi} \mathbf{E}$, where ε_0 is the vacuum permittivity and $\hat{\chi}$ is the electric susceptibility. This is just a linear approximation and at high electric fields ($\gtrsim 10^6$ V/m), such as in a laser pulse, higher order terms come into play. The second order term is quadratic in \mathbf{E} . Taking into account its frequency dependence $\mathbf{E}(\omega, t) = \mathbf{E}_0 e^{i\omega t}$ this contribution to the polarization is

$$\mathbf{P}(2\omega) = \varepsilon_0 \hat{\chi}^{\text{ED}}(2\omega, \omega) \mathbf{E}(\omega) \mathbf{E}(\omega) \quad , \quad (2.1)$$

where $\hat{\chi}^{\text{ED}}(2\omega, \omega)$ is the SHG susceptibility tensor. Writing out the components, this reads

$$P_i(2\omega) = \varepsilon_0 \chi_{ijk}^{\text{ED}}(2\omega, \omega) E_j(\omega) E_k(\omega) \quad . \quad (2.2)$$

Since the exciting electric fields each have a frequency dependence $E_{j,k} \propto e^{i\omega t}$, the polarization $P \propto E_j E_k \propto e^{i2\omega t}$ oscillates at 2ω . It is formed by the electrons of the material oscillating in their potentials and driven by the electric field of the light wave. Being charged oscillators, they act like dipole antennas and re-emit a wave at their oscillation frequency 2ω .

Another approximation usually made in linear optics is to consider only electric dipole transitions. The light electron interaction is described in quantum mechanics via the transition matrix element $\langle e | q \cdot e^{ikr} | g \rangle$, where $|g\rangle$ and $|e\rangle$ are the initial and final electron wave functions, q is the electron charge and e^{ikr} is the spatial variation of the light field. Since the wavelength λ is much larger than typical displacements r , the product $kr = \frac{2\pi r}{\lambda}$ is small and one can expand the exponential function $e^{ikr} = 1 + ikr - \frac{1}{2}(kr)^2 + O((kr)^3)$. The linear term results in the electric dipole (ED) transition matrix element $\langle e | qr | g \rangle$. The next order term results in a magnetic dipole (MD)

$$M_i(2\omega) = \frac{c}{\varepsilon_0(\omega)} \chi_{ijk}^{\text{MD}}(2\omega, \omega) E_j(\omega) E_k(\omega) \quad (2.3)$$

and an electric quadrupole oscillation (EQ)

$$Q_{ij}(2\omega) = \frac{\varepsilon_0 c}{2i\omega n(\omega)} \chi_{ijkl}^{\text{EQ}}(2\omega, \omega) E_k(\omega) E_l(\omega) \quad . \quad (2.4)$$

2.1. Second harmonic generation (SHG)

The solutions of Maxwell's equations for a linearly polarizable medium are wave equations. If one incorporates the additional nonlinear contributions (equations (2.2), (2.3) and (2.4)), the wave equation is modified to

$$\left(\Delta - \frac{\varepsilon}{c^2} \frac{\partial^2}{\partial t^2}\right) \mathbf{E} = \mathbf{S}^{\text{SHG}}(2\omega) \quad , \quad (2.5)$$

where $\mathbf{S}^{\text{SHG}}(2\omega)$ is a source term of the form

$$\mathbf{S}^{\text{SHG}}(2\omega) = \mu_0 \frac{\partial^2 \mathbf{P}(2\omega)}{\partial t^2} + \mu_0 \left(\nabla \times \frac{\partial \mathbf{M}(2\omega)}{\partial t} \right) - \mu_0 \left(\nabla \frac{\partial^2 \mathbf{Q}(2\omega)}{\partial t^2} \right) \quad , \quad (2.6)$$

which describes the emission of a wave at 2ω .

The indices ijk of the tensor elements define the light polarizations, i.e. the direction of the \mathbf{E} -field of the light wave. The last two indices correspond to the incident light polarization. Since both link to the same quantity, the electric field \mathbf{E} , the SHG tensor is always symmetric in these last two indices.

In the case of ED tensors, the polarization direction of the emitted light S_i^{SHG} corresponds to the first index of the SHG tensor χ_{ijk}^{ED} . For the MD term, it is not that obvious because the curl in equation (2.6) rotates the first index, so $\chi_{x..}^{\text{MD}}$ does not describe the emission of x -polarized light. Instead it is y - or z -polarized light.

These relations of the incident and emitted light polarizations are used in the experiment to selectively probe single tensor components. The selection of a certain tensor component, e.g. χ_{yzz}^{ED} , is achieved by setting the incident light polarization to z and filtering the output for y -polarized light.

Different sample orientations are needed to access different tensor component. For example χ_{yzz}^{ED} is best measured in an x -cut. Here, the wave vector of the light k is set along x (normal incidence). As light is a transversal wave, the incident and SHG light can then be z - or y -polarized. In contrast, no tensor component containing x in any index can be excited in this geometry.

In general, it is not possible to measure tensor components with three different indices, e.g. χ_{xyz} , without admixture of signals from other tensor components. Therefore, such components are not used in measurements if possible. For all other tensor components, it is best to align the light propagation vector k with one of the crystallographic axis. This directly excludes the excitation or emission of tensor components containing this axis as an index. Rotating the sample away from such a geometry admixes additional tensor components. While the analysis gets more complicated because multiple excited tensor components and the projections of their signals have to be considered, this can be a desired effect for the generation of domain contrast (see section 2.1.3 and section A.2).

Tensor components χ_{ijk} with two different directions $j \neq k$ in the last two indices are accessible with the incident polarization set in between these direction. Projecting onto the two different directions, some photons will have the one polarization and some the other. Therefore, there is a finite chance that the polarization of the two photons involved is different, so that such a tensor component can be excited. However, a tensor with identical components

$j = k$ will be excited as well. This implies that tensors with mixed last two indices (like χ_{xyx}) cannot be measured background free. The measurements will always have admixtures of the corresponding equal-index tensors (e.g. χ_{xxx} and χ_{xyy}), provided these are non-zero.

2.1.2 SHG on ferroic materials

The following section explains how symmetry can yield an effective link between SHG measurements and material properties, in particular (anti-)ferroic order. This symmetry sensitivity renders SHG an ideal tool for studying multiferroics.

SHG and Symmetry

Any ferroic phase transition changes the symmetry of the material. The idea behind SHG measurements is to detect this change in symmetry. This is in principle possible due to *Neumann's principle* [111]:

The symmetry of any physical property of a material is always equal to or higher than the symmetry of the material itself.

This principle allows to infer the symmetry of the material from the symmetry of measured properties, like e.g. SHG tensors. However, the symmetry of a property may be higher than the symmetry of the material, in which case it yields only information on a subset of the material symmetries. An extreme example is heat capacity. As a scalar it is invariant under any symmetry transformation and does not provide any information on the material symmetry at all. Therefore, it is reasonable to use directionally sensitive quantities as a probe for the symmetry. Mathematically, this corresponds to a vector or, even better, a higher rank tensor, like the SHG susceptibility tensor.

Symmetry transformations impose constraints on the possible tensor components [112]. Certain tensor components may be equal to others or zero. The lowered symmetry at a phase transition relaxes these constraints, which usually leads to the emergence of new SHG tensor components.

The case is particular simple for a ferroelectric transition: The material is inversion symmetric above the transition temperature. Inversion symmetry forbids all SHG tensor components to leading order (i.e. all ED tensor components are identical to zero). Higher order terms like magnetic dipole or electric quadrupole tensors may still be present. Below the ferroelectric phase transition, the inversion symmetry is broken, allowing for additional ED-SHG signals.

The coupling between SHG susceptibilities and the order can be described by expanding the susceptibility in the order parameter η . [113]:

$$\hat{\chi}(\eta) = \hat{\chi}^0 + \hat{\chi}^1 \eta + \hat{\chi}^2 \eta\eta + \dots \quad (2.7)$$

The tensors $\hat{\chi}^i$ are the expansion coefficients. In a first approximation, we can assume them to be temperature independent. Strictly this is not true, e.g. because of the drift of the lattice

2.1. Second harmonic generation (SHG)

constants. However, these effects are small and usually negligible. The major temperature dependence of the susceptibility stems from the temperature scaling $\eta(T)$ of the order parameter.

The first term $\hat{\chi}^0$ does not depend on the order parameter. Because the ferroic order does not influence it, it is purely defined by the crystal structure and thus called *crystallographic SHG*. It will not or only weakly depend on temperature. In contrast, all other terms are temperature dependent because they contain the coupling to the order parameter, which strongly changes with temperature, at least close to the phase transition. Most significant is the linear coupling term $\hat{\chi}^1$, which is often sufficient to explain observed temperature dependencies. In the following we will use this linear approximation:

$$\chi(\eta) \propto \eta \quad . \quad (2.8)$$

This relation holds for MnWO_4 [114] and our measurements on CuO will prove that it is valid also in the case CuO (compare figure 5.2).

Because of the above proportionality it is easy to measure the scaling of the order parameter. It just scales like the SHG susceptibility. However, determining its amplitude, e.g. the magnitude of a polarization, is not possible because the proportionality factor between the order parameter and the susceptibility is not known. In fact, these two macroscopic quantities are related in a non-trivial way by the microscopic properties of the material.

Even measuring the absolute value of the SHG susceptibility would be cumbersome because it requires to exactly determine all proportionality constants between the signal generated in the sample and the detector signal. This would include reflection and absorption losses in the optics and the sample, detector quantum efficiency, and the signal electronics. Therefore most SHG intensities are only measured up to an unknown proportionality constant and thus given in arbitrary units.

Since SHG is a purely symmetry-based technique for measuring ferroic orders, there is no fundamental difference between ferroic and antiferroic orders. This is in contrast to other measurement techniques that directly couple to macroscopic quantities like the electric polarization or magnetization of a sample. While there are other methods to measure antiferromagnetic order (e.g. polarized neutron diffraction or X-ray magnetic linear dichroism (XMLD)), SHG has the combined advantages that it can measure both the electric and magnetic order with high temporal and spatial resolution. This makes it an ideal tool for studying the dynamics of magnetoelectric switching.

SHG on multiferroics

The distinction between crystallographic and order-related SHG signals is straightforward because the former do not show any or only a weak temperature dependence. In multiferroics there are at least two ferroic orders. This poses the additional question which of the orders is responsible for the SHG signal: Is the order parameter in equation (2.8) the polarization ($\chi(\mathcal{P})$) or the magnetic order ($\chi(\sigma)$)?

Common methods for assigning a specific SHG signal to a certain order parameter rely on mapping either the transition temperature or the scaling law of the order parameter and the SHG signal. This works well in split-order-parameter multiferroics. In joint-order-parameter multiferroics, both orders set in at the same temperature, so the transition temperature cannot be used as a criterion. Moreover, the temperature scaling may also be identical. In the case of spin-spiral-induced ferroelectricity in MnWO_4 and CuO , the coupling between ferroelectric (\mathcal{P}) and magnetic order parameters (σ_1, σ_2) reads $\mathcal{P} \propto \sigma_1 \sigma_2$. Additionally, this yields exactly the same symmetry for the magnetic and electric system, making it difficult to decide to which order parameter a SHG tensor is coupling.

Fortunately, this distinction is often not necessary in joint-order-parameter multiferroics because the order-parameters are directly linked. Therefore, it may not matter if the actual measured system was the magnetic or the electric one.

However, for some measurements this is relevant. The first example are comparisons of SHG efficiency [82], in which the SHG is normalized to the value of the polarization. This is only meaningful if the SHG directly stems from the polarization and not from the associated magnetic order.

A second type of measurements that may require knowledge about the actual system, are dynamic measurements. The coupling between magnetic and electric order, as expressed by equation (1.6), results from a minimization of the free energy. It is only valid in energetic ground states. This condition is not fulfilled in non-equilibrium states during dynamic switching. As a result, electric and magnetic orders can in principle decouple temporarily during a switching process. Then, it is important to know which system is measured. At best, there may be different SHG signals coupling to either system, so that both can be monitored.

2.1.3 Domain imaging

Exploiting the spatial resolution of SHG as an optical technique, it is possible to acquire images of the domain structure of ferroics. This can be simply achieved by using a CCD camera as detector and imaging the SHG light from the sample onto the CCD chip.

Different domains have the same amplitude of the order parameter, but a different orientation or phase. From equations (2.6), (2.1) and (2.8) it follows that the SHG light intensity is proportional to the absolute square of the order parameter:

$$I(2\omega) \propto |\mathbf{S}^{\text{SHG}}(2\omega)|^2 \propto |\chi(\eta)|^2 \propto |\eta|^2 \quad (2.9)$$

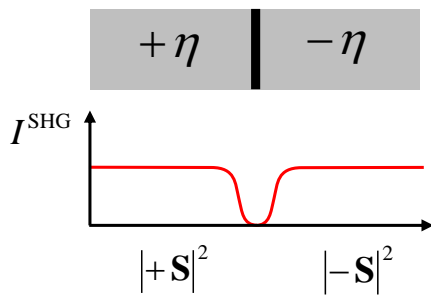
This is the same for every direction or phase of the order parameter. As a consequence, 180° -domains and translation domains are indistinguishable in simple SHG measurements.

In the following, we limit the discussion to ferroelectric polarization domains and helicity domains in spin spirals. In both cases the transition from one domain orientation to the other can simply be described by a sign change of the order parameter, or thinking of it as a complex number, a 180° phase shift.

Though it is not possible to determine the orientation of the order parameter inside the domains with a simple SHG intensity measurement, one can still see the domain pattern

2.1. Second harmonic generation (SHG)

$$(a) \quad I^{\text{SHG}} \propto |\mathbf{S}^{\text{SHG}}(\eta)|^2 \propto |\eta|^2$$



$$(b) \quad I^{\text{SHG}} \propto |\mathbf{S}^{\text{Ref}} + \mathbf{S}^{\text{SHG}}(\eta)|^2 \propto |c + \eta|^2$$

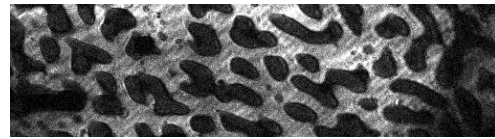
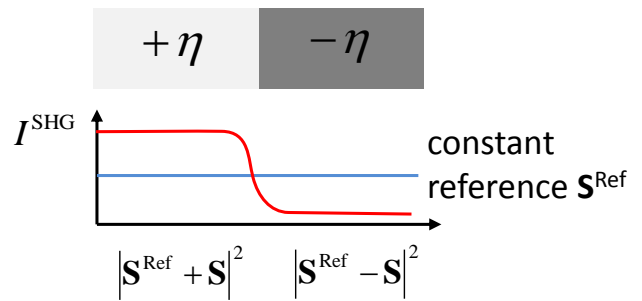


Figure 2.2 – The principle of generating domain contrast in SHG intensities is explained for an arbitrary order parameter η . In the present work, this will correspond either to the spontaneous polarization or the helicity of the spin spiral.

(a) Because the SHG light amplitude \mathbf{S}^{SHG} scales linearly with the order parameter and the intensity is the absolute square of the amplitude, both domain orientations yield the same SHG intensity. The light waves from the different domains have a relative phase shift of 180° . Therefore, they interfere destructively at the domain boundary, making domain walls visible as black lines. (Domain image from [115])

(b) The phase contrast between the domains can be turned into an intensity contrast by superimposing a constant reference light wave. Constructive and destructive interference, respectively, will then result in a different brightness of the domain states.

because of the domain walls (figure 2.2 (a)). At the domain wall the order parameter has a phase shift of 180° . Because of the linear coupling (equation (2.8)) this translates to a corresponding phase of the susceptibility tensor and finally of the emitted light wave. If two points are not further separated than the optical resolution of the setup, SHG emitted from them will interfere on the CCD chip. If they additionally lie on different sides of a domain wall, they have a phase shift of 180° and thus interfere destructively. Therefore, domain walls will appear as dark lines. The width of these lines is not correlated to the domain wall width, but is solely determined by the optical resolution. Domain wall widths are typically in between few lattice constants in ferroelectrics and few 10 nm in ferromagnets. This is still much smaller than the optical wavelength, which in the best case of the diffraction limit determines the resolution and hence the area of interference. For this reason, the black lines rather just indicate the change of order parameter from one domain to the other. They do not yield information on the actual type and width of the domain wall.

Equation (2.9) does not allow to uniquely identify the orientation of the order parameter within a domain. Furthermore, is it difficult to obtain the domain population, i.e. the relative area fractions of both types of domains¹.

Both, the unique assignment of the orientation of the order parameter as well as an easy way to measure domain population without the need for images, is a key requirement for studying magnetoelectric switching. It can be achieved by interference with a constant reference that does not depend on the order parameter. This reference might be external [116] or an internal crystallographic SHG contribution, which may be mixed in by rotating the sample as in the case of MnWO_4 (see section A.2).

The interference turns the phase contrast of the domains into an intensity contrast. The intensity of the interfered light reads

$$I(2\omega) \propto \left| B \frac{\eta}{|\eta|} + B_{\text{Ref}} e^{i\phi} \right|^2, \quad (2.10)$$

where B and B_{Ref} are the amplitudes of the SHG coupling to the order parameter and to the reference signal, respectively. ϕ is the relative phase between both waves. Expanding the term yields

$$I(2\omega) \propto B^2 + B_{\text{Ref}}^2 + \frac{\eta}{|\eta|} 2BB_{\text{Ref}} \cos \phi. \quad (2.11)$$

Now, the intensity depends on the sign of the order parameter via the interference term $\frac{\eta}{|\eta|} 2BB_{\text{Ref}} \cos \phi$. Maximal contrast is achieved, when the intensities B and B_{Ref} are of the same size. Furthermore, the relative phase ϕ should be close to 0° or 180° . Then one can obtain totally constructive or destructive interference.

The order parameter in 180° domains, like ferroelectric or magnetic helicity domains, has two possible orientations. This leads to a 180° phase shift between different domains. As a result, domains of the one order parameter direction appear dark, while the others are bright (figure 2.2 (b)). The same effect can be used to visualize the magnetic translation domains in MnWO_4 , which can have arbitrary relative phases [117].

¹In principle this is possible from SHG images like figure 2.2 (a), however, image acquisition is time-consuming. Moreover an automated analysis of the images would be complicated.

Domain population

Spatially integrated measurements can be performed to speed up the measurement process if no information on the actual domain pattern is required, but only the relative population of the domain states. The following section explains how the domain population relates to the SHG intensity.

When measuring the SHG intensity of a sample without spatial resolution, the signal from equation (2.11) is integrated

$$I(2\omega) \propto C + \int dx dy \frac{\eta(x,y)}{|\eta|} 2BB_{\text{Ref}} \cos \phi \quad . \quad (2.12)$$

The term $f = \int \frac{\eta(x,y)}{|\eta|} dx dy$ represents the *domain population*. Splitting the integral into two parts, each containing only one order parameter orientation, the integrals become trivial and the domain population can be rewritten as

$$f = f_+ - f_- \quad \text{with} \quad f_+ = \frac{A_+}{A}, \quad f_- = \frac{A_-}{A} \quad . \quad (2.13)$$

Here, A is the total sample area and A_+ and A_- are the areas, which are covered with order parameters of orientation (+) or (−) respectively. Therefore, f is a measure for the relative area fractions of the domain states. It has the following properties:

- The lowest value is -1 , corresponding to a (−) single domain state.
- The highest value is $+1$, corresponding to a (+) single domain state.
- f scales linearly with the area fractions f_{\pm} . (This is because $f_{\mp} = 1 - f_{\pm}$)
- A value of $f = 0$ is reached for an equal distribution of both domain states.

Figure 2.3 visualizes the relation between f and an example domain pattern.

Using the domain population, we can further rewrite equation (2.12) to

$$I(2\omega) \propto C + C' \cdot f \quad , \quad (2.14)$$

where $C' = 2BB_{\text{Ref}} \cos \phi$. This equation shows that integral SHG signals can be easily interpreted in terms of domain population. First, there is a constant background C . On top of this, the SHG intensity rises linearly to a maximum $C + C'$ with increasing area fractions of (+) domains with respect to (−) domains.

If the order parameter is a macroscopic quantity, like a magnetization or polarization, the population can be used to express the averaging over the domains. For example the macroscopic polarization of any domain state of a ferroelectric with 180° domains will be $P = P_0 \cdot f$, where P_0 is the maximal polarization realized in a single domain state.²

²This holds true only as long as the domain sizes are larger than the optical resolution limit of the setup.

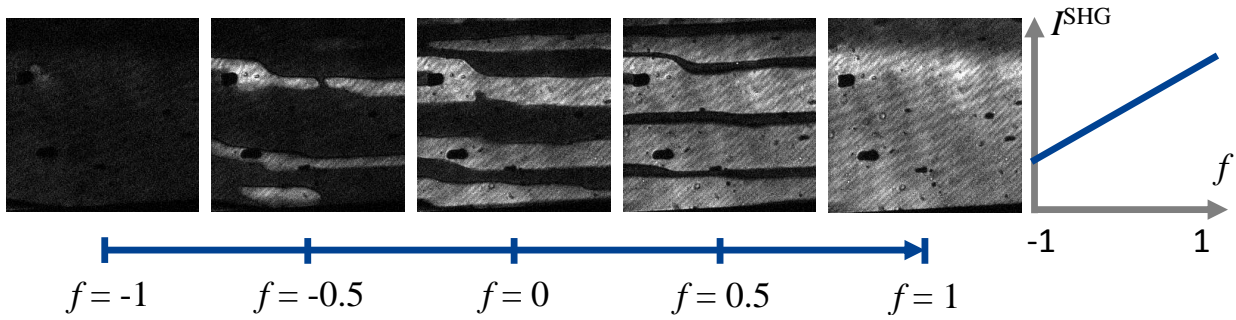


Figure 2.3 – Example to visualize the meaning of the values of the domain population f . f is extremal (± 1) for both single domain states. It linearly scales with the area fractions f_+ , f_- of both domain states. The measured SHG intensity increases linearly with f but may have an offset due to non-complete destructive interference with the reference light.

2.1.4 Measured volume and intensities

Two effects limit the measured SHG intensity. One is absorption of the light in the sample and the second is phase matching. As we will detail below, the absorption reduces the intensity by limiting the spatial region from which SHG can be detected, while a lack of phase matching leads to destructive interference.

The absorption coefficient $\alpha(\omega)$ at fundamental and SHG wavelengths determines the volume inside the sample from which SHG is measured in transmission experiments. In a transmission setup, the investigated samples have to be transparent either at the fundamental wavelength or at the SHG wavelength. In the former case, the fundamental beam penetrates the sample up to a depth equal to the absorption length at the fundamental frequency. SHG will be generated only in this volume.

If the sample is only transparent for the fundamental, SHG will be generated everywhere in the crystal. However, the light from the front of the sample is reabsorbed before it reaches the rear side, so that only SHG from a layer at the back side will leave the crystal (figure 2.4). The width of this layer equals the absorption length at the SHG frequency. This is the most common case and also holds true for MnWO_4 and CuO . Typical fundamental photon energies are between 0.7 and 1.5 eV. Many samples are transparent in this region because of the band gap. The corresponding SHG photon energies lie between 1.4 and 3.0 eV, which is the visible region. Here, absorption is strongly material dependent.

SHG may as well be used in reflection geometry if the samples are transparent neither in the fundamental nor in the SHG range.

The second effect reducing the SHG intensity is a lack of phase matching [118, 119]. In general, the refractive indices at fundamental and SHG wavelengths are different. This results in a global phase shift between SHG from different points along the beam axis and finally leads to destructive interference. Therefore, the amount of detected light is equivalent to the one

Otherwise interference of signals from neighboring domains has to be taken into account. Furthermore this requires a flat-top profile of the laser. An unequal intensity distribution would weight the positions in the spatial integral according to the local intensity squared. In such a case, the integrated intensity will still monotonically depend on the domain population, but $I(f)$ will not be linear any more.

2.1. Second harmonic generation (SHG)

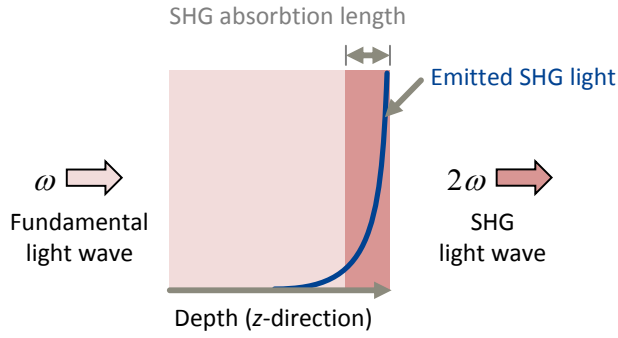


Figure 2.4 – Emission region of SHG in a transmission setup for the most common case of a sample that is transparent for the fundamental light wave and opaque for the SHG wavelength. SHG will be generated everywhere in the crystal. However, it is reabsorbed except for an area at the back of the sample, whose depth corresponds to the absorption length.

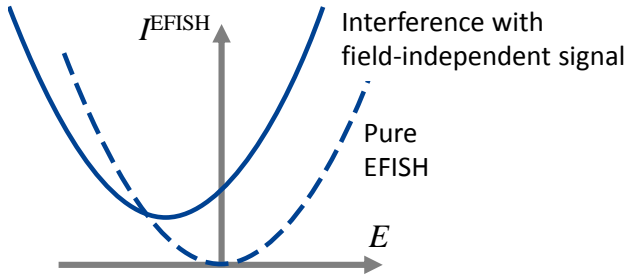


Figure 2.5 – Field dependence of electric field induced SHG (EFISH). A pure EFISH signal scales quadratically with the applied electric field (dashed line). The interference with a field independent signal leads to a shift of the parabola. Such a field dependence is a clear signature for EFISH and can be exploited to separate it from SHG changes due to a switching of the spontaneous order.

generated in a volume with a depth L , in which the phase shift builds up to 180° . In many cases L is smaller than the absorption length $\frac{1}{\alpha(2\omega)}$. However, phase-matching does *not* reduce the probed volume. If there are any local phase changes of the generated SHG light within the absorption length $\frac{1}{\alpha(2\omega)}$, e.g. because of a reversed domain, this will affect the interference term and will consequently be detectable in the SHG intensity.

2.1.5 Electric field induced SHG (EFISH)

Electric field induced SHG (EFISH) is a third order nonlinear process, in which one of the incident fields is a DC electric field [120]

$$\mathbf{P}^{(3)}(2\omega) = \varepsilon_0 \chi^{(3)}(0, \omega, \omega) \mathbf{E}(0) \mathbf{E}(\omega) \mathbf{E}(\omega) \quad . \quad (2.15)$$

It emits frequency doubled light like a true second order SHG process. EFISH can be understood as the DC electric field inducing a polarization. Like in the case of the spontaneous ferroelectric polarization, the induced polarization may reduce the symmetry and allow additional tensor components.

EFISH signals have to be separated from the ferroic order related signals. An EFISH signal can be identified by its field dependence. From equation (2.15) follows that the amplitude rises linearly with the applied field. Thus, the intensity shows a parabola profile, centered around $E = 0$.

The interference of EFISH with a constant background signal, e.g. crystallographic SHG, leads to a vertical and horizontal shift of the parabola:

$$\left| A \cdot E + B e^{i\phi} \right|^2 = A^2 \cdot E^2 + 2AB \cos \phi \cdot E + B^2 \quad . \quad (2.16)$$

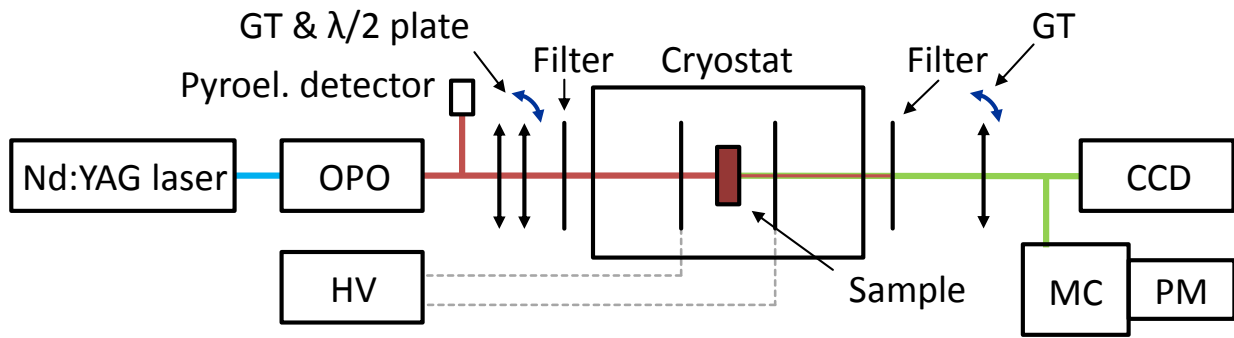


Figure 2.6 – SHG setup. Laser and OPO form a tunable pulsed light source. A pyroelectric detector measures a reference signal that is coupled out via a glass plate. The incident polarization is set using a Glan-Taylor prism and a rotatable half-wave plate. The sample is located in a cryostat for cooling. A long-pass filter in front of the sample removes any light at the SHG wavelength, but transmits the fundamental laser beam wavelength. Conversely, a short-pass filter behind the cryostat removes the fundamental beam, but transmits the SHG light. The measured SHG polarization is selected by a rotatable Glan-Taylor prism. Finally, the light is acquired either using a CCD camera or a combination of monochromator and photomultiplier. Optionally, additional electrodes and a high voltage source provide an electric field at the sample position.

Here, $A \cdot E$ and B are the EFISH and background amplitudes respectively. ϕ is the relative phase of the light waves.

Furthermore, EFISH can only be seen if the DC field is perpendicular to the light propagation vector k . This can be understood from symmetry. If the DC field is applied along the beam axis, the transversal electric polarization of the light wave cannot couple to the induced dipole, which is perpendicular to it.

2.2 Experimental setups

This section introduces the experimental setups used. The basic SHG setup is only introduced briefly because it has already been extensively covered in other publications [47, 115, 121]. Separate subsections describe the extension for measurements in static electric fields and the electrical-pump–optical-probe method for dynamic magnetoelectric switching.

2.2.1 Basic SHG setup

The typical SHG setup is depicted in figure 2.6. It is driven by a Nd:YAG nanosecond laser (Continuum Powerlite Precision II) that generates 5 ns wide pulses with a repetition rate of 10 Hz. Its light is frequency-tripled internally, so that it emits at 355 nm, which is used to pump an optical parametric oscillator (OPO) (GWU VersaScan).

The OPO process is a nonlinear process that splits up the photon energy of one photon into two photons within a nonlinear crystal. The relative amount of photon energy of the two emitted photons can be tuned by a rotation of the crystal. This results in a frequency-tunable

2.2. Experimental setups

laser source, which is a tremendous advantage for SHG measurements. It allows to tune the incident frequency to a value at which SHG light is generated efficiently.

Incident polarization selection is achieved via a rotatable half-wave plate. A Glan-Taylor prism in front of the half wave plate guarantees that the light polarization is strictly linear, which prevents the accidental simultaneous excitation of multiple SHG tensor components.

A long-pass filter (typically RG780-RG1000 glass filters, depending on the wavelength used) directly in front of the sample filters out SHG light that might have been produced on optics along the beam path, particularly on the half-wave plate. Furthermore, it largely reduces ambient light in the experimental setup.

The sample itself is located in a cryostat (Janis SVT-400), allowing for cooling by liquid helium or nitrogen. The fundamental light is filtered out behind the cryostat typically using KG5 or BG39 filters. It is important to place at least one filter directly behind the cryostat, so that the fundamental intensity is reduced enough to prevent SHG generation in any of the following components. It is advisable to block possible third harmonic generation (THG) signals using a suitable short pass filter, e.g. GG395 or GG495. A rotatable Glan-Taylor prism is used for SHG polarization selection.

The SHG detection can be performed either using a CCD camera or using a monochromator-photomultiplier combination. A CCD has the advantage of spatial resolution. Used models are Photometrics CH270 and Horiba-Jobin-Yvon Symphony. In contrast, the photomultiplier yields only a spatially integrated signal. The benefit of detection with a monochromator-photomultiplier combination lies in its strong spectral and temporal filtering capabilities. This makes the suppression of backgrounds like ambient light and luminescence much easier. Furthermore, a photomultiplier allows the separate detection of every single laser pulse, which can be advantageous for normalizations.

A fraction of the light is coupled out in front of the half-wave plate using a reflection from a glass plate. It is measured by a pyroelectric detector (Coherent J3-05 or PS19) and used as a correction for the spectral dependence of the OPO in spectrum measurements. Additionally, it serves as a monitor of laser stability.

For simplicity, imaging and beam guiding optics like lenses and mirrors are left out in the description.

The complete setup is computer-controlled, which allows for fast and precise measurements. The control software was completely redesigned during this work for more flexible and reliable operation and easier extensibility (see section D.2).

2.2.2 Extension to E-field setups

Magnetolectric switching experiments require the application of electric fields to the samples under investigation. Specific sample holders were designed for this, in which the sample is mounted in between electrodes. If the electrodes are connected to external high-voltage sources, a homogeneous electric field penetrates the sample.

Depending on the geometry, two different types of electrodes are used. As described in

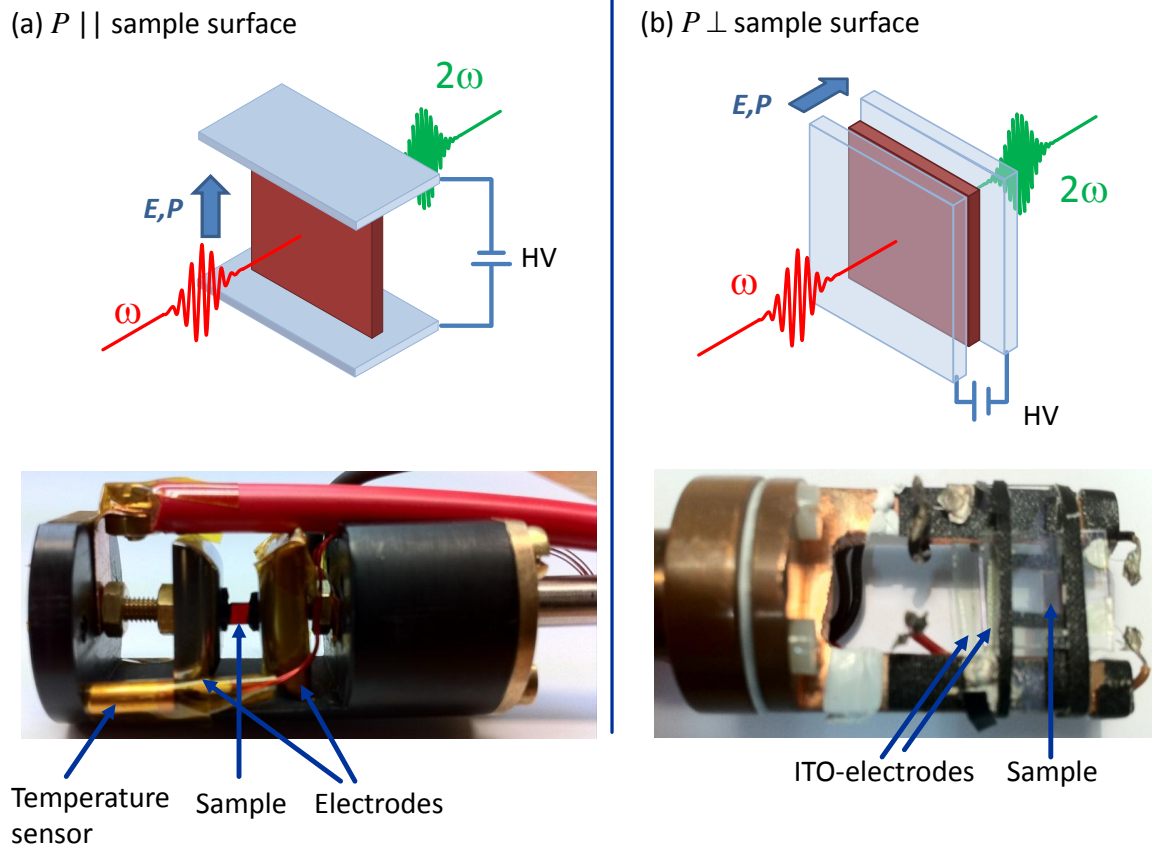


Figure 2.7 – Sample holders for the application of electric fields.

(a) Transversal-field holder ($\mathbf{E} \perp \mathbf{k}$) for sample geometries, in which the polarization is in plane. In this case specially formed aluminum electrodes are used, which provide a homogeneous electric field in the center.

(b) Longitudinal-field holder ($\mathbf{E} \parallel \mathbf{k}$) for sample geometries, in which the polarization is out of plane. Electrodes are realized by ITO-coated glass plates.

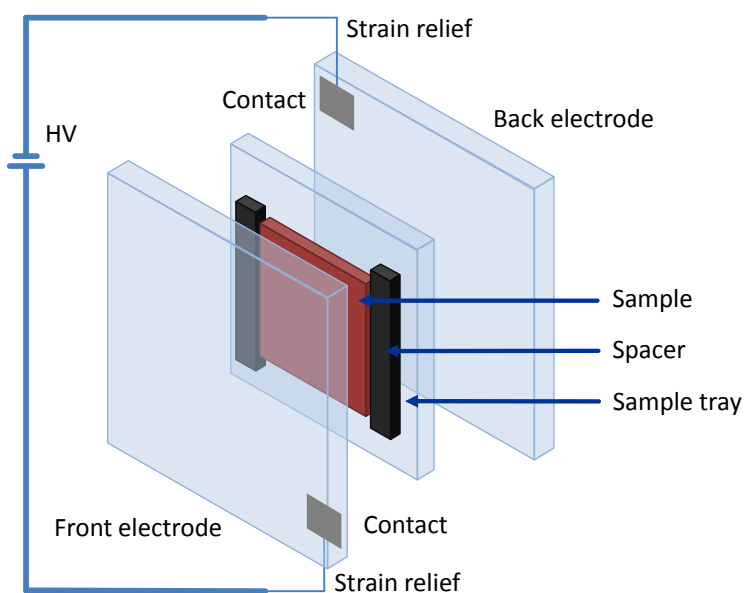


Figure 2.8 – Detailed view of the longitudinal-field sample holder. The sample is mounted on a thin glass plate, serving as tray for easy sample exchange. On both sides of the tray, there are spacers, which ensure parallel electrodes and thus a homogeneous electric field, when the sample tray is sandwiched between the electrodes. The ITO coating on both electrodes faces towards the sample to reduce the electrode distance, resulting in a higher electric field for a given voltage. It is contacted by silver paste. The first part of the wiring consists of a thin angled wire, which functions as a strain relief (not visible in the photo in figure 2.7).

2.2. Experimental setups

section 2.1.1, the choice of SHG tensor components, which are to be measured, determines the orientation of the sample with respect to the laser beam. Because the field has to be applied in the direction of the ferroelectric polarization, also the position of the electrodes is dictated by the sample. We can distinguish two different cases: Ferroelectric polarization in plane or perpendicular to the sample surface.

If the ferroelectric polarization is perpendicular to the wave vector of the light ($\mathcal{P} \perp k$), which is the case for a ferroelectric polarization in the plane of the sample surface, we use polished aluminum electrodes (figure 2.7 (a)). Their shape is designed to create a homogeneous field at the position of the sample in the center. If the sample is large enough and regularly shaped, it can be placed directly on the electrodes and fixated by vacuum grease. Alternatively, it can be glued to a glass plate or attached to a plastic holder.

However, if the polarization is oriented out of plane (i.e. $\mathcal{P} \parallel k$), the electrodes will necessarily lie in the optical beam path. Opaque electrodes, like the aluminum plates, would block the beam. In this case, we resort to indium tin oxide (ITO) as electrode material because it is transparent and conducting at the same time (figure 2.7 (b)). ITO coated glass plates are commercially available. For easy exchange of the samples it is convenient to mount the sample on a sample tray formed by a thin glass plate, either by glue or by taping the outline. This holder can then be placed between the electrodes. A thin wire forms the last part of the wiring. It is attached with conductive paste to the electrodes. In combination with the geometry of the wiring this prevents mechanical stress due to thermal expansion. Otherwise, stress could rip off the contacts from the ITO when cooling down the sample holder.

For static and quasi-static magnetoelectric measurements any high voltage source can be connected directly to the sample holders. The high voltage source should provide a switchable polarity, to pole the sample in both directions. When using liquid helium to cool to low temperatures, the electrical breakthrough of gaseous helium at approximately 1 kV/mm limits the maximal applicable field. Higher fields are possible if nitrogen gas is used for cooling (suitable only at temperatures > 77 K) or if the sample is immersed in liquid helium (at temperatures < 4.2 K). Typical sample distances amount to some hundred micrometers for the ITO holder and few millimeters for the transversal field holder. To achieve the maximal field of 1 kV/mm in helium, one needs some hundred volts in the former case (e.g. from the voltage source Keithley K2410), and some kilovolts for the latter (e.g. from the voltage source iseg HV T2DP).

2.2.3 Electrical-pump–optical-probe setup for magnetoelectric dynamics

A primary goal of the present work is the temporally resolved measurement of magnetoelectric switching.

The laser repetition rate of 10 Hz determines the temporal distance at which data can be obtained in an optical SHG measurement. The time between the laser pulses (100 ms) is far too large to directly follow the response of the material with temporal resolution.

Using a pump-probe technique (figure 2.9) drastically increases the temporal resolution. Here, the electric field applied to the sample is rapidly changed at $t = 0$. The ferroelectric

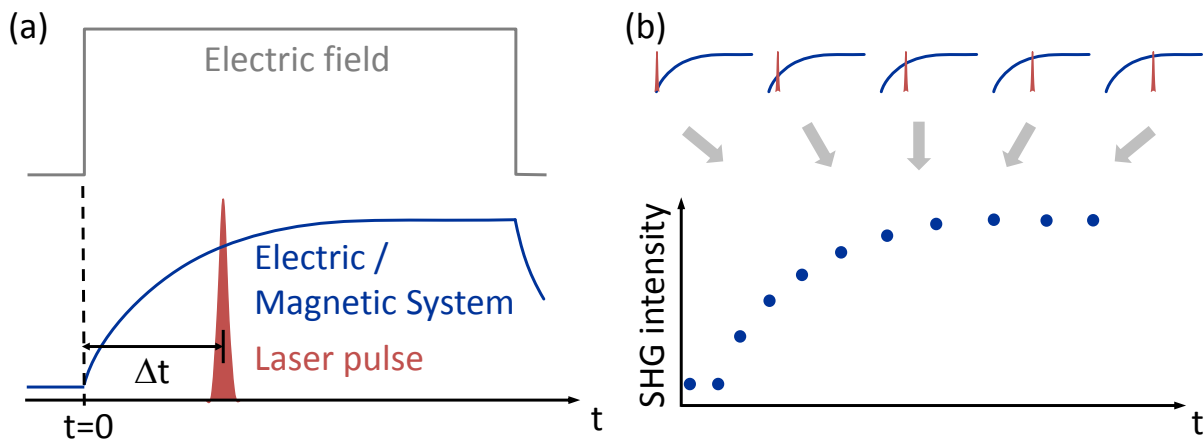


Figure 2.9 – Measurement scheme of the electric-pump–optical-probe method for magnetoelectric switching. (a) At time $t = 0$ the electric field applied to the sample is rapidly changed. This defines a new ground state for the coupled electric and magnetic systems in the material. They will propagate towards this state on their intrinsic timescale. At a time Δt later the laser arrives at the sample. The SHG it generates reflects the state of the electric or magnetic system at that time. (b) The complete temporal evolution is recovered by scanning the delay Δt and sequentially measuring each time step in a separate switching cycles.

polarization, and in magnetoelectric materials also the magnetic order, will respond to the change of field. At a later time Δt , the laser pulse hits the sample. The generated SHG probes the state of the magnetic or electric system, which one depends on the tensor component used. By changing the delay Δt the complete switching process can be recovered in successive measurements.

A high-voltage switch (DEI PVX-4140) is used to rapidly change the voltage applied to the electrodes and thus the electric field. Depending on a gate signal, it feeds either of two input voltages to the output. Internally, it uses a semiconductor switch, which is backed by large capacitors to quickly provide the current required to recharge the field-generating electrodes. Ideally, the rise time of the field should be infinitely short. But in practice it is sufficient if it is significantly faster than all switching related processes in the material. The above setup achieves a rise time of the electric field of 80 ns. An improvement to approximately 20 ns would be possible by optimizing capacitance and impedance of the electrodes and wiring. However, this has not been done because it turned out that 80 ns is sufficiently fast for all measurements reported here.

It is advantageous to switch the electric fields at a fixed time and vary the point in time at which the laser pulse arrives, not vice versa. This guarantees that the time slots between switching the material are always exactly of the same size. Equidistant timing is important for reproducibility if there are processes in the material that take longer than the repetition period of the experiment.

A delay / pulse generator (Stanford Research Systems DG535) is used as master time source. It provides a gate pulse with adjustable width to the high-voltage switch, which applies the field accordingly. Furthermore the DG535 provides trigger signals for the flash lamp and the Q-switch of the nanosecond laser. Their delay with respect to the pump trigger is adjustable

2.2. Experimental setups

via the measurement control software (section D.2) allowing for automatic measurements of temporal dependencies. Details of the wiring and switching timings can be found in [121].

Temporal resolution

The rise time of the electric field determines the fastest changes that may be induced in the sample. If possible, the temporal resolution of the detection should be slightly higher to be still able to resolve the slope. Two experimental parameters limit the detection resolution: First, the SHG signal contains information averaged over a time interval equal to the pulse width of the laser (5 ns). Faster processes cannot be resolved. Second, timing accuracy between HV-pulse and laser pulse may be a limiting factor, particularly in the case of femtosecond laser pulses. This includes jitter of the trigger electronics and of the laser (≈ 300 ps).

Repeatability requirements

The electrical-pump–optical-probe technique is a repetitive technique. Because each data point is taken from a separate cycle, the processes studied must be repeatable. For the case of magnetoelectric switching different degrees of repeatability are required depending on the detection method:

Integral measurements When measuring SHG intensities it is sufficient if the evolution of the domain population is repeatable, i.e. at a given time t the fraction of switched domains has to be the same for every switching cycle. No assumption has to be made on the domain pattern.

Imaging For domain images, not only the domain population has to be repeatable, but the whole pattern has to evolve in the same way in every switching cycle.

Repeatability is essential for the comparability between intensities or images at different delays. Additionally, it is already required for every single image. Because the SHG intensities are low, the SHG light from many laser pulses has to be integrated. Typical exposure times at the nanosecond laser are between one to five minutes, but may be up to two hours. At 10 Hz repetition rate, one minute corresponds to 600 laser pulses and thus switching cycles. The image obtained is an average over the patterns in all these cycles. So a lack of repeatability would cause the images to be blurred.

Reduced repetition rates

The time between the laser pulses (100 ms for the nanosecond laser) determines the repetition period of the experiment. Processes longer than this timescale cannot be measured. Moreover, such processes are abruptly disturbed after the repetition period of the experiment because the electrical pump is periodically changing the external conditions. If such slow processes exist, the sample is also not in an equilibrium state before the field pulse is applied at $t = 0$.

To measure processes slower than 100 ms, a modified setup was developed in this work. It operates at any period that is a multiple of the original repetition period by controlling the Q-switch of the laser. Detailed wiring and timing diagrams of the setup are given in reference [121].

The longer delay times are paid for by increased measurement times. To get the same number of laser pulses, and thus SHG intensity, a 1 s repetition period experiments takes ten times longer than the equivalent 100 ms repetition period experiment.

Chapter 3

Investigated materials

The two investigated model compounds, MnWO_4 and CuO , are joint-order-parameter multiferroics. In both, ferroelectricity is induced by the magnetic spin-spiral order. This particular class of multiferroics was chosen for the investigation of magnetoelectric switching because it provides an intrinsically strong coupling between the electric and the magnetic order.

MnWO_4 represents the large class of spin-spiral multiferroics with low ordering temperatures $T \lesssim 40$ K [30–33]. It is a prototypical example of spin-spiral induced ferroelectricity and therefore a suitable model compound for studying magnetoelectric switching.

In contrast, CuO becomes magnetically and electrically ordered at the significantly higher temperature of 230 K. Furthermore, it exhibits an unusual sequence of phase transitions in which the multiferroic phase is directly reached from the paramagnetic phase. A purely magnetic intermediate phase is missing¹. The high ordering temperature and the unusual sequence of phase transitions renders CuO an interesting system for investigation.

This chapter we will review the relevant material properties of MnWO_4 and CuO .

3.1 MnWO_4

MnWO_4 is chosen as a classic example for spin-spiral induced multiferroicity. It is one of very few multiferroic materials that can be found in nature. Anyway, these natural crystals contain many defects and impurities. Therefore, they are not well suited for studies of the fundamental physical properties. Instead, synthetically grown crystals are used for all measurements.

¹The intermediate phase has not been observed in any standard measurements that are used to identify phase transitions. However, there are preliminary results from ultrasonic measurements which claim an intermediate phase [122].

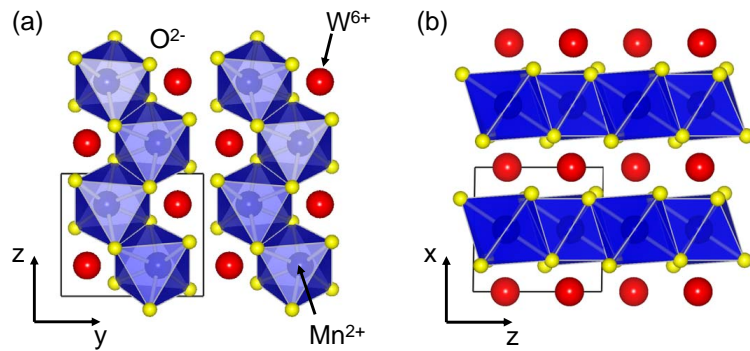


Figure 3.1 – Crystal structure of MnWO_4 . Chains of MnO_6 octahedra and of WO_6 octahedra are stacked alternately in the x -direction. Both types of octahedra chains form a zig-zag structure in the yz -plane. The black line denotes the unit cell.

3.1.1 Crystal structure

The crystal forms a monoclinic lattice with space group $P2/c1'$ (point group $2/m1'$). The lattice constants at room temperature are $a = 4.830\text{\AA}$, $b = 5.7603\text{\AA}$ and $c = 4.994\text{\AA}$ and enclose an monoclinic angle of $\beta = 91.14^\circ$ [123]. Because the monoclinic angle is close to 90° , previous symmetry analysis and SHG measurements [115] use a Cartesian coordinate system x, y, z which approximately coincides with the crystallographic axes a, b, c . For consistency, this convention will be applied also in the present work. The error introduced is only small and the results below do not critically depend on it².

Figure 3.1 displays the atomic positions. Distorted MnO_6 octahedra are stacked in a zig-zag chain along the z -axis, sharing edges. A zig-zag chain of distorted WO_6 octahedra is located half a unit cell shifted in the x -direction. For clarity, only the MnO_6 octahedra are marked in the figure, but, the chain of WO_6 octahedra would look analogous. The shift of half a unit cell results in an alternating stacking of the two types of octahedra chains along the x -direction. The monoclinic unit cell is outlined in black. In part (a) of the figure the glide plane $\perp y$ can be seen (e.g. mirror at the right border of the unit cell and shift by $\frac{z}{2}$). The twofold rotation symmetry 2_y is directly obvious in the view along the y -axis (part (b)).

3.1.2 Phase diagram

Mn^{2+} is the only magnetic ion in MnWO_4 . Its five $3d$ electrons align parallel according to Hund's Rules, resulting in a total Mn spin of $S = 5/2$. Neighboring Mn^{2+} ions are connected via O^{2-} ions in 90° and 180° angles. This results in competing Mn – O – Mn superexchange interactions, leading to magnetic frustration, which will give rise to the spin spiral. As a consequence of the alternating stacking of MnO_6 and WO_6 octahedra along the x -direction, the magnetic exchange is weakest along this direction [124].

The magnetic phase diagram of MnWO_4 is shown in figure 3.2. It is prototypical for spin-spiral multiferroics. At low temperature, it consists of a sequence of different antiferromagnetic

²Essentially, it would mean that certain SHG tensor components are not measured exactly, in particular signals originating from other tensor components may be admixed. Depending on the actual measurement the error is at most $\sin 1^\circ \propto 1.7\%$, but in almost all measurements this factor appears at least squared, rendering it practically negligible.

3.1. MnWO₄

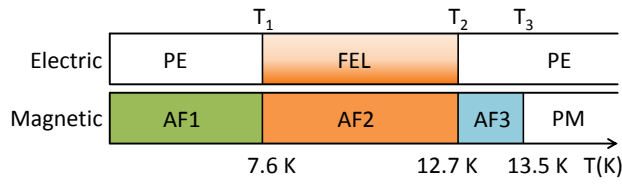


Figure 3.2 – Electric and magnetic phases of MnWO₄. Spins order in an incommensurate spin density wave below T_3 . Upon further cooling the AF2 phase is reached. Here, an additional component of the magnetic moment along y is present, which results in an elliptical spin spiral. This induces a ferroelectric polarization. Below T_1 the magnetic structure obtains an antiferromagnetic $\uparrow\downarrow$ configuration and consequently the polarization is no longer present. (image from [121])

phases. These phases will be labelled AF1 to AF3 and the corresponding ordering temperatures T_1 , T_2 and T_3 .

Above $T_3 = 13.5\text{K}$, MnWO₄ is paramagnetic and paraelectric. A second order phase transition to the antiferromagnetic AF3 phase occurs at the transition temperature T_3 . Here, the spins align along the magnetic easy axis, which lies in the xz -plane and has an angle of $\approx 35^\circ$ to the x -axis (figure 3.3 (a)). The amplitude of the spins is sinusoidally modulated, resulting in an incommensurate spin density wave with wave vector $\mathbf{k}_{AF3} = (-0.214, \frac{1}{2}, 0.457)$ [123]. The value $k_y = \frac{1}{2}$ implies a doubling of the magnetic unit cell along y . This is caused by an antiferromagnetic spin-alignment in adjacent crystallographic cells. $\mathbf{k}_x, \mathbf{k}_z$ are irrational, which implies that the periodicity of the spin density wave is not a multiple of the crystallographic cell in these directions. Therefore, translation invariance along x and z is lost. However, the point group symmetry ($2/m1'$) remains the same as in the paramagnetic phase. Still, no electric polarization can exist because inversion symmetry is maintained.

When cooling further, the AF2 phase is reached via another second order phase transition at $T_2 = 12.7\text{K}$. The spins now obtain an additional finite component along the y -direction (figure 3.3 (a)). This results in a spiral magnetic structure. Effectively, the spins rotate in a plane spanned by y and the easy axis. Their amplitude slightly varies ($m_y/m_{\text{easy}} \approx 0.9$) resulting in an elliptical spin spiral [125]. The periodicity and hence the wave vector remain the same $\mathbf{k}_{AF2} = \mathbf{k}_{AF3} = (-0.214, \frac{1}{2}, 0.457)$.

This spin structure might look helicoidal on a first view (cf. figure 1.11). However, the plane of rotation is not normal to the z -axis, which is the direction, the spin chain is running along. Therefore, the cross-product $\mathbf{S}_i \times \mathbf{S}_j$ is not parallel to the direction of propagation, which will induce a ferroelectric polarization according to equation (1.6)³. From a symmetry point of view, the cycloidal component of the spin-spiral breaks the inversion symmetry and reduces the point group to $21'$. This allows for a ferroelectric polarization along the y -direction. Pyroelectric measurements yield a maximal value of $\mathcal{P}_y \approx 5\text{nC cm}^{-2}$ [45, 126]. This is three orders of magnitude smaller than in classical ferroelectrics like BaTiO₃ or PZT, but a common order of magnitude for magnetically induced ferroelectricity.

At $T_1 = 7.5\text{K}$ the spin spiral locks in to a commensurate modulation $= \mathbf{k}_{AF1} = (\frac{1}{4}, \frac{1}{2}, \frac{1}{2})$. Just

³Actually even for $\mathbf{S}_i \times \mathbf{S}_j \parallel z$ the zig-zag character of the chain would induce a local polarization because the spin connecting vector \mathbf{e}_{ij} would not point along z , but it would be tilted up and down alternatingly. In that case the polarizations at a 'zig' and a 'zag' step would be exactly opposite and therefore no macroscopic polarization would occur.

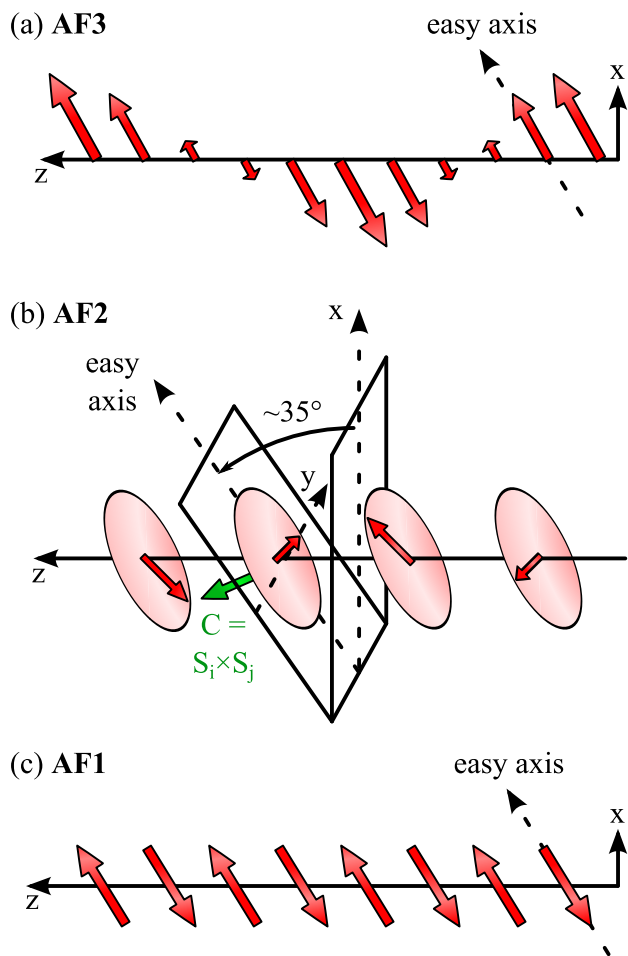


Figure 3.3 – Magnetic orders in MnWO_4 .

(a) AF3 phase: The spins align along the easy axis, which encloses an angle of $\approx 35^\circ$ with the x -axis. The spin amplitude is sinusoidally modulated.

(b) AF2 phase: An additional spin component along y -orders below $T_2 = 12.7$ K, resulting in an elliptical spin spiral.

(c) AF1 phase: The spins lock in to an antiferromagnetic up-down arrangement while remaining aligned along the magnetic easy axis.

like in the y -direction, the structure in z -direction is now a simple antiferromagnetic $\uparrow\downarrow$ order (figure 3.3 (c)). The magnetic unit cell quadruples along x because of an $\uparrow\uparrow\downarrow\downarrow$ spin sequence along that direction. Since all spins point along the easy axis no ferroelectric polarization can be induced. The point group is again $2/m1'$, which corresponds to the one in the paramagnetic and AF1 phase.

Magnetic fields affect the stability regions of the phases [45, 126, 127]. In general they lower T_2 and raise or lower T_1 depending on their orientation. For large fields $H_y > 11$ T the ferroelectric polarization flops from the y - to the x -direction. This reflects the strong interplay of electric and magnetic order. The presence of a magnetic field will likely also influence the properties of magnetoelectric switching by an electric field. Such types of measurements have not been performed, but may give additional insights into the magnetoelectric coupling in the future.

3.1.3 Order parameters

Since the SHG measurements are sensitive to the order parameters in the material, we will now detail the order parameters for the different phases in MnWO₄. Using Landau theory one can derive the order parameters from the symmetry of the corresponding phases. This procedure is described for MnWO₄ in [92]. Therefore, we only sum up the results here and relate them to the physical properties.

The complete phase diagram can be described by two two-component order parameters

$$\eta_1 = \begin{pmatrix} \sigma_1 e^{i\theta_1} \\ \sigma_1 e^{-i\theta_1} \end{pmatrix} \quad \eta_2 = \begin{pmatrix} \sigma_2 e^{i\theta_2} \\ \sigma_2 e^{-i\theta_2} \end{pmatrix} \quad (3.1)$$

Both η_1 and η_2 are magnetic order parameters. As every antiferromagnetic order parameter, they represent certain linear combinations of the spins. The exact linear combinations are given in reference [92].

The notation using the complex conjugate (equation (3.1)) is advantageous for the mathematical treatment. Each order parameter is fully described by the amplitude σ_i and the phase θ_i .

Figure 3.4 displays the temperature dependence of the order parameters. In the AF3 phase only η_1 is non-zero. The amplitude of the order parameter describes the degree of order. At T_3 thermal fluctuations completely destroy the magnetic long-range ordering. So the order parameter amplitude σ_1 is zero here. When entering the AF3 phase the spin density wave emerges and σ_1 becomes finite. As the temperature is lowered further, the spin density wave gets less distorted by thermal fluctuations, so σ_1 rises. Apparently the stabilization happens in a small temperature range because σ_1 does not show any critical behavior below T_2 , i.e. it is temperature independent. This is described by the term the order parameter is "frozen". Physically this means that the spin density wave is perfect now and not affected by thermal fluctuations any more. The phase θ_1 could be related to the phase of the spin density wave. However, it is not important in the AF3 phase.

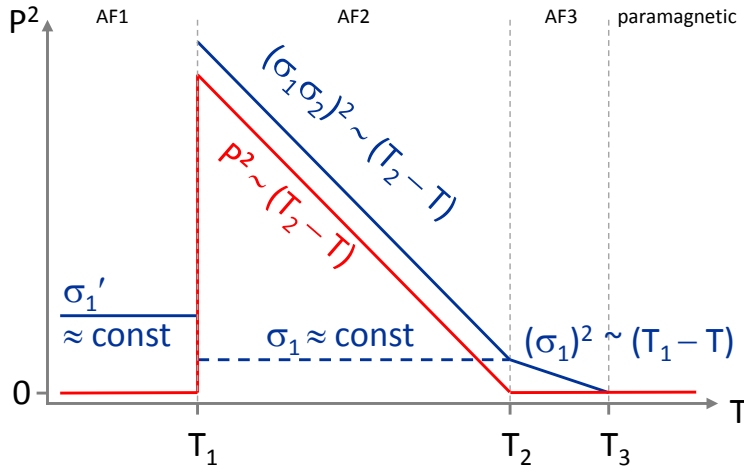


Figure 3.4 – Temperature dependence of the order parameter amplitudes in MnWO_4 . For easier display the squares of the order parameters are plotted because all order parameters exhibit a square-root scaling law. The magnetic order parameter σ_1 in the AF3 phase reflects the sinusoidal spin modulation. At T_2 the ordering of an additional spin component along y leads to a second magnetic order parameter σ_2 . The coupling of the two give rise to the polarization \mathcal{P} . In the AF2 phase σ_1 is frozen. The spin component along y vanishes again in the low temperature AF1 phase, resulting in $\sigma_2 = 0$. Furthermore the lock-in to the commensurate up-down spin arrangement leads to a change in the amplitude of σ_1 .

As discussed in the previous section, a transverse spin component ($\parallel y$) orders at T_2 . This leads to the emergence of a new order parameter η_2 in the AF2 phase. The exact relation of the order parameter to the structure is complicated because of the elliptic spin-spiral with the tilted plane of rotation. Therefore, we restrict ourself to a simplified model. Essentially η_2 can be regarded as a second sinusoidal wave, just like η_1 .

Minimizing the free energy in the Landau theoretical analysis leads to an equilibrium condition $\theta_1 - \theta_2 = \pm \frac{\pi}{2}$ [92]. The superposition of the two linear spin modulations with a relative phase of $\pm \frac{\pi}{2}$ results in a spin spiral. This is completely analogous to the creation of circularly polarized light by overlapping two linear polarized beams which are perpendicularly polarized with respect to each other and have a phase shift $\frac{\pi}{2}$. Within this model it is immediately clear, why two magnetic order parameters are necessary to describe the spin spiral.

Because the rotation plane of the spiral incorporates the easy axis, there is an angle between $\mathbf{S}_i \times \mathbf{S}_j$ and the spin-connecting vector \mathbf{e}_{ij} . This induces a polarization \mathcal{P} along b via the inverse Dzyaloshinskii-Moriya interaction. The polarization is a secondary order parameter because it does not drive the phase transition. Instead, it is just a consequence of the onset of the order parameter η_2 . Using Landau theory, the coupling between \mathcal{P} and the magnetic order parameters can be calculated [92]:

$$\mathcal{P} \propto \sigma_1 \sigma_2 \quad (3.2)$$

From that, the temperature dependence of the polarization can be directly derived. σ_1 is frozen in the AF2 phase. Therefore, only σ_2 scales with the temperature. Since it emerges during a second order phase transition one obtains

$$\mathcal{P}(T) \propto \sigma_2(T) \propto (T_2 - T)^{\frac{1}{2}} \quad (3.3)$$

This pseudo-proper scaling (section 1.2.3) is consistent with experimental results from pyrocurrent and SHG measurements [45, 114, 126].

3.1.4 Domains

We restrict the discussion of domains in MnWO₄ to the multiferroic AF2 phase, which is required for magnetoelectric switching. A spin spiral structure allows for two different types of domains. First, the *helicity* of the spiral can be right-handed (σ^+) or left handed (σ^-). Because the helicity is directly related to the polarization via equation 1.6 there are also two different ferroelectric domains $\mathcal{P}^+, \mathcal{P}^-$, which coincide with the magnetic helicity domains. The second type of domain are *translation domains*. They can be visualized as a discontinuous step in the phase of the spin spiral. The name translation domains stems from the fact that they can be transformed into each other by applying a translation, which corresponds to a global phase shift. Since the helicity does not change at a translation domain wall, also the polarization will be the same on both sides. Hence, translation domains do not play a role in magnetoelectric switching using electric fields. Both domain types have been observed experimentally by SHG [38, 114].

It is possible to relate the order parameters to the domains in the material and even predict which types of domains may occur. Since domains represent energetically equivalent realizations of the order parameter orientation, the amplitude of the order parameters has to be the same in all domains. However, the sign or phase can differ. Minimization of the free energy in MnWO₄ leads to the relation $\theta_1 - \theta_2 = \pm \frac{\pi}{2}$. These two possible values of the relative phase correspond to the two helicity states. This becomes immediately clear, when looking at the simplified model of superposition of linear waves discussed above. A change of the relative phase $\theta_1 - \theta_2$ can be obtained by shifting one order parameter by π . This is equivalent to a 180° phase shift of one of the linear waves and changes a right-circular wave into a left circular one and vice versa.

MnWO₄ is already magnetically ordered in the AF3 phase. However, this order does not predefine the magnetic helicity domains in the AF2 phase. The sign of the helicity corresponds to the relative phase $\phi = \pm \frac{\pi}{2}$ of the order parameters η_1 and η_2 . Since η_2 just emerges at T_{N2} , its relative phase to η_1 and thus the helicity domain states will only be determined when actually entering the AF2 phase.

Translation domains exist for the following reason. Only the relative phase $\theta_2 - \theta_1$ of the order parameters η_1 and η_2 occurs in the free energy. Adding a global phase to both order parameters leaves the free energy invariant. Therefore, any value of the global phase constitutes a separate phase domain. As a result, there can be infinitely many different translation domain states, while there are only two helicity domain states.

Translation domains will only occur in a zero-field cooled domain state. Different parts of the sample will independently choose the global phase of the spin spiral upon nucleation. In contrast, translation domains are not expected in magnetoelectric switching. They cannot be introduced by the electric field because they have the same direction of the ferroelectric polarization. Nevertheless, information on translation domains can be valuable for magne-

toelectric measurements. Because they are only present in the magnetic system but not in the electric system, their observation in a certain SHG tensor component verifies that this tensor component is directly coupling to the magnetic system. This knowledge is important in dynamic measurements, in which a decoupling of the magnetic and electric orders is possible in principle. See section 3.1.6 for a more detailed discussion on the coupling of the SHG to the order parameter.

The 180° domains of both the electric and the magnetic system coincide. The polarization direction is one-to-one linked to the helicity of the spin spiral. Furthermore, both the electric and magnetic properties of the 180° domains determine their structure. Because of the inseparable entanglement, at least in equilibrium, as well as the influence of both types of order, these domains were termed *multiferroic domains* [38].

3.1.5 Magnetolectric measurements on MnWO₄

The first magnetolectric effect reported on MnWO₄ was the polarization flop from the *b*-axis to the *a*-axis in magnetic fields larger than 10 T [45]. Subsequent measurements investigated the dependence of the polarization on magnetic fields in detail [128, 129]. Depending on its direction the magnetic field either stabilizes or destabilizes the spin spiral, resulting increased or decreased ferroelectric polarization respectively. Kundys et al. studied the dependence of the ferroelectric hysteresis loop on the applied electric field [130]. Aside from the reduction of the polarization a destabilization of the spin spiral by the magnetic field leads to a decreased coercive electric field. A reemergence of the ferroelectric polarization has been observed in extremely high magnetic fields around 40 T [131].

The inverse effect, i.e. the influence of an electric field on the magnetic order was studied by neutron diffraction [132, 133]. This showed that it is possible to switch the helicity of the spin spiral using an electric field. Furthermore Meier et al. provided first SHG images, which reveal the influence of the electric field on the domains [38].

3.1.6 SHG signals in MnWO₄

This section briefly reviews the SHG properties of MnWO₄, which are relevant for the following measurements, including the SHG tensor components coupling to the electric and magnetic order parameters. More detailed descriptions of SHG on MnWO₄ can be found in [38, 114, 115, 134, 135].

A complete analysis of allowed tensor components in MnWO₄ based on symmetry [112] has been performed in [115]. The paramagnetic/paraelectric phase, the AF1 phase and the AF3 phase are inversion symmetric and therefore no ED tensor components are allowed. In contrast, the inversion symmetry is broken in the AF2 phase, giving rise to a number of allowed ED tensor components for $k \parallel x$ and $k \parallel z$: χ_{yyy}^{ED} , χ_{yxx}^{ED} , χ_{yzz}^{ED} , χ_{zyz}^{ED} and χ_{xyx}^{ED} . The latter two have not been observed experimentally. The other ones are listed in table 3.1 together with their spectral position. Because these tensor components emerge as a result of the broken inversion symmetry, they couple to the order parameter(s) of the AF2 phase. It is

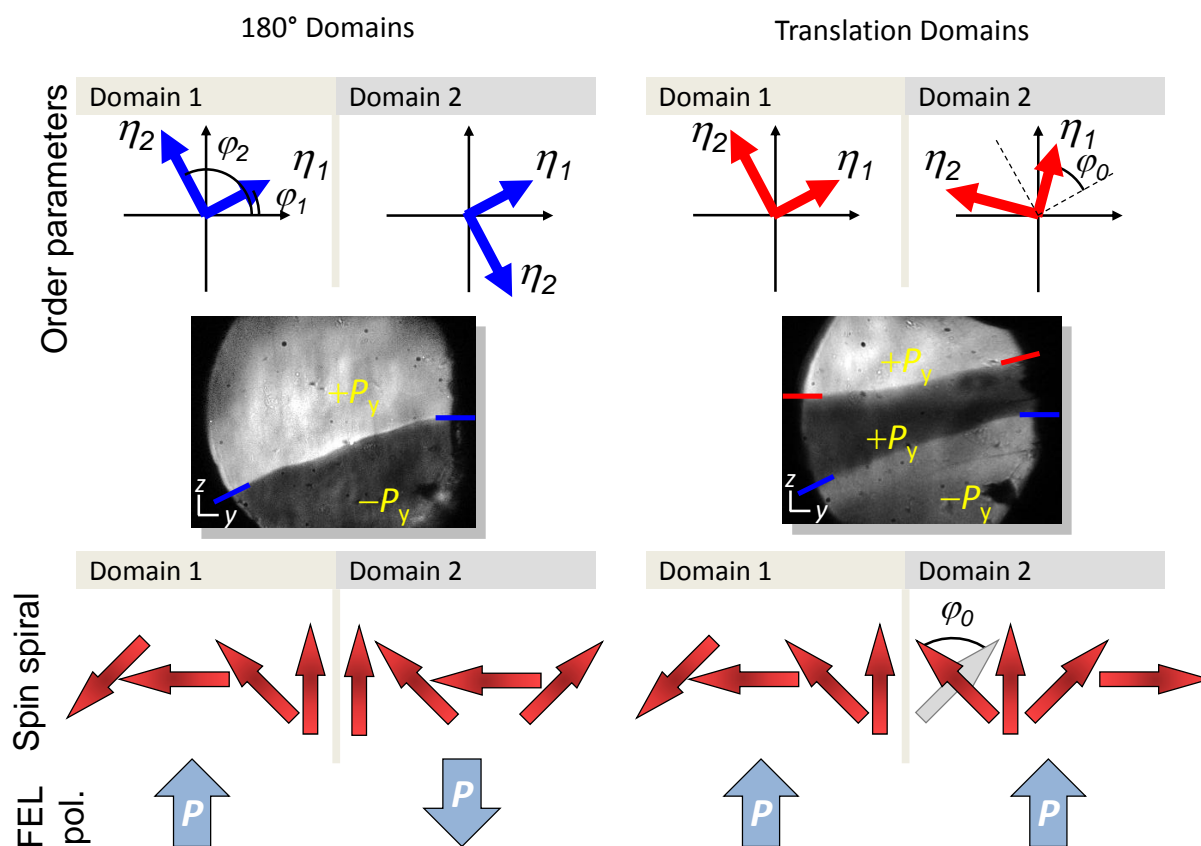


Figure 3.5 – Relation between order parameters and domain types in MnWO₄.

The relative phase shift $\theta = \phi_2 - \phi_1$ of the order parameters between two 180° domains is 180°. This corresponds to right-circular and left-circular helicity states of the spin spiral. The ferroelectric polarization is coupled to the helicity of the spiral and therefore changes sign between adjacent 180° domains.

In different translation domains only the global phase ϕ_0 of the order parameters differs, the relative phase θ is the same. This can be interpreted as an discontinuity of the rotation angle at the domain wall. The sense of rotation, and hence the polarization, remain the same.

Domain images from [115]

Incident light field	Tensor component	Photon energy	Coupling order parameter
$k \parallel x$	χ_{yzz}^{ED}	2.75 eV (SHG)	electric
$k \parallel y$	$\chi_{x'z'z'}^{\text{ED}}$	2.22 eV (SHG)	magnetic
$k \parallel z$	χ_{yyy}^{ED}	1.50 eV (SHG)	unknown
$k \parallel z$	χ_{yxx}^{ED}	1.95 eV (SHG)	magnetic

Table 3.1 – SHG tensor components coupling to the multiferroic AF2 phase in MnWO_4 [115]. The coupling of the SHG to the magnetic state can be proven for $\chi_{x'z'z'}^{\text{ED}}$ and χ_{yxx}^{ED} by symmetry and by the observation of translation domains respectively. Since no translation domains have ever been observed in χ_{yzz}^{ED} , it is assumed to couple to the electric order. No experiments have been performed on χ_{yyy}^{ED} in this work and there are too few prior results to be able to determine the coupling for this tensor component.

not a priori clear if they primarily couple to the magnetic or electric order. This issue will be detailed in the following section.

From the point symmetry, no SHG is allowed for light propagating along the y -axis in any phase. Despite this, a sharp peak is observed in the AF2 phase for photon energies around 2.22 eV. Its polarization direction does not coincide with the crystallographic axes. Instead it has its own reference coordinate system (x', y, z') which is rotated by $\approx 25^\circ$ around the y direction with respect to the crystallographic axes. This signal $\chi_{x'z'z'}^{\text{ED}}$ at 2.22 eV can be explained by taking into account the incommensurability of the magnetic order. The incommensurability violates translation symmetry on a large scale. Strictly speaking, there is no translation symmetry at all in the crystal. Even an approximate reproduction of the structure may require long-range translations. Originally it was argued that SHG is only sensitive to the point group because any translation of a fraction of a unit cell is so small compared to the wavelength of the light that it can be neglected. This argument does not hold anymore if long-range translations exceeding the size of the unit cell are symmetry transformations. The resulting symmetry is lower than for a similar commensurate structure, which gives rise to additional SHG tensor components.

Additional MD tensor components are allowed for $k \parallel x$ and $k \parallel z$ in any phase. These are of crystallographic origin, i.e. result from the symmetry of the crystal structure, and do not depend on the magnetic or electric order parameters. Detailed measurements of these signals have not been performed because they do not contain any information on the multiferroic state. Nevertheless, these signals are useful as constant reference for the generation of domain contrast by interference (section 2.1.3 and A.2).

Coupling to the order parameters

The close entanglement between electric and magnetic system in spin-spiral multiferroics makes it difficult to distinguish, which of the systems is responsible for the SHG (see section 2.1.2). As pointed out there, the distinction does not make sense in most cases, e.g. in static domain patterns. However the clarification of this question is important for certain types of measurements such as SHG efficiency and dynamic switching processes.

The relation between polarization and the magnetic order parameters is given by equa-

tion (3.2). The order parameter σ_1 is already frozen at the phase transition temperature T_2 to the AF2 phase, i. e. it does not show any critical temperature dependence. \mathcal{P} and σ_2 emerge simultaneously at T_2 and scale with the temperature in the same way because they are proportional to each other. Furthermore, the point symmetries of the electric and the magnetic structure are the same in the AF2 phase. Therefore, a rigorous distinction between the possible couplings $\chi(\mathcal{P})$ and $\chi(\sigma_2)$ is not possible by tensor components or temperature dependence.

However, taking into account that the magnetic order is significantly more complex than the electric order, SHG signals stemming from the magnetic order can be uniquely identified in certain cases. The ferroelectric polarization \mathcal{P} can only have two orientations. These domains directly correspond to helicity domains of the spin spiral. But because the spin spiral is a periodic structure it may possess translation domains. These domains have the same helicity, but differ in phase. Particularly, the domain wall consists only of a discontinuity in the rotation angle of the spins. This phase shift directly translates to a phase shift of the emitted SHG light. Therefore, a phase shift other than 180° between domains can only be realized in a SHG signal originating in the magnetic system. This is most easily seen in domain images with multiple domains when the order parameter dependent SHG is interfered with an order-parameter-independent background. If more than two different intensities are present, this implies the existence of more than two phases, which can only be realized by the translation domains. Such domains have been observed for χ_{yyy}^{ED} at 2.15 eV [135], which proves that this tensor component couples to the magnetic order.

χ_{yzz}^{ED} at 2.75 eV did never exhibit any translation domains. If it was coupling to the magnetic order, such domains would be expected. Thus, their absence hints at a ferroelectric origin of this component.

A further degree of freedom of the spin spiral in MnWO₄ is its incommensurability. This lowers the symmetry and allows for the additional tensor component $\chi_{x'z'z'}^{\text{ED}}$ at 2.22 eV. Here it is possible to unambiguously attribute this signal to the magnetic order because only the magnetic system is incommensurable, but not the ferroelectric order.

The above methods can only confirm the coupling to the magnetic order. The tensor components that do not show additional hallmarks of the degrees of freedom of the magnetic system and that fulfill the selection rules of 21' are assumed to be of ferroelectric origin.

3.1.7 Samples

The present work mainly uses top-seeded melt grown MnWO₄ crystals that were produced in Cologne (Prof. Dr. P. Becker, Institut für Kristallographie, Universität zu Köln, Germany). Additional crystals were synthesized in Caen using the floating zone technique (Dr. C. Martin, Laboratoire de Cristallographie et Sciences des Matériaux, ENSICAEN, France). We used them to check the influence of the growth method (section 4.4). The samples were lapped and etch-polished to a thickness of 0.1-1.0 mm with Al₂O₃ powder and a silica slurry, respectively.

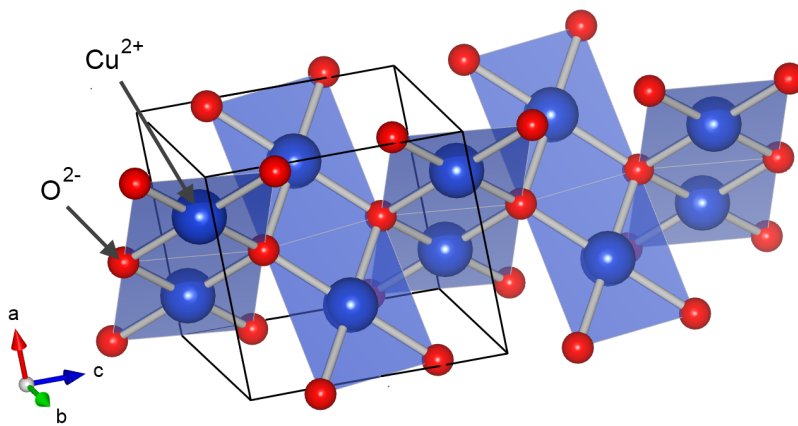


Figure 3.6 – Crystal structure of CuO.

Each Cu^{2+} ion is coordinated to four O^{2-} ions resulting in approximately square plates. These plates form ribbons along $[110]$ and $[\bar{1}\bar{1}0]$, which are connected via the O^{2-} ions. The unit cell is outlined in black.

3.2 CuO

Most magnetically induced ferroelectrics become multiferroic only at very low temperatures, typically $< 40\text{K}$, because the frustration leading to spiral magnetic order also reduces the phase transition temperature. In that sense CuO is a very unusual material because it exhibits magnetically induced ferroelectricity at much higher temperatures up to $T_2 = 230\text{K}$ [46].

3.2.1 Crystal structure

Each Cu^{2+} ion is coordinated to four O^{2-} ions forming nearly rectangular CuO_4 plates (figure 3.6)⁴. Rows of edge sharing plates extend along $[110]$ and $[\bar{1}\bar{1}0]$, alternately stacked along the c -axis. This results in a monoclinic crystal structure (space group $C2/c$, point symmetry $2/m$) with an angle of $\beta = 99.5^\circ$. The lattice constants are $a = 4.6826\text{\AA}$, $b = 3.4235\text{\AA}$ and $c = 5.1267\text{\AA}$ [137].

3.2.2 Phase diagram

Figure 3.7 (a) shows the magnetic and electric phase diagram of CuO. Two magnetic phase transitions have been observed at $T_1 \approx 213\text{K}$ and $T_2 \approx 230\text{K}$ using various techniques, such as magnetic susceptibility measurements, specific heat measurements, dielectric constant measurements and neutron measurements [46, 138–140]. The temperature values reported in different publications vary by approximately 1 K. Recent, yet unpublished ultrasonic measurements hint at the existence of an additional AF3 phase above T_2 with a width of approximately 0.7 K [122]. However, this phase transition has not been seen in the other measurements and thus its existence is still an open question.

Below $T_2 \approx 230\text{K}$ in the AF2 phase the spins order in the form of an incommensurate cycloidal spiral with $\mathbf{q} = (0.506, 0, -0.483)$ [141]. Figure 3.7 (b) shows the configuration of the magnetic moments. The dominant exchange interaction is along $[10\bar{1}]$. Its large value of 60 meV to

⁴Drawing produced using VESTA [136]

3.2. CuO

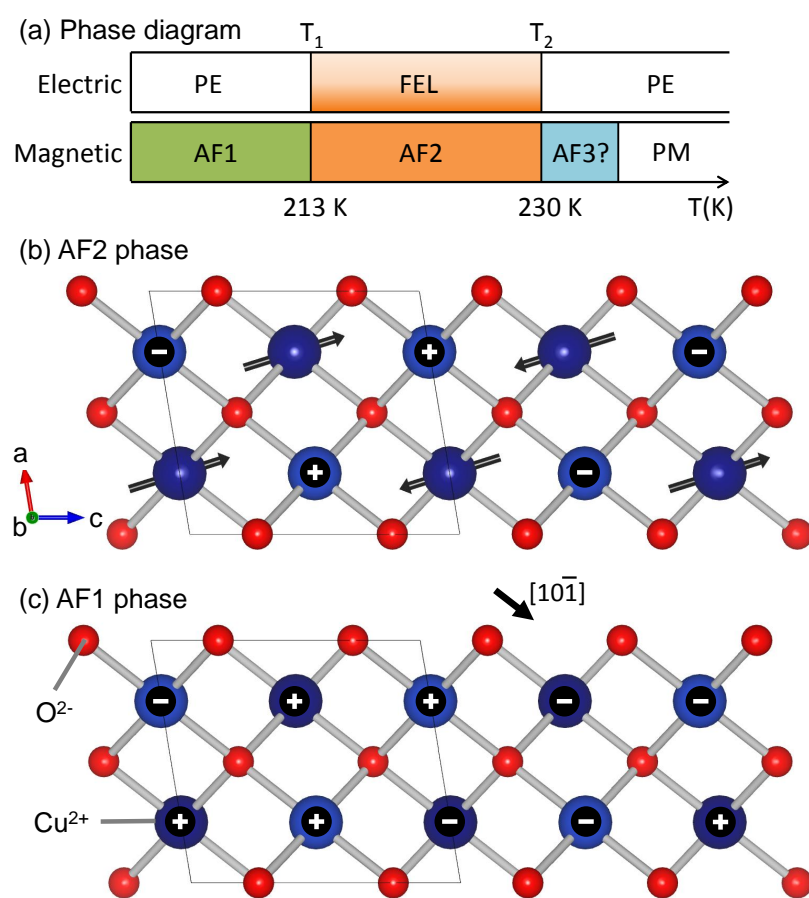


Figure 3.7 – Phase diagram and magnetic structure of CuO.

(a) Magnetic and electric phases. (b), (c) Magnetic structure of CuO. Darker Cu atoms are in the lower ac -plane at height b ; brighter CuO atoms are in the upper ac -plane at height $b + \frac{1}{2}$. Arrows and $+$, $-$ signs indicate the orientation of the magnetic moments. The dominant magnetic exchange in both phases is antiferromagnetic and runs along $[10\bar{1}]$. The outline shows the crystallographic unit cell.

80 meV is caused by the large Cu–O–Cu bond angle $\phi = 146^\circ$ [139, 142]. This strong coupling is responsible for the extraordinary high ordering temperatures in CuO. All other exchange interactions are much weaker, resulting in a quasi-one-dimensional system. The rotation plane of the spiral is given by $(a^*, 0.506b^* + 1.517c^*)$ and the envelope is nearly circular [141]. The spiral gives rise to a ferroelectric polarization along b . It has been experimentally observed in pyroelectric measurements with a value of up to $\mathcal{P}_b = 15 \text{ nC cm}^{-2}$ [46]. This size is comparable to other magnetically induced ferroelectrics. From the point of view of symmetry, the spin spiral configuration breaks the inversion symmetry, allowing the polarization to emerge as an improper order. The resulting point symmetry in the AF2 phase is $21'$. The actual mechanism leading to ferroelectricity is still under theoretical discussion [143–145].

Below $T_1 \approx 213 \text{ K}$, all spins align parallel or antiparallel to the b -axis. This results in an $\uparrow\uparrow\downarrow\downarrow$ arrangement along c , while the strong antiferromagnetic coupling along $[10\bar{1}]$ is maintained (figure 3.7 (c)). The spin modulation locks in at a wave vector $\mathbf{q} = (\frac{1}{2}, 0, -\frac{1}{2})$, yielding a commensurate magnetic order. This wave vector also indicates that the magnetic unit cell is doubled with respect to the crystallographic one. The point symmetry of the AF1 phase reverts to $2/m1'$, and consequently the ferroelectric polarization is no longer present.

3.2.3 Order parameters

The magnetic order parameters can be deduced from Landau theory [143]. Two two-component order parameters $\eta = (\eta_1, \eta_2)$ and $\zeta = (\zeta_1, \zeta_2)$ are necessary to describe the AF1 and AF2 phases. The existence of an AF3 phase is still in question (see above). If there is no AF3 phase, both order parameters would emerge simultaneously. This is very unconventional and does not happen in any other spin-spiral multiferroic. However, such a scenario is possible and can be explained by a triggering-coupling mechanism [146]. In this mechanism, only the magnetic order drives the phase transition. Due to a certain form of the free energy and a coupling term between magnetic and electric order parameters the polarization will set in simultaneously with the magnetic order. In the case of CuO, this results in a bilinear coupling

$$\mathcal{P} \propto (\eta_1 \zeta_1 + \eta_2 \zeta_2) \quad (3.4)$$

3.2.4 Ferroelectric and magnetoelectric measurements on CuO

Direct measurements of a ferroelectric hysteresis loop were reported, but do not yield reliable results due to large leakage currents [147]. Kimura et. al reconstructed a hysteresis loop using the following method [46]. The sample was field-cooled below T_2 to provide an electric single domain state. Then the field was switched off and a reverse poling field with certain amplitude E was applied. Finally, a pyroelectric measurement in zero field was performed to determine the polarization \mathcal{P} . Plotting \mathcal{P} versus E results in a hysteresis. It has to be emphasized that this indirect method indicates the existence of a switchable ferroelectric polarization. However, the obtained curve does not necessarily resemble the true ferroelectric hysteresis for the following reasons. First, the field cooling may prepare the sample in states that would not be reachable in zero-field cooling with subsequent application of the electric field at fixed T in the ferroelectric phase. Second, switching off the test field E before performing the pyroelectric measurement is necessary to prevent leakage currents, which would obscure the measurement of the surface charges. But in this switching the polarization may relax, so that only the remanent polarization would be measured.

Measurements of magnetization, dielectric constant, and electric polarization with and without magnetic fields report the absence of a linear magnetoelectric effect in CuO [148]. Even at magnetic fields up to 12 T the induced magnetization is low. This reflects the stability of the spin spiral, which is based on the exceptionally large antiferromagnetic exchange interaction. Consequently, no influence of the magnetic field on the polarization is observed. While magnetic fields do not have any influence, an applied electric field may switch the helicity of the spin spiral. Neutron polarimetry measurements indeed indicate that a partial magnetoelectric switching is possible, however, no single domain states could be obtained [149].

3.2.5 Sample

Only one sample was available for measurements on CuO. It is a z -cut fabricated in the group of Prof. Tsuyoshi Kimura (Division of Materials Physics, Graduate School of Engineering Science, Osaka University, Japan). It was lapped and etch-polished to a thickness of 100 μm .

Chapter 4

MnWO₄

Temporally and spatially resolved measurements of magnetoelectric switching have not been performed so far in any multiferroic. It is the primary goal of this work to elucidate the temporal aspects (How fast is magnetoelectric switching?) as well as the domain patterns in such a switching process. MnWO₄ was chosen as a model material for a classical low-temperature spin-spiral multiferroic.

Switching processes in ferroics are mostly dominated by domains. Therefore, a good knowledge on the domains in the material is essential for the understanding of magnetoelectric switching. Section 4.1 will cover static domain structures of MnWO₄ in detail. In a next step, we investigate the influence of static or slowly varying fields (section 4.2). This demonstrates the feasibility of magnetoelectric switching in MnWO₄ and reveals the effect of the electric field on the domains under equilibrium conditions. With the knowledge from the previous sections it is then possible to understand the dynamics of the magnetoelectric switching process. While the experimental findings are covered in section 4.3, a separate section discusses them in detail (section 4.5).

Supplementary measurements and discussions concerning experimental details can be found in appendix A. This information is required for correctly measuring and interpreting the SHG signals in MnWO₄. It contains the effects of certain specialties of SHG in MnWO₄ and of the setup used. Therefore, it is particularly written as a reference for a reader, who wants to perform and analyze own SHG measurements.

4.1 General domain structures and properties

In this section, we investigate the domain structure of the multiferroic 180° domains in the AF2 phase of MnWO₄. Their two possible orientations are given by the helicity of the spin spiral in the AF2 phase. The Dzyaloshinskii-Moriya interaction uniquely connects the helicity with the ferroelectric polarization via equation (1.6). Thus, magnetic helicity domains and ferroelectric domains will coincide in equilibrium states. Due to this one-to-one correlation a distinction between both subsystems is pointless in the static case.

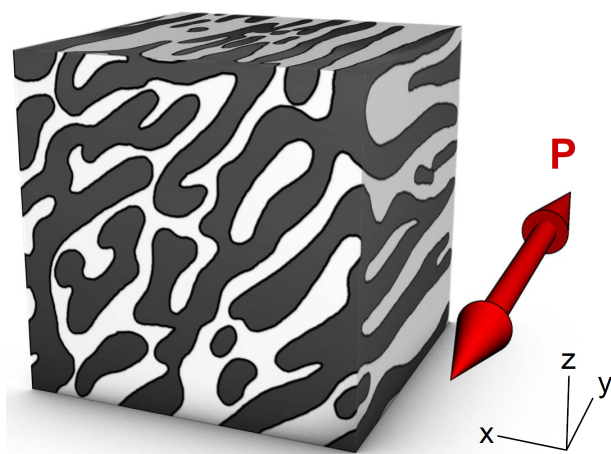


Figure 4.1 – Schematic picture of the preferential domain wall orientations in MnWO₄ based on SHG images [38].

Stripe-like structures are formed on the x - and z -face, which run along the polarization axis. More bubble-like patterns can be observed on the y -face. Here, slight preferences for the alignment of the walls perpendicular to the x -axis and along the magnetic easy axis.

As introduced in section 3.1.1, a Cartesian coordinate system (x, y, z) will be used, which approximately coincides with the crystallographic coordinates (a, b, c) . For simplicity planes will be denoted by their normal vector, i.e. (100) is an x plane. Domain images on the y -face are acquired using $\chi_{x'z'z'}^{\text{ED}}$ at 2.22 eV (SHG). The ones on the x -surface are based on χ_{yzz}^{ED} at 2.75 eV (SHG).

4.1.1 Preferential domain wall orientations

Figure 4.1 shows a schematic image of the domain distribution of 180° domains in the AF2 phase of MnWO₄. The patterns were obtained from SHG images in three different samples and projected onto the cube to give an impression of the three-dimensional structure of the domain pattern [38]. They tend to form stripes in the x - and z -plane with the walls running along the y -axis. On the y -surface exists a slight preference for the alignment along the magnetic easy axis, or alternatively perpendicular to the x -axis.

Stripe formation, as is observed on the x - and z -planes, is a typical behavior of ferroelectric domains [55]. A domain wall perpendicular to the polarization direction would correspond to a head-to-head or tail-to-tail configuration of dipole moments. Such a domain wall costs more energy than a wall, which is parallel to the polarization direction. As a result, the walls will align along the polarization direction (y). From this we deduce that the domain structure on the x - and z -faces is primarily dictated by the ferroelectric system.

The domain pattern looks completely different on the y -surface. The main axis of alignment is the magnetic easy axis, which encloses an angle of $\approx 35^\circ$ with the x -axis. It defines the plane of rotation for the spins in the spiral (figure 3.3 (b)). Aligning the domain wall with the plane of rotation may be an indication for the type of the domain wall. This will be discussed separately in section 4.1.4.

As we will see later, a second preferential axis exists that leads to walls aligning perpendicular to the x -axis (c.f. figure 4.5 or figure 4.10). This can be explained in terms of magnetic wall energy. The x -axis is the axis of weakest magnetic exchange energy because the MnO₆ octahedra are separated by layers of W (see figure 3.1 (b)). Since the spins cannot be optimally aligned with respect to each other at a magnetic domain wall, a magnetic domain wall will

4.1. General domain structures and properties

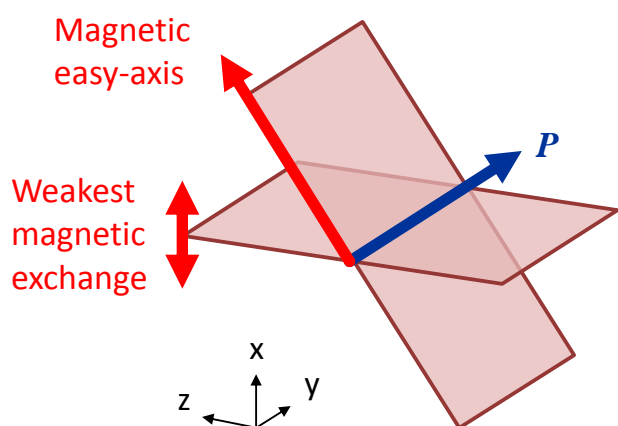


Figure 4.2 – Preferential planes for 180° multiferroic domain walls in MnWO_4 . The avoidance of energetically expensive ferroelectric head-to-head walls requires to align the walls along the polarization direction. This still leaves a rotational degree of freedom around the y -axis. Here are two axes preferred, the magnetic easy axis and a wall perpendicular to the weakest magnetic exchange.

always cost exchange energy. Consequently, it is energetically favorable to align the normal of the wall to the direction of weakest magnetic exchange.

The fact that two domain wall orientations may appear on the y -face, hints at a roughly equal domain wall energy for both orientations. As we will see below their relative fraction subtly depends on a number of parameters, which also supports this hypothesis. Furthermore, deviations from these directions are far more frequent than a deviation from a strict stripe pattern in the x - and z -planes. This implies that the magnetic domain wall energy is lower than the ferroelectric one. In summary, the orientation of a domain wall is defined by both the magnetic and the ferroelectric order. The ferroelectricity requires the wall to coincide with the polarization direction y . This leaves still a rotational degree of freedom around y , which is used to minimize the magnetic wall energy.

4.1.2 Memory effects and pinning

The stripe domain patterns in the x and z -plane look always the same independent of the sample temperature. This strict stripe-like structure is dictated by the comparably large energy, a head-to-head or tail-to-tail ferroelectric wall would cost. We have seen in the previous section that the magnetic system enforces less strict constraints because of the lower energy involved. It is thus more susceptible to thermal fluctuations and its stability decreases with increased temperature. Therefore the domain pattern on the y -face is temperature dependent.

Domains stability

Figure 4.3 shows a sequence of domain images, while increasing the temperature. At $T = 9$ K, which is deep inside the AF2 phase, the two preferential axes (easy-axis and perpendicular to x) are clearly visible (figure 4.3 (a)). Upon heating up, local deviations from these axes appear, while the overall orientation is maintained (figure 4.3 (b,c)). Close to the phase transition the overall structure breaks down to a bubble topology. Only a very slight preferential orientation remains (figure 4.3 (d)). The additional thermal energy at higher temperatures destabilizes the domain structure. Note that the bubble topology emerges close to the transition temperature independent of the temperature scan direction; i.e. when heating from deep within the

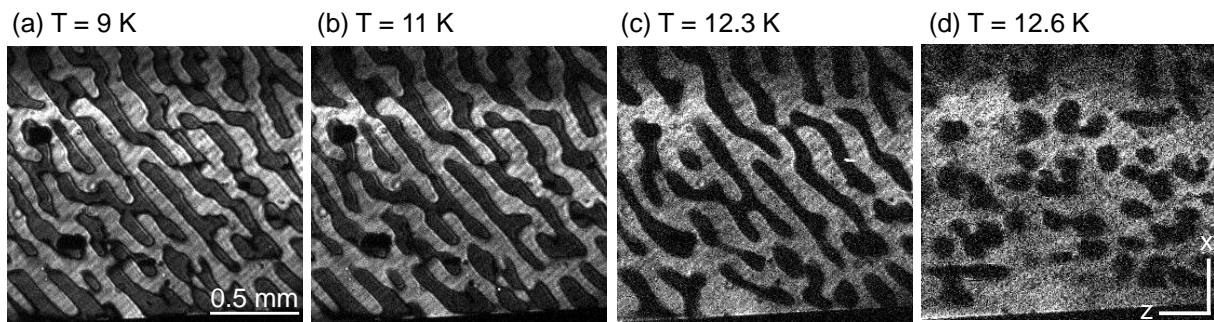


Figure 4.3 – Temperature dependence of the domain pattern in MnWO₄ on the y -surface. The additional thermal energy destabilizes the domain pattern. Thus, the domain walls do not have to be aligned along the energetically favourable directions anymore.

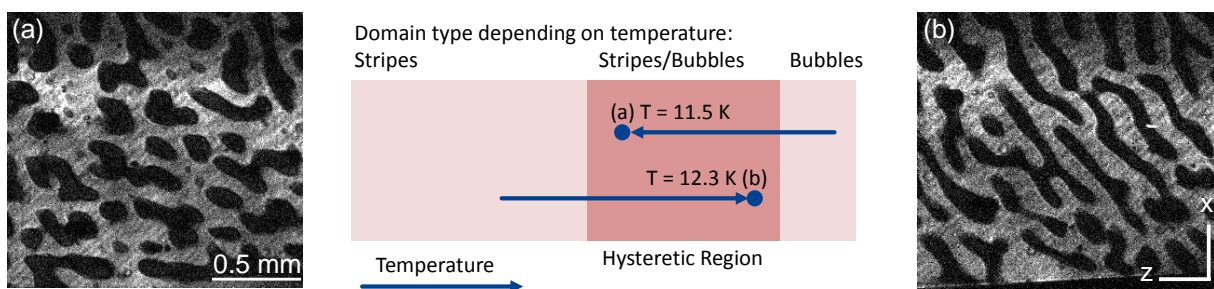


Figure 4.4 – Thermal hysteresis of the domain pattern in the AF2 phase of MnWO₄. At lower temperatures domains order more stripe-like, while close the phase transition at $T_2 = 12.7$ K are more bubble-shaped. These patterns exhibit a thermal hysteresis. When cooling down, the bubbles are still present at 11.5 K (a). However, when heating up, the stripe pattern is stable at least up to 12.3 K (b). Thermal hysteresis is an indication for pinning effects, which limit the free evolution of domains.

AF2 phase, as well as when cooling from AF3 to AF2. This hints at a thermal process and contraindicates a pure domain nucleation effect¹.

Thermal Hysteresis

The bubble structure of the domain pattern is not exclusively determined by the temperature because it exhibits a thermal hysteresis. There exists a region, in which the pattern depends on the temperature history of the sample. Cooling from high temperatures, the bubble topology is still present at 11 K (figure 4.4 (a)). Contrary, stripes remain visible up to 12.3 K when heating up the sample (figure 4.4 (b)). This is a first indication for pinning effects limiting the free evolution of domains.

¹Currently we cannot completely exclude the possibility that nucleation may still play a role. Because the derived sample temperature is close to the transition temperature ($T_{N2} - T = 0.1$ K) it might be, that the each laser pulse temporary heats the sample to the AF3 phase. This would imply a phase transition after every laser shot and a periodic renucleation of the domains. Measuring this effect with varying laser intensities could clarify this point.

4.1. General domain structures and properties

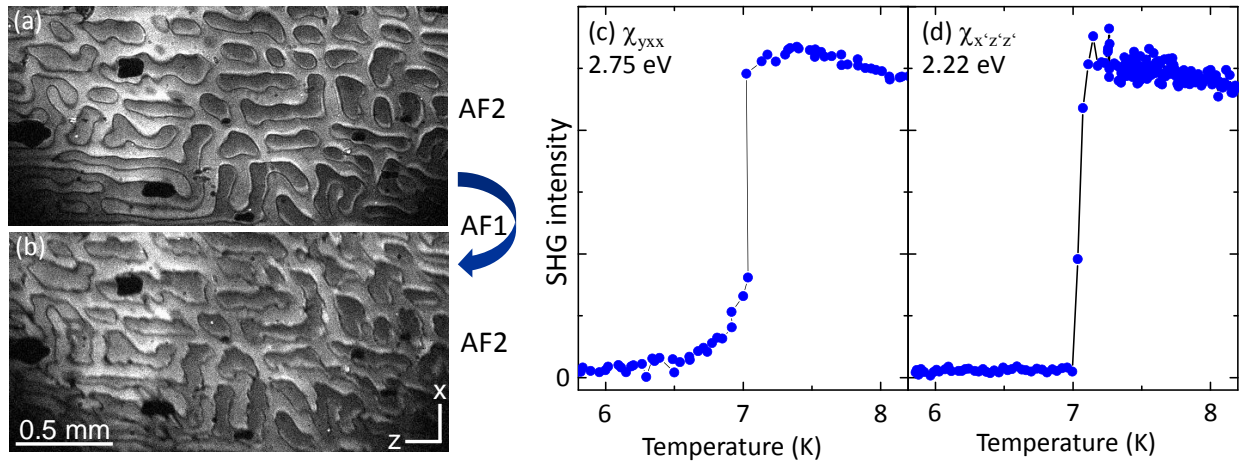


Figure 4.5 – Memory effect in the AF2 → AF1 → AF2 transition in MnWO₄. The domain pattern approximately reappears (a),(b), except for more jagged domain walls, which can be explained by missing thermal energy. This memory effect was explained by remaining domain nuclei in the AF1 phase [115] and correlated to a gradual decay of χ_{yxx}^{ED} at the phase transition ((c) Data from [115]). However, the present images (a),(b) were taken with $\chi_{x'z'z'}^{\text{ED}}$. Its temperature dependence was recorded in the actual switching cycle between the images (d). Here, the abruptly vanishing SHG signal implies that the pinning mechanism is more fundamental than just remaining nuclei.

Memory effects at the AF2 → AF1 transition

More drastically pinning effects can be seen when leaving the AF2 phase and entering back. Domains reappear almost identical in an AF2 → AF1 → AF2 cycle (figure 4.5 (a,b)). The locations and shape of most of the domains is approximately the same. After the cycle, domain wall corners tend to be less rounded and the domain walls are more jagged. Both can be attributed to thermal effects in the history of the domain formation. Coming from higher temperatures domains are formed with more thermal energy available. As in the extreme case with the bubble topology the thermal energy allows for more rounded corners. At the same time this energy may be used to overcome local pinning centers, so domain walls can be smoothed out. Conversely, this energy is missing when domains are formed in the AF1 → AF2 transition, which explains the pronounced corners and jagged edges. These differences in domain wall smoothness are another hallmark of the thermal hysteresis discussed before (figure 4.4). More important than the smoothness of the walls is the re-emergence of the overall domain pattern. These measurement are in agreement with memory effects reported in the AF2 → AF1 transition concerning the ferroelectric polarization [150] as well as the complete domain pattern [38, 115]. It is explained in terms of domain coexistence at this first order phase transition. Nuclei of the AF2 phase are believed to remain present in the AF1 phase. Remainder SHG signals from χ_{yxx}^{ED} even below the phase transition appear to support this [38]. In this publication, a memory effect in the domain pattern was observed. Additionally, they measured remainder SHG signals in the AF1 phase (figure 4.5 (c)), albeit in a tensor component different from the one in which the images were taken. Therefore, we repeated the experiment, recording the temperature dependence of the tensor component $\chi_{x'z'z'}^{\text{ED}}$, which was also used for acquisition of the domain images. In contrast to the former measurements, we do not see such a broadened transition region in this tensor component

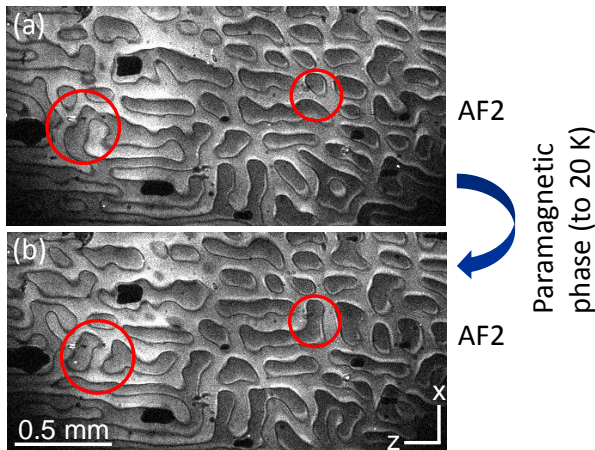


Figure 4.6 – Memory effect in the AF2 → paramagnetic → AF2 transition in MnWO₄. The domain pattern reappears approximately when heating the sample far into the paramagnetic phase (20 K) and returning back to $T = 9.7$ K. This very robust memory effect might be related to structural deformations of the crystal, which the magnetic system has imprinted into the AF2 phase.

(figure 4.5 (d)). The data are taken in exactly the cooling between the images figure 4.5 (a,b). We cannot unambiguously clarify, why a transition region is only observed in χ_{yxx}^{ED} , but not in $\chi_{x'z'z'}^{\text{ED}}$. It may just be sample dependent. Nevertheless, our results show that a memory effect is possible even without remainder SHG signals in below the AF2 → AF1 transition. This suggests that the mechanism responsible for the memory effect is more fundamental than just phase coexistence at this first order phase transition. Further evidence for a fundamental memory effect can be observed in an AF2 → *paramagnetic phase* (PM) → AF2 temperature cycle.

Memory effects at the AF2 → paramagnetic transition

Figure 4.6 shows the domain structure before and after a AF2 → *paramagnetic phase* (PM) → AF2 temperature cycle. Here the domain pattern reemerges, in contrast to the measurements in [115], in which no memory effect was observed across this transition². The PM → AF3 as well as the AF3 → AF2 phase transitions are both second order, so there cannot be any phase coexistence. Furthermore, the sample was heated up to 20 K in the present measurements before returning to 9.7 K in the AF2 phase. 20 K is far outside all ordered phases and excludes any direct influence of the magnetic or electric order on the memory effect. Cooling/heating rates between 0.5 K/min and 10 K/min were tested, but do not have any influence on the reproducibility of the pattern.

Structural deformations of the crystal are a possible explanation for the observed memory effect.³ In this scenario, the magnetic order in the AF2 phase slightly distorts the crystal structure. This distortion could persist even if the magnetic order is gone. When the magnetic order reemerges, the deformation would favor the domain pattern, which created it. Thus the magnetic structure would create an imprint in the crystal structure to which it will always return. The memory effect is not present anymore if the sample is heated up to 100 K and

²There is a memory effect, in a AF2 → AF3 → AF2 cycle when driving this transition by a magnetic field [114].

³This may also explain, why crystallographic signals in the paramagnetic phase sometimes appear to be temperature dependent (measurements not shown here).

back into the AF2 phase. Here, the much larger thermal energy may remove the deformation from the crystal.

4.1.3 Domain sizes

The typical domain width on the y -surface depends on the sample thickness. Figure 4.7 shows the domains in the AF2 phase in samples #165 ((a), thickness 400 μm), #194 and #193 (b) and (c), each with a thickness of 100 μm). Images (a) and (b) were even observed in the same measurement. Therefore, all experimental conditions, including the history, are the same, only the thickness of the sample is different. While the 400 μm sample exhibits an average domains width of 100 μm , both of the 100 μm thick samples show typical domain widths of 40 μm . In the present work no detailed analysis of the domain size dependence on the sample thickness has been performed. However, the observations are consistent with the Landau-Lifshits-Kittel scaling law, which states that the domain width scales with the square root of the thickness of the sample [151, 152]. It appears to be an universal law for all ferroic domains [153–155] and is valid from the nanometer to the millimeter scale. Figure 4.7d shows this dependence for some ferroelectric and magnetic materials. The proportionality constant is rather independent of the material, but depends on to the type of the ferroic order. Catalan et. al found that these differences can be attributed to the different wall thicknesses [156]. However, applying this relation to the scaling law found in MnWO_4 would imply that the domain walls in MnWO_4 are even smaller than in ferroelectrics. This seems rather unlikely, when taking into account that ferroelectric domain walls are already are at most a few unit cells wide. Moreover, domain walls in DyMnO_3 , another spin-spiral multiferroic, are estimated to be on the order of 20 unit cells [71].

In summary, the Landau-Lifshits-Kittel scaling law appears to be valid also in MnWO_4 , albeit it exhibits a scaling coefficient distinct from the ones in ferroelectrics and ferromagnets. In contrast to ferroelectrics and ferromagnets, this difference cannot be explained by the domain wall width. Further measurements of domain scaling in multiferroics as well es theoretical calculations taking into account both, the ferroelectric and magnetic order, are necessary to understand the peculiar scaling coefficient found in MnWO_4 .

4.1.4 Domain walls of 180° spin-spiral domains

Domain walls are the transition regions between different domains (section 1.1.4). However, little is known on the structure of domain walls in spin-spiral multiferroics so far. Magneto-capacitance measurements as well as simulations hint at a domain wall width of approximately 20 unit cells [71]. The actual substructure of spin-spiral domain walls, has only been discussed for the case of polarization flop-domain walls in DyMnO_3 [71]. In that case, the plane of rotation of the spin spiral is rotated by 90° in adjacent domains. There is only one way, to perform this 90° rotation, so the wall is unambiguously determined by the two domains it connects. The structure of 180° spin-spiral domains walls, like the ones in MnWO_4 , has not been discussed in the literature. While an actual simulation is beyond this work, we consider possible types of domain walls between 180° spin spiral domains.

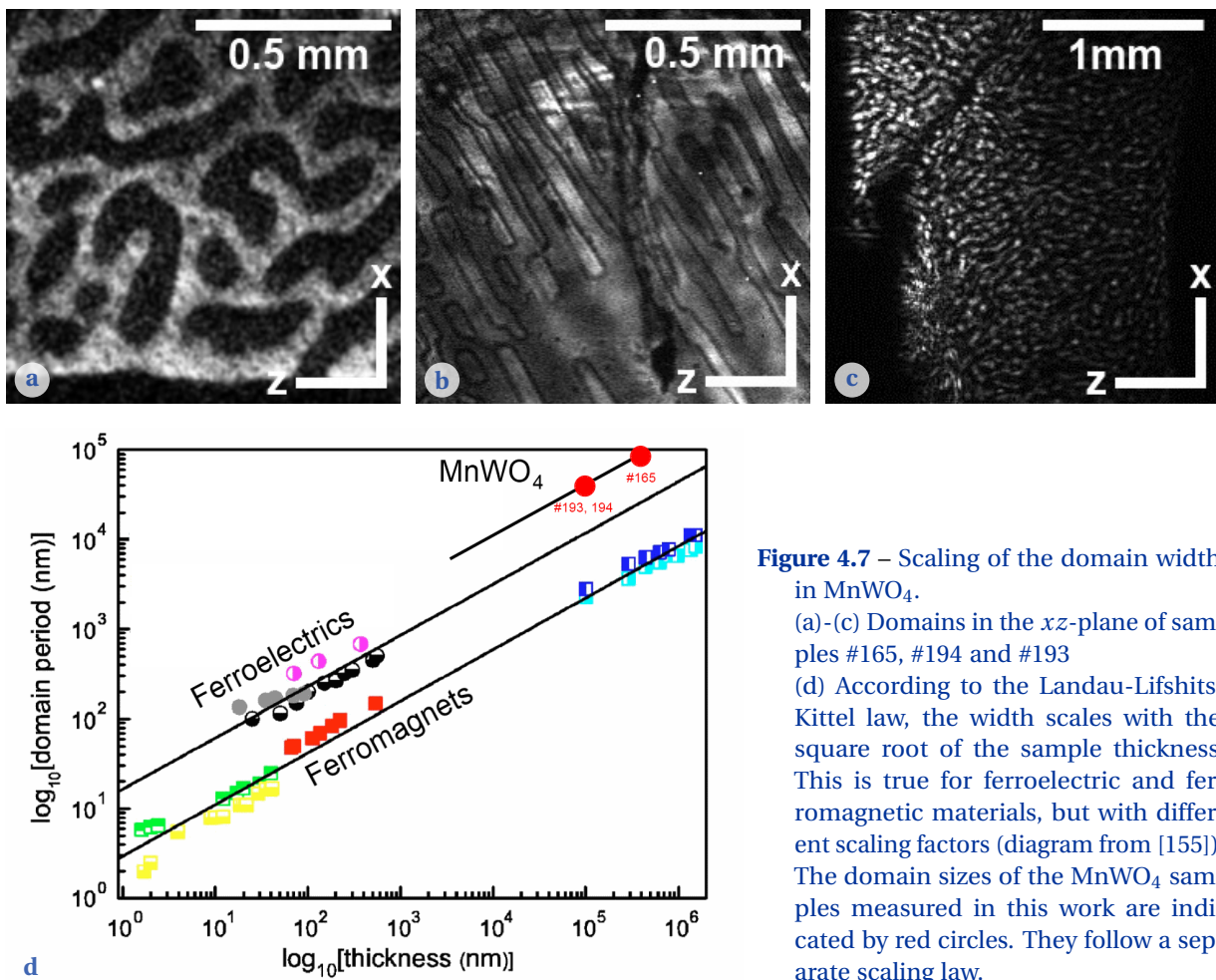


Figure 4.7 – Scaling of the domain width in MnWO_4 .

(a)-(c) Domains in the xz -plane of samples #165, #194 and #193

(d) According to the Landau-Lifshits-Kittel law, the width scales with the square root of the sample thickness. This is true for ferroelectric and ferromagnetic materials, but with different scaling factors (diagram from [155]). The domain sizes of the MnWO_4 samples measured in this work are indicated by red circles. They follow a separate scaling law.

4.1. General domain structures and properties

From one domain to the other, the helicity of the spin spiral has to change. Looking at the geometry, we find that three different transition types are possible in principle:

Angle Variation The plane of rotation may be preserved (Figure 4.8 (a)). In this case, the angle α between neighboring spins is reduced and finally reversed at the domain wall. This keeps the spins within their preferred plane of rotation, which contains the easy axis. However, it costs exchange energy due to the modified angles of neighboring spins in the wall.

The magnitude of the polarization depends on the angle between the spins. It will go to zero and build up again in angle-varying walls.

Furthermore, summing up the spin vectors across the wall, it appears that angle-varying walls may have a net magnetic moment.

Plane Rotation (normal or parallel to the wall) Alternatively, the spins can maintain their relative angles if the plane of rotation itself rotates. Its rotation axis may either be normal to the wall (figure 4.8 (b)) or in the plane of the wall (figure 4.8 (c)). Here, only anisotropy energy has to be paid. Both plane-rotating wall types (b) and (c) come in two subtypes, which have different senses of rotation.

Because the angle between the spins remains constant, the absolute value of the polarization does not change across a wall. However, following the plane of rotation, the polarization will rotate across the wall to reverse its sign.

A similar structure to a plane-rotating wall with the rotation axis normal to the wall (b) has been proposed in theoretical calculations of terahertz-induced chirality switching in spin-spiral multiferroics [157]. However there, the rotation planes of the outer spins oscillate in a rotation around the propagation direction. Because they have a phase shift of 180° , the central spin forms a node of the oscillation. This shows that structures as depicted in (b) may exist, however it is an open question, if they are realized also in the static structure of a domain wall.

Which type of domain wall will be realized depends on the relative strength between exchange and anisotropy energy.

Qualitatively, all types of spin-spiral domain walls can lower their energy if they are aligned parallel to the easy axis. This explains one of the preferential orientations observed in the domains patterns.

The interaction between domains during a switching process can hint at the type of domain walls involved. When two domains of the same type come close, we observe avoidance in some experiments (figure 4.9 (a)) and coalescence in others (figure 4.9 (b)). Here, the interaction between the domain walls plays a role, which depends on the type of wall. If two angle-varying domains walls are brought close together, these domains should always coalesce and remove both walls (figure 4.8 (d)). In the case of plane-rotating walls, it depends on the sense of rotation of both walls. Two walls with opposite rotation senses can annihilate, thus the domains can easily join (figure 4.8 (f)). In contrast, the double twist of two walls of the same rotation senses cannot be removed easily (figure 4.8 (e)). This prevents those domains

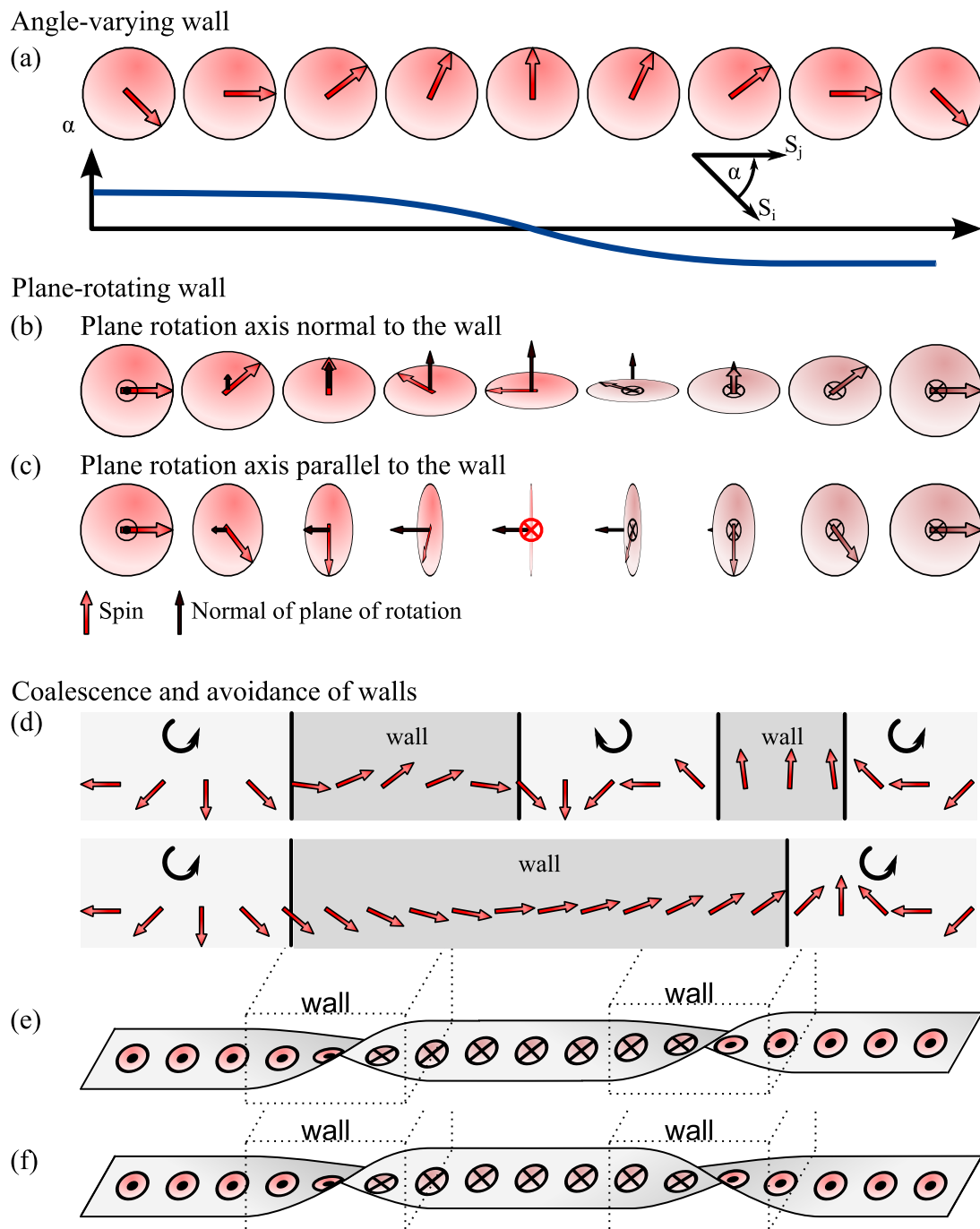


Figure 4.8 – Possible types of spin-spiral domain walls. Red circles depict the plane of rotation of the spin spiral. (a) Angle-varying wall: The angle α between neighboring spins S_i and S_j decreases across the wall and changes sign. (b), (c) Plane-rotating walls: The angle α between neighboring spins remains constant. Instead the rotation plane itself rotates, either normal to the wall (b) or parallel to the wall (c). (d)–(f) Coalescence and avoidance of domain walls. While angle-varying walls can always coalesce (d), this depends on the sense of rotation in case of plane-rotating walls (exemplified for a plane rotation normal to the wall): If the sense of rotation is the same in both walls (e), they will avoid each other. Note the double twist of the plane of rotation, which cannot be removed by local changes. In contrast, the domains may coalesce if the senses of rotation in the walls is opposite (f), so that the walls can annihilate.

4.1. General domain structures and properties

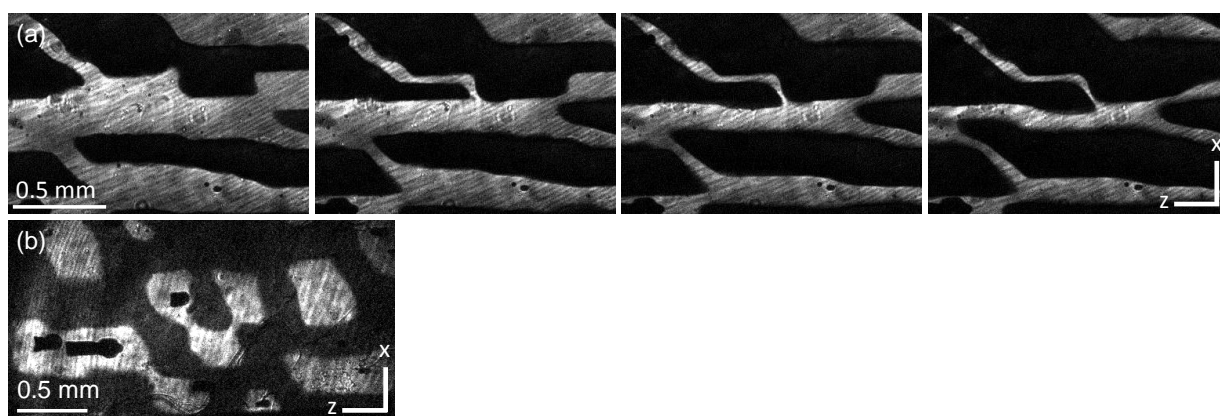


Figure 4.9 – Both, coalescence and avoidance of domains can occur in MnWO_4 depending on experimental conditions. This behavior can be explained by plane rotating domain walls with opposite senses of the rotation.

(a) Quasi-static magnetoelectric switching experiment at 10.9 K. Domains of the same type may avoid each other instead of joining.

(b) Coalescence of domains in a dynamic switching experiment.

from joining and could explain the avoidance. Only at higher fields, when the electric field energy becomes comparable to the magnetic exchange energy, such a double twist could be removed to obtain a field-induced single domain state.

4.1.5 Summary

To conclude this section, we sum up the information gained on the domain structures and domain properties in MnWO_4 . The orientation of the domain walls is a combined result of their ferroelectric and magnetic properties. As area separating volumes of different order parameter orientation, domain walls extend along two directions. Primarily, all walls in MnWO_4 contain the direction of polarization. For the second direction, two preferential wall orientations exist: perpendicular to the direction of weakest magnetic exchange, or alternatively along the magnetic easy axis. Finally a thermal hysteresis of the bubble-to-stripe transition of the domain pattern as well as a pronounced memory effect both for $\text{AF2} \rightarrow \text{AF1}$ as well as $\text{AF2} \rightarrow \text{paramagnetic}$ phase hint at strong pinning effects that can limit the free evolution of domain walls.

The domain walls of 180° degree spin spiral domains are not yet discussed in the literature. This work presents a first description of the possible domain wall types that change the helicity of the spin spiral, either by varying and reversing the angle between the spins, or by rotating the plane of rotation. Furthermore, we discussed the costs in exchange and anisotropy energy as well as the ferromagnetic and ferroelectric properties of such walls qualitatively. Coalescence and avoidance of domains observed in dynamic magnetoelectric switching experiments hint at the existence of plane-rotating domain walls in MnWO_4 .

Though there are still many open questions concerning domains properties in MnWO_4 in the static and field-free case, the above results provide a reasonable insight in the domain patterns

and mechanisms governing the domains in MnWO₄. This knowledge allows to take the next step towards magnetoelectric switching by investigating the influence of static electric fields on the domain structures.

4.2 Static magnetoelectric effects

The previous section covered the basic properties of the multiferroic domains in MnWO₄. Now we investigate, how static or slowly varying electric fields affect these domains. In general, application of an electric field will raise the energy of one polarization orientation and lower the energy of the other. Thus, the balance is changed, driving the ferroelectric system towards a single domain state. Due to the magnetoelectric coupling, this holds true for the magnetic system simultaneously.

While applying the electric field, we monitor the evolution of the domain patterns using SHG images (section 4.2.1). Furthermore, we determine the hysteresis loop and the coercive field from spatially integrated SHG intensities (section 4.2.2). A constant crystallographic SHG signal is used as reference signal in both cases to generate domain contrast as discussed in section 2.1.3 and appendix A.2.

4.2.1 Three-dimensional domain pattern during quasi-static magnetoelectric switching

The three-dimensional domain pattern of MnWO₄ in zero field has been summarized in section 4.1.1. The following section addresses the three-dimensional domain pattern during quasi-static magnetoelectric switching.

Domain pattern normal to the polarization direction

Measurements of the domain pattern normal to the plane of polarization are performed on an y -cut at the tensor component $\chi_{x'z'z'}^{\text{ED}}$ at about 2.22 eV.

Figure 4.10 (a) shows the domain pattern after zero-field cooling into the AF2 phase ($T=11.5$ K). A slight preference for the alignment of the walls along z and along the magnetic easy axis can be seen. This pattern has been discussed in sections 4.1.1 and 4.1.2. These zero-field measurements already showed that domain walls extend along the y -direction throughout the complete crystal.

When gradually increasing the applied electric field, one of the domain states grows, until a single domain state is reached (figure 4.10 (a)-(d)). Growth is realized by a movement of domain walls, both in x and z -direction. The domains shrink most along the direction of their elongation. As a result, all domains evolve towards a circular shape (figure 4.10 (c)), which clearly indicates a change of domain population under the constraint of minimizing the domain wall surface. Finally a single-domain state is reached (d). The dark spots in (d)

arise from mechanical defects at the sample surface, which scatter the light and thus appear black. They are not remaining domains of the opposite domain state.

When lowering the field again, domains of the opposite direction nucleate (figure 4.10 (f)-(i)). They are remarkable in a number of ways. First, the nucleation sets in at still positive values of the field. Second, nucleation starts preferably at defects on the y -surface or at the side faces (xy -planes). Third, some areas of the new domains are not directly completely dark, see upper central area and left edge in (f). Finally and most notably, instead of the bubble pattern of the virgin curve (a)-(d), a stripe pattern appears along the z -direction.

Before discussing each of the above observations, we briefly introduce the hysteresis loop (e). Displayed are integrated SHG intensities measured in the quasi-static electric field switching cycle. Like in the images, domain contrast is achieved by interference with crystallographic SHG. The brightest and lowest intensity levels correspond to the single domain states. Intensities in between stem from a mixed domain population, as explained in section 2.1.3. In figure 4.10 (e) the open circles mark the virgin curve after zero-field cooling. The increasing intensity corresponds to a growth of the bright domains (compare images (a)-(d)). At about 600 kV/m the SHG intensity saturates because a single domain state is reached. When decreasing the field the intensity stays constant and thus the single domain state remains present down to 250 kV/m. The details of the hysteresis loop will be discussed in section 4.2.2. In the present context, it rather serves as an orientation to illustrate under which conditions the images were taken.

Nucleation of reverse domains at still positive field Figure 4.10 (f) is taken after reducing the electric field from $E = 750$ kV/m to 100 kV/m, i.e. at still positive fields. Nevertheless, reverse domains have already nucleated. This nucleation of reverse domains in still positive field can also be seen in the hysteresis loop, in which the SHG intensity starts to drop, when the field is decreased below 250 kV/m.

Nucleation of domains is a consequence of the material trying to lower its energy. Three contributions play a role in a ferroic system: (i) the wall energy, (ii) the energy of the depolarizing field, created by the order, and (iii) the energy of the order in the external field. These contributions exist for each ferroic order in a multiferroic. However, for antiferroic orders only the wall energy is non-zero because the order parameter is not a macroscopic quantity (section 1.1.4). Considering the magnetic subsystem in the present case, every multi-domain state only costs energy due to the walls. Therefore, it will favor single domain states. Consequently, the nucleation has to be related to the ferroelectric nature of the domains. Since the domains already nucleate in a field opposite to their preferred orientation, the external electric field cannot be the driving force of the nucleation. Instead, it is the ferroelectricity in the sample itself that naturally tends to a multi-domain state due to the depolarizing field and thus is responsible for the nucleation of the domains. At the time of nucleation only the depolarizing field favors a multi-domain state. Here the external field just gets weak enough to permit this.

Nucleation centers and domain pattern The nucleation of domains at defects or surfaces is a common effect in ferroelectrics [158]. Nucleation at crystal surfaces is preferred energetically

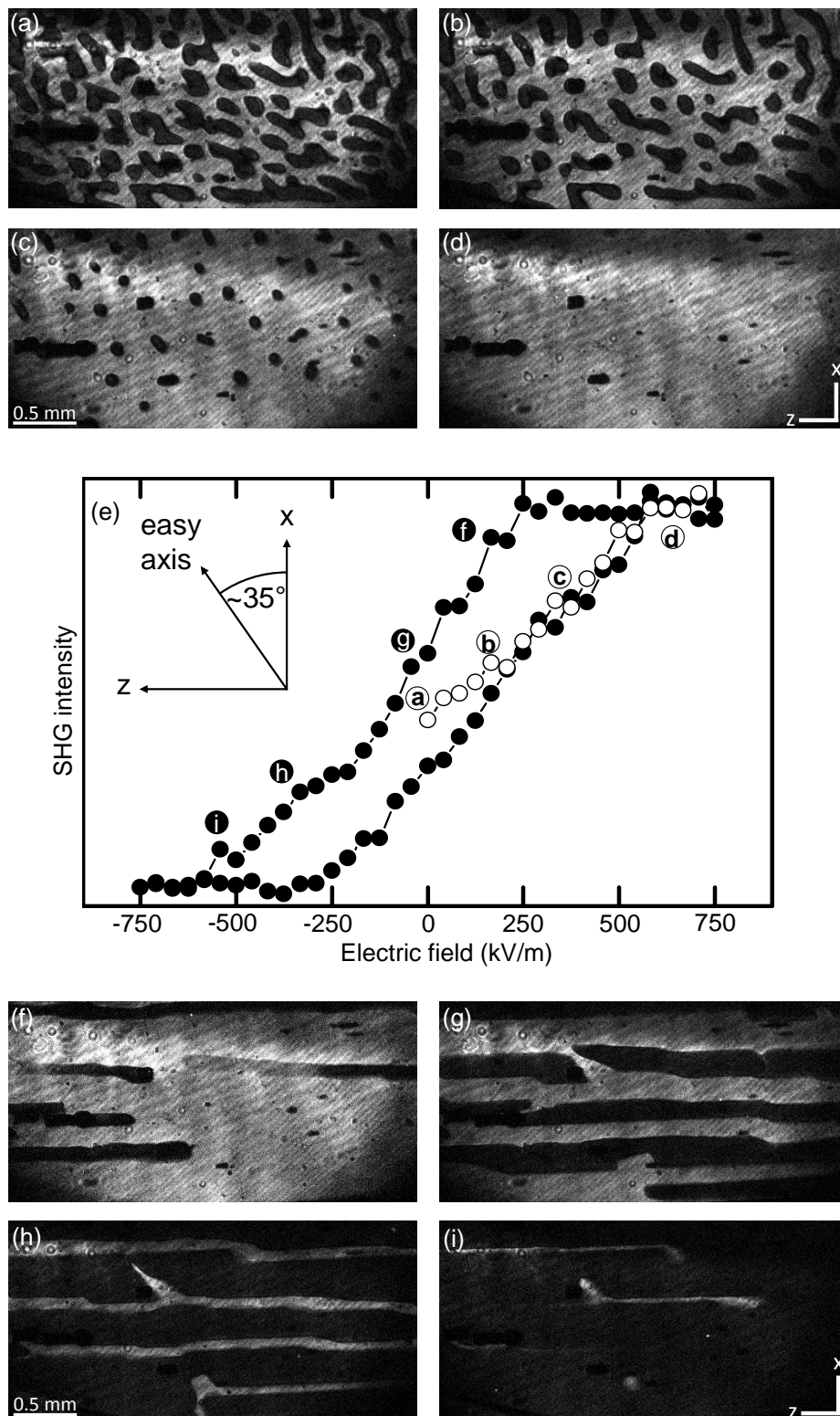


Figure 4.10 – Domain images and hysteresis loop in quasi-static magnetoelectric switching measured MnWO_4 on the y-face. The positions of the domain images are marked in the hysteresis loop (e). (a)-(d) Domain pattern in the virgin curve. After zero-field cooling the domains exhibit a bubble topology. Increasing the electric field shrinks the dark domains until a single domain state is obtained. (f)-(i) Domain pattern when lowering the applied field after a single domain state was induced. In contrast to the pattern after zero-field cooling, stripes are formed along z .

because part of the domain surface can coincide with the crystal surface. Here, no domain wall is needed, which would cost additional energy. Likewise, the incorporation of defects into the domain wall may lower its energy. Note, that this reduced energy at defects is also a source of pinning phenomena.

Ferroelectricity drives the nucleation of the domains and enforces the domain wall to contain the direction of polarization. However, as discussed in section 4.1.1, it cannot set any preferred wall direction on the y -surface because the polarization is perpendicular to it. Like in the pattern after zero-field cooling (figure 4.10 (a)), there are two preferential directions for the alignment of magnetic domain walls (easy-axis and perpendicular to x), which are much more pronounced in the case of magnetoelectric switching (figure 4.10 (f)-(i)). Furthermore, walls perpendicular to the x -axis seem to be preferred.

Both, figure 4.10 (a) and (g) show domain patterns without electric field applied. Since the external conditions are the same, the difference in the patterns has to arise from the history of the sample, especially from the conditions during domain nucleation and from the driving forces. In the case of zero-field cooling, the order emerges at the phase transition. Just at $T_2 = 12.7$ K, every volume element chooses an arbitrary orientation of the order parameter. Then they merge together across certain distances. So domains are locally formed without any preferred orientation. In contrast, the nucleation during the magnetoelectric switching loop is driven by the depolarizing field, as discussed above. When the multi-domain state becomes energetically favorable, nucleation of the reverse domains does not occur homogeneously across the sample but preferably at defects or the sample surface. Here, the cost of the domain wall energy can be lower, resulting in a reduced coercive field. The desired domain population is then achieved via growth of just these few nucleated domains. Since the external field is lowered slowly, this growth happens under quasi-static conditions. Thus, in contrast to the zero-field cooled domain pattern, the domain pattern in zero field after removing a poling field will be close to the ground state, i.e. it the stripe pattern with walls perpendicular to x is a configuration that minimizes the free energy.

Partially dark domains The brightness of a domain in an image depends on the exposure time. Therefore, the appearance of an intermediate brightness (figure 4.10 (f)) points to a switching of the corresponding area during the time of the image acquisition (1 min in the present case). Since there are only two different intensities and the walls are sharp, the change must have happened abruptly. This again may be caused by pinning in the sample.

Domain pattern in the polarization direction

Analogue measurements to the ones discussed in the previous section have been performed on the surfaces that contain the polarization direction. Using an electric field and slowly changing the field strength, the system is driven from one single domain state to the other and back (Figure 4.11). The following data are measured at an x -cut (χ_{yzz}^{ED} @ 2.716 eV, $T = 9.3$ K).

The images show the domain pattern on the x -surface during quasi-static magnetoelectric switching. In both half-cycles of the hysteresis loop the reverse domain nucleates at the sample edge and then propagates through the sample. Only one or very few domains are

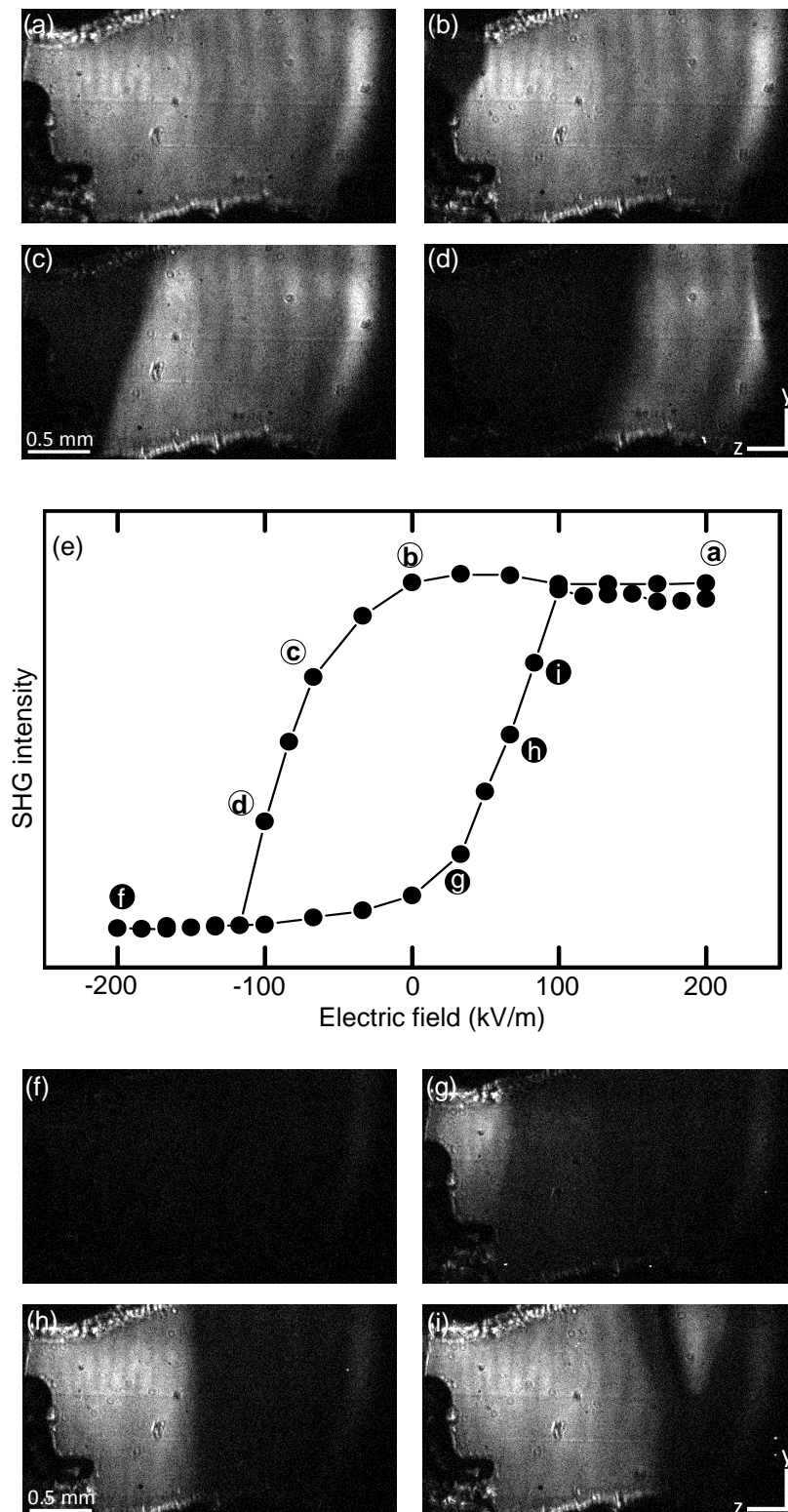


Figure 4.11 – Domain images and hysteresis loop in quasi-static magnetoelectric switching measured MnWO_4 on the x-face. The positions of the domain images are marked in the hysteresis loop (e).

Only one or two domains nucleate at the side and then grow through the crystal. The domain walls approximately align along the ferroelectric polarization axis y . Furthermore a needle-domain is visible in picture (i). Both are hallmarks of the ferroelectric properties of the domains. The blurred walls stem from a depth-effect.

formed. The walls run approximately along the polarization direction y , though they appear to have a small angle to it. The preferential alignment along y has already been discussed for the zero-field SHG images (section 4.1.1).

The observed needle-like structure (figure 4.11 (i)) is a typical ferroelectric behavior (section 1.1.4, [2]). Domains grow quickly along the direction of polarization (top-to-bottom in the image). This forward growth is enhanced by the electric field because a head-to-head or tail-to-tail alignment of the dipoles has a net charge, which is not the case for the side-to-side configuration. Therefore, the forward growth is much quicker than the sideways growth. Forming needle-shaped domains is energetically favorable because it prevents a large energetically costly head-to-head or tail-to-tail wall. The needle shape is usually much more pronounced in classical ferroelectrics, i.e. the tip angle as well as the ratio of width to length is smaller. The less pronounced features in the case of MnWO_4 can be attributed to the small polarization, which relaxes the energy constraints leading to this pattern.

In contrast to figure 4.10, the domain boundaries are not sharp but look blurred. The width of this transition region is on the order of $100 \mu\text{m}$. To a certain extent, this is a depth-effect. As known from the y -cut, the domain walls run along the magnetic easy axis. Therefore they do not contain the normal to the images in figure 4.11, but have an angle to it. An alternative explanation as broad domain walls is unreasonable. First, $100 \mu\text{m}$ wide domain walls would be exceptionally large. Second, this wall width would also be visible in the domain walls parallel to the easy axis in the y -cut, but that is not the case (figure 4.10).

Reconstruction of the three-dimensional domain pattern during quasi-static magnetoelectric switching

Using the above results, a three-dimensional picture of the domain evolution during quasi-static magnetoelectric switching in MnWO_4 can be reconstructed. (figure 4.12).

First, domains nucleate preferably on the y -surface and there especially at an edge. The main growth direction is along the polarization direction y for two reasons. One is the high energy cost for head-to-head domains. The other is the local charge of such walls, which allows the electric field to drive the walls through the sample [2]. So this process is based on the ferroelectric properties of the domains. To enlarge the domains further, plates are formed in the x -plane. This removes the walls parallel to the easy axis and leaves only walls perpendicular to x . The latter are least costly in terms of magnetic exchange energy because of the weak exchange perpendicular to x . Hence this second step is related to the magnetic nature of the domains. Finally, sideways wall motion along x leads to the single domain state.

The quasi-static switching nicely demonstrates the inherent multiferroic nature of the domains. Only by taking into account both the ferroelectric and the magnetic properties it is possible to understand the evolution of the domain pattern throughout the switching process.

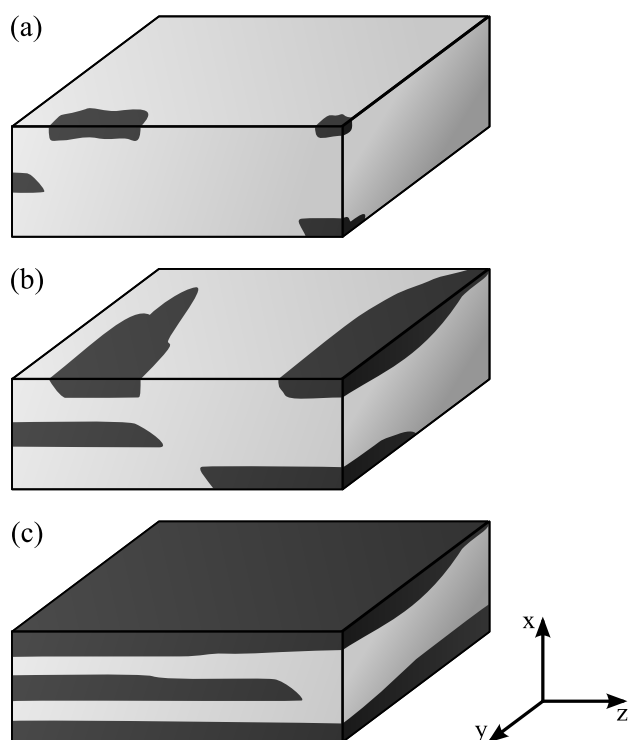


Figure 4.12 – Illustration of the three-dimensional domain growth during quasi-static magnetoelectric switching in MnWO₄.

(a) First, domains nucleate on the y -surface, preferably at an edge.

(b) The ferroelectric nature of the domains leads to a fast forward growth along the polarization direction y . (c) At slightly higher electric fields sideways growth along z is completed, so that plates stacked along x remain. These wall directions cost the least magnetic exchange energy. Now, the x -face is single-domain, but still higher fields are necessary for the growth of the domains along x to finally obtain a single domain state of the whole volume.

4.2.2 Hysteresis and coercive field

Directional influence

When comparing the hysteresis loops from SHG measurements on the y -surface (figure 4.10 (e)) with the ones on the x surface (figure 4.11 (e)), three striking differences are visible. First, the remanence seems to be much larger in the latter case. Second, the switching slopes are steeper. And third, the coercive field is lower. These differences can be understood from the three-dimensional domain pattern during the switching.

SHG measures only to a limited depth because of absorption (section 2.1.4). Therefore, the SHG signal from the tensor components used here ($\chi_{x'z'z'}^{\text{ED}}$ at 2.22 eV (SHG) and χ_{yzz}^{ED} at 2.75 eV (SHG)) reflects the domain structure close to the surface. An absorption spectrum for MnWO₄ can be found in reference [159]. For the used SHG photon energies the absorption coefficients are $\alpha(2.22 \text{ eV}) = 138 \text{ cm}^{-1}$ and $\alpha(2.75 \text{ eV}) = 400 \text{ cm}^{-1}$, which translate to absorption lengths of 70 μm and 25 μm respectively.

On the y -surface, stripes extend along the z -axis. If a wall is present on the x -surface, this implies that the top stripe domain does not run along the complete sample, i.e. the top domain plate is not complete (c.f. figure 4.12). Remembering the measurements on the y -cut, this is a rare situation. If a domain is nucleated, it takes just a little more field to completely extend it along the z -axis of the crystal. So, what one actually sees at the surface of an x -cut is the sideways growth of one of the stripes. Therefore, it is clear, that the slopes of the hysteresis are steeper here.

The difference can also be understood in terms of area fractions and volume fractions of the

domain population (see section 2.1.3). Strictly speaking, measurements on both cuts only reflect the domain evolution on the corresponding surface. The SHG intensity determines the relative area fractions of the domains on that surface. However, considering the sample as a whole, we are interested in the switching of the three-dimensional volume, i.e. the relative volume fractions of the domains. Fortunately, the area fractions on the y -surface coincide with the volume fractions because the domain walls extend approximately straight along y through the complete crystal. This is not true on an x -surface.

Likewise the measured coercive field in an x -cut reflects only the coercivity of the stripe formation. Here, one does not see the switching process of the whole sample, but only the growth of one domain plate along the z -axis. The quick growth along this direction compared to the slower growth along x (Figure 4.10 (f)-(i)) indicates that the energy barrier for growth along z is lower. This corresponds to the reduced coercive field. At ± 150 kV/m the growth of the domain plate is complete. However, the different plates stacked along x have not yet merged. The x -surface is now single domain, but not the complete crystal. Consequently coercive fields obtained from SHG measurements on x -cuts and, more generally, switching experiments of this cut should be interpreted with great care.

The increased remanence in an x -cut can be explained as follows. If stripes are formed in such a way that the x -surface consists of a still unswitched stripe, the measured volume has not switched yet, even though lower lying layers are already reversed. In this geometry, switching of the surface will finally occur because of the sideways growth of the stripes, which requires larger fields. This gives the impression of a higher remanence.

Because the measurements were taken at slightly different temperatures, they must be scaled to be directly comparable. From the scaling of the coercive field in the y -cut (section 4.2.2) we deduce that it will be larger than 500 kV/m at 9.3 K on the y -surface. In contrast, the presented SHG measurements on the x -surface show a coercive field of less than 100 kV/m at that temperature. Consequently, the discussed differences between domain area fractions on the x -surface and the volume fractions are in fact stronger than the comparison of the unscaled data shows. Hence, the proposed qualitative switching model still applies.

Summarizing the above results, SHG yields only information on the area fractions of domains in the first place. In contrast to an x -cut, the area fractions in a y -cut of MnWO_4 correspond to the volume fractions. Therefore, a y -cut is the preferred system to measure the three-dimensional volume response of the domain population in magnetoelectric switching.

Temperature dependence

For the determination of dynamic switching times it is essential that switching is performed between single domain states. Therefore, one has to be sure, that the applied electric field is high enough to drive the system into such a state.

Figure 4.13 (a) displays hysteresis curves at various temperatures measured in a y -cut. The absolute SHG intensities rise with lowering temperatures because the nonlinear susceptibility couples linearly to the order parameter, which in turn is temperature-dependent (equation (3.3)). The field required to drive the sample into a single domain state also rises with

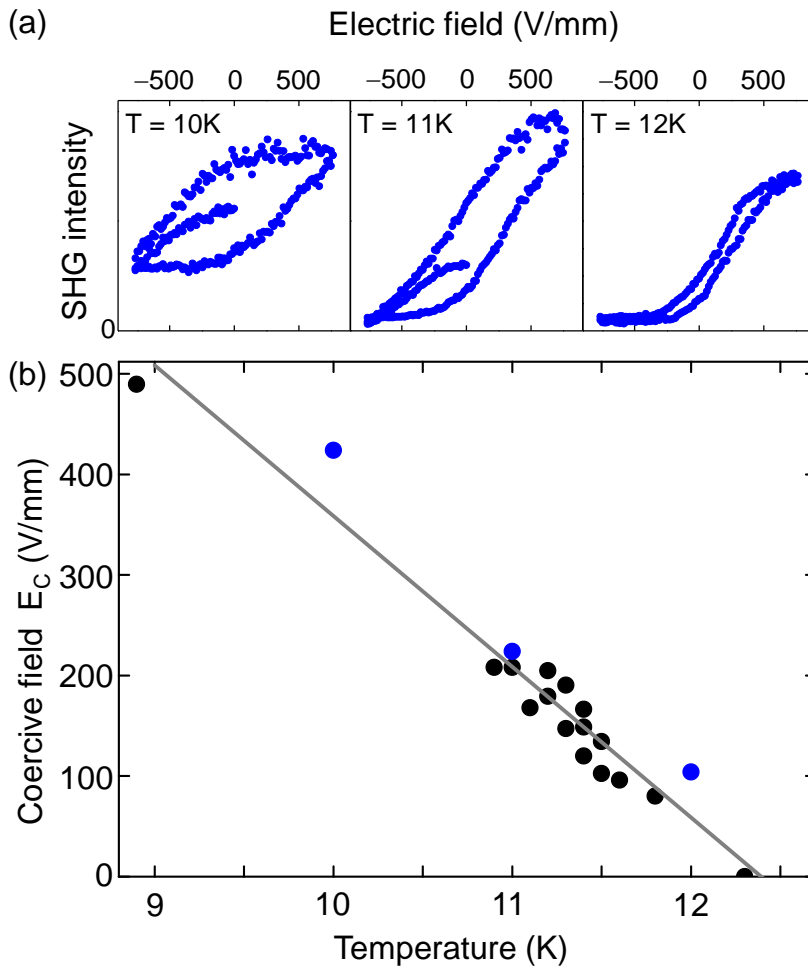


Figure 4.13 – Temperature dependence of the hysteresis in MnWO₄ measured on a y -cut. (a) Hysteresis loops at various temperatures. With lowering temperatures, the order parameters P and σ_2 increase. Thus, the SHG intensity rises. Also the coercive field increases, so that at low temperatures (10K) no single domain state can be reached. (b) Temperature dependence of the coercive field. Using the y -cut surface for measurements ensures that the SHG intensity corresponds to volume fractions of the sample switched. The blue dots mark the three measurements depicted in (a). The linear fit verifies a linear scaling according to $E_C \propto (T_0 - T)$.

decreasing temperature. Because of limits in the maximally applicable field single domain states cannot be reached at lower fields anymore and the hysteresis loop is only a minor loop at 10 K. The coercive field can be determined as half the width of the hysteresis loop.

Figure 4.13 (b) summarizes the coercive fields from hysteresis loops at various temperatures. In contrast to earlier measurements, which proposed a field dependence of $E_C \propto (T_0 - T)^{\frac{1}{2}}$ [115], the present data exhibit a linear relation. This difference may be attributed to the fact that the earlier measurements were performed on an x -cut, which only reflects the formation of domain plates, whereas the y -surface reveals the switching of the three-dimensional volume. Apparently, the coercive fields for forming plates and for switching the complete sample scale differently with temperature. As expected, the coercive fields for switching the complete sample are higher than the coercive fields for the formation of the domain plates throughout the whole temperature region. In agreement with the x -cut data, T_0 is smaller than the transition temperature T_2 . There exists a small region $T_2 - T_0 = 0.5$ K below T_2 , in which domains can be switched in an applied electric field, but there is no coercivity, i.e. the domain state does not depend on the history of the sample.

Direct measurements of the ferroelectric hysteresis loop have been performed in reference [130]. Even though there are only four data points, they rather seem to support the linear

temperature scaling.

4.2.3 Low-temperature quasi-static switching

The domain pattern on the y -surface changes for quasi-static switching cycles deep inside the AF2 phase (figure 4.14) compared to the ones closer to T_2 described so far (figure 4.10). The domain wall orientations perpendicular to x and parallel to the easy axis correspond to the preferred directions of the magnetic subsystem. The alignment along these directions is more strict at lower temperatures, which can be explained by a changed energy balance between domain wall energy and field energy as well as the reduced thermal energy at lower temperatures. Among these two directions the one perpendicular to x is preferred in quasi-static switching close to T_2 . This changes deep inside the AF2 phase. Now, walls along the easy axis seems to be energetically favored. The occurrence of both directions in the zero-field domain pattern already shows that the energy difference between those two walls is small. Apparently the energies slightly change with temperature, so that their balance tips at some point inside the AF2 phase.

The properties deep inside the AF2 have not been investigated in detail. With the present sample holders the maximal electric field is limited by the helium breakthrough threshold of 1 kV/mm. Because the coercive field rises with lowering temperature, it is not possible to induce single domain states at low temperatures with the fields available.

Reliable and reproducible magnetoelectric switching measurements cannot be performed without the possibility to drive the sample single domain because the existing domain pattern introduces a dependence on the history. This is illustrated in figure 4.14 (b) and (c)). Meaningful magnetoelectric measurements in this temperature region would thus require electric fields higher than 1 kV/mm, which is a limit imposed by breakthrough in the helium used for cooling. Higher fields may become possible if ITO electrodes are directly grown on the sample.

This section introduced the static aspects of magnetoelectric switching. Based on the understanding of the influence of the electric field under equilibrium conditions it is now possible to take the step to magnetoelectric dynamics.

4.3 Dynamics of magnetoelectric switching

Up to now, we have investigated MnWO_4 at various temperatures and in static or slowly varying electric fields. To learn about the intrinsic timescale and dynamics of the magnetoelectric effect, we have to expose the sample to non-equilibrium conditions and monitor its relaxation to the equilibrium state. The electrical-pump–optical-probe method used for these measurements is detailed in section 2.2.3.

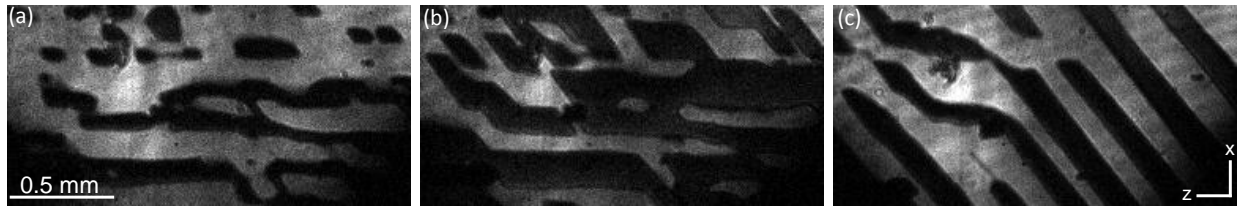


Figure 4.14 – Domain patterns of quasi-static magnetoelectric switching deep inside the AF2 phase ($T = 9.3\text{K}$). The wall direction with the lowest energy changes from $\perp x$ to the easy axis.

(a) Domain pattern in zero field. Before cooling down, static switching experiments have been performed at higher temperatures in the AF2 phase. This explains the preference for horizontal stripes.

(b) After application of $E = 900\text{ V/mm}$ the domains grow, but a single domain state cannot be reached. Here, the polarization and thus the depolarizing field is too large.

(c) Like (b) the image was taken at $E = 900\text{ V/mm}$ but in another annealing cycle. However, here the initial pattern (not shown) did not have the preference for horizontal stripes like in (a) because the sample was directly zero-field cooled to 9.3 K without performing switching experiments at higher temperatures. The difference between (b) and (c) demonstrates the stronger dependence on history if the sample cannot be switched to a single domain state to erase the memory. Starting from (a) the domains grow along the easy axis. Since only a certain volume fraction can be switched, the initial z -stripe pattern still remains dominant (b). However, if the initial state is more bubble-like, growth along the easy axis can happen over larger distances, so that a pattern like (c) can be obtained.

4.3.1 Switching timescale

The present knowledge on the dynamics of magnetoelectric switching is very limited. In particular, one of the most fundamental questions is still open: How fast is magnetoelectric switching? In the following we investigate the dynamics of magnetoelectric switching using the electric electric-pump–optical-probe method and SHG for detection of the ferroic order.

The ferroelectric polarization and the helicity of the spin spiral are coupled via the Dzyaloshinskii-Moriya interaction (DMI). Minimization of energy results in an one-to-one relation between the polarization direction and the sense of the helicity (equation (1.6)). However, in non-equilibrium states, the energy is not minimal and therefore this relation does not necessarily hold anymore. Looking at the coupling model (figure 1.10), one realizes that the electric field acts on the ferroelectric order and only then via the DMI onto the magnetic system. It is conceivable, that both systems decouple in a non-equilibrium switching process. Then the polarization would switch first and the helicity would follow later on. Anyway, after a sufficiently long timescale, both systems must have switched because this state is the new energy minimum.

In the quasi-static case, it did not make sense to distinguish between the electric and magnetic order, because they were coupled anyway. Since this is not necessarily true in dynamic measurements we can exploit the sub-system selectivity of SHG (section 2.1.2) to directly look at either the ferroelectric order or the magnetic order. For that, we have chosen $\chi_{x'z'z'}^{\text{ED}} \propto \sigma_2$ as a tensor components that couples to the magnetic order. It is only present because of the incommensurability of the spin spiral. In contrast, χ_{yzz}^{ED} can be induced by a ferroelectric polarization \mathcal{P} (section 3.1.6).

4.3. Dynamics of magnetoelectric switching

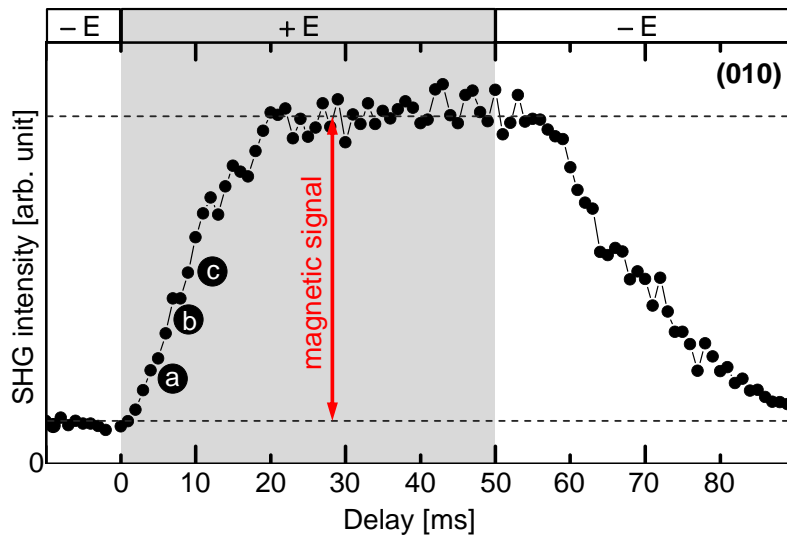


Figure 4.15 – Response of the magnetic subsystem in MnWO_4 on a fast electric field reversal at $T = 11.8$ K. The electric field is switched between $E_y^\pm = 750$ kV/m at $t = 0$ and back at $t = 50$ ms. Its rise time is 80 ns, which is instantaneous on the timescale shown. The domain population in the magnetic subsystem is tracked using SHG from $\chi_{x'z'z'}^{\text{ED}}$ at 2.22 eV. The changes from one single domain state to the other takes 20 ms. Spots (a)-(c) mark the position of domain images presented in figure 4.17.

First, we measure the response of the magnetic subsystem, which determines the timescale of the magnetoelectric switching. In a second step, the ferroelectric system is discussed.

Magnetic subsystem

The tensor $\chi_{x'z'z'}^{\text{ED}}$ @ 2.22 eV exclusively couples to the magnetic order because it arises from the incommensurability of the spin spiral (section 3.1.6). Thus it can be used to probe the magnetoelectric effect, i.e. the reaction of the magnetic system on an electric field.

In the experiment, the electric field was switched between $E_y^- = -750$ kV/m, to $E_y^+ = +750$ kV/m. The repetition rate of 10 Hz is given by the laser. The duty cycle was set to 50%, resulting in equally long 50 ms periods of E_y^- and E_y^+ . The 10%-90% rise time of the electric field is 80 ns.

The measurement shown in figure 4.15 was performed at $T = 11.8$ K, so that the applied electric fields are high enough to drive the system alternately into both single domain states. Due to interference with crystallographic background, the SHG intensity corresponds to the domain population. The magnetic system switches on a surprisingly slow time scale of approximately 20 ms. The rise time of the electric field is much faster, and can be regarded as instantaneous compared to the timescale displayed. The comparably slow response of the magnetic systems is discussed and interpreted together with the other dynamic measurements in section 4.5.

Ferroelectric subsystem

To see, whether the ferroelectric polarization decouples from the magnetic order, we measure the SHG from χ_{yzz}^{ED} @ 2.75 eV. Since the polarization of the SHG light is along the ferroelectric polarization direction y , the transversal field sample holder has to be used. Naturally, this sample geometry requires larger electrode distances. Because of the limited voltage available from the HV sources in this experiment, the maximal field strength was $E_y^\pm = \pm 330$ kV/m.

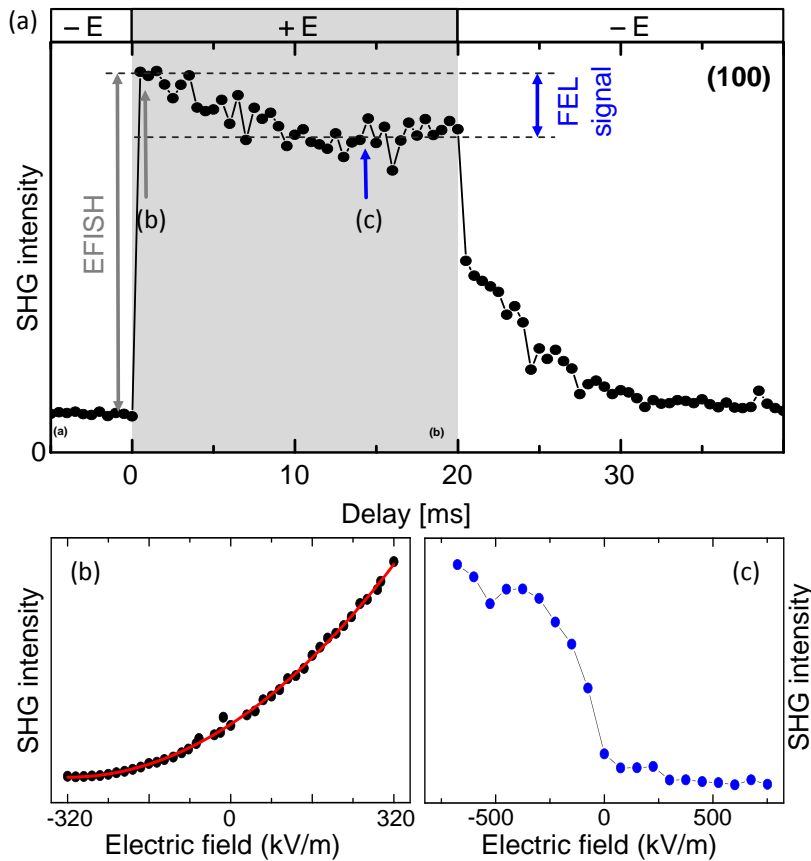


Figure 4.16 – Response of the electric subsystem in MnWO₄ on a fast electric field reversal at $T = 10.7$ K. The electric field is switched between $E_y^\pm = 330$ kV/m at $t = 0$ and back at $t = 20$ ms. Its rise time is 80 ns, which is instantaneous on the timescale shown. The domain population in the ferroelectric subsystem is tracked using SHG from χ_{yxx}^{ED} at 2.75 eV.

(b) Electric field dependence at a delay of 100 ns. The parabolic shape confirms that the instantaneous change in SHG intensity stems from EFISH.

The successive slower change on a scale of 10 ms can be assigned to the ferroelectric polarization because it exhibits a threshold-like field dependence (c) (Curve is only exemplary because it was taken in an analogous experiment).

However, it was checked with SHG images that this was large enough to drive the material to single domains states.

The SHG signal changes abruptly at the switching of the field, followed by gradual change on the millisecond timescale (figure 4.16 (a)). At first view, one might think that the abrupt change is created by the ferroelectric order, and the long-time change is a hallmark of the equilibration of the magnetic system. However, this is not the case. The abruptly changing contribution to the signal is electric-field induced SHG (EFISH, section 2.1.5). Only the change on the 10 ms timescale can be attributed to a switching of the ferroelectric order, as will be detailed in the following.

The EFISH origin of the initial abrupt change can be verified by investigating its field dependence. While the SHG intensity at a short delay $t = 100$ ns follows a parabolic electric field dependence, it exhibits a threshold-like behavior for long delays (figure 4.16 (b), (c)). The parabolic dependence is a clear indication for EFISH (section 2.1.5). The EFISH signal will be present as long as the field is applied. However, the threshold-like behavior stems from the hysteretic nature of the ferroelectric polarization and proves that the observed millisecond-scale process indicates the switching of the polarization.

A further indication can be obtained from images at the corresponding timescales. While EFISH changes the SHG intensity homogeneously across the whole sample, the long-time changes are realized by nucleation and growth of domains (see section 4.3.2).

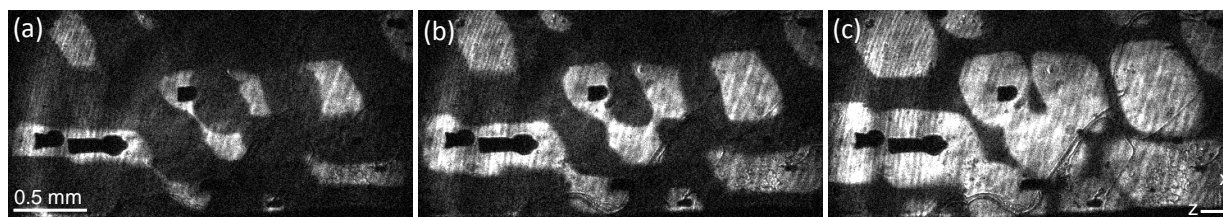


Figure 4.17 – Evolution of the non-equilibrium domain pattern on the y -face ($\perp \mathcal{P}$) during fast magnetoelectric switching in MnWO_4 . The images were taken in an electrical-pump–optical-probe experiment during the response of the magnetic system to the applied electric field. The points in time of the images are marked in figure 4.15.

To accommodate to the reversed electric fields domains nucleate, preferably at defects on the sample surface. They extend in both directions and show rounded corners. Both are hallmarks of the non-equilibrium state of the domain pattern.

In (b), the domains coalesce, which is probably related to the domain walls (see section 4.1.4).

Because the electric field needs to be applied in the direction of the spontaneous polarization, by symmetry, both the spontaneous and the induced polarization point along y and thus yield the same set of tensor components. The induced polarization may even be just a reversible modification of the size of the ferroelectric dipole. In that case not only the set of tensor components, but also the spectra are the same.

Section 4.3.2 will discuss the dependence of the magnetoelectric switching time on the temperature and the applied electric field. The switching time obtained for the electric and magnetic system are equal, when correcting the measured times for these effects. This proves that the ferroelectric and the magnetic subsystem remain coupled also in the non-equilibrium states of fast magnetoelectric switching.

4.3.2 Dynamic domain patterns

Like in the quasi-static case, one can acquire the SHG signal from the sample with spatial resolution. This allows to measure the domain patterns in the non-equilibrium states of magnetoelectric switching.

Figure 4.17 shows the evolution of the domain pattern on the y -face in a dynamic switching experiment similar to the one in figure 4.15. There is still a slight preference for the alignment of domain walls along the magnetic easy axis, or alternatively, normal to x , which is known from zero-field and quasi-static switching (figure 4.1 and 4.10). In contrast to the quasi-static switching, no stripes appear, but the domains are more bubble-shaped with a tendency for rounded corners.

As discussed in section 2.2.3, repeatability of the domain patterns over many switching cycles is a key requirement for the acquisition of dynamic domain images. Fortunately this is the case for MnWO_4 . Sharp domain patterns without any blur, especially also across complete image sequences, confirm that repeatability is given at least for more than 100 000 switching cycles.

To get an idea of the three-dimensional structure, also images on the x -cut surface were taken (figure 4.18). Compared to the y -face, domains are more irregularly shaped, but there is still a

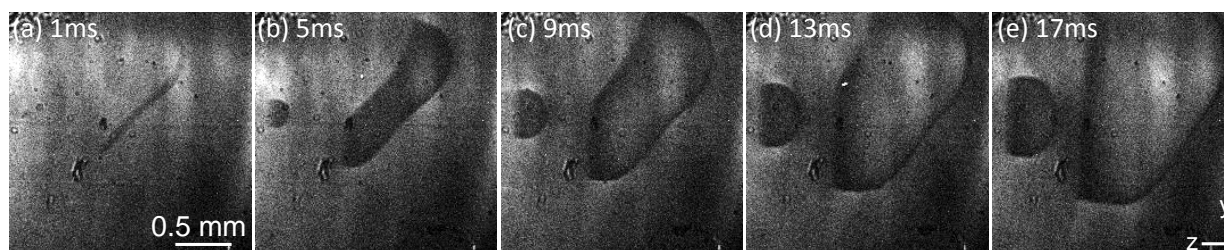


Figure 4.18 – Evolution of the non-equilibrium domain pattern of the x -face (\mathcal{P} in plane) during fast magneto-electric switching in MnWO₄. The images were taken in an electrical-pump–optical-probe experiment during the response of the magnetic system to the applied electric field.

The domains are irregularly shaped. Only some domain walls align along the polarization direction while others are more curved and do not follow a particular direction. The domains grow in both directions, albeit growth along the polarization direction y is slightly preferred.

tendency for rounded corners. While some walls are aligned along the polarization direction y , others are more curved and do not seem to strictly align along a certain direction. The growth along the polarization direction is slightly preferred over the sideways growth along z , leading to a slight elongation of the domains along y .

Comparison of quasi-static and dynamic domain patterns

During quasi-static switching, the domains are guided through a series of approximate equilibrium states by the slowly varying field. Two reasons exist for a slight deviation from the ground state in these measurements: (i) Due to experimental limitations the field could only be changed stepwise between successive images in the quasi-static measurements. This results in small deviations from equilibrium when changing the field to the value for the next image.⁴ (ii) Thermal fluctuations allow deviations from the strict energy minimum.

The quasi-static switching results in the formation of plates in the z -plane, which is the multi-domain ground state. The actual formation process and position slightly varies from cycle to cycle because of the aforementioned reasons. The depolarizing field is the driving force for the nucleation and initial growth of the domains.

After fast field reversal, the single domain state is far from equilibrium. Therefore, the force to adapt the domain population is stronger than in the case of quasi-static switching, where the intermediate plate-like structures are close to the ground state. The domains grow in all three directions to quickly gain as much volume as possible, resulting in the bubble-structure observed. In contrast to the quasi-static switching, in which only the depolarizing field initiates the nucleation and growth process, these processes are additionally supported by the external field in the dynamic switching. The preferential domain wall alignment perpendicular to x and parallel to the easy axis as well as the slight elongation along y are still hallmarks of the energy landscape of the magnetic and ferroelectric system. However, the bubble structure shows that a fast gain of domain volume is more important than totally conforming with the energetically preferred directions of the domain walls. This is equally expressed by the

⁴This issue has been resolved in later measurements by improvements of the experiment control software.

4.3. Dynamics of magnetoelectric switching

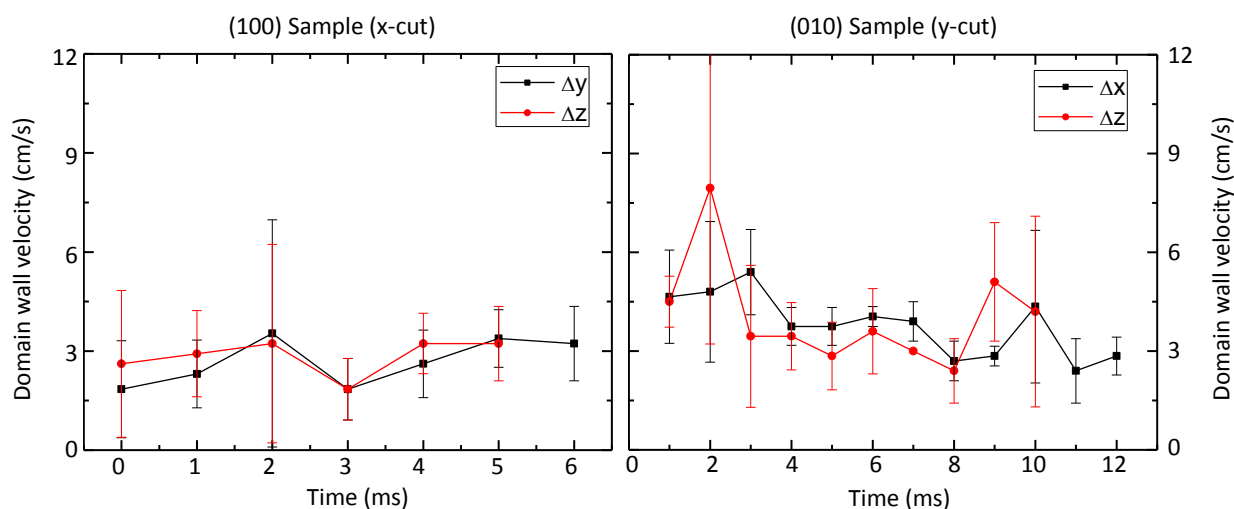


Figure 4.19 – Domain wall velocities obtained from image sequences in dynamic magnetoelectric switching on the x and y -surface. There are two curves for each surface displaying the velocities along both crystallographic axes. Since all of them yield the same value of approximately $30 \mu\text{m/ms}$, the expansion of the domains is isotropic in all directions. Furthermore, the domain wall velocity remains constant over the whole switching process.

rounded corners, which naturally arise if walls are moved away from the nucleation centers in all directions.

The image sequences of the switching process reveal that switching is governed by domain wall motion. Hence, the wall velocities determine the switching time. They are investigated in the following section.

Domain wall velocities

Domain wall velocities can be directly extracted from image sequences of the domain pattern. For this purpose one measures the distance Δs , which the wall has moved in two successive images, which are taken with a temporal difference Δt of the pump-probe delay. The domain wall velocity follows as $v = \frac{\Delta s}{\Delta t}$. A detailed description of the procedure can be found in [121]. The domain wall velocities appear to be roughly equal in all directions of the sample (figure 4.19). This is consistent with the observation of bubble-like structures in the dynamic switching process because equally fast expansion in all directions from a nucleation center leads to bubble-structures. Within the resolution of the images, the velocity does not change during the switching process, so walls move through the material at a constant velocity of approximately 3 cm/s. The constant domain wall velocity is in agreement with the KAI model of ferroelectric switching (section 1.1.4).

Intrinsic mobility

Even though the overall domain wall velocity and evolution of the domain pattern during magnetoelectric switching is slow, it sometimes happens that a single domain collapses very

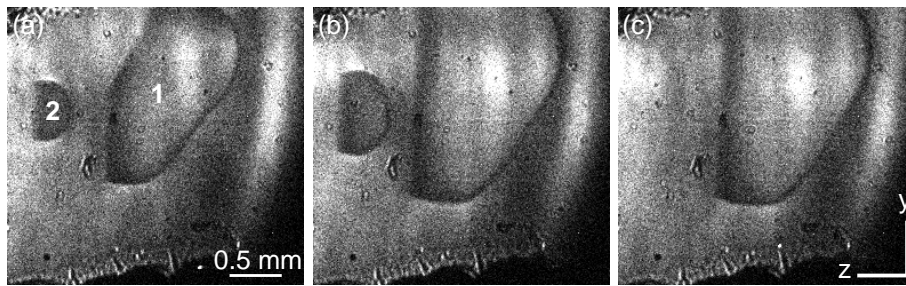


Figure 4.20 – Fast spontaneous collapse of domains during dynamic magnetoelectric switching.

The images were taken at delays of 12 ms, 19 ms, 20 ms after the field reversal ($\pm 330 \text{ kV/m}$.) The small change between (a) and (b) reflects the slow motion of domain walls. Between (b) and (c) the domain 2 vanishes within 1 ms, indicating a high mobility of the domain wall.

fast (figure 4.20). Such a process has been observed to be faster than 25 ns, which was the temporal resolution limit of the setup used and applies to both the ferroelectric as well as the magnetic system. The effect is not controllable, but appears spontaneously. However, once it is there, it is reproducible in every switching cycle. Otherwise it would not be possible to observe it in the images because in this repetitive type of experiment, they average over a few thousand switching cycles. Furthermore, it has been checked by moving the delay back and forth across the time of domain collapse, that it is not a one time change in the sample.

The reason for this fast domain collapse is unknown, but its existence yields valuable information about the mobility of domain walls in MnWO_4 . The domains that spontaneously vanish are of macroscopic size (few hundred micrometre). Since the process of collapsing was faster than the temporal resolution, it could not be resolved. However, it is reasonable to assume that it will also happen via domain wall motion. From the domain size and the observed collapse time we directly get an upper bound of $4 \cdot 10^5 \text{ cm/s}$ for the domain wall velocity in this process. This is five orders of magnitude faster than the average domain wall velocities of the overall domain pattern in the magnetoelectric switching process. It shows, that the domains themselves are much more mobile than it would appear from the overall evolution of the domain pattern under applied electric field. The reasons for this are discussed in section 4.5.

Dependence on external parameters

It is well known for ferroelectrics that the switching time depends on the amplitude of the applied field and the temperature [55, 56]. Both dependencies are investigated in the following for the magnetoelectric switching in MnWO_4 .

Electric field Switching times have been measured for different applied electric fields at 12.0 K. Because the switching time has to be measured from single domain states, valid results can only be obtained for field strengths larger than the coercive field. Choosing a temperature close to the transition ($T_2 = 12.7 \text{ K}$), and hence a low coercive field, allows to investigate a reasonably large range of electric fields. The maximum field is limited by the breakthrough field of the helium used for cooling the sample ($\approx 1000 \text{ kV/m}$).

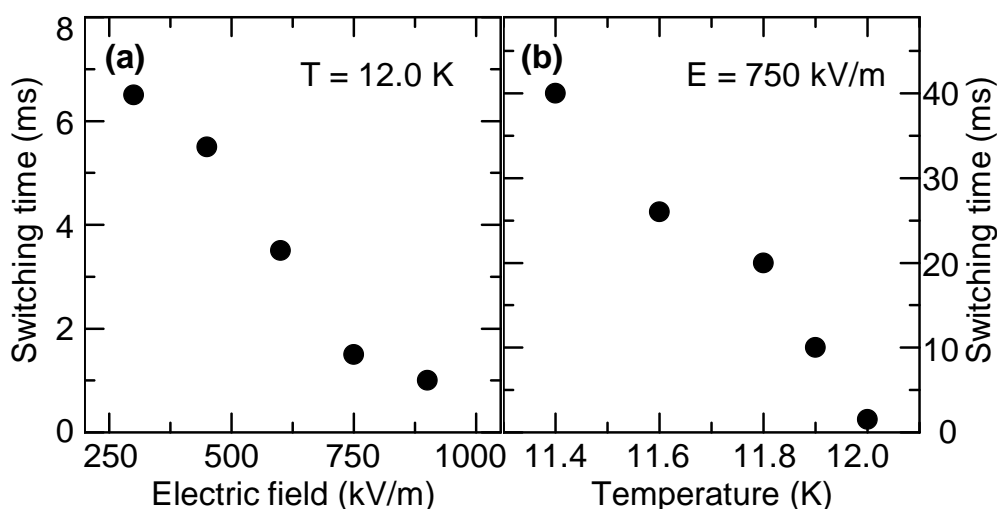


Figure 4.21 – Dependence of the magnetoelectric switching time on electric field and temperature

(a) The switching time decreases with increasing field. The data suggest a linear dependence. However, more precise measurements would be necessary to verify the scaling law, if possible covering a larger field range.
 (b) The switching time changes by a factor of 40 within only 0.6 K. This strong temperature dependence hints at a thermal activation of the switching process.

Figure 4.21 (a) shows the dependence of the switching time on the applied electric field. As the field is increased, the switching becomes faster. The relation appears to be linear in the range observed. However, it is likely that this is just a local approximation and not valid for fields much larger than the coercive field. In particular in the classical ferroelectric BaTiO₃ a scaling of $\tau \propto E^{\frac{3}{2}}$ was found for ferroelectric switching [160]. It would be interesting, to check if a similar law holds also in the case of magnetoelectric switching. This requires more measurements with increased precision. Further it would be useful to be able to measure at higher fields. Since the electric breakthrough of the helium gas used for cooling limits the maximal field to 1 kV/mm, one possibility to achieve this is to directly grow the electrodes on the sample. From the present data, we can only conclude that there is a moderate but clear dependence of the switching time on the applied field. The trend to decrease the switching time with increasing field is expected because the electric field is the driving force for the switching and a stronger driving force should result in a faster reversal time.

Temperature Dynamic switching experiments were performed at different temperatures for fixed field amplitudes $E^{\pm} = 750$ kV/m (figure 4.21 (b)) to investigate the temperature dependence of the switching time. The experimentally accessible temperature range is very limited ($T = 11.4 - 12.0$ K). As the SHG signal vanishes when approaching the phase transition, a reasonable strong signal could not be obtained for temperatures larger than 12.0 K. Again, the lower bound is imposed by requiring switching between single domain states. The maximal available field strength together with the rise of the coercive field yields a lower bound of 11.4

K. This bound could also be improved with modified electrodes for higher electric fields.⁵ The switching time strongly varies with temperature. Within only 0.6 K it changes by a factor of 40. This can not only be explained by the change of coercive field. From figure 4.13 we see that the coercive field changes approximately by a factor of two for the given temperature range. Comparing now with figure 4.21 (a), the direct effect of the temperature dependent coercive field should result in a change of the switching time by roughly a factor two to four for the given temperature range. The much larger observed effect indicates, that thermal activation plays an important role in the switching process.

4.3.3 Relaxation

Apparently, the bubble domain pattern observed in the dynamic switching is not a ground state. In the following we investigate how such a pattern relaxes. The repetition rate of the experiment was reduced to 1 Hz, to have a longer possible delay and give the material more time to relax. For details of the setup, see section 2.2.3.

Figure 4.22 displays two measurements of SHG from $\chi_{x'z'/z'}^{\text{ED}}$ at a reduced repetition rate. A field pulse of $E_y^+ = 750$ kV/m is applied at $t = 0$ for 50 ms in both cases to initialize the sample in a single domain state. The rest of the time a reverse field of $E_y^- = -750$ kV/m is applied the in the first measurement (black data points). Except for the reduced repetition rate, the experiment equals the one in figure 4.15, i.e. it switches between single domain states and is given here only for comparison.

No reverse field is applied in the second measurement (red data point). When the the 50 ms positive poling pulse is removed the sample relaxes in zero field. After a fast drop, there is a further slow exponential decrease with a decay constant of approximately 0.3 s (blue line). The increased signal around 0.35 s stems from fluctuations in the laser intensity. In total, the SHG intensity remains significantly higher compared to the measurement with reverse field applied because the sample remains in a multi-domain state.

The SHG images in figure 4.23 reveal the domain pattern during relaxation in zero-field. Images (a)-(d) are taken at the correspondingly marked times in figure 4.22. The quick drop in SHG intensity after removing the field results from the emergence of bubble domains (a). These still non-equilibrium bubbles, slowly grow further, mainly along the z -direction. This process corresponds to the slow 0.3 s decay of the SHG intensity.

The growth along z results in a more stripe like structure on the y -face, which corresponds to the energetic ground state as shown by the quasi-static measurements (figure 4.10). Relaxation to the ground state is expected. However, the decay constant of 0.3 s suggests that 95% of the evolution is performed after 0.9 s. In contrast, the corresponding domain pattern (figure 4.23 (d)) is not yet completely stripe-like, indicating that further growth will happen, but not following the exponential law any longer. This may hint at domain wall creep and justifies the investigation of the long-term evolution of the domain pattern.

⁵The maximal duration of a field pulse is 50 ms for 10 Hz laser repetition rate and a duty cycle of 50%. Therefore, the repetition rate would have to be reduced to measure slower switching times. See also section 2.2.3 and section 4.3.3.

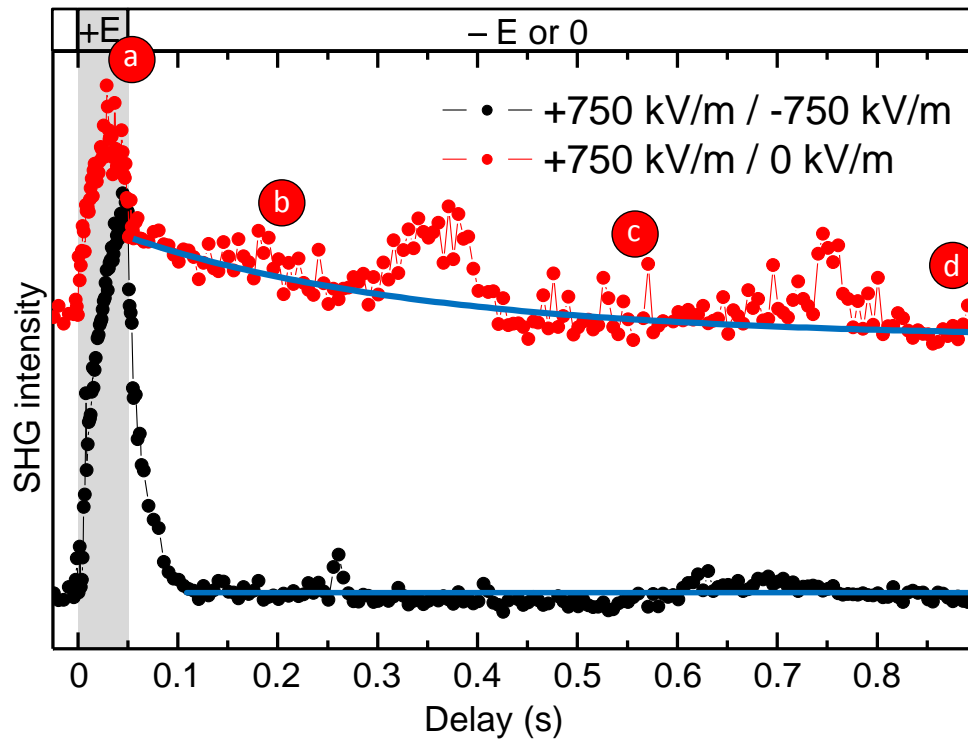


Figure 4.22 – Relaxation of the non-equilibrium bubble domain state. The black curve shows a standard E^+/E^- switching for comparison. In the actual experiment (red curve) the electric field is switched between $E^+ = 750\text{kV/m}$ and 0. During applied field (shaded area) the sample is driven to a single domain state. After switching off, domains nucleate and grow for some milliseconds as in the E^+/E^- case. But they stop at an intermediate state because no external field is present. Next, these non-equilibrium bubbles, start to relax very slowly towards the ground state. Note the slow decay of the SHG intensity. Domain images at positions (a) to (d) are shown in figure 4.23.

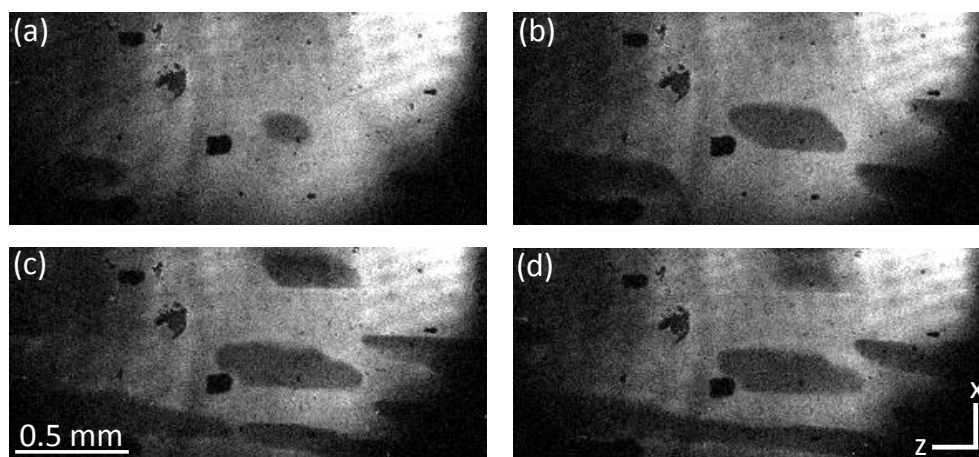


Figure 4.23 – Images of the domain pattern relaxation. After quickly switching off the electric field, the non-equilibrium bubbles are formed (a). Consecutively, they slowly grow towards the ground state stripe pattern. Images (a)-(d) correspond to the times indicated in figure 4.22.

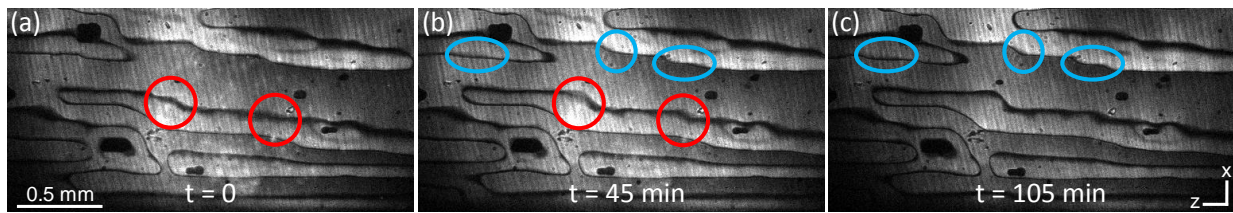


Figure 4.24 – Long-term relaxation of stripe domains on the y -face of MnWO₄. Image (a) is taken immediately after quasi-statically ramping down the electric field from $E^+ = 750$ kV/m to 0 kV/m. Slowly, the domain walls align more along their preferred directions (perpendicular to z and parallel to the easy axis). While the changes are tiny (marked by the circles for easier spotting), they proceed for more than 100 minutes, indicating domain wall creep.

Long-term evolution

A simple non-repetitive method is used to investigate the long-term stability of the stripe domain pattern. The sample is poled single domain by an electric field of $E^+ = 750$ kV/m. After slowly ramping down the field to zero, the known stripe pattern emerges on the y -face. While no external parameters are changed any longer, the domain pattern is monitored by regularly taking SHG images (Figure 4.24). Over a timescale of several minutes the domain walls become slightly more aligned to their preferential directions (perpendicular to x and along the easy axis). The adjustments are tiny, but they proceed for more than 100 minutes. This is a clear indication for domain wall creep [70].

In summary the relaxation measurements confirm that the stripe pattern on the y face is the ground state domain structure. The two preferential axes for walls on the x -face are also found in the relaxation processes. Furthermore, the relaxation processes are quite slow. A first elongation from the non-equilibrium bubble domains towards stripes happens within a second. However, domain wall creep leads to slow adjustments of the wall alignment on a timescale of more than 100 minutes.

4.3.4 Transition from quasi-static to dynamic regime

The quasi-static switching and the dynamic switching using the electrical-pump-optical-probe method form the limiting cases of very slow and very fast changes of the electric field. The first is based on slow changes of the electric field (typically ≈ 50 kV m⁻¹ s⁻¹) plus additional waiting times for the actual measurement (2.5 s in the case of spatially integrated measurements and one to five minutes for images). In the pump-probe measurements the voltage is switched within 80 ns, resulting in slew rates of 1×10^{10} kV m⁻¹ s⁻¹. In comparison to the magnetoelectric switching time in MnWO₄ (≈ 10 ms), the time of the field reversal is much slower (quasi-static case: seconds) or much higher (dynamic case: 80 ns). Correspondingly, the equilibrium and non-equilibrium domain patterns differ significantly.

It would be interesting to also investigate the transition region, in which the rise time of the electric field is on the same order of magnitude, as the magnetoelectric response of the material. However, the above mentioned methods cannot be extended to cover that region:

4.3. Dynamics of magnetoelectric switching

Because of the acquisition times, quasi-static measurements will always take at least seconds between two data points and thus changes in the field. In the pump-probe experiment, the rise time is given by the resistance and capacitance of the electric circuit (HV pulser, sample holder, wiring). It may be slightly adjusted, but a decrease to the millisecond-scale would be difficult.

Two techniques will be used in the following to obtain information on the magnetoelectric response to electric field changes on the millisecond time scale. First, we investigate the domain pattern after ramping down an applied electric field within 1 ms. Second we will use sinusoidally modulated electric fields for switching.

Single field changes

A very simple experiment can be performed with the HV source (Keithley K2410) used in quasi-static measurements. Here, the slew rate of the device is specified as $0.5 \text{ V}/\mu\text{s}$. This translates to a switching time of 1 ms to go from 500 V to 0 V (or correspondingly $8 \times 10^5 \text{ kV m}^{-1} \text{ s}^{-1}$ for the transversal E-field holder with an electrode distance of $600 \mu\text{m}$).

Figure 4.25 was taken after such a switch-off process, in which the field was ramped down from 750 kV/m to 0 kV/m within 1 ms. The domain pattern is different from the stripes in quasi-static switching (figure 4.10 (g)) as well as from the bubbles in a strong non-equilibrium process (figure 4.17 (b)). We see a tendency to elongate the domains in the z -direction, which can be interpreted as a remainder of the stripe structure. Nevertheless, there are still walls both perpendicular to x and along the easy axis. The ratio between the long and the short extension of the domains is about two. Apparently the domain walls propagate in both direction x and z , like in the dynamic non-equilibrium case. There, we attributed this behavior to the need to quickly accumulate domain volume in order to accommodate to the far-off new energy minimum. Since the system can follow the change of electric field almost in time in the present case, this need for fast domain growth is partly relaxed. Therefore, the domain pattern can almost grow through a series of ground states, which forms stripes perpendicular to x , as we have seen in the quasi-static measurements. The elongation is a precursor of the stripe pattern. Furthermore, some domain corners are sharp (like in the equilibrium pattern), while others are rounded (like in the non-equilibrium pattern). In summary, this picture shows a slight non-ground-state pattern, which is intermediate between the one in static and in dynamic measurements.

The domain pattern recorded in such an experiment does not necessarily correspond to the one directly after the switch-off of the electric field. Due to the exposure time required for the image, it averages over a few minutes after the switch-off process. However, this is not an issue in the present case. We know from section 4.3.3 that only minor changes occur on this timescale. Furthermore, the image exhibits sharp domain walls. This confirms, that the walls did not move during exposure.

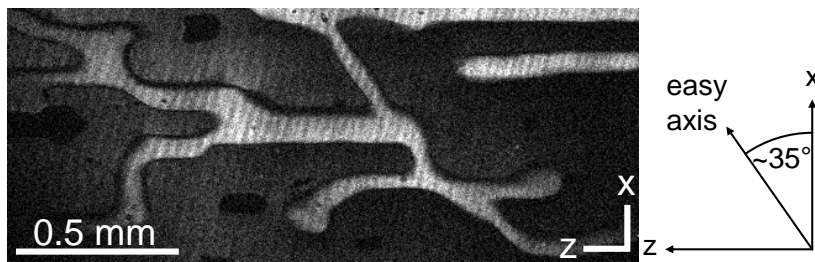


Figure 4.25 – Domain pattern in zero field after switching off from 750 kV/m within 1 ms. The timescale of the electric field change is slightly shorter than the magnetoelectric response time of the sample. This results in a new type of domain pattern, which is intermediate between the equilibrium stripe patterns in quasi-static switching and the bubble pattern observed in the strong non-equilibrium states of fast field reversal.

Sinusoidally modulated fields

The previously discussed single field change shows that there is a transition between equilibrium and non-equilibrium domain patterns, when the ramp time of the electric field is on the same order of magnitude as the magnetoelectric response time of the sample. However, this type of experiment does not allow to follow the evolution of the domain pattern with temporal resolution. Therefore, we performed another experiment to monitor the complete switching process and obtain a hysteresis in the transition region. Essentially, this is also an electrical-pump–optical probe setup, but instead of the rectangular pulse used in the dynamic measurements, we use a sinusoidally modulated electric field. This yields the slowest possible slew rates for a repetitive experiment. The repetitive character only requires that the applied field repeats for every laser pulse. This is also fulfilled for frequencies of the electric field, that are multiples of the laser frequency. Changing the frequency results in different rise times of the electric field, which are given by the half-period of the oscillation.

The experimental setup used is quite simple. The DG535 delay/pulse generator is used as master trigger for the laser (Continuum ns laser) and for a triggerable function generator (American Reliance Inc. FG-506). Using an audio amplifier and a custom built transformer from a Sawyer-Tower circuit [161] the function generator output is amplified to ± 500 V amplitude and fed into the longitudinal E-field holder for measurements on a y -cut. The time, and correspondingly the applied electric field, at which the laser pulse arrives at the sample can be adjusted via the delay between the triggers for the function generator and the laser.⁶

Figure 4.26 (a) shows hysteresis loops taken at 20 Hz, 50 Hz and 500 Hz. This corresponds to half-periods of 25 ms, 10 ms and 1 ms respectively. The minimum and maximum SHG intensities approach each other with increasing frequency. This can be explained as follows. At higher repetition rates, the half-period of the field gets shorter, and thus also available time for the domains to adapt. If a half-period is shorter than the switching time of the material, no single domain states are reached anymore. At a few multiples of the switching time, there

⁶At low frequencies $\lesssim 500$ Hz, it is also possible to use a non-triggerable function generator. Then the function generator frequency is manually adjusted to the laser repetition rate. The match will not be perfect, which causes a slow drift of the relative phase of laser and function generator. This results in a natural sweep of the delay, and the applied field at the time of measurement respectively.

is essentially one domain pattern. Within one field cycle the domain walls can only move forward and backward a little bit (figure 4.26 (d)). So the domain population will only change slightly. As a result, the SHG intensities at maximum positive field (maximum intensity in the hysteresis loop) and at maximum negative field (minimum intensity in the hysteresis loop) both approach each other. At 500 Hz a half-period of the field is only 1 ms, which is an order of magnitude faster than the magnetoelectric switching time. Therefore, the material does not have time at all to react to the changing field. Consequently, the hysteresis loop collapses to a flat line. With lower switching frequencies a hysteresis is visible.

Figure 4.26 (b) plots the minimum and maximum intensity of the hysteresis loops versus the frequency. A substantial decay of the intensity difference is reached at 100 Hz, which corresponds to a half-period of 5 ms. This is in good agreement with the switching times obtained in the electrical-pump–optical-probe measurements using fast field reversal for the given temperature and field amplitude (figure 4.21).

No nucleation process is involved at intermediate frequencies because only existing domains are modified. Hence, this method purely measures domain wall motion. It may in principle be used to separate the influences of nucleation and domain wall motion. For the case of MnWO_4 , we know from the electrical-pump–optical-probe measurements that nucleation is very fast and the domain wall velocity is the limiting factor. Therefore, the switching times obtained with both methods are of comparable size.

The hysteresis loops obtained in the sinusoidally modulated switching (figure 4.26 (a)) exhibit one particular feature. In contrast to the quasi-static hysteresis loop (figure 4.10 (e)), the minimum and maximum SHG intensities do not occur at minimum and maximum field values in the hysteresis. Instead, the amplitude keeps rising, despite the fact that the field is already decreasing again. This is a result of the non-equilibrium state in the measurement. It can be understood, when comparing the equilibrium polarization values for the current field with the actual (non-equilibrium) polarization values in the process.⁷ The switching is schematically depicted in (figure 4.26 (c)). If the sample could react fast enough, the polarization would always be in equilibrium with the electric field, resulting in a simultaneous change of both (depicted by the blue line). But because the switching process is not fast enough the polarization is in a non-equilibrium state $P_{\text{non-eq}}$ (red line), which lags behind. Since it always moves towards the equilibrium state, there are regions (shaded areas in the figure), in which the field decreases, but $P_{\text{non-eq}}$ is still smaller than P_{eq} and thus keeps increasing. The field change ΔE in this region corresponds to the width of further increasing SHG in already decreasing field in the hysteresis (c.f. ΔE in figure 4.26 (a)). This feature may be used to quantify the degree of non-equilibrium in future measurements. It is not present at all in the quasi-static hysteresis curves, in which the material is in equilibrium with the field. In the sinusoidally modulated field hysteresis presented here, the deviation from equilibrium and thus ΔE increases with the modulation frequency.

In summary, observing the frequency dependence of SHG signals on a sinusoidally modulated field is a complementary approach for the determination of the magnetoelectric switching speed. Here, the material is kept close to equilibrium conditions, in contrast to the measure-

⁷Inertia of the domain wall movement [162, 163] as cause of the further growth is unlikely because of the low repetition frequency.

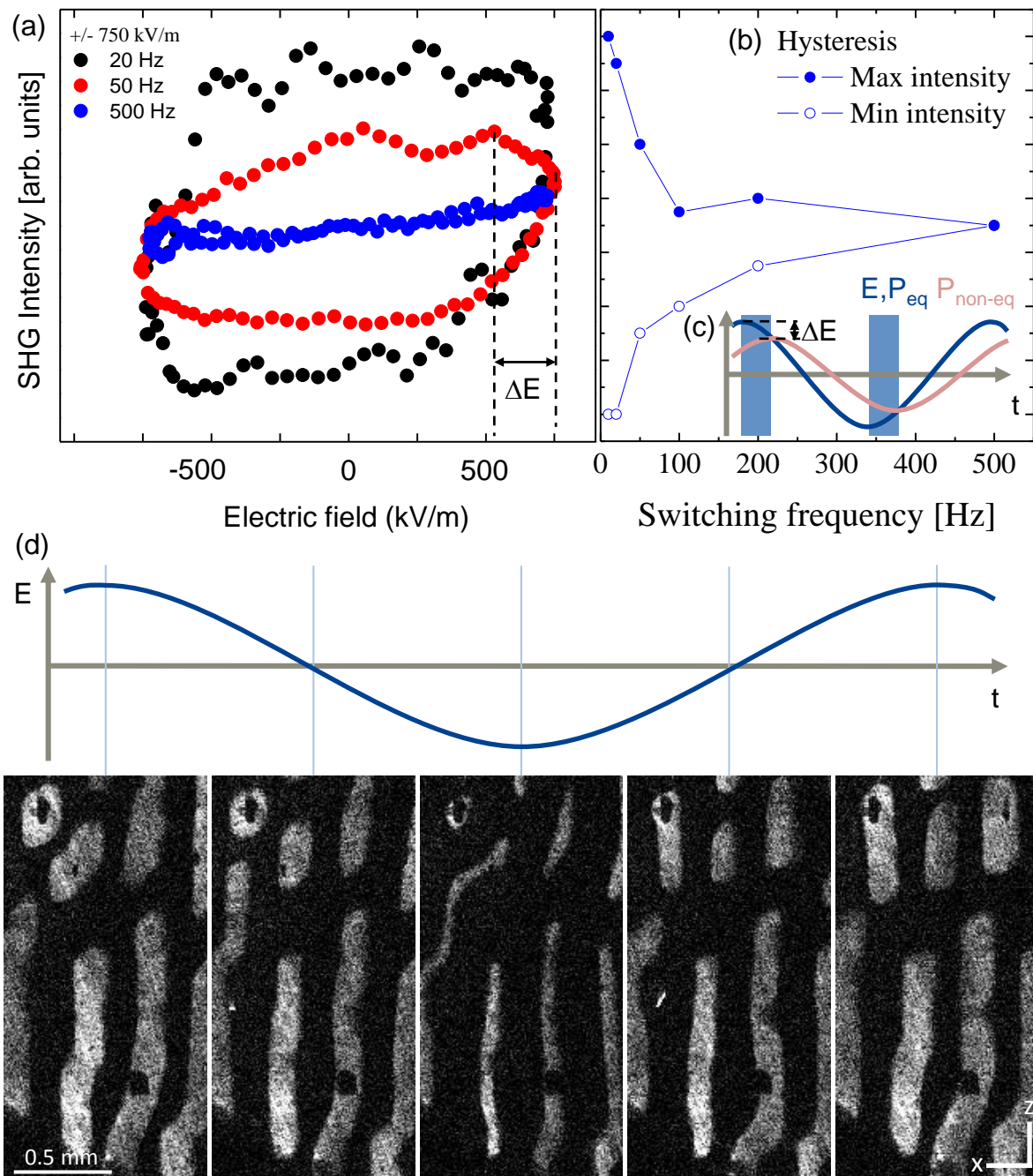


Figure 4.26 – Periodic modulation with a sinusoidal electric field (amplitude $E = \pm 750 \text{ kV/m}$) at $T = 10.7 \text{ K}$.
 (a) Hysteresis loops at different frequencies. At higher frequencies, the time is not sufficient for the sample to become single domain. Therefore minimal and maximal SHG intensity approach each other.
 (b) Minimal and maximal amplitude of the hysteresis loops depending on the frequency. The reduction of the intensity difference occurs at a characteristic frequency, whose inverse is directly related to the magnetoelectric response time of the sample.
 (c) Schematic picture explaining, why the SHG intensity keeps increasing for some time in (a) even though the field is already decreasing. The non-equilibrium Polarization $P_{\text{non-eq}}$ always moves towards the equilibrium state P_{eq} , which directly relates to the electric field E . In the shaded areas the equilibrium value is already decreasing, but still larger than the non-equilibrium value. Therefore, the latter increases further.
 (d) Image sequence illustrating that domain walls are only moved forward and back a little bit at higher frequencies.

ments with fast electric field pulses. Rather than nucleating domains from single domain states, the degree of modification of multi-domain states at different frequencies serves as probe. Hence, this method may explicitly be used also in cases, in which the field strength is not high enough to reach single domain states. In the present case of MnWO_4 the timescale extracted from the frequency dependence matches the one of the time-domain measurements. This implies that the switching time is solely determined by domain wall motion and not by the domain nucleation process.

4.3.5 Fatigue

First measurements on the repeatability of the switching have been performed in [115]. There it was shown that switching between single domain states remains possible for more than 10 000 cycles. This statement can now be strongly extended based on the results presented above. As discussed in the context of dynamic switching images (section 4.3.2), the switching is still possible for more than 100 000 cycles. Moreover, the material even progresses through the same domain pattern in these cycles. For the overall repeatability, we can impose a much higher limit. Because of the periodic switching in the dynamic measurements, each sample was switched many millions of times in the course of the experiments. No sign of degradation or fatigue could be observed over the whole time.

This is remarkable because polarization fatigue is a certain problem in ferroelectrics [164] and thus generally extends also to multiferroics. A very drastic example is BiFeO_3 , which is a promising split-order-parameter multiferroic because it is multiferroic at room temperature. Here, fatigue can already set in after 20 switching cycles [165]. However, this strongly depends on the experimental conditions [166–168].

We will not discuss the details of fatigue here. But as a very general statement, large polarizations seem to be more prone to fatigue [164]. From that point of view, magnetically induced ferroelectricity has the major advantage that the induced ferroelectric polarization is small, typically three orders of magnitude below conventional ferroelectrics. It may be much less susceptible for the mechanisms causing fatigue because all changes in physical quantities are much smaller. The small polarization corresponds to small charge displacements and surface charges.

It is not finally decided if the polarization in MnWO_4 is of electronic or ionic nature. The spin-current mechanism and the inverse Dzyaloshinskii-Moriya mechanism can both explain the creation of a polarization by a spin spiral (section 1.4). One would expect less fatigue for an electronic polarization because the atomic positions and thus the crystallographic structure are not changed at all in a switching process. The lack of fatigue may be one more hint that the polarization in MnWO_4 is electronic. Albeit this hypothesis is also supported by the observation of a giant SHG efficiency in MnWO_4 [82], it has yet to be proven.

In summary, we did not observe any fatigue in magnetoelectric switching. This may be an indication of the electronic nature of the polarization. The high durability is a key requirement for applications with many switching cycles such as memory devices.

4.4 Influence of growth method

A number of experimental observations are attributed to pinning of the domains at defects. This includes repeatable static and dynamic domain structures (section 4.2 and 4.3.2) as well as the memory effects (section 4.1.2) and possibly also the asymmetries sometimes observed in the hysteresis loop and in the switching time [121, 133]. The growth method can have a significant influence on the number and type of defects. Thus we checked, whether a different growth method yields samples with different properties.

Samples fabricated using two different growth techniques were used (section 3.1.7). Most of the measurements above were performed on top seeded melt grown samples. These results were compared to a MnWO₄ crystal, which was grown by the floating zone method. No significant differences could be found between crystals from these two types of growth techniques. Domain patterns, look similar, taking into account the thickness dependence (section 4.1.3). Also the magnetoelectric properties are comparable, including hysteresis loops, coercive fields, domain patterns and dynamic switching times. Therefore, we refrain from showing additional data here.

4.5 Discussion of magnetoelectric switching

This section provides a summarizing discussion of the results on magnetoelectric switching in MnWO₄.

4.5.1 Domain patterns

Already in zero-field, the domain pattern shows hallmarks of both the electric and the magnetic nature of the domains. In combination with the rigid coupling between the order, this lead to the denotation of multiferroic domains [38] whose properties can only be fully understood taking into account both orders.

The same is true for quasi-static magnetoelectric switching. The ferroelectric polarization enforces domain walls along the polarization direction (y -axis). Deviations from this orientation appear to be costly, so that on x - and z -faces only stripe-like structures are visible. As a compromise during growth, domain needles are formed as known from ferroelectrics. Conversely, the domain pattern normal to the polarization (on y -faces) is purely determined by the magnetic properties of the domain walls. Only minor energetic differences for walls perpendicular to x and parallel to the easy axis lead to patterns that critically depend on external conditions.

Albeit the domain structure results from combined influences of the magnetic and electric order, the overall need to form a multi-domain state is based purely on the ferroelectric nature of the domains because domain. This manifests in the nucleation of reverse domains in a still positive field, which is driven by the depolarizing field. Features of both orders become less pronounced in non-equilibrium states after fast field reversal. First, there is more energy in

4.5. Discussion of magnetoelectric switching

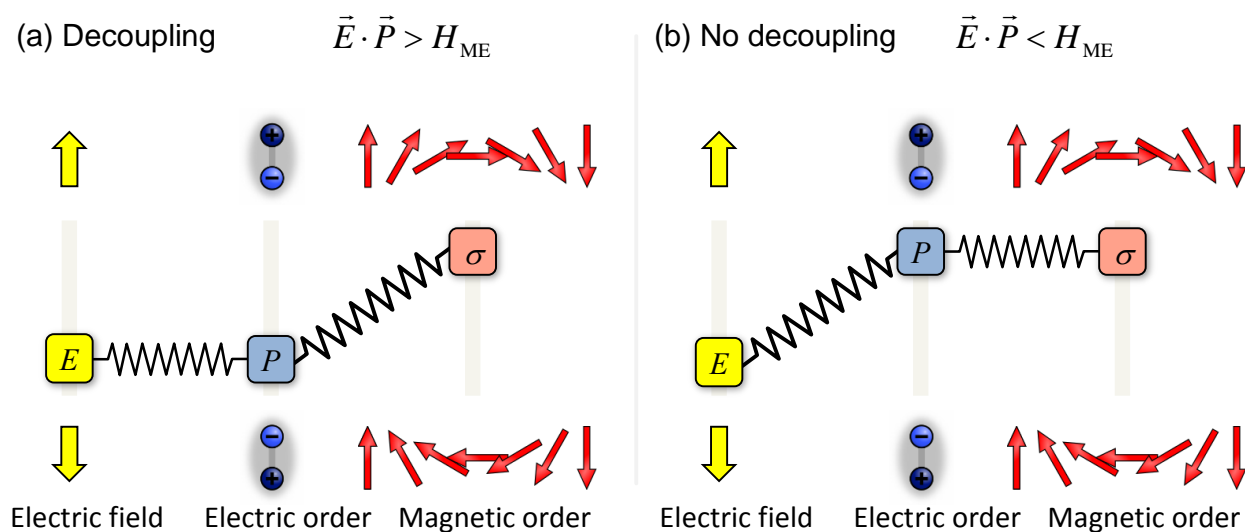


Figure 4.27 – Possible decoupling of the orders in a magnetoelectric switching process. After the reversal of the electric field the polarization can either directly adapt to the new field direction (a) or it remains aligned with the magnetic order (b) and switches together with it later on. Which one will occur depends if the energy of the polarization in the field EP is larger or smaller than the energy of the magnetoelectric interaction H_{ME} .

the system because it is not in the ground state. Second, the need to gain domain volume results in domain walls being pushed forward in all directions.

4.5.2 Rigid magnetoelectric coupling

In equilibrium states, the ferroelectric polarization and the helicity of the spin spiral are directly coupled via equation (1.6). Though theoretically allowed, we did not observe any decoupling of the orders in non-equilibrium states of a magnetoelectric switching process. This can be explained in terms of energy.

Assume for simplicity that the ferroelectric order can adapt arbitrarily fast to any external condition. When the electric field is reversed, it may either choose to immediately follow the field (figure 4.27 (a)) or it can remain aligned with the magnetic order and switch jointly with it later on (figure 4.27 (b)). Since it cannot comply with both, this results in a competition between the energy of the polarization in the electric field and the energy of the magnetoelectric interaction. Depending on which one is higher, the polarization will conform to the one or the other.

Comparing the sizes of the energy terms, the field energy amounts to $\approx 1 \mu\text{eV}$ per unit cell with the fields used in the experiments, while the Dzyaloshinskii-Moriya interaction results from spin-orbit coupling which is on the order of meV. According to these energies a decoupling of the orders is not expected in MnWO_4 , which agrees with the experimental results.

If significantly higher field strengths are available, e.g. in thin films, the decoupling might be used in future experiments to determine the coupling strength of the magnetoelectric interaction.

4.5.3 Timescale

The timescale of the magnetoelectric switching is a crucial, but also surprising result. Intuitively the millisecond response time appears to be very slow, when comparing with nanosecond switching times known from primary ferroelectrics and ferromagnets.

The magnetic system in the present case is antiferromagnetic and not ferromagnetic. Therefore, there are no classical switching times because there is no macroscopic conjugate field that could be used to manipulate the order. However, experiments using other driving forces, like exchange bias, spin polarized currents or short laser pulses [65, 66, 169] suggest that the response time of an antiferromagnet is comparable to that of a ferromagnet. Hence, it is reasonable to assume that the antiferromagnetic order in MnWO₄ can in principle be changed fast. Experimentally this is supported by the observation of the non-controllable domain collapse within nanoseconds (figure 4.20).

Now we turn to the ferroelectric part of the system. It is important to know that the nanosecond switching times in ferroelectrics are achieved in thin films with much higher field strength than used in the above experiments. As shown in section 4.3.2, higher electric fields will reduce the switching time. For a fair comparison, switching of bulk ferroelectrics at equivalent field strength has to be taken as reference. In BaTiO₃, a classical ferroelectric, the switching time at 800 kV/m is roughly 1 μ s [160]. This is still lower than the shortest time we measured (1 ms), but it is only a factor of 1000 and not a six orders of magnitude difference between nanoseconds and milliseconds. Thus, part of the slow response results from the comparably low electric fields used in the experiments. The use of thin films (appendix C) may be a promising way to speed up the switching process because much higher electric fields can be applied.

However, the magnetoelectric switching is still three orders of magnitude slower than direct switching of a conventional ferroelectric. In general, the switching speed results from a competition between forces hindering a change, i.e. pinning, and forces that drive the switching, i.e. the field energy. We have observed pinning in various measurements. This includes repeatable static and dynamic domain structures (section 4.2 and 4.3.2) and the memory effects (section 4.1.2). All these form constraints for the domain pattern and may limit the motion of domain walls. Thus, pinning will influence the switching speed. However, as we will explain in the following, it is not the main reason for the slow switching speed.

The observed fast domain collapse (section 4.3.2) implies that pinning can be overcome efficiently. Here, macroscopically sized domains can vanish within nanoseconds. We have shown that this holds for both the ferroelectric and magnetic subsystem. Even though the reasons and details of this process are still unclear, simply the fact that it happens proves that the domain wall mobilities can be significantly higher than the ones observed in magnetoelectric switching. Hence, the domains can change fast (within nanoseconds), but in the case of magnetoelectric switching they react on a timescale of milliseconds, which is six orders of magnitude slower.

This slowness can be understood when looking at the driving force of the switching: The applied electric field deforms the free energy potential, so that one polarization direction is preferred (figure 4.28 (a)). After instantaneously changing the polarity of the field (figure 4.28

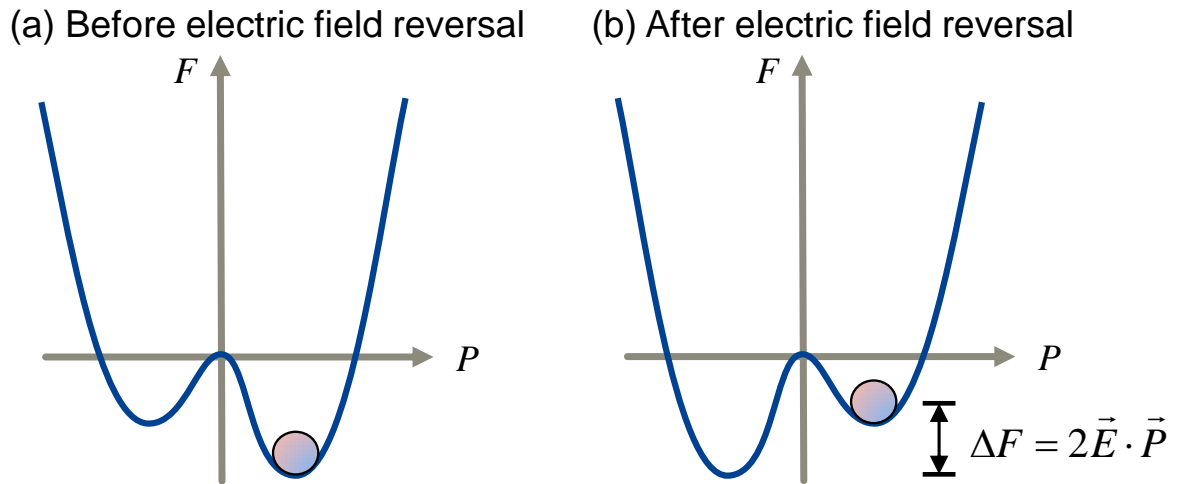


Figure 4.28 – Free energy during a magnetoelectric switching process.

(a) The applied electric field deforms the energy potential. This favors a certain orientation of the polarization and hence helicity of the spin spiral. The current system state is indicated as the ball.

(b) After field reversal, the ground state changed. The system is above this state by an amount $\Delta F = 2\mathcal{E}\mathcal{P}$ because the polarization is misaligned in the electric field. This will drive the switching, so that finally the new ground state is reached.

The low polarization in magnetically induced ferroelectrics results in a small value of ΔF , and consequently in slow switching.

(b)), the free energy of the system is raised by an amount

$$\Delta F = 2E\mathcal{P} \quad (4.1)$$

because the polarization is misaligned with respect to the external field. It is this energy that drives the switching process. Considering now that the polarization \mathcal{P} in magnetically induced ferroelectrics is typically three orders of magnitude smaller than the polarization in conventional ferroelectrics, we propose that the main reason for the slow switching is the low driving energy.

The proposed relation between the switching time and the energy difference ΔF is also backed by our experimental results from the electric field strength dependence of the switching time. Instead of changing the polarization, this changes the applied field to vary the size of ΔF . We have observed that larger fields speed up the process. This can now be understood because they increase the energy difference ΔF .

More formally, the dependence of the switching speed of ferroelectrics on the polarization can be derived from Landau theory (section 1.1.1). By applying the Landau-Khalatnikov-Equation (1.3) to the free energy in applied field (1.2), one finds that the rate of change of the polarization $\frac{\partial P}{\partial t}$ depends non-linearly on the polarization. This implies that larger polarizations switch faster.

The model proposed above is a strong simplification because it completely leaves out the microscopic physics of domains. Nevertheless, it illustrates a core issue in magnetoelectric switching of magnetically-induced ferroelectrics, which is has not been realized up to now: The coupling between the orders may be rigid, i.e. the equilibrium domain states are one-to-

one correlated. This guarantees that switching has to happen because the material has to go to the new ground state. However, rigid coupling does not necessarily imply fast switching. The speed of the switching process depends on the energies involved. Here, the crucial point is that the complete system is less affected by electric fields, due to low polarizations. This is especially the case in non-equilibrium switching, in which the field drives the transition. Based on the above explanations and the fact that all magnetically induced ferroelectrics, have low polarizations, we propose that comparably slow magnetoelectric switching speed is a general property of this class of multiferroics.

Chapter 5

Cupric Oxide – CuO

CuO has an exceptional position among spin-spiral multiferroics in that it exhibits a high ordering temperature of 230 K. The spin spiral is stable at such high temperatures because of the large magnetic exchange interaction. Both, the high ordering temperature as well as the strong magnetic exchange, render CuO particularly interesting for magnetoelectric switching.

Since no SHG measurements have been performed on CuO so far, we provide a full characterization of CuO, including a theoretical symmetry analysis of the allowed SHG tensor components and their experimental verification. After determining the tensor components coupling to the multiferroic AF2 phase, these components are used to image the domain structure after zero-field cooling and under applied electric field.

5.1 Symmetry analysis

All possible non-zero SHG tensor components can be derived from a symmetry analysis [112]. The present analysis is limited to a c -cut of CuO which is oriented perpendicular to the laser beam ($k \parallel c$) because that is the experimental setup used for all the measurements. SHG tensors up to the electric quadrupole (equation (2.6)) are considered.

The crystal structure of CuO possesses a space group $C2/c$, which corresponds to a point group $2/m$. This is the symmetry of the paramagnetic phase. No electric dipole (ED) tensor elements are allowed because it contains an inversion center. This restriction does not apply to magnetic dipole (MD) and electric quadrupole (EQ) tensor components. In the experimental geometry used ($k \parallel c$) the following tensor components can be non-zero: χ_{bbb}^{MD} , χ_{baa}^{MD} , χ_{aab}^{MD} ¹ and χ_{acaa}^{EQ} . Since these signals arise from the crystal structure, they are present in every phase of CuO.

The onset of spiral magnetic order in the AF2 phase below $T_2 = 230$ K breaks the inversion symmetry and reduces the point-group to $21'$, which allows for ED tensor components. Since these components can only exist because of the symmetry-lowering ordered state, they will

¹Because the SHG tensor is symmetric in the last two indices, it holds $\chi_{aab}^{\text{MD}} = \chi_{aba}^{\text{MD}}$. For brevity we will leave out the second one.

phase	symmetry	coupling to the polarization	crystallographic
paramagnetic	$2/m$	-	$\chi_{bbb}^{\text{MD}}, \chi_{baa}^{\text{MD}}, \chi_{aab}^{\text{MD}}, \chi_{acaa}^{\text{EQ}}$
AF2 (spiral)	2	$\chi_{bbb}^{\text{ED}}, \chi_{baa}^{\text{ED}}, \chi_{aab}^{\text{ED}}$	$\chi_{bbb}^{\text{MD}}, \chi_{baa}^{\text{MD}}, \chi_{aab}^{\text{MD}}, \chi_{acaa}^{\text{EQ}}$
AF1 (collinear)	$2/m$	-	$\chi_{bbb}^{\text{MD}}, \chi_{baa}^{\text{MD}}, \chi_{aab}^{\text{MD}}, \chi_{acaa}^{\text{EQ}}$

Table 5.1 – List of allowed SHG tensor components for a CuO crystal with light propagating along the c axis.

couple to the order parameter. In the experimental geometry used, $\chi_{bbb}^{\text{ED}}, \chi_{baa}^{\text{ED}}$ and χ_{aab}^{ED} are symmetry allowed.

In the AF1 phase below $T_1 = 213$ K, CuO shows a collinear spin structure, which is inversion symmetric again (point-group $2/m1'$). Thus, only MD tensor components are allowed. Aside from the contributions coupling to the crystallographic order, there may now be additional MD signals related to the magnetic order. However, they have the same symmetry as the crystallographic signals and therefore appear in exactly the same tensor components. The symmetry allowed tensor components are listed in table 5.1.

5.2 Experimental details

The following data are acquired with a nanosecond laser and a standard transmission setup (sec. 2.2.1). It turns out that SHG signal amplitudes from CuO are quite low. Some apparently unpolarized background signal was present, which is likely to be luminescence in the cryostat windows or the sample itself. A strongly nonlinear, threshold-like behavior of this signal was observed when changing laser focus position and intensity. By tuning these parameters, it was not possible to completely suppress the background while maintaining significant SHG intensity. Therefore, all non-spatially resolved measurements were performed using a monochromator and a photomultiplier, which filter the background temporally and spectrally.

To remove the remaining background signal, it was numerically determined in the following way and then subtracted from all measurements. According to the symmetry analysis, CuO cannot emit any SHG light polarized along b in the paramagnetic phase, no matter if the incident polarization is along a or b . These geometries would correspond to hypothetical χ_{baa}^{ED} and χ_{bbb}^{ED} components. The complete signal measured in these polarization configurations can be attributed to the background. A reference background spectrum is obtained by taking the mean of the signals in the two configurations at a number of photon energies (step size 0.01 eV). It is not advisable to directly subtract this background spectrum from the data because it would remove the background, but at the same time it would add the error of the background measurement to the data. Therefore, the background spectrum was smoothed by a 10 point moving average, which corresponds to an averaging window of 0.1 eV. This procedure is valid because the spectrum varies only slowly with SHG energy. The moving average significantly reduces the noise. As a result, a low-noise background value is available for every SHG energy and can be subtracted from all the other measurements. Comparing numbers, the background reaches about 30% of the small χ_{bbb}^{ED} signal in the AF2 phase. Spectra are additionally corrected for the spectral dependence of the OPO intensity, which is measured

at a reflection from a glass plate in the fundamental beam path using a pyroelectric detector. For the visual presentation of spectra and temperature dependencies a weak 3 point moving average was applied to reduce noise and make trends in the data more clear.

For SHG images, a nitrogen cooled CCD camera was used. Due to the low overall intensity, long exposure times of up to two hours are necessary. Therefore, on top of the usual shielding a second box around the complete experiment was used to further reduce ambient stray light. All temperature values were corrected for laser heating effects as described in appendix A.1.

5.3 Characterization by SHG

5.3.1 SHG spectra

First, we identify the non-zero SHG tensor components and their spectral dependence. Comparing SHG spectra in all phases allows to determine the SHG contributions coupling to the multiferroic AF2 phase.

SHG spectra of all possible tensor components were obtained in a range between 1.5 and 3.1 eV in the paramagnetic phase (248 K), AF2 phase (218 K) and AF1 phase (203 K). The spectra show broad features between 2.2 and 2.6 eV (figure 5.1). This indicates a band gap of approximately 1.2 eV². At SHG energies larger than twice the band gap, the excitation by the first incident photon is already resonant, resulting in a large enhancement of the SHG yield [171]. We ascribe the fine structure of the peaks to d - d -excitations of the Cu²⁺ ion. The Cu²⁺ ion in CuO is surrounded by four O²⁻ ions, forming approximately square plates with Cu²⁺ in the center. The oxygen ligand field splits the d^9 levels of Cu²⁺ and gives rise to a number of transitions to d^{10} with energies between 1.6 and 3 eV [172–174]. If 2ω matches one of these transitions, the probability for the SHG process rises.

The tensor components χ_{baa}^{MD} and χ_{bbb}^{MD} are non-zero in any phase (figure 5.1 (a, b)). They exhibit exactly the same spectral behavior in the paramagnetic and AF2 phases. This reflects their crystallographic origin. A slight increase in these components can be seen in the AF1 phase around 2.5 eV. It may be explained by an additional order-related MD signal on top of the crystallographic background. This could be verified experimentally by a temperature measurement. However, we refrain from further analysis because we are primarily interested in the multiferroic AF2 phase.

The symmetry analysis predicts a third crystallographic tensor component χ_{aab}^{MD} . It cannot be measured independently because the ab configuration in the last two indices requires one photon to be polarized along a and a second photon to be polarized along b . This can be achieved experimentally by setting the incident light polarization at an angle of 45° between the a and b axis. However, such a configuration also excites SHG tensors with aa and bb as the last two indices. The existence of χ_{aab}^{MD} is verified by a measurement, in which the analyzer is fixed and the polarizer is rotated (figure 5.1 (e)). Maximum SHG intensity is

²The values for the band gap strongly vary in the literature [170].

obtained at 45° between a and b , which confirms that this component arises from mixed a - and b -polarizations in the incident light.

SHG from χ_{baa}^{ED} and χ_{bbb}^{ED} is only present in the AF2 phase (figure 5.1 (c, d)) because it requires a broken inversion symmetry. The small paramagnetic signals observed in χ_{baa}^{ED} and χ_{bbb}^{ED} in the paramagnetic and AF1 phases are background signals of χ_{baa}^{MD} and χ_{bbb}^{MD} due to limited efficiency of the polarization optics³. A pronounced signal from the multiferroic order arises in χ_{baa}^{ED} around 2.4 eV. In addition, a small signal appears in the χ_{bbb}^{ED} component. The small amplitude makes it hard to recognize, but temperature dependent measurements will finally confirm its coupling to the multiferroic state (section 5.3.2).

The symmetry analysis also predicts an order-related signal for χ_{aab}^{ED} . Like in the case of χ_{aab}^{MD} this cannot be measured background free. However, in this case one of the background signals is the large crystallographic χ_{baa}^{MD} . Assuming that the intensity for χ_{aab}^{ED} is comparable to the other order-related signals, it will be screened completely by the much stronger crystallographic signal.

The ED-tensor components are equal or smaller than the MD-tensor components. This is uncommon because the MD-transition is a higher order process, which usually results in reduced intensity. It may be explained by the coupling of the ED-tensors to the ferroelectric polarization. Applying equation (2.8) to the present case, we see that the size of the tensor component scales with the polarization. Since the polarization is magnetically induced, it is small compared to conventional ferroelectrics and consequently also the resultant SHG intensity is limited.

In summary, the experimentally observed SHG tensor components agree with our theoretical symmetry analysis. The strongest signal coupling to the AF2 phase is χ_{baa}^{ED} at 2.4 eV, which will be used for most further measurements.

5.3.2 Order parameter scaling

Temperature dependent SHG measurements uniquely verify if a SHG tensor component is order-related or of crystallographic origin. Furthermore, the coupling to the order parameter allows to determine the order parameter scaling.

Figure 5.2 shows temperature dependent SHG measurements of the non-zero tensor components of CuO determined from the spectra. The MD tensors χ_{baa}^{MD} and χ_{bbb}^{MD} exhibit a constant intensity throughout the whole temperature range. This verifies their crystallographic origin, as it is predicted from the symmetry analysis.

In contrast, the order-related ED tensors χ_{baa}^{ED} and χ_{bbb}^{ED} are only present in the AF2 phase.

³ χ_{baa}^{MD} has the same polarization as a hypothetical χ_{aaa}^{ED} component for the case $k \parallel c$ due to the rotation in equation (2.6). The only difference in the measurements of this component and χ_{baa}^{ED} is a 90° -rotated analyzer. The observed background in χ_{baa}^{ED} is approximately a factor 100 weaker than χ_{baa}^{MD} , which is a typical extinction value for the analyzer. Furthermore, the χ_{baa}^{MD} -background hypothesis is supported by the similar spectral dependence of the signals. A similar argument holds for χ_{bbb}^{ED} .

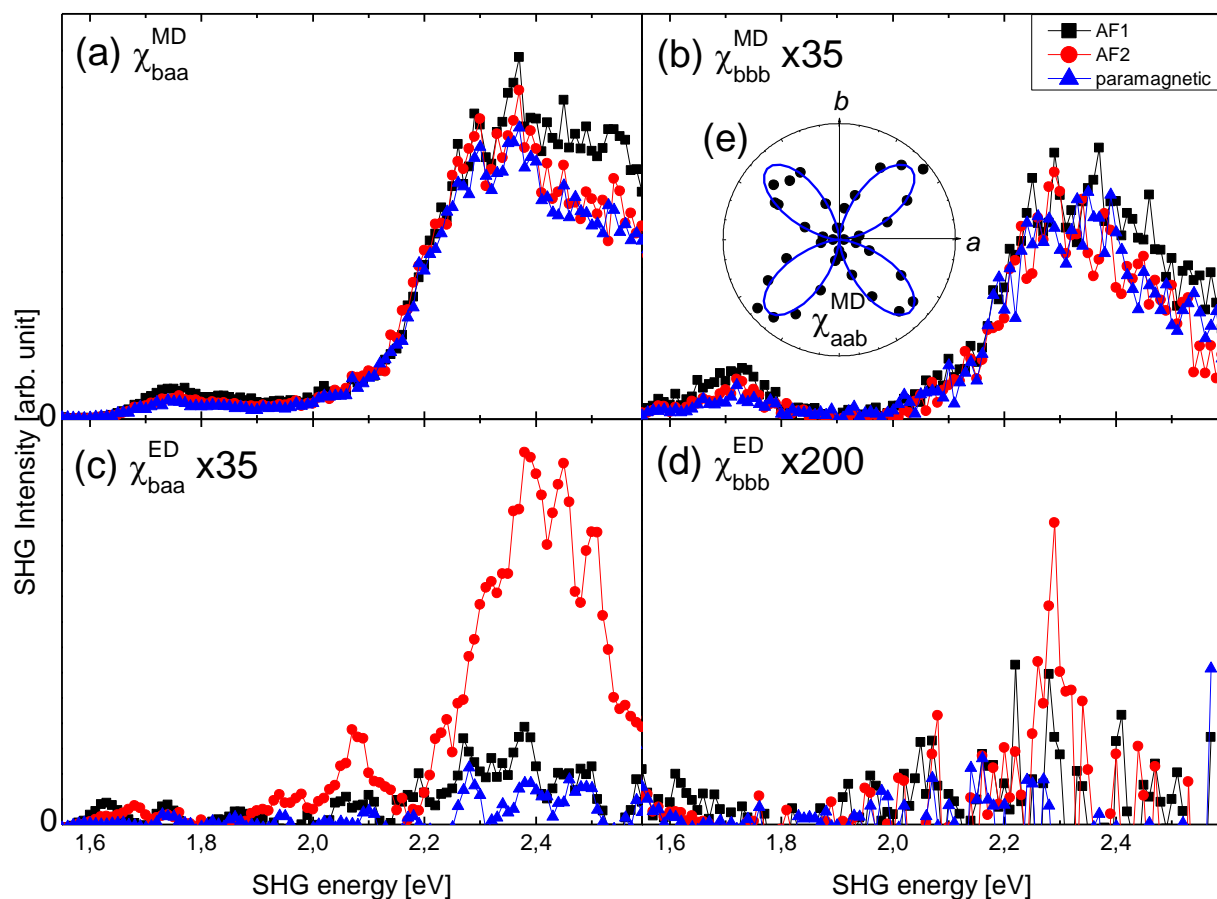


Figure 5.1 – SHG spectra in all phases of CuO. The spectra were taken in the paramagnetic phase (248 K), the AF2 phase (218 K) and the AF1 phase (203 K).

(a), (b), (e) In agreement with the symmetry analysis, the tensor components χ_{baa}^{MD} and χ_{bbb}^{MD} , χ_{aab}^{MD} are temperature independent, and thus are of crystallographic origin.

(c), (d) The ED-tensors χ_{baa}^{ED} and χ_{bbb}^{ED} are non-zero only in the AF2 phase, which reflects their coupling to the multiferroic order.

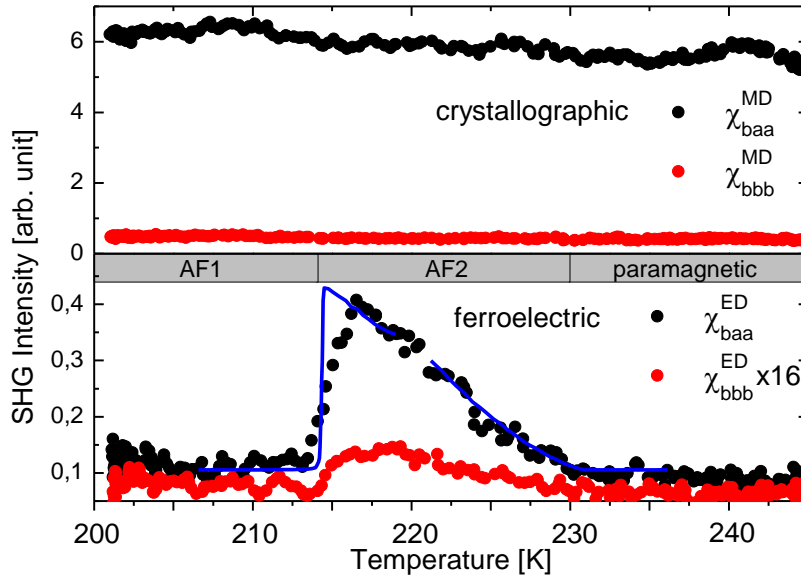


Figure 5.2 – Temperature dependencies of SHG signals in CuO at 2.4 eV. The tensor elements χ_{baa}^{MD} and χ_{bbb}^{MD} only show a very weak temperature dependence because they stem from the crystallographic structure. Contrary χ_{baa}^{ED} and χ_{bbb}^{ED} are sensitive to the multiferroic order in the AF2 phase. The blue line overlaid to χ_{baa}^{ED} displays the scaling of \mathcal{P}^2 which was obtained from pyrocurrent measurements.

When entering the AF2 phase, they continuously rise and quickly fall off at the transition to the AF3 phase. Within experimental errors both signals exhibit the same temperature scaling. The blue line overlaid to χ_{baa}^{ED} represents the temperature dependence of the square of the ferroelectric polarization, which was obtained from pyrocurrent measurements [46]. The perfect agreement between the SHG intensity and $|\mathcal{P}|^2$ proves the linear coupling between the susceptibility and the polarization:

$$\chi^{ED} \propto \mathcal{P} \quad (5.1)$$

We find, that the polarization can be described phenomenologically by

$$\mathcal{P} \propto (T_C - T)^\beta \text{ with } \beta = 0.71 \pm 0.01, \quad (5.2)$$

where β was determined as a free fitting parameter. This non-rational value is particularly noteworthy. It neither complies with the pseudo-proper value ($\beta = \frac{1}{2}$) of MnWO_4 and other spin-spiral multiferroics [91, 92, 126, 175], nor does it match a standard improper behavior ($\beta = 1$). In this context we emphasize that the SHG measurement yields the same scaling law as the pyroelectric measurement. While pyroelectric measurements are prone to artifacts because of the need to apply electrodes and because of leakage currents, SHG is a non-invasive technique. As a consequence, the unusual value of $\beta = 0.71$ is the real critical exponent of the polarization and cannot be explained by experimental artifacts. It may result from the fact that the polarization arises from the coupling of the two magnetic order parameters (equation (3.4)) and could even indicate the successive onset of these order parameters as proposed from ultrasonic measurements [122]. However, this is speculative at the moment. Further theoretical analysis is required to finally clarify this issue.

At T_1 the order-related signals drop back to zero. The SHG measurements exhibit a larger transition region than the pyrocurrent data. We will briefly discuss possible explanations. On the background of the heating by the laser (section A.1), an inhomogeneous temperature

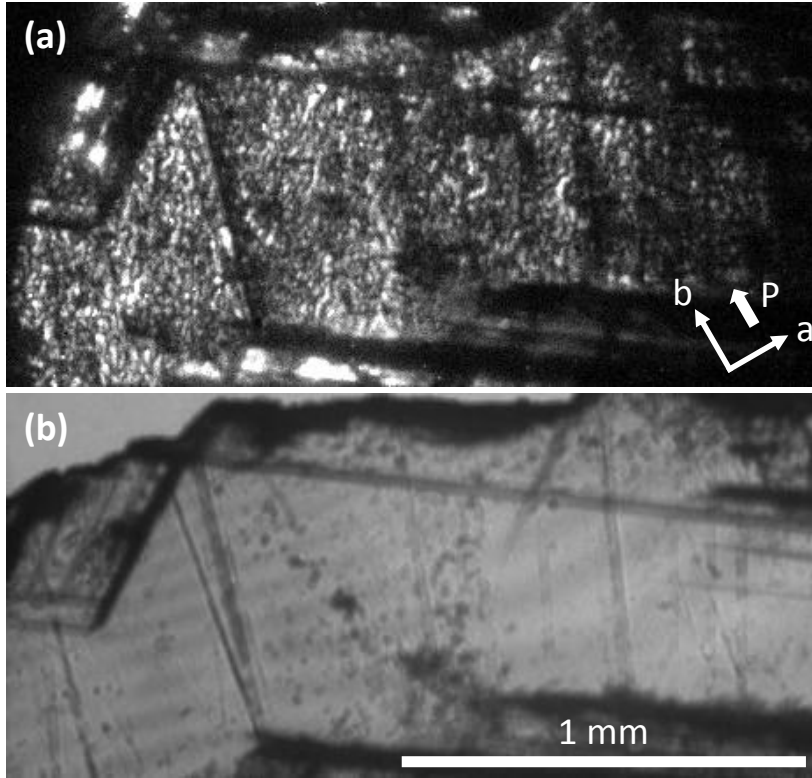


Figure 5.3 – (a) SHG image of the tensor component χ_{baa}^{ED} at 2.4 eV and 219 K. The domains are on the size of $\approx 10 \mu\text{m}$, which is significantly smaller than in other magnetically induced ferroelectrics and conventional ferroelectrics. Furthermore, the domains do not possess a preferential orientation along the polarization axis.

(b) Linear optical transmission image at 1000 nm ($\cong 1.24 \text{ eV}$). The dark lines also found in the SHG image are surface defects and not related to the domain pattern.

profile across the sample might be considered. However, this is not supported by SHG images (not shown), which indicate that the signal intensity decreases homogeneously across the sample. An alternative explanation for the gradual decrease is phase coexistence on a microscopic level at this first order transition. This would be consistent with the observation of remaining ordered nanoregions in the AF1 phase [176]. However, the reason for the difference between SHG and pyroelectric measurements remains to be investigated further. Note that the measurements have been performed on different samples. Performing both measurements on the same sample would clarify if this difference is sample dependent or originates in the measurement method.

5.4 Domains

SHG images of the AF2 phase at 219 K were acquired using χ_{baa}^{ED} at 2.4 eV (figure 5.3 (a)). They reveal an inhomogeneous intensity distribution with regions in the order of 10-20 μm .

In this image, we did not apply any external or internal reference signal to generate domain contrast. Therefore, domains will be equally bright independent of the orientation of the order parameter. Each bright region corresponds to one domain. The dark areas in between stem from interference of the SHG at domain walls (section 2.1.3).

The straight dark lines running through the image are not related to the multiferroic order. Instead, they are scratches on the sample surface, which scatter the light, as can be seen in the comparison with a linear transmission image (figure 5.3 (b)).

The domain size of approximately $10\ \mu\text{m}$ is one order of magnitude smaller than in MnWO_4 (section 4.1.3) and other multiferroics [175]. The reason for this is unclear because there is no theoretical model for the formation of multiferroics domains. One may speculate that it is related to the width of the domain walls, as in the case of ferroelectrics [154], however, further theoretical and experimental work is required.

It is not possible to extract details of the domain shape because of the small size of the domains and the limited optical resolution of the experimental setup ($\approx 10\ \mu\text{m}$). Nevertheless, we can conclude that the domain extension along a and b is approximately equal. No preferential elongation or even stripe formation along the polarization direction b is observed, which stands in contrast to MnWO_4 and conventional ferroelectrics. This indicates that the ferroelectric domain wall energy does not play a dominant role in the formation of domains in CuO. Compared to conventional ferroelectrics we may explain this by the small value of the polarization. However, the polarization is approximately equally large in MnWO_4 , where it primarily determines the domain pattern (figure 4.2 and figure 4.12). Only on the y -face of MnWO_4 the magnetic properties determine the domain structure because the polarization is perpendicular to it and thus cannot define a preferred direction. Because the magnetic exchange interaction is much stronger in CuO compared to MnWO_4 , it is conceivable that the magnetic wall energies outweigh the electric wall energies and thus determine the complete domain structure. Since the detailed structure of spin spiral domains is not known, we cannot verify this in an exact calculation. As an order-of-magnitude estimate, typical conventional ferroelectric wall energies are on the order of $100\ \mu\text{J}/\text{m}^2$ while ferromagnetic walls cost only a few $\mu\text{J}/\text{m}^2$ [70]. Because of the lower polarization in magnetically induced ferroelectrics magnetic and ferroelectric domain wall energies may be comparable in size in these materials. The particularly strong exchange interaction in CuO may then lead to a dominance of the magnetic system in the domain pattern.

5.5 Static magnetoelectric effects

Static magnetoelectric switching experiments analogous to the ones in MnWO_4 (section 4.2) have been performed in CuO using χ_{baa}^{ED} at 2.4 eV. Electric fields up to 1000 kV/m were applied along the polarization axis b to switch the ferroelectric polarization and simultaneously the helicity of the spin spiral. A slight rotation of the analyzer away from the b axis mixes in the crystallographic χ_{baa}^{MD} signal, which is used as constant reference to generate domain contrast.

Domain images were taken using a femtosecond-laser instead of a nanosecond-laser to increase the SHG yield. Nevertheless, the signal intensity close to the phase transition was too low, so that the experiment had to be performed at 218 K. After applying poling fields of $\pm 1000\ \text{kV}/\text{m}$ SHG images of the sample were taken. Since only minor changes are visible between these images it is difficult to see the effect when directly comparing the images. To illustrate the influence of the electric field, we show a difference image instead (figure 5.4). By subtracting one image from the other, regions that do not respond to the electric field have zero SHG intensity difference. In contrast, if a domain switches, the interference with the crystallographic reference signal changes from destructive to constructive, or vice versa,

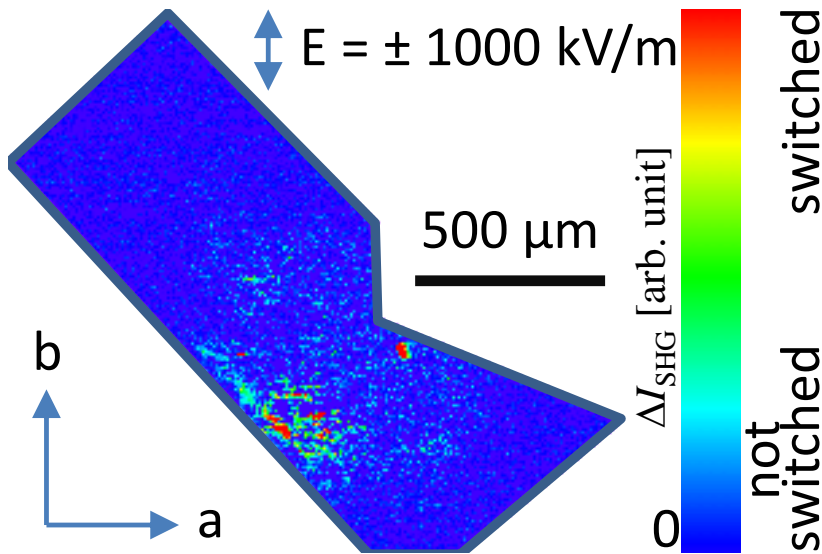


Figure 5.4 – Magnetolectric switching in CuO. Shown is a SHG difference image, which was generated by subtracting two SHG images after applying poling fields of ± 1000 kV/m, respectively. The images were obtained at a temperature of 218 K using χ_{baa}^{ED} at 2.4 eV. Zero difference (blue) indicates no switching, while a SHG difference between the images indicates switching. Because the magnetolectric switching is only partial, the coercive field is on the order of $\gtrsim 1000$ kV/m.

depending on the domain orientation and the phase of the reference SHG wave. This results in a changed SHG intensity.

Obviously only a minor part of the sample switches. This implies that the coercive field is on the order of the applied field of ± 1000 kV/m, but still a bit higher than this value. Incomplete magnetolectric switching in CuO has been recently inferred also from reduced flipping ratios in polarized neutron experiments [149], albeit they report a lower coercive field of about 150 kV/m at 218 K.

Furthermore, the switching is distributed inhomogeneously across the sample. There seems to be no switching at all outside a nearly circular central region. This could be related to thermal heating by the laser. In contrast to the flat-top profile of the nanosecond laser, the femtosecond laser has a Gaussian beam shape. Therefore, light intensity and thus heating is most prominent at the center of the beam. The increased sample temperature will lower the coercive field, facilitating the switching in the central region.

Apart from this thermal effect, the switched regions are very localized. Even when two switched areas are close together, there is no tendency to coalesce. This and the overall small size of the switched areas point to a strong suppression of domain wall motion.

5.6 Summary

We provide the first characterization of CuO in terms of SHG. This includes a theoretical symmetry analysis as well as the experimental determination of the SHG tensor components, including their spectral positions and their coupling to the multiferroic AF2 phase. The latter is used to obtain domain images of the multiferroic ferroelectric-polarization/spin-spiral-helicity domains. The domain structure significantly differs from that of other spin-spiral multiferroics and of other ferroelectrics. The domains are smaller than in MnWO_4 and seem not to be determined by the ferroelectric wall energies. This may result from the extraordinarily strong

magnetic exchange interaction in CuO. Partial magnetoelectric switching shows that the coercive field is $\gtrsim 1000$ kV/m and domain wall motion appears to be strongly suppressed.

The experiments prove that the multiferroic order in CuO can be investigated using SHG. The characterization given above forms the basis for possible further experiments. Using a setup with optimized spatial resolution, the shape of the domains and the alignment of domain walls could be determined. Furthermore the aspect of switching should be investigated further. On the background that other experiments report significantly lower coercive fields, comparing experiments on another CuO sample would be recommended to exclude strong pinning by growth-related defects. Moreover, it is possible to increase the field strength used, which was limited by the maximum voltage of the HV source in the present experiment. In contrast to the low temperature measurements on MnWO₄ the 1000 kV/m breakthrough limit of helium does not hold because liquid nitrogen is sufficient for cooling CuO to the AF2 phase. Therefore, higher electric fields are possible. Once this has been established all the dynamic measurement methods that have been developed in this work and exemplified on MnWO₄ can be readily applied to CuO.

Conclusion and outlook

Spin-spiral multiferroics provide an intrinsically strong coupling mechanism between ferroelectric and magnetic order. As such, they are promising candidates for large and robust magnetoelectric effects. This work investigates the static and dynamic aspects of the magnetoelectric effect in spin-spiral multiferroics. Special attention is paid to the domain patterns in equilibrium and non-equilibrium states and on the timescale of the switching process.

While the domain patterns in zero-field cooled MnWO_4 are more bubble-like, the domains form plates in quasi-static magnetoelectric switching. This can be explained in terms of the different conditions for domain nucleation in the two processes. In the case of quasi-static magnetoelectric switching, the ferroelectric depolarizing field drives the nucleation of the reverse domains. Nevertheless the domain pattern results from a combined action of the electric and magnetic system. By reconstructing the 3-dimensional evolution of the domains, we find that both orders have to be taken into account to explain the actual patterns throughout the switching process. This reflects the inherently multiferroic nature of the domains.

For the first time in any multiferroic we observed the dynamic domain patterns in a fast magnetoelectric switching process. These differ significantly from the quasi-static patterns. The latter are close to the energetic ground state and thus align along preferred directions. In contrast, more bubble-like shapes and rounded corners are hallmarks of the strong non-equilibrium character in the case of dynamic switching.

While rigidly coupled in equilibrium, a decoupling between ferroelectric and magnetic order is in principle possible in the non-equilibrium states of a magnetoelectric switching process. No such decoupling has been observed, which can be explained in terms of the energies involved.

Addressing the question of the speed of magnetoelectric switching, we provide the first measurements of the switching time of such a process. It lies in the millisecond range and depends on the strength of the applied electric field and particularly strong on the temperature. The latter hints at thermal processes playing a role in the domain wall movement.

Compared to classical ferroelectrics, the switching time is approximately three orders of magnitude slower, when using equivalent conditions. In general, the switching time results from a competition between pinning, which slows down the process, and the field energy, which drives the transition. While we reported several indications for pinning in MnWO_4 , high domain wall mobilities observed in spontaneous domain collapse hint that pinning is not the main cause of the slow switching.

Based on our results and a simple energy model, we postulate that the small value of the ferroelectric polarization hampers a fast magnetoelectric switching. Since the small polarization is a general feature of magnetically-induced ferroelectrics this implies that magnetoelectric switching is slow in all materials of this class. Given the fundamental character of this claim and the importance of the switching time for possible applications, this needs further investigation from theory and from experiment. A systematic measurement of switching times on different spin-spiral multiferroics is required to verify the general nature of this influence. $\text{CaMn}_7\text{O}_{12}$ would be of particular importance in this context because it exhibits an exceptionally large polarization [177, 178]. Furthermore it is necessary to develop a theory of magnetoelectric switching, by adapting ferroelectric switching theories and taking into account the coupled magnetic system.

Disregarding the switching times, we have proven that magnetoelectric switching in spin-spiral multiferroics is fatigue-free. This renders them good candidates in applications that rely on a high durability.

The setups and methods developed during this work allow for an easy measurement of magnetoelectric switching. Processes from the nanosecond scale up to hours can be measured. Simultaneously, spatial resolution allows to image domain structures in static and dynamic situations. In combination with the control and analysis software developed as part of this work, they form a ready-to-use general-purpose tool set for magnetoelectric measurements on any multiferroics.

Essentially, all sub-fields of multiferroics need to take the step from static equilibrium conditions to dynamics. All types of multiferroics should be reinvestigated for their dynamic properties because switching speed is a crucial factor in many applications. Among spin-spirals multiferroics, those containing conical spin spirals deserve special attention because they possess a macroscopic magnetization. Alternatively the exchange bias effect could be used to mediate between the mostly antiferromagnetic multiferroics and ferromagnetic materials. Here, in particular, the dynamics of the combined magnetoelectric and exchange bias coupling needs to be investigated.

Other non-spin-spiral multiferroics should be considered as well. They may not possess a coupling in the bulk. However, it can be sufficient to have a clamping of ferroelectric and magnetic domain walls.

Boosted by improvements of deposition techniques, there is a general trend towards thin films. Their properties can be tailored much stronger, e.g. by varying the thickness or by straining. Furthermore, likely all possible applications will be based on thin films and not bulk materials. From the point of magnetoelectric dynamics thin films are also promising. It is possible to generate much higher fields here. As we have shown this will increase switching speed. Furthermore, one needs only low voltages on the order of one volt.

Heterostructures can be seen as a generalization of thin films in that they are layered structures. The interface between the layers can introduce new physics, not present in either single layer. For the case of magnetoelectric switching, this means that one is not limited to multiferroics anymore. It can be sufficient to bring a ferroelectric and a magnetic constituent together to couple them via the interface [179]. This greatly increases the number of available materials

for magnetoelectric switching. The magnetoelectric coupling in these composite ferroelectric and magnetic materials is realized via the strain at the interface of the two compounds [180, 181]. Introducing this third ferroic order into the magnetoelectric switching process may significantly influence the dynamics of the process because then there are three coupled systems involved.

Another interesting topic are multiferroic nanostructures [182]. Generally new physics emerges, when the dimensionality of a system is restricted. In particular, new effects can be expected, when reducing the extension of a multiferroic below the typical domain width. In such a case, domain wall motion would not play a role and the magnetoelectric switching process would be purely determined by nucleation. This may be a route for faster magnetoelectric switching.

The field of dynamic properties of magnetoelectric switching is still in its infancy. Given the importance for possible applications, a substantial increase in interest can be anticipated. Our experimental results and the developed methods indicate directions for further research and simultaneously provide a powerful tool-set for the experimental measurement.

Appendix A

Supplementary measurements

In this section we summarize important supplementary measurements in the context of SHG experiments on MnWO_4 . This information is not required to understand the main results on magnetoelectric switching in MnWO_4 presented in this work. However, it contains valuable information and background knowledge required to correctly perform these measurements and interpret their results.

If the measurements are temperature sensitive, it is important to know the correct sample temperature. Due to limited thermal coupling the temperature sensor reading and the actual sample temperature are usually different. Section [A.1](#) describes the relation and provides a correction method to obtain the actual sample temperature. In section [A.2](#) we give details on the SHG signals used to generate domain contrast. Finally section [A.3](#) discusses a temperature dependent spectral shift of the SHG in MnWO_4 . This influences the measured SHG intensities and has to be accounted for if physical properties of the sample, like the magnitude of the order parameter or the domain population are derived from SHG intensities at different temperatures.

A.1 Temperature dependence

It is not possible to directly obtain the sample temperature in the cryostat. The only temperature information available is the one from the sample temperature sensor, which is located on the sample holder close to the sample. Here close still means that the sensor is a few millimeters up to a centimeter away due to the design of the sample holders. Particularly in the case of electric field sample holders the thermal coupling between sample and sensor is limited because of the necessary electrical insulation. Consequently the temperatures of the sensor and the sample may differ.

When measuring the temperature dependence of some order-parameter related SHG signal, we notice two things: First, the transition temperature appears to be lower than reported in the literature. And second, the measured ordering temperature depends on the sweep direction of the temperature scan. Both effects arise from a limited thermal coupling between sample and

sensor. The temperature measured with the sensor is always lower than the actual sample temperature. The reason is that part of the laser beam is absorbed by the sample. Hence, it is warmer than its environment, which the sensor measures. The actual difference mainly depends on the heating and the thermal coupling. The absorbed laser power determines the heating. Here relevant parameters are the absorption coefficient, which is material and laser wavelength dependent, and the incident laser power. The helium gas used for cooling appears to play an important role in the thermal coupling because it is observed that the temperature difference between sample and sensor depends on the helium flow. In terms of experimental parameters this corresponds to the opening width of the needle valve as well as the remaining level of liquid helium in the reservoir. The latter influences the helium flow because its weight determines the pressure on the helium in the capillary from the reservoir to the sample chamber.

For temperature sensitive measurements, it is essential to know the correct sample temperature. Therefore, one has to understand and quantify the relation between the sample temperature and the sensor reading. In the context of this relation, as a rule of thumb, we can regard a measured quantity temperature sensitive if a temperature change of 1 K leads to a sizable change of the quantity. The dependence on temperature may be explicitly SHG related (e.g. because the intensity of some order-parameter-related SHG signal scales with the temperature) or material related (e.g. because the switching time or the coercive field are not temperature-independent). Both are examples in which precise knowledge of the sample temperature is essential for a correct interpretation of the data.

How can one find the relation between sample temperature and sensor temperature experimentally? In general, we cannot determine the sample temperature. However, phase transitions can be seen in temperature scans of order-related SHG signals. At the time of a phase transition the sample has the critical temperature. Its value can be obtained from non-optical measurement techniques that do not suffer from the heating effect. Simple examples are susceptibility, heat capacity, thermal expansion, or pyrocurrent measurements, and values can often be found in the literature. Thus, we know both the temperature of the sample and the sensor reading at the phase transitions. This allows to calculate an offset correction for the the sensor data. It is important to remember that all the aforementioned parameters (i.e. material, laser wavelength and intensity, helium flow and helium level) will influence this offset. Summarizing this section, the offset between the actual sample temperature and the sensor reading in thermal equilibrium can be determined using a phase transition as reference point. To give numbers, this offset can be up to 5 K in MnWO_4 figure A.1 (a).

Additional differences can appear in temperature scans. Here, the assumption of thermal equilibrium does not hold any more, except for very low cooling rates. To estimate the size of the equilibration time, the following experiment was performed. MnWO_4 was cooled to a temperature slightly above $T_1 = 12.7$ K. The laser was operated at 2.226 eV (SHG) measuring the $\chi_{x'z'z'}^{\text{ED}}$ component associated with the magnetic order. Then an additional filter NG11/1 was introduced in front of the sample. By that, the laser intensity and thus the heating effect was reduced by approximately 50%. Therefore, the sample got cooler and entered the AF1 phase. This can be seen as a sudden drop of the SHG intensity (figure A.1 (b)), which is a consequence of the phase transition to the collinear spin state in AF1. Within the

A.1. Temperature dependence

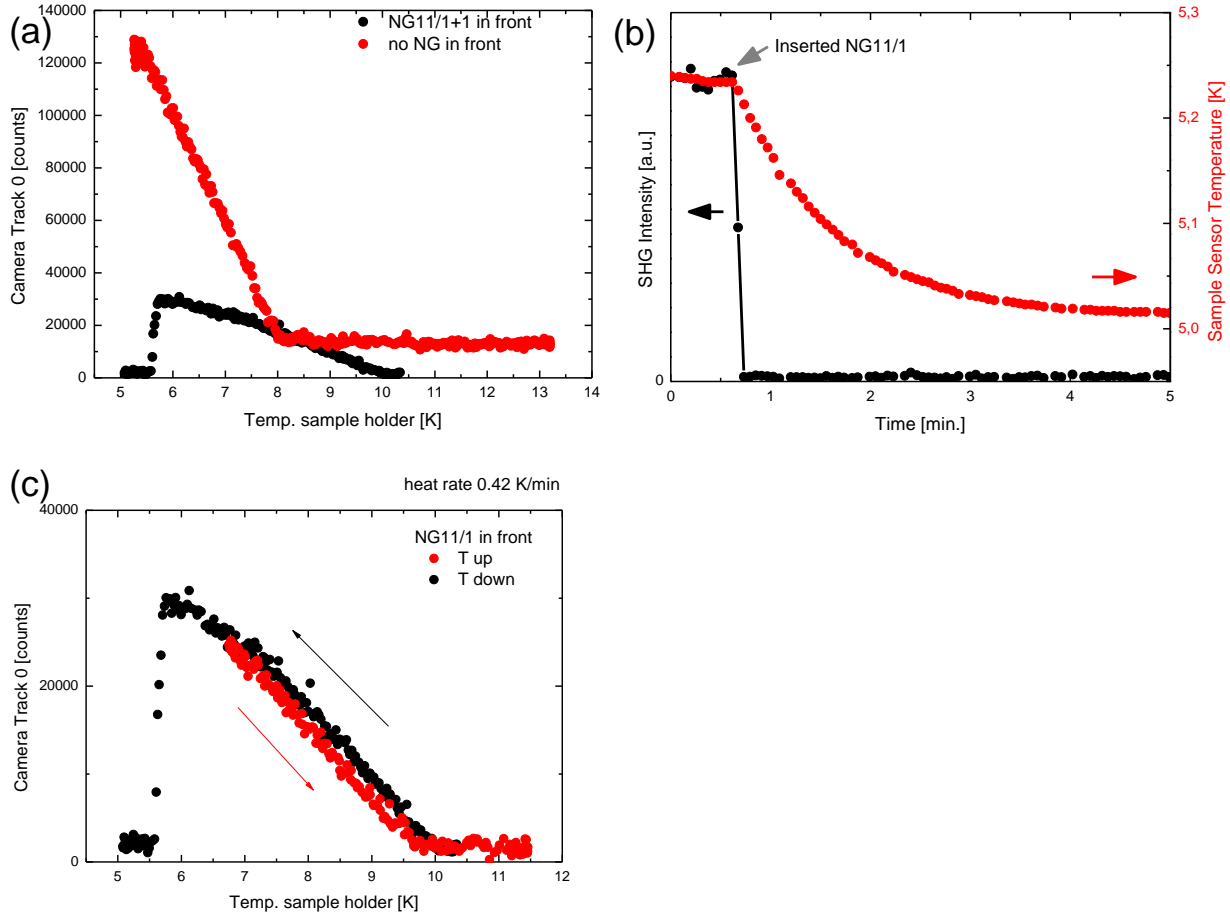


Figure A.1 – Effects that influence the relation between sample temperature and the temperature reading of the sensor.

(a) Heating the sample by the laser causes a constant offset. The actual phase transition temperature is 12.7 K. With 2 mm NG11 filter the sensor reading at time of the phase transition is 10.1 K, which corresponds to a difference of 2.6 K between sample and sensor. Removing the filters increases the laser intensity by a factor of four. At the same time, the difference between sample and sensor is increased to 4.7 K. The steeper rise of the SHG in the latter case results from the four times higher laser intensity, which yields a 16 times stronger SHG signal.

(b) Time constant of thermal coupling between sample and sample temperature sensor. After insertion of a filter, the sample is less heated and crosses the phase transition from AF2 to AF1. The immediate drop of the signal confirms that the sample directly accommodates to the new environmental conditions. However, due to the limited thermal coupling between sample and sensor, the temperature reading changes over a time of four minutes.

(c) Dynamic drag of the temperature sensor. At a moderate cooling/heating rate of 0.4 K/min the difference between the two scan directions amounts only to 0.3 K, which is negligible in many cases.

measurement resolution (2.5s per data point in that measurement) the sample temperature immediately changes. This is an important piece of information: The sample equilibrates on a timescale faster than the usual acquisition time per data point in experiments using the nanosecond laser. Consequently, we do not have to wait for the sample to equilibrate after changing some measurement parameters. Now the sample radiates less heat, and therefore, the environment and eventually the sample temperature sensor will get cooler. It turns out that this equilibration timescale is 4 minutes (see figure A.1 (b)). If one would like to have a temperature scan with sample and sensor in thermal equilibrium, the sweep rate should be much smaller than $\frac{1\text{K}}{4\text{min}}$. Using such low sweep rates is not desirable because the measurements would take much time. It is nevertheless viable to use higher cooling rates. However, in that case one has to keep in mind that the temperature difference between sample and sensor will be modified due to the non-equilibrium conditions. The modification reverses sign depending on the temperature sweep direction. In measurements this is seen as a gap between the transition temperatures in a cooling and a heating cycle figure A.1. The equilibrium temperature will lie in between. While in MnWO_4 this non-equilibrium shift is small (≈ 0.5 K), in CuO the gap was found to be more than 10 K, depending on sample holder and experimental parameters.

In most cases, both the equilibrium and the non-equilibrium offsets do not depend on temperature. If possible, this should be verified, by measuring across two phase transitions, and check that the temperature shifts of both transition temperatures are equally large. This is most easily checked by comparing the measured width of the phase with the literature value. If they coincide, both transition temperatures are shifted by the same amount.

In summary, there is a temperature difference between the sample and the sample temperature sensor resulting from heating by the laser and limited thermal coupling. It consists of two contributions, an equilibrium difference and a non-equilibrium addend, which occurs in temperature sweeps and depends on sweep direction and speed. Both contributions are temperature independent. Thus, they can be accounted for by a constant shift of the temperature sensor reading. As discussed their size depends on a number of experimental parameters. If accurate temperature knowledge is necessary for the measurements, the following calibration procedure is proposed to calibrate the temperature reading. It should be performed before starting a set of measurements (i.e. once a day) or after significantly changing the experimental parameters mentioned above (e.g. strongly changing helium flow or refilling helium in the cryostat). At least one relatively slow temperature sweep ($\leq 0.5\text{K min}^{-1}$) across a known phase transition should be performed. The change of SHG intensity at the phase transition allows to determine the time of the phase transition. Then the difference between the sample temperature and the sensor reading is $\Delta T = T_N - T_{\text{meas.}}$. This offset is correct for the temperature sweep itself. However, it is only an approximation for the offset when the temperature is held constant, e.g. in magnetoelectric switching experiments, because the value is modified due to the non-equilibrium condition of the temperature sweep. If more accuracy is needed, temperature sweeps in both directions should be performed. Using $\Delta T = T_N - \frac{T_{N,\text{meas.}}^{\downarrow} + T_{N,\text{meas.}}^{\uparrow}}{2}$ then cancels out the offsets arising from the non-equilibrium conditions. The above correction method was applied to all data presented in this work, most of the time the simplified version was used to speed up the calibration process.

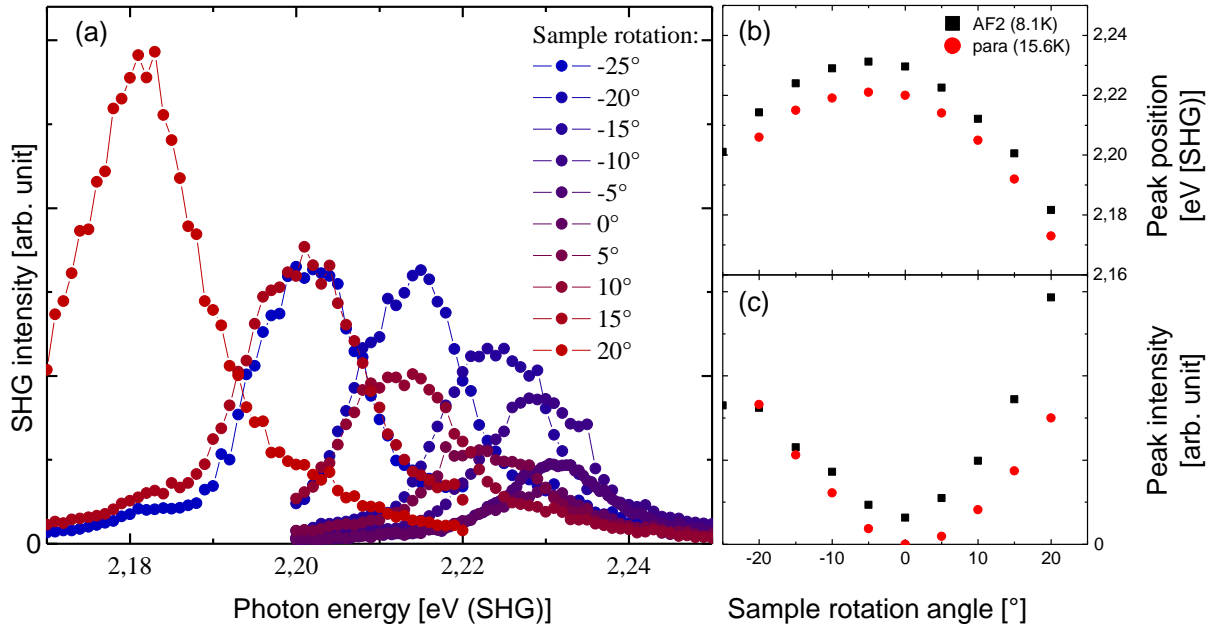


Figure A.2 – (a) Birefringence changes the spectral position of the SHG peak of $\chi_{x'z'z'}^{\text{ED}}$ in MnWO_4 when rotating the sample.

(b) Dependence of peak position on the rotation angle.

(c) Dependence of peak intensity on the rotation angle.

A.2 Signals for the generation of domain contrast

We use interference between order-related and non-order-related SHG signals to generate a contrast between different orientations of the order parameter (section 2.1.3). This section explains the used SHG components and experimental details in the context of contrast generation.

In MnWO_4 , we use an internal crystallographic SHG signal as an order parameter independent reference. It can be admixed by rotation of the sample around the x -axis [115]. Here, we present data from a y -cut. At normal incidence, it only generates a signal $\chi_{x'z'z'}^{\text{ED}}$ related to the magnetic order. The rotation admixes other components, as well be explained in the following.

Figure A.2 (a) shows a set of SHG spectra measured in a polarizer/analyzer configuration for $\chi_{x'z'z'}^{\text{ED}}$ taken at various rotation angles around the x axis. The spectral peak of the SHG slightly changes with rotation. Because the change is more than two times the FWHM of the peak, the laser photon energy has to be adapted to the rotation angle. After rotation, a spectrum should be measured and the energy at the peak position should be used for the following measurements. Otherwise one would measure at very low intensities. This angular dependence of the SHG energy is likely related to the birefringence of the crystal. A much more pronounced angular shift is observed in χ_{yxx}^{ED} , also stemming from birefringence [115]. The stronger shift in the latter case is a result of phase matching in that component. Phase matching is very sensitive to the refractive index, which depends on the direction

due to birefringence. The shift observed here is likely to be of the same cause. But because fundamental and SHG are not phase matched in $\chi_{x'z'z'}^{\text{ED}}$, the magnitude of the shift is much smaller. For performing the experiments presented in this work, it is just important to know that this shift effect exists and that the laser energy should be adapted after sample rotation. Therefore, we refrain from giving details on the physics of birefringence or phase matching and refer to the aforementioned work [115] and standard literature on nonlinear optics [119].

When comparing the peak positions in the paramagnetic and the AF2 phase, we see that there is an additional angular-independent offset between those two (figure A.2 (b)). This temperature dependent spectral shift will be discussed in section A.3. In the context of domain contrast we are primarily interested the signal intensities because they relate to the order parameter. But because of the shifts, one has to compare not the SHG intensity at a fixed energy but at the peak positions. Figure A.2 (c) plots these intensities in dependence of the rotation of the sample around the x axis. In the paramagnetic phase only the crystallographic signal is present. As expected from symmetry it is zero at normal incidence (0°) in a y -cut. By rotation projections of other tensor components start to appear. The intensity follows a $\sin^2(\alpha) \cos^2(\alpha)$ dependence. This is consistent with a signal from the allowed crystallographic tensor χ_{xyz}^{ED} (or any permutation of the indices) in the measurement geometry used¹. Inside the AF2 phase this signal is superimposed with the $\chi_{x'z'z'}^{\text{ED}}$ component related to the magnetic order. At normal incidence only this order-related component contributes (see finite value for $\alpha = 0^\circ$ in the AF2 in comparison with zero value in the paramagnetic phase). For other angles, both contributions interfere. A pure $\chi_{x'z'z'}^{\text{ED}}$ signal would scale like $\cos^6 \alpha$. However, the interference term scales like $\sin(\alpha) \cos^4(\alpha)$, which gives rise to the asymmetry in the AF2 phase with respect to the rotation angle.

Ideally one would like to have both interfering signals equally large because that results in complete constructive or destructive interference, which yields maximum domain contrast. This corresponds to -6° or 12° for the data shown. In practice it is sufficient to rotate the sample, while acquiring low resolution domain images (e.g. using 4×4 or 8×8 binning) until a reasonably good domain contrast is achieved. However, one should keep in mind that the optimal value will change with temperature because the order parameter amplitude and its related SHG intensity will scale with the temperature, while the background signal remains constant.

A.3 Spectral shifts

In the previous section, we discussed spectral shifts due to the sample rotation, which are related to the birefringence of the crystal. Additionally, the peak position depends on the temperature in the AF2 phase. Figure A.3 (a) shows spectra at different sample temperatures

¹To obtain the angular dependence of a SHG signal when rotating the sample, the electric field of the incident and emitted light wave have to be transformed from the laboratory coordinate system to the rotated crystal coordinate system. For the present case of a rotation around x this results in $E_x(\omega) = E'_x(\omega)$, $E_y(\omega) = E'_y(\omega) \sin \alpha$ and $E_z(\omega) = E'_z(\omega) \cos \alpha$. Because the intensity is proportional to the square of the amplitude, a $\sin^2(\alpha) \cos^2(\alpha)$ dependence indicates SHG from a tensor component with one x , one y and one z index.

A.3. Spectral shifts

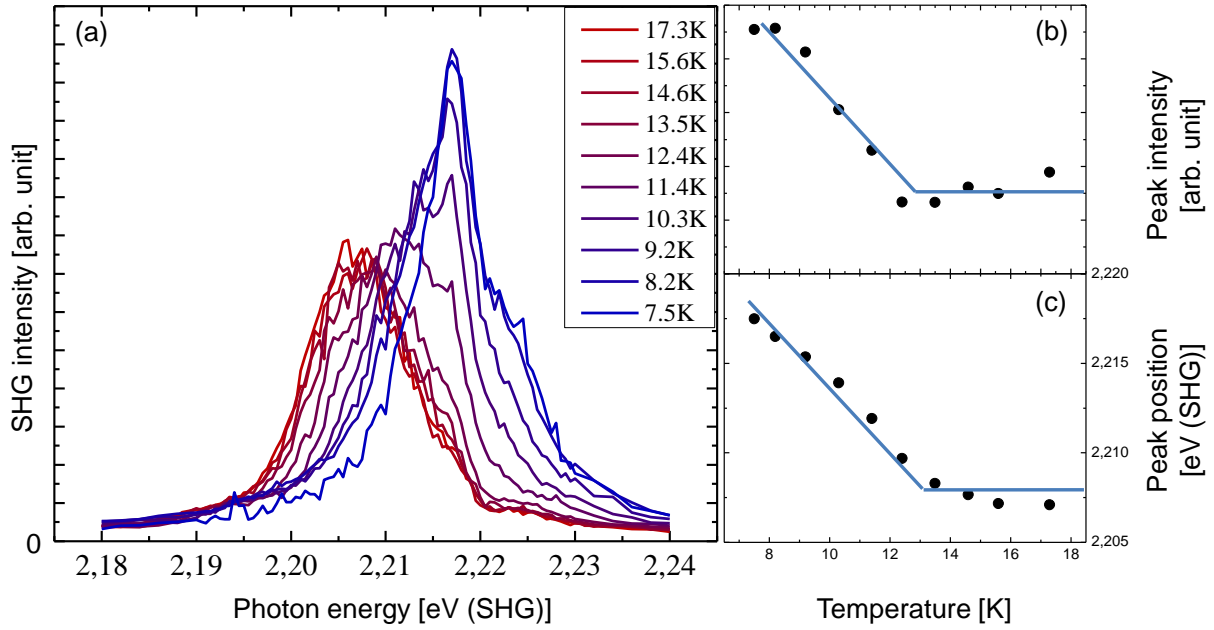


Figure A.3 – Spectral shift of the SHG signal $\chi_{x'z'z'}^{\text{ED}}$ in the AF2 phase of MnWO_4 depending on temperature.
(a) Spectra at various temperatures.
(b) Temperature dependence of the SHG peak intensity extracted from the spectra in (a).
(c) Temperature dependence of the peak position extracted from the spectra in (a).
Lines are guides to the eye.

for a slightly rotated geometry introduced in the previous section. They are temperature-independent in the paramagnetic phase because the SHG is purely of crystallographic origin. Most noticeably, the intensity linearly rises in the AF2 phase (figure A.3 (b)). This is a result of the onset of the magnetic order. The additional tensor component $\chi_{x'z'z'}^{\text{ED}}$ and the associated magnetic order parameter scale with like $(T_2 - T)^{\frac{1}{2}}$, and therefore the intensity rises linearly.

At the same time, the peak position shifts (figure A.3 (c)). This might be caused by a slight modification of the energy levels in the material due to the magnetic order (or the related electric order). Furthermore the interference between the two SHG contributions can shift the peak position. The peak width remains almost constant, with just a tiny decrease in the AF2 phase.

This shift has to be taken into account if one wants to determine the magnitude of the order parameter from the SHG intensity. In that case one has to separate changes in SHG intensity stemming directly from a changed order parameter from those resulting just from the spectral shift. Usually one measures at fixed photon energy. For example, if one starts at the peak position 2.206 eV (SHG) in the paramagnetic phase and cools down, one will only measure at the slope of the peak in the AF2 phase. It appears that the measured SHG intensity decreases, even though the order parameter and thus the intensity at the peak increase. Using interference for domain contrast adds even more complexity. This is particularly important to understand the SHG intensity curves of field-cooled measurements in MnWO_4 .

In the following we show field cooling measurements at different SHG energies (Figure A.4)

and provide a simple model that can correctly describe the observed intensities. This is important to be able to disentangle shift-related intensity changes from order-related intensity changes. Each measurement was performed in positive field and in negative field ($E = \pm 800 \text{ kV m}^{-1}$). This induces single domain states of opposite helicity of the spin spiral, i.e. the order parameter differs in sign. By interference with the crystallographic background this generates the contrast. Small changes of the photon energy drastically change the temperature dependence of the SHG intensity. This is a combined effect of the interference required for the contrast and the shift of the peak. All data sets can be described by a relatively simple model. The signal is created by interference of the crystallographic signal A and the temperature and order parameter dependent $\chi_{x'z'z'}^{\text{ED}}$ component. For simplicity, the phase between the signals is neglected. We assume a Gaussian spectral profile with a width of $w = 0.0055 \text{ eV}$ extracted from the spectra and a temperature-dependent peak position $E_0(T)$. From the data in Figure A.3 (c) we extract a linear scaling of the peak position $E_0(T)$ in the AF2 phase and a constant value above. The resulting intensity reads

$$I(E_{\text{SHG}}, T) = e^{-\frac{E_{\text{SHG}} - E_0(T)}{2w}} |A + B(\sigma(T))|^2 \quad (\text{A.1})$$

The magnetic order related amplitude scales like $B(\sigma(T)) = B' \cdot (T_{N2} - T)^{\frac{1}{2}}$ in the AF2 phase and is zero above. The amplitude B' changes sign, depending on the field direction applied. Using only the amplitude of the crystallographic signal A and the amplitude of the order-parameter-related signal B' as free parameters, we can describe all the different temperature dependencies at the different SHG energies. Both, the positive and the negative field cooling data are simultaneously fitted using one common set of parameters. The good agreement shows that the model contains all significant effects which affect the SHG intensity.

In summary, the susceptibility χ simply couples linearly to the order parameter σ and also the order parameter itself obeys a standard square root scaling law. Nevertheless, the actual scaling of the SHG intensity with temperature is quite complicated. As a combined effect of temperature and rotation dependent spectral shifts as well as interference, it critically depends on the the sample rotation and the photon energy used in the measurements. This has to be taken into account when selecting measurement parameters and interpreting SHG data at different temperatures.

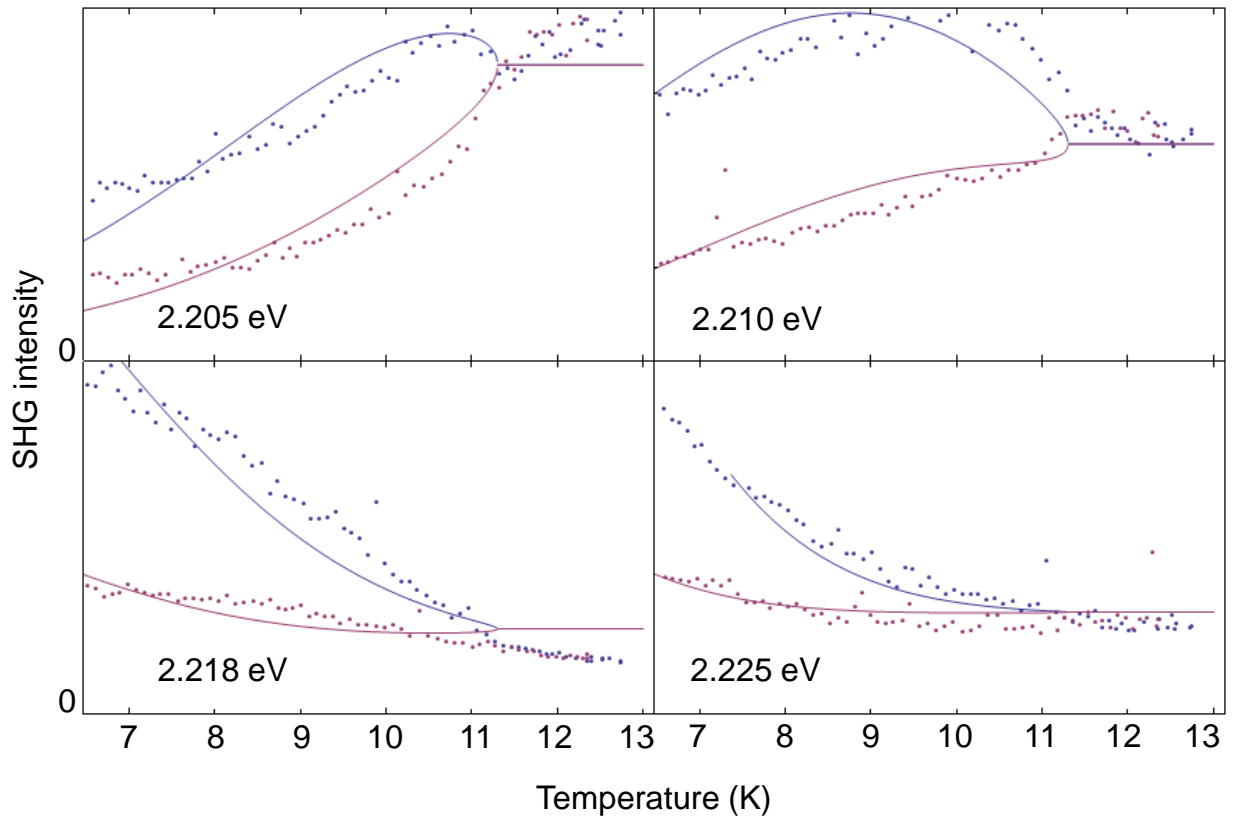


Figure A.4 – SHG intensities of $\chi_{x'z'z'}^{\text{ED}}$ for field cooling of MnWO_4 at various SHG photon energies. The interference with a crystallographic background leads to a contrast between the domains. This results in a field-direction dependent SHG intensity in the AF2 phase. The strong dependence on the SHG photon energy is a combined effect of the interference with the crystallographic signal and a temperature dependent shift of the SHG peak in the AF2 phase. It can be explained by the model detailed in the text (continuous lines).

Appendix B

Optical pump-probe measurements on MnWO_4

The optical pump-probe method achieves temporal resolution down to the femtosecond scale. Like the electric-pump–optical-probe measurements (section 2.2.3), optical pump-probe measurements are a repetitive technique. Instead of the electric field, a femtosecond laser pulse is used to excite the system at $t = 0$. However, these two techniques yield complementary information on the dynamics of the system due to the different excitation mechanisms. When the electric field is used as pump, it changes in a step-like manner defining a new ground state for the material. In contrast, the laser pulse is only present for a short time (≈ 100 fs). It strongly excites the material and the actually investigated process is the relaxation to the original ground state. Furthermore, the excited systems are different. The electric field in electrical-pump–optical-probe measurements deforms the free energy potential and directly acts on the ferroelectric order. In contrast, the optical pump pulse does not change the energy potential. Instead, it primarily deposits energy in the material. For example, this additional energy can destroy ferroic order. Using an optical pump-probe technique one can then measure how it is destroyed, and how fast it builds up again when the energy has dissipated. While this is not directly related to magnetoelectric switching, it may be combined with external electric fields. The recovery in applied field is similar to fast field cooling and can induce a preferential domain orientation. Alternatively, the order does not have to be destroyed completely. If a constant electric field below the coercive field is applied, the material will not switch. Now, the energy of the optical pump brings the system closer to the phase transition and thereby lowers the coercive field. Thus, even though the external field is not changed, switching may be provoked. Furthermore, it is possible to selectively excite certain subsystems (electronic states, magnons, phonons etc.) with a properly tailored pump pulse. Hence, optical pump-probe measurements yield information on the couplings and the dynamic properties of the material complementary to the ones obtained in electrical-pump–optical-probe measurements.

B.1 Experimental setup

The experimental setup for optical pump-probe measurements is an extension of the basic SHG setup (section 2.2.1). Two major differences exist: First, a femtosecond laser is used instead of a nanosecond laser to provide short pulses allowing for high temporal resolution. Second, the laser beam is split up into a pump beam and a probe beam. The probe beam corresponds to the measurement beam in the basic SHG setup. Due to the short pulse durations, an optical parametric amplifier (OPA) has to be used for its frequency conversion instead of an optical parametric oscillator (OPO). The pump beam is usually not frequency converted and has a fixed wavelength of 800 nm. Its time of arrival at the sample with respect to the probe beam can be adjusted by changing the length of its optical path via a delay line. This defines the time delay between excitation (pump) and measurement (probe). In the setup used, the beam path length can be varied by 4 m, corresponding to a maximal delay of 13 ns. A more detailed description of the setup can be found in reference [183].

The following type of measurement has been performed: The MnWO₄ *x*-cut sample is cooled into the AF2 phase, slightly below T_2 . Then the energy of the pump beam will drive the sample above the phase transition temperature. Afterwards, the multiferroic order should build up again, which can be measured with temporal resolution using χ_{yzz}^{ED} @ 2.72 eV. The *x*-cut was chosen for simplicity because it allows the use of a transversal field holder, which can be easily added to the setup to introduce the electric field.

Here we have to state that these experiments could not be performed successfully on MnWO₄. In the following we will discuss the reasons for this. A reader only interested in the dynamics of MnWO₄ may skip this section because no physical information on that topic can be obtained here. However, the reasons for the failure of the experiment shall be detailed, as that can give valuable insights into pump-probe measurements for other people willing to perform such experiments. Furthermore, we give indications how the experiment may be modified to work also on MnWO₄.

B.2 800 nm pumping

In pump-probe experiments, a magnetic order is usually destroyed within femtoseconds to picoseconds [184–187]. However, no time-dependence could be found in the SHG signal (figure B.1 (a)). For comparison and determination of $t = 0$ the same experiment was also performed on HoMnO₃. Here, the typical pump-probe signature is present. A rapid decay at $t = 0$ and a recovery of the signal afterwards (figure B.1 (b)). This proves that the experimental setup is working. Note, that the MnWO₄ measurement is already magnified by a factor of 10 with respect to the HoMnO₃. Albeit not relevant for the dynamics of the magnetic and electric order, we will nevertheless detail why no effect of the pump can be seen at $t=0$ because it illustrates valuable insights into pump-probe measurements and is useful knowledge for further experiments.

It is unreasonable to assume that couplings between electrons, spins and lattice in MnWO₄ are special in such a way that the energy deposited in the electronic system will not influence

the ferroelectric and magnetic order. Indeed, when looking at the SHG intensity for different pump energies, obviously the pump affects the material (figure B.1 (c)). Higher pump energies lead to lower SHG signals. This can be easily explained, when looking at the temperature dependence of the SHG signal (figure 3.4). Essentially the pump beam heats up the sample, which reduces the intensity. Note that the signal is reduced by 30% at 30 μJ pump energy. This is a large effect compared to the 3% fast decay at $t = 0$ in HoMnO_3 , which shows that the pump pulse in fact strongly affects MnWO_4 . But how can we explain that there is no change in signal after the arrival of the pump pulse? A simple test for the influence of the pump is to switch it off. Then the sample will cool down and the SHG intensity has to rise again from 70% to 100%. Figure B.1 (d) shows that the signal slowly rises over a time of more than one second, which corresponds to the time constant of cooling. In contrast, the intensity and thus the temperature in HoMnO_3 changes immediately after blocking the pump beam (figure B.1 (e)). The low cooling rate in MnWO_4 means that the actual energy in the sample is a moving average over many pulses. For a time constant of one second and a pump repetition rate of 500 Hz, this would mean an averaging over 500 pulses. The intensity difference between pumped and unpumped operation is a result of the accumulated energy of these pulses. Thus the intensity change by a single pulse is on the order of 1/500 of the total change¹. Converting this to measured units, it corresponds to a change in signal at the output of the gated integrator of 1 mV, which is only a little above the theoretical resolution limit of the ADC. More important, this is just a 0.1% change to the overall intensity, which is below the accuracy of the experiment. In summary, the low cooling rate leads to a strong averaging over the pump-pulses, so that the change induced by a single pulse is too small to be observable. The next section will explain, why the observed cooling rates in MnWO_4 and HoMnO_3 are so different and how that is related to the pump beam absorption.

B.3 Pump beam absorption

The pump beam is split off from the output of the regenerative amplifier. It is thus fixed to 800 nm (1.55 eV). Looking at linear-optical transmission spectra of MnWO_4 [188] this is not optimal because approximately half of the light is transmitted. At first sight, this seems not to be a big issue. The pump beam is very strong (several hundred micro joules per pulse). Therefore, one can adjust its intensity so that enough energy is deposited in the crystal. However, it turned out that, despite this, the experiment does not work because the energy cannot be removed fast enough. Because of absorption only SHG from the last part of the sample ($\approx 25 \mu\text{m}$) can leave the crystal (section 2.1.4). It is only this SHG emission region that is measured and that needs to be pumped. Therefore, most of the time pumping from the back is used (figure B.2 (a)). In the following we discuss the influence of the pump absorption length on the energy dissipation. The pump-pulse induces strong electronic excitations and non-equilibrium states on the femtosecond to picosecond timescale (see e.g. the three-temperature model [189]). For the longer timescales of energy dissipation we can safely assume that electrons, spins and lattice have equilibrated. Thus the temperature of each volume element is well defined and equivalent to the deposited energy. In a next step,

¹Actually it is a bit larger if one takes into account the decay of the energy of earlier pulses

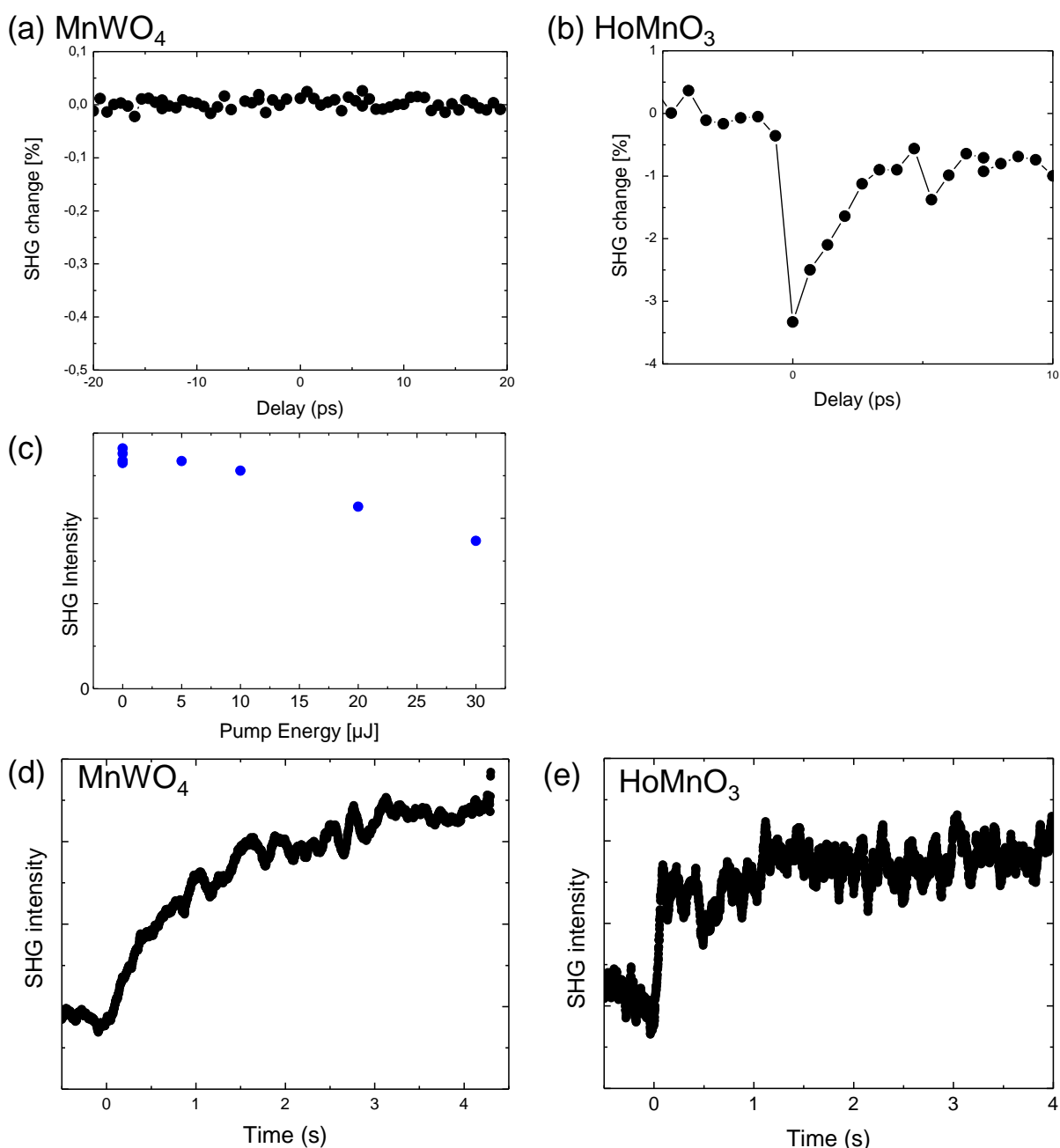


Figure B.1 – Pump probe measurements on MnWO₄ using a pump beam with a photon energy of 1.55 eV (800 nm).

(a) No time dependence can be found in MnWO₄ when pumping with 30 μJ.

(b) In contrast, a typical immediate decay and recovery within picoseconds is found in HoMnO₃ (same pump energy), which was used for comparison.

(c) Absolute SHG intensity in dependence on the pump energy. The pump clearly affects the sample. At higher pump energies, the sample becomes warmer, thus the SHG intensity decreases.

(d), (e) Simple time sequence with blocking the pump beam from at $t = 0$. The slow increase of intensity reflects a bad cooling of the SHG emission volume MnWO₄. HoMnO₃ immediately reacts to the closing of the pump beam. The bad cooling in the case of MnWO₄ leads to a strong averaging, so that the effect of a single pulse is below the detection threshold. This explains, why no time dependence could be seen in (a). The reason for the delayed cooling is detailed in section B.3.

B.4. 400 nm pumping

all volume elements of the sample will exchange energy by thermal conduction (internal equilibration). At the same time the sample transfers energy to the cooling helium gas, which surrounds it. But the time-scale of external cooling is much slower than the internal equilibration because of limited thermal coupling and the low heat capacity of helium gas.

The case of low to medium pump absorption (figure B.2 (b)) has two major disadvantages compared to a high pump absorption (figure B.2 (c)). To obtain comparable pump strength for a SHG pump-probe experiment, we have to adjust the pump strength such that the deposited energy in the SHG emission range is the same. At low absorption, the total amount of deposited energy is much higher. Because it eventually has to be cooled away externally by the helium, which provides a limited cooling capability, temperatures will be higher in the long run. Not only the total amount of deposited energy plays a role, but also its distribution. At low absorption the energy is distributed all over the crystal. Therefore, internal equilibration via heat conduction will not significantly change the temperature of the probed volume. Only the external cooling reduces the temperature in the SHG emission region. In contrast, mainly the SHG emission region is heated if the pump is strongly absorbed. Thus heat conduction will already transfer a significant part of the energy away from it. This will increase the cooling rate observed in SHG measurements. The unprobed part of the sample then serves as a temporal energy sink until the energy is finally cooled away from the sample. This additional mechanism may be especially helpful in optical pump-probe experiments because the available temporal delay is limited (13ns in our case).

Summarizing the above, a low to medium pump absorption leads to delayed cooling. In the case of 800 nm pumping MnWO_4 , the deposited energy is too large to be removed from the sample within the pump repetition period (2 ms). Different optimizations were performed to overcome this issue. First we increased the pump repetition period from 2 ms to 20 ms (or only 1 out of 20 laser pulses instead of 1 out of 2) by a modified chopper blade and an adjusted data analysis algorithm. This reduces the deposited energy by a factor of ten, or equivalently allows for a ten times longer relaxation time. But the statistics also goes down by the same factor. So, aside from technical issues, one cannot make the repetition period arbitrary long. Additionally, we reduced the pump and probe spot size and the pump energy. That way less energy is deposited and the unpumped sample area may serve as reservoir, similar to the bulk volume in the strong absorption case. Still these optimizations did not suffice to obtain a measurable signal.

Concludingly, we remark that it is strongly advised not to use a pump in the low or medium absorption regime.

B.4 400 nm pumping

As detailed above, 800 nm cannot be used as a pump energy in MnWO_4 . Therefore, the pump-beam was frequency doubled to 400 nm (3 eV) using a BBO crystal. At this wavelength MnWO_4 is strongly absorbing, so that the high pump absorption scenario from above applies. Thus the energy built-up issues do not occur and a temporal signature is expected.

As a technical complication, a strong background signal occurs when pumping with 400 nm.

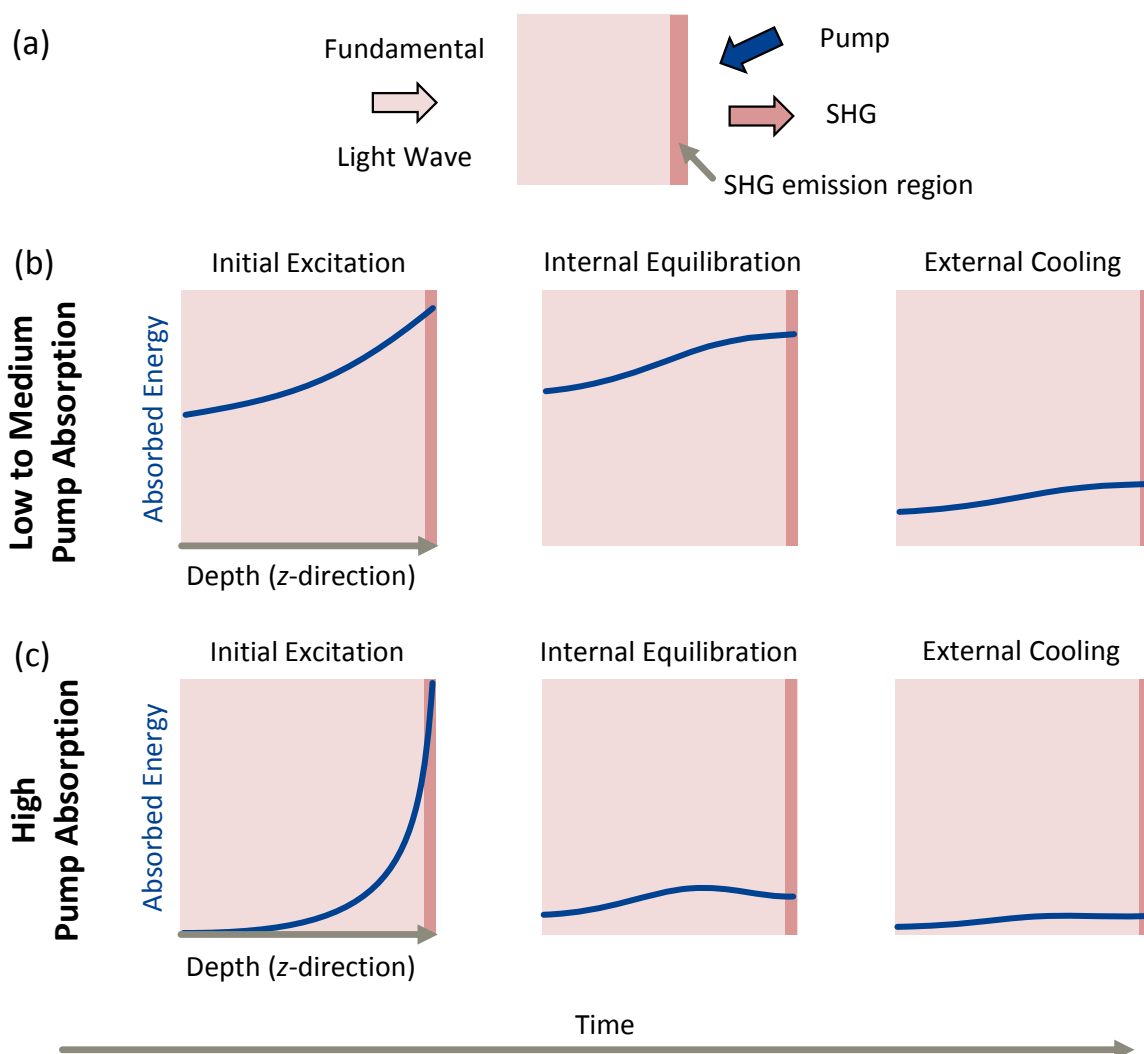


Figure B.2 – Influence of the absorption of the pump beam on energy dissipation from the SHG emission region. (a) Schematic pump-probe setup for transmission SHG experiments. SHG is often emitted only from a thin layer at the back of the sample (shaded area). Its size is limited by absorption at the SHG wavelength. Therefore, the sample is pumped from the back. (b), (c) Evolution of the absorbed energy (or equivalently temperature) for low to medium (b) and high (c) pump absorption. In a first step, the sample temperature equilibrates internally via heat conduction. The energy dissipation to the surrounding cooling helium takes much longer. Considering the energy dissipation away from the SHG emission region, a low to medium pump has two disadvantages. First, the total amount of energy deposited in the sample is much larger. At comparable external cooling efficiency this implies higher remaining energies on the long run. The difference is even more drastic in the short term. At a high pump absorption, a large part of the total absorbed energy is deposited in the SHG emission region. Thus already the internal equilibration significantly reduces the energy in probed region.

Figure B.3 (a) shows the spectrum of this pump-background. Also indicated are the SHG energies for possible tensor components. At χ_{yzz}^{ED} @ 2.72 eV the background is very intense, so that it is preferable to switch to χ_{yyy}^{ED} @ 2.19 eV. Still here, the background is non-negligible. Its final origin could not be determined, but the tests performed hint at luminescence from the sample itself. A number of optimizations were performed to reduce its size. This includes the polarization direction of the pump, prefiltering the pump with an interference filter, and optimization of pump angle as well as monochromator entrance slits slit. Spectral filtering was performed by adjusting the monochromator exit slit, albeit this cannot remove the background completely because it is also present exactly at the SHG energies. Temporal filtering is limited to the maximal delay (13 ns) because the gate has to be open for the complete delay time. It can only cut off longer lasting decays of the background signal. The combined effect of the above optimizations reduces the background to approximately the size of the SHG signal. Still, this is not sufficient because in the pump-probe experiments, we need to detect changes of the SHG signal in the low percent regime. Therefore, additional data processing was performed: The pump background I_{back} is numerically subtracted, using the difference between I_{on} and I_{off} at $t = -400$ ps as an estimate. Because here the probe pulse arrives earlier than the pump pulse, the pump pulse cannot directly influence the SHG signal. All differences have to originate from the background. This value is subtracted as an offset from the pump-on data points. Only after this correction, the usual normalized difference is calculated. This leads to a modified formula for the relative changes:

$$r = \frac{(I_{\text{on}} - I_{\text{back}}) - I_{\text{off}}}{I_{\text{off}}}$$

Figure B.3 (b) shows the final results. The precision is limited because the value results from the difference of two large signals, including the assumption of a constant background. To improve the experimental precision averaging over 30 to 50 measurement cycles has been used for the data presented. Anyway a clear trend can be observed. The SHG intensity decays with a time constant larger than the available delay of 13 ns. This implies a lack of magnon emission from the photo-excited electrons and an extremely weak thermal contact between spins and lattice [190], which would be very unusual. Within the accessible delay range (13 ns) the investigated sub-systems are still in the process of heating up, i.e. destruction of the order. It is thus not possible to observe the recovery of the order.

Because of the unusual slow decay, experiment and analysis have been intensely checked for possible systematic errors that would yield such an effect, but none could be found. The decay becomes more pronounced, when the pump intensity is increased. This is consistent with the picture of pump energy heating up the sample and thus reducing SHG intensity. On the other hand it proves that it is not a simple consequence of the background. A stronger pump background would increase I_{on} and thus would cause exactly the reverse effect.

One last possibility for optical pump-probe experiments on MnWO_4 would be to vary the photon energy of the pump pulse. Instead of using 400 nm, it should be possible to tune it to an excitation of electron levels that are directly involved in the magnetic exchange. Here, a much faster response to the pump is expected. Experimentally this implies the use of a second OPA for the pump beam, which was not freely available during the time of the experiment.

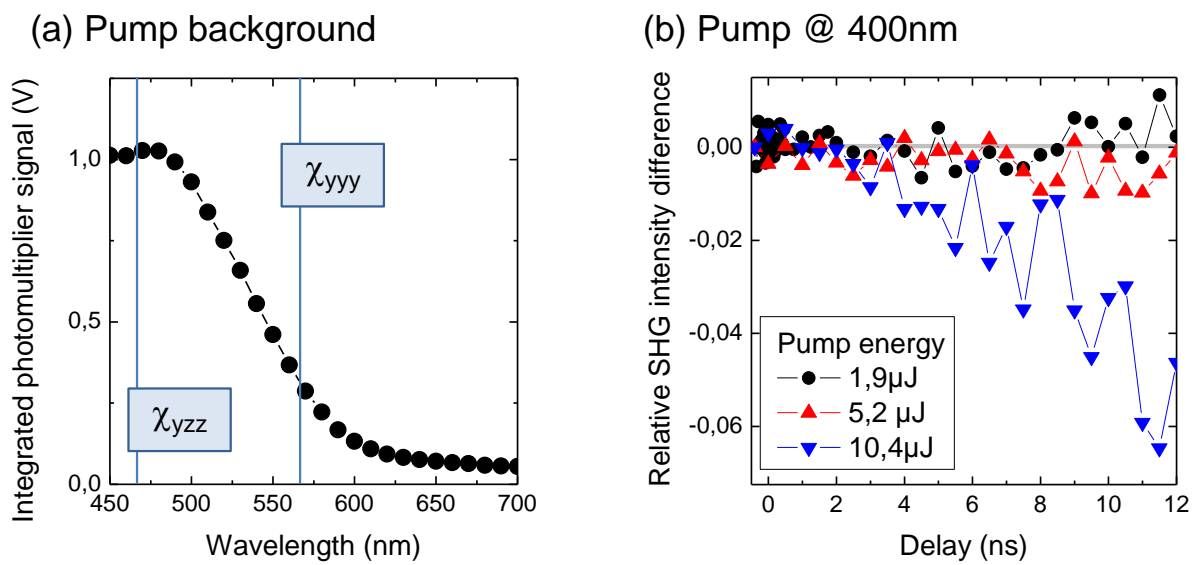


Figure B.3 – (a) Spectrum of the background signal from the frequency-doubled pump beam (400 nm). The probe is blocked in this measurement. The width of the signal is much broader than the spectral width of the laser, hinting a luminescence. The two possible SHG tensors with their energy are also indicated. At χ_{yyy}^{ED} @ 2.19 eV the background is less intense. Therefore, this tensor component was chosen for the pump-probe measurements at 400 nm.

(b) Pump-probe measurements on MnWO_4 pumping at 400 nm.

Appendix C

MnWO₄ thin film

Thin films add degrees of freedom to the material. Their properties may vary with their thickness and can be tailored using strain. Furthermore, the distance between electrodes is significantly reduced. On the one hand, this allows to generate sufficiently large electric fields for magnetoelectric switching with a voltage on the order of 1 V, instead of 1 kV like in the case of bulk materials. Furthermore, this allows to apply significantly higher electric fields, which can reduce the switching time. This motivated the investigation of a MnWO₄ thin film.

The sample was grown at University California Berkeley (Dr. D. Meier, CONCEPT Research Group). A MnWO₄ film with a thickness between 20 nm and 40 nm was deposited on a NdScO₃ substrate. The *b*-axis is out of plane. Afterwards the back side of the substrate was polished in Bonn to allow transmission measurements. A second bare NdScO₃ substrate is used as reference.

Experimental details

Because of the low thickness of a thin film, there is only little active volume in the sample. Therefore, high laser intensities are necessary to obtain measurable signals, which requires the use of a femtosecond laser. The actual experimental setup is a standard SHG transmission setup. The transmission of the bare NdScO₃ substrate is at most 60% (figure C.1). If the intensity profile was flat, one would orient the sample, so that the film is directed towards the laser. This would yield higher SHG signals. In this orientation only the SHG is absorbed, while with the film on the rear side, the fundamental is damped. Since the latter occurs quadratically in the SHG intensity, this implies lower signals. However, there is a strong oscillation of the transmission in the visible range. Correspondingly some SHG signals may not be measurable, and in general the SHG spectrum would be strongly distorted. In contrast the transmission is flat in the typical wavelength range of the fundamental beam (1.53 - 2.22 eV (Signal) and 2.22 - 2.88 eV (Second Harmonic Idler)). Therefore, the film is oriented to the back in the experiments. Here we trade in 40% intensity loss for a non-distorted spectrum.

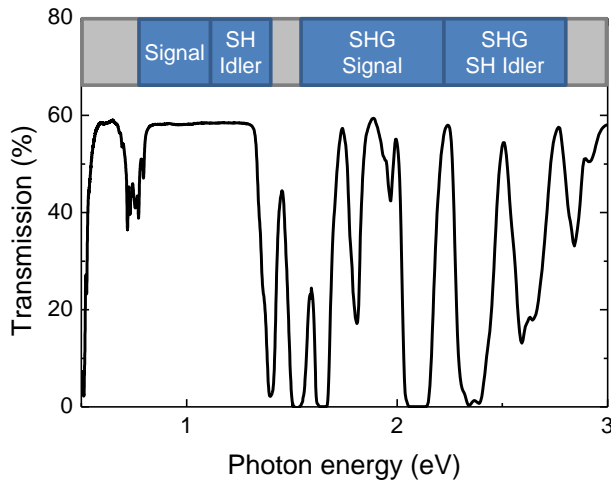


Figure C.1 – Transmission spectrum of the NdScO_3 substrate. The transmission curve is flat in the region of the fundamental beam (Signal and Second Harmonic Idler). It strongly oscillates at the SHG wavelengths. Therefore, the film is oriented towards the detection part of the setup to ensure a non-distorted spectrum.

SHG Spectra

The polarization in the film is out-of-plane. This corresponds to a MnWO_4 y -cut. Since the in-plane orientation of the sample is not known, a full set of polarizer/analyzer settings is used to measure all possible tensor components. Also the thin film may lead to a shift of electronic levels and thus a modified SHG spectrum. Therefore, spectra were obtained in the signal range (1.53 - 2.22 eV) and in the SH Idler range (2.22 - 2.80 eV). The NdScO_3 substrate itself produces a sizable SHG signal itself. Comparing to the measurements with the MnWO_4 thin film on the substrate, only slight differences can be observed. Moreover, there is no temperature dependence for the thin film in the range between 10 K and 20 K. From bulk MnWO_4 we would expect additional signals to appear at the ordering temperatures $T_{N3} = 13.5$ K and $T_{N2} = 12.7$ K. Since no such changes could be observed, it is questionable if any of the observed signals stem from MWO. It may be that all of them are related to the substrate. This could imply that the spin spiral is not present in the thin film, or is at least not incommensurate. Remember that the only signal for $k \parallel y$ was $\chi_{x'z'z'}^{\text{ED}}$, which arises due to the incommensurability of the spin spiral (section 3.1.6).

To access other tensor components, the sample was rotated by 30° from normal incidence. Also here, a complete set of spectra and polarization dependencies was obtained. Figure C.2 (a) shows such a spectrum¹. The spectrum is independent of the temperature in the range 4.3 K to 20 K, implying that it does not contain a signal coupling to a ferroic order. The peak at 2.32 eV vanishes when heating the sample to 100 K. In principle this temperature dependence could be a sign of a ferroic order. In comparison with a pure NdScO_3 substrate it turns out that also the substrate exhibits a temperature dependence (figure C.2 (b)). From the different scaling we conclude that part of the signal is related to the MnWO_4 film and part is related to the substrate. However field cooling did not show any influence on the MnWO_4 part of the signal (not shown). Therefore, it is questionable if this signal is related to a ferroic order of the film.

¹Since the in-plane orientation is not known, it is unclear if the rotation axis is x or z . Therefore, it is also not possible to determine the measured tensor component. The incident light was polarized along the rotation axis, the detected SHG was polarized perpendicular to it.

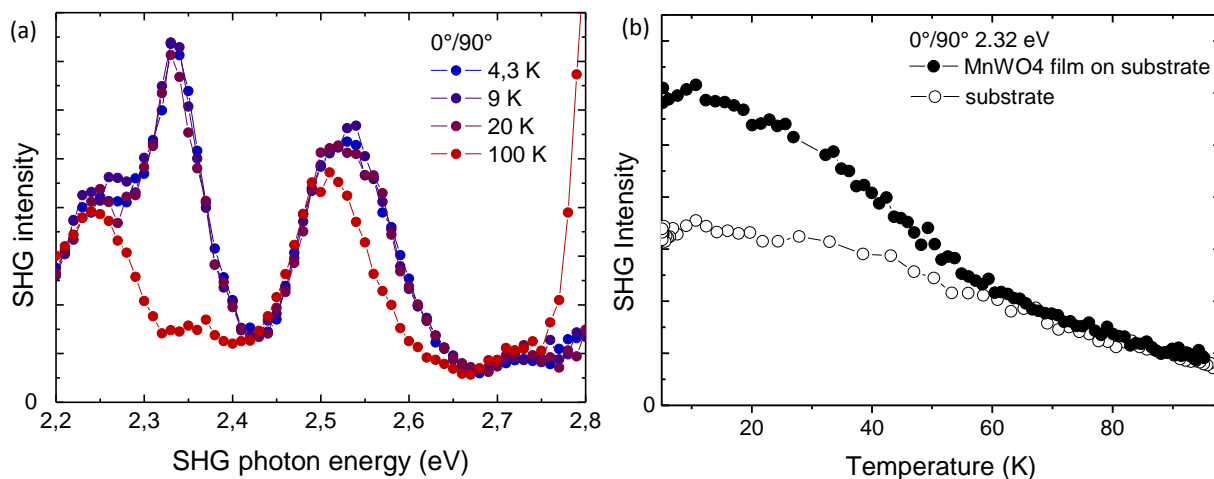


Figure C.2 – (a) Spectrum of the MnWO_4 thin film, which is rotated by 30° from normal incidence. The spectrum is temperature independent between 4.3 K and 20 K. However, at 100 K the peak around 2.32 eV vanishes. (b) shows the temperature dependence of the signal at that peak. The same signal from a pure NdScO_3 substrate is given for comparison. Part of the temperature dependence results from the substrate, but the film starts generating additional SHG below 60 K.

In summary, the MnWO_4 film produces SHG signals, but precise detection and analysis of the signals is hampered by the background from the NdScO_3 substrate. The disadvantage of transmission is that the fundamental passes much more substrate than film. Consequently, substrate signals are much more enhanced. This could be remedied in a reflection setup. Alternatively other substrates may be used.

Appendix D

Developed software

As part of his work, significant effort was put in the development of software tools which enhance measurement and data analysis capabilities. Section D.1 describes three tools for image conversion and processing of SHG images. `mpsConvert` and `csv2tif` are two command line programs that convert images acquired using *MAPS* or *Symphony*, respectively. *SIV* is a program for interactive, scaling and analysis of SHG images. While being extremely useful, in their scope, these tools are rather small and contain only a few hundred lines of code. Most development work has been invested into the measurement program *Infinity* (section D.2). This program is able to control more than 25 different devices in the labs and is used at all six laser workplaces. It is designed to allow automated measurement of almost every type of SHG-related measurement.

All source code and released versions are maintained in a version control system (SVN).

D.1 Image handling

Two types of liquid-nitrogen cooled CCD cameras were used for SHG imaging. The *Photometrics* CH270 camera, is controlled by the commercial software *MAPS* 2.0, which stores images in a proprietary format (*.mps). For the *Symphony* cameras by *Horiba Jobin-Yvon* a custom control program was written in LabView [191]. Both have proprietary output formats that have to be converted to standard image formats for display and further analysis.

D.1.1 mpsConvert

The program *MAPS* stores images from the camera in a proprietary file format (*.mps). The details of the format are documented in the manual [192]. A mps-file contains one or more images encoded in 16-bit gray scale plus additional meta information like exposure time and binning. An image viewing and conversion tool called *LightView* is shipped together with *MAPS*. However, due to its age it has a number of shortcomings. First, it does not run on Windows 7 any more. Also it is not designed to manipulate many images. There are no

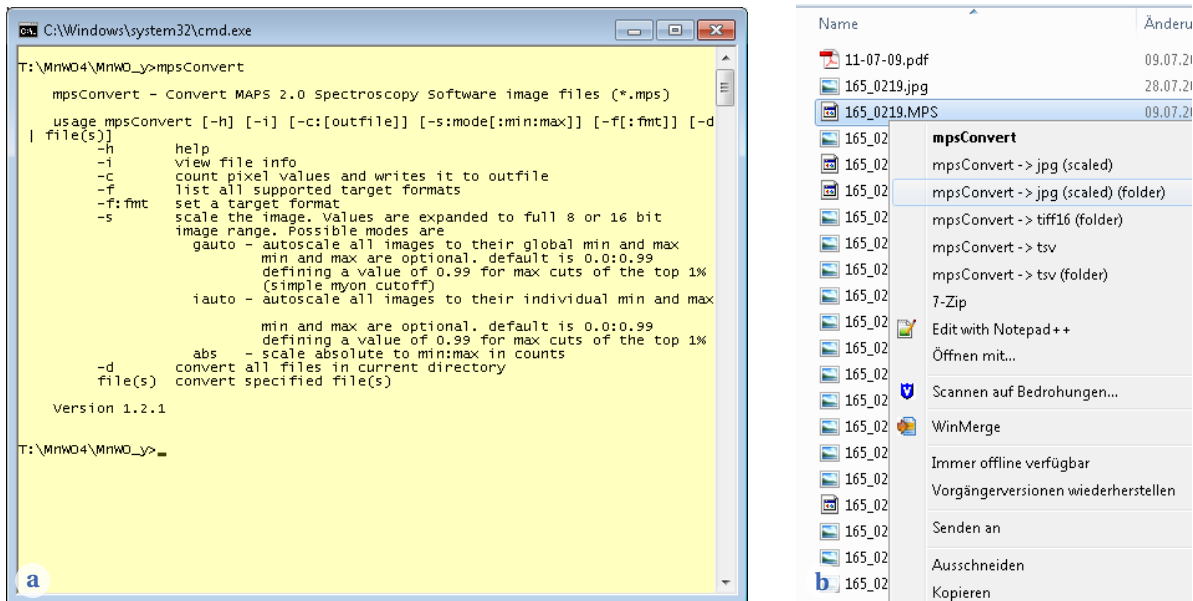


Figure D.1 – The two possible modes for the operation of `mpsConvert` for the conversion of MAPS image files.
 (a) Directly calling from the command line gives full access to all capabilities of the program
 (b) The `mpsConvert` Explorer integration allows to quickly apply the most common operations on individual files or a complete folder.

batch capabilities. Every image has to be opened separately, scaled manually and can then be exported to 16-bit TIFF for further processing in other tools like *Adobe Photoshop* or *Wolfram Mathematica*. Even when opening a mps-file with a sequence of images, only one image out of that sequence can be opened at a time.

The above issues made it necessary to develop a more efficient conversion tool. This tool, named *mpsConvert* (or *mps2tif* in earlier versions), is command line based (see figure D.1a). For rapid development it was written in Python (v. 2.7) and makes use of the Python Image Library (PIL) [193]. A windows executable is generated from the python script using py2exe [194], so Python and the Python Image Library do not have to be installed on every PC, on which the program should be used. Furthermore, a setup script integrates some of the most used features into the Windows Explorer context menu for easy access (figure D.1b). However, the full set of features is only available via the command line.

The target file formats for conversion include 16-bit TIFF, CSV, TSV, and JPG image file formats, as well as a histogram data file. Note that in the JPG format information is lost. First, it does not support 16-bit gray scale, so the data are converted down to 8-bit. This step already includes a scaling. Second, JPG uses a lossy compression algorithm. Therefore, it is not suited for further data analysis. The advantage of JPG over 16-bit TIFF is that it is widely used. Its main use is the easy integration into presentations or documentations and the possibility to quickly browse the images in standard images viewers.

Further features include extraction of some of the meta data like track position, binning and exposure time. For a sequence of images, the total intensity of each image can be extracted and directly written to a data file. This allows to easily plot the intensity of an image sequence.

Finally, a number of different scaling options are available. The details and use-cases of the different variants is described in the following section.

SHG image scaling

Scaling is very important for SHG images. Typically, the exposure time is chosen so that a photon count on the order of 100 counts/pixel is achieved in the bright areas. This yields a sufficiently good signal-to-noise ratio and contrast. However, only below one percent of the 16-bit dynamic range is actually used in that case. When viewing such an image unscaled it would look essentially black everywhere. Furthermore if one wants to perform more advanced image processing operations on an image, using the full dynamic range is advantageous. Finally a reasonable conversion to 8-bit formats like JPG requires a scaling because a simple cut-off at a pixel count of 255 can distort the data significantly.

`mpsConvert` provides a scaling mechanism, in which a selectable range [min...max] is linearly scaled to the range of the target format, i.e. [0...255] for 8-bit and [0...65535] for 16-bit. Manually finding good min and max values is cumbersome and simply automatically choosing global minima and maxima does not work well due to background signals from cosmic myons. From time to time cosmic myons will hit the CCD chip and create free electrons in a small region (a few pixels). These electrons are equivalent to a photon count of a few thousands up to some ten-thousands. Therefore, myons manifests in the image as very bright spots. Because their intensity is one to two orders of magnitude larger than the usual SHG pixel count, a simple global scaling approach fails. If one would just scale the minimum and maximum intensities of an image to the full 8-bit or 16-bit range, still most of the real SHG data would only be in the very lower part. The data would still look black. A scaling approach is needed that neglects the myons.

Essentially we should just calculate the maximum over all pixels that are not affected by myons. Real myon detection is in principle possible, but would require advanced image detection methods. A much simpler approach is chosen here. Because the myons are very localized, they will only affect a small number of pixels. If there are for example five myons in an image, with an area of 10 pixels per myon, then this is just a fraction of $\alpha = 0.02\%$ on a chip with the size of 1024×256 pixels. Furthermore, myon create usually a higher signal per pixel than the SHG photons. They will thus lie at the highest intensities in a histogram (figure D.2). It is possible to remove them by introducing a cut-off intensity, which corresponds to the highest SHG intensity in the image. This cut-off equals an $(1-\alpha)$ quantile, where α is the fraction of the image, that is covered by myons. Determining α exactly would again require a pixel based myon detection. But the advantage is that α can be roughly estimated by a typical number of myons per image and their typical pixel area (see above). If α is too small, some myons will be included in the $1 - \alpha$ quantile, which directly results in bad scaling. On the other hand with α a bit too large, some of the SHG signal will be outside of the quantile and will be cut as well. However, usually significant area fractions of the CCD contain approximately equally sized SHG intensities. The cut-off intensity will only weakly depend on α in that case, which will only introduce a minor error. Consequently α should be chosen rather a bit larger than too small. Usually values of $1 - \alpha = 0.99 \dots 0.999$ give reasonable results. Optionally also a lower

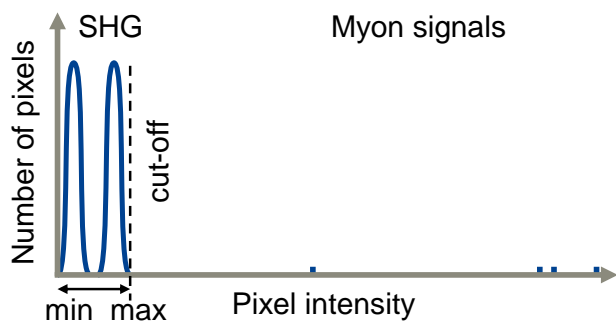


Figure D.2 – Schematic illustration of typical histogram for SHG images. The SHG signal typically has a low intensity, but it spreads across the whole image region, resulting in a high number of pixels. The actual distribution may vary, exemplary depicted is a double peak, which can result from a pattern of bright and dark domains. In contrast, the myons are very localized (low number of pixels), but have high intensities. The optimal scaling range [min...max] for the image intensity ends just above the largest SHG intensity value. The value of max can be reasonably well determined by an $(1 - \alpha)$ quantile.

cut-off may be specified, e.g. to account for low-intensity background or for images taken without bias subtraction.

Additionally, one can choose if the scaling parameters should be determined globally or individually for every image. An individual determination will give the best results for each image. But the images are not comparable any more because each image is scaled differently. This is undesirable for an image sequence, like a domain evolution during switching. Alternatively, the global scaling uses the maximum of the $(1 - \alpha)$ quantiles of all images fed to the program. This yields the best scaling under the constraint that all images should be scaled equally.

D.1.2 csv2tif

The control program for the *Symphony* camera [191] saves images only in a CSV format. A conversion to 16-bit TIFF is necessary for further analysis and viewing of the images.

Like `mpsConvert`, the program `csv2tif` is written in Python. The usage via command line or Explorer context menu is analogous to that of `mpsConvert`, with the restriction that `csv2tif` can only convert to 16-bit TIFF and does not provide any advanced functionalities like scaling or integrated intensities.

A specialty of the *Symphony* output format is that while being 16 bit, the pixel values are not necessarily $0 \dots 65535$. Because of an internal background subtraction, the range can be $x \dots 65535 + x$, where x may be positive or negative and is unknown. It changes every time a new offset image is taken, which happens at every single image acquisition and at every start of a measurement sequence that is controlled by the measurement program *Infinity*. `csv2tif` allows only for a direct conversion without scaling, therefore 0 is the lowest valid pixel value. Lower values may automatically be adjusted to 0. This introduces only a minor error if the offset image is valid (e.g. they should not contain a myon). More detailed scaling is possible using SIV (see the following section).

D.1. Image handling

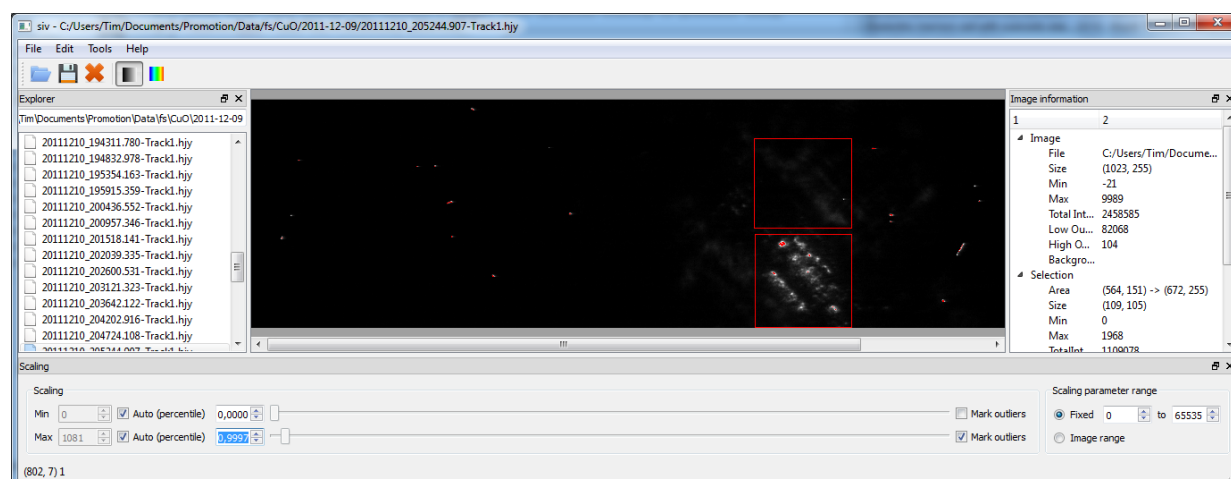


Figure D.3 – User interface of the Symphony Image Viewer (SIV).

Images can be selected in the Explorer view on the left. Two selections are set (red rectangles). Their corresponding parameters can be read on the information panel on the right. Scaling is adjusted via the bottom controls. Currently the automatic quantile-scaling is active and the high-intensity outliers are marked (red dots). Note that they correspond to the myons in the image.

D.1.3 SIV

As discussed in section D.1.1, a good automatic scaling is difficult to achieve due to the myon signals. While the quantile-based scaling discussed there gives reasonably good results, the choice of the quantile α is not optimal in general. This could be improved by a direct visual feedback. However, even advanced image processing tools like *Adobe Photoshop* do not directly allow this. Furthermore, one often needs to determine the intensity of certain specific pixel or that of a specific area on the image. It became apparent that this couldn't be achieved using the command line tools described above. Therefore, I started the development of SIV, the *Symphony Image Viewer*, which provides a user interface for the handling of image files. SIV is in an early development stage. While being fully functional, the number of features currently implemented is limited. Images can be load via the menu or most easily via the Explorer-like file system view. The scaling can be set manually or using the quantile-based scaling described above (section D.1.1). Top and bottom outliers of the scaling can be directly marked on the image to see which pixels are really cut-off by the scaling. All changes are directly applied to the image, so that the user can easily optimize the scaling parameters. While browsing through the files, the scaling method and parameters are kept. Using the quantile-based scaling then results in best scaling per image, while the fixed scaling maintains direct comparability of the intensities. Furthermore it is possible to select a background image, which is subtracted from the viewed image and thus allows removal of background signals that cannot be filtered out in the experiment itself.

Furthermore, one can select regions in an image and measure their minimum and maximum pixel intensities and the integral intensity. Limitations currently include the lack of 16-bit TIFF export and missing batch capabilities. Some further improvements could be the generation of intensity profiles of an image, creation of intensity plots of an image sequence or thresholding for the determination of the domain area fractions. Also it might be advisable to implement

the loading of mps files. With these improvements, SIV could finally replace `mpsConvert` and `csv2tif`, uniting all conversion and image analysis capabilities in one tool.

SIV is written in C++ using the Qt libraries by Nokia [195]. Higher requirements on computation speed for the live view of changes motivated choice for C++ instead of Python. QtCreator was used as an integrated development environment and mingw as C++ compiler. Both are contained in the Qt SDK (software development kit). The present version of SIV uses a custom image implementation (see classes `SHGImage` and `SHGImageWidget`). However, should the software be developed further, I would suggest to replace this and base all image processing on the Open Source Computer Vision Library *OpenCV* [196].

D.2 Measurement program – Infinity

Automated measurements are a key requirement for fast and reliable data acquisition. For that purpose a measurement program called *Infinity* exists, which controls the devices in the experimental setup and enables automated acquisition of measurements. The roots of *Infinity* date back to the late 1990s. Over time it was extended by adding more and more functions. However, started as a small control application, its design did not hold proper structures for managing the increased complexity. Furthermore, today's increased computing power and memory allows for more flexible data handling.

This made a general overhaul necessary. Since completely rewriting from scratch would take significant time in which neither the old program was improved or adapted to new needs nor the new program would be fully functional, it was decided to gradually rewrite the program. The advantage was that programming time could be flexibly spend as needed and the users directly benefited from improvements. On the down side, a few limitations imposed by the old program structure are still present.

Primary goals in the redesign process were:

Usability: The program is designed to be used intuitively, so that the user does not have to know any details of the program structure or any hardware interface to a controlled device. This leaves room for focusing on the physics instead of having to think about technicals aspects of the measurement. Furthermore, it allows new users to quickly learn the program and make full use of its capabilities without a long learning period. A good usability includes abstractions from the technical details and prompt feedback on the state of the program.

Flexibility: Ideally, the user should be able to run any measurement he can think of with the devices or device combinations available. The measurements performed should not be limited by a lack of capabilities of the program. Instead, it should enable the user to perform the type of measurement which he deems most appropriate for the situation.

Stability: The program should not crash or hang under any circumstances. This includes prevention or graceful handling of invalid user input as well as recovery from failing communication with connected hardware devices.

Maintainability: The program should be easy to maintain and extend. This is achieved by proper abstraction layers, modularization and the definition of interfaces between the modules. It ensures that the program can be easily adapted to changing needs like new devices or measurement modes.

The name *Infinity* goes back to the first laser system at which the program was used. Today, the name may stand for the unlimited measurement and control functionality which the program offers. In the present state, the program is able to control more than 25 different devices, including:

- Different optical parametric oscillators (OPOs) and optical parametric amplifiers (OPAs)
- Polarization optics
- Different high-voltage sources
- Magnetic field control
- Different temperature controllers for cryostats
- Different electronic delay generators
- CCD cameras for integral measurements as well as for image sequences
- Different monochromators
- Analog digital converter (NI-DAQ PCI-6221)
- Various linear stages used for optical delays in pump-probe measurement
- A motorized filter wheel including feedback measurement for intensity adjustment

Program features include among others:

- Easy to setup standard measurement ranges, but with the option to completely customize the data points to measure
- Simultaneous measurement of multiple configurations with flexible settings
- Multi-cycle measurements with included statistics for improved signals
- Live display of measured data and progress indicator
- Live data analysis to monitor derived quantities during a measurement
- Myon signal detection for CCD cameras (integral and track-based)
- Shot control: synchronization of laser and camera shutter (currently only for the laser Coherent Infinity)

- Automatic PDF report generation
- A measurement explorer to browse previous measurements
- Email notification mechanism for finished measurements and in case of errors

Program structure

The program is developed in C using the framework *LabWindows CVI* from *National Instruments*, which provides a library with useful functions for measurement and control applications, GUI support and an integrated development environment (IDE).

Figure D.4 shows the basic structure of the program. The modularization and installation of defined interfaces between separate parts of the program is a key requirement for the flexibility and maintainability of the program. Here, the device manager plays a central role. It decouples all hardware devices from the main user interface, from the measurement control logic and from each other. Upon startup each device announces its capabilities to the device manager and provides a set of functions (as function pointers) which allow the device manager to control it. The device logic mediates between the abstracted device interface and the actual hardware interfaces, which is used to control the physical device. Optionally a device can have an own GUI window for advanced settings and status feedback. For the control logic of a device there are two paths to interact with the rest of the program. It may address other devices via the device manager (e.g. the intensity control may close a shutter to the experiment before moving the filter wheel). Furthermore it can write its measurement data into *Channels*, which it has created upon initialization. For example a camera may provide one channel for every track. Aside from writing, the device can read all the channels from the other devices. So the filter wheel may access information of a reference detector which is connected to the analog digital converter. This design allows to add new devices without the need to adapt existing code.

The standard program flow in a measurement is as follows. The measurement control loop informs the data storage unit about the next data point to measure. After adjusting all required devices to the desired settings via calls to the device manager, it sends readout commands to all data acquisition devices. They acquire the desired data and write them to their channels. When readout is finished the control loop tells the data storage unit to read all data from the channels and persistently store them. This scheme is repeated for every data point. At the end of a measurement the report engine is called.

Modularization between the program components is achieved by using separate header and include files for every program component, while dependencies between the modules are reduced as far as possible. For better overview, all functions of a module start with a common prefix (e.g. `dev_` for the device manager). The use of global variables is deprecated. Instead, data should be sent or received between modules via their functions. Some modules, including the channels and the measurement data storage, are implemented using a pseudo-object-oriented scheme to encapsulate the data. A function `obj_Create()` instantiates an object and yields either a direct pointer to the data structure or a handle. This one is passed

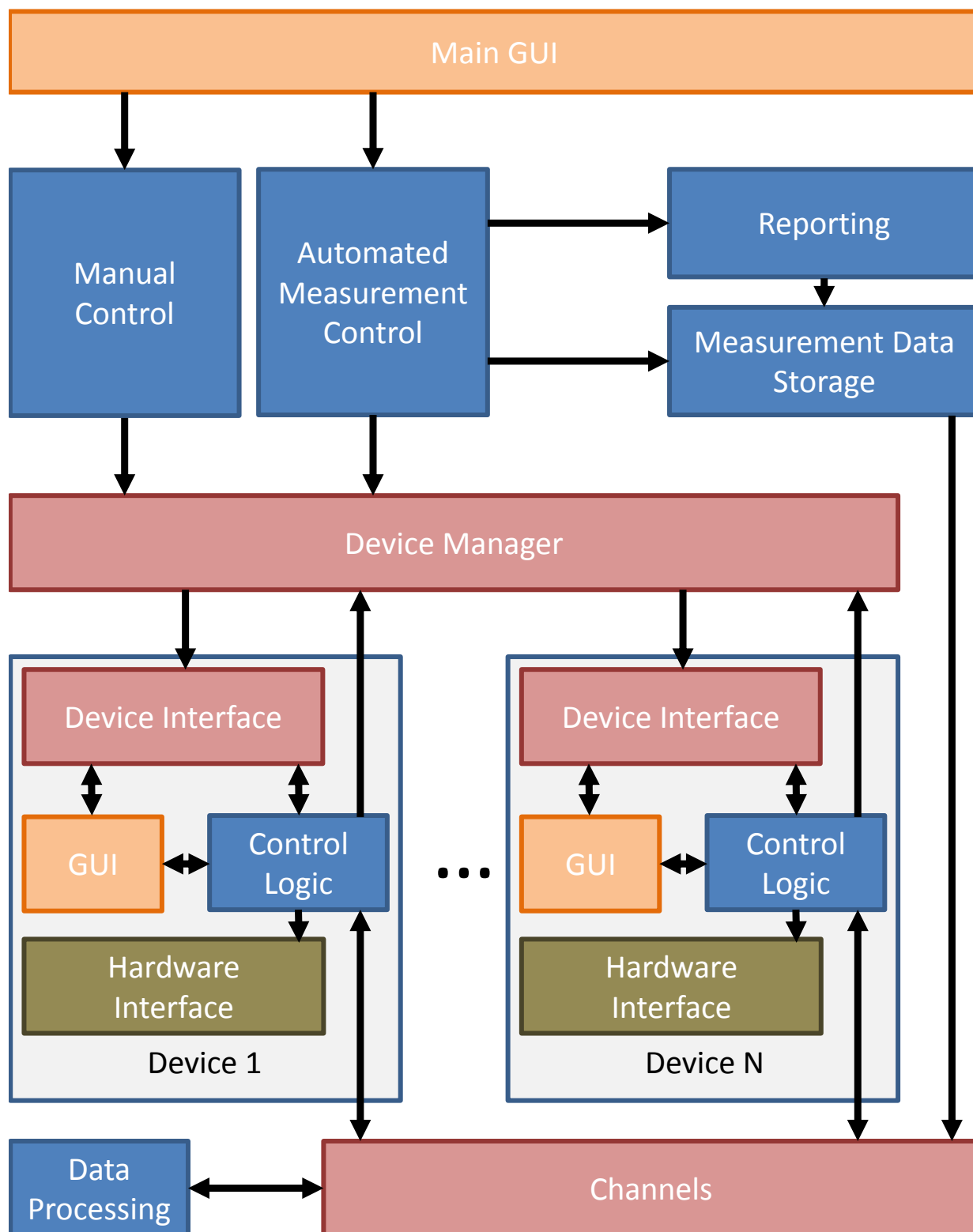


Figure D.4 – Simplified schematic program structure of the measurement program *Infinity*. Standardized APIs and interfaces guarantee a decoupling of different program components. This significantly improves maintainability and extendability. Arrows indicate communication paths. See text for details.

as first argument to all functions that operate on the object. After usage, the object has to be cleaned up by a corresponding call to `obj_Free()`.

Step-by-step guide to implement a new device

In a nutshell, the following steps are required to implement a new device:

1. Create a new module (source file and header file)
2. Implement the device functionality and in particular a function `mydev_GetInterface(DeviceInterface *devif)` which provides all necessary information for the device manager. See documentation in `devices.h` for details.
3. Assign a device ID in `devices.h`
4. Include the device header file in `devices.c` and register the device interface in `dev_Init()` using `dev_Register()`.
5. Optionally create basic GUI controls for the device on the main window
6. Optionally create a separate GUI window for the devices (You may use the *property*-framework for easier passing of parameters and status information between the device control and the window).
7. Optionally create a dedicated measurement mode for the devices in `measparams.h`.

It is not possible to document every aspect of *Infinity* here. Many functions are documented in the source-code if necessary. In particular for the device implementation, existing devices may be used as templates and can help to understand how the program works.

Appendix E

List of measurements

In the description of measurements we focused on the most important parameters only. A complete description of all experimental details would be too long and distract from the central information. However, it may sometimes be important to know exactly how a measurement was performed. The following table lists dates and data sets for all measurements presented in this work. All details can be obtained from the corresponding measurement protocols¹. For domain images there are usually more pictures available than could be shown here. Especially for the measurements on the evolution of domain patterns, detailed image sequences have been obtained and converted to videos. These additional data can also be found in the archive.

Table E.1 – List of measurements presented in this work and corresponding data files.

Figure	Data Files	Date
4.3	mwo_y15o.mps, mwo_y15p.mps, mwo_y15t.mps, mwo_y15u.mps	21.10.2009
4.4	mwo_y15y.mps mwo_y15t.mps	21.10.2009
4.5	165_0078, 165_0079, Nr011	21.06.2011
4.6	165_0077, 165_0078	21.06.2011
4.7 (a)	mwoy1048.mps, image 0040	09.02.2010
4.7 (b)	mwoy1058.mps	09.10.2010
4.7 (c)	B.tif	13.02.2009
4.9 (a)	MWOY1042.mps, images 0008, 0010, 0011, 0012	01.02.2010
4.9 (b)	165_0012.mps	16.09.2010
4.10 (a)-(d)	MWO_y15y.mps, MWO_y16b.mps, MWO_y16f.mps, MWO_y16h.mps	21.10.2009
4.10 (e)	Nr003	21.09.2010
4.10 (f)-(i)	MWO_y16m.mps, MWO_y16o.mps, MWO_y16q.mps, MWO_y16s.mps	21.10.2009

¹The raw data and measurement protocols are archived in the workgroup (currently www.ferroic.mat.ethz.ch)

4.11	Nr006, MWOX_012.mps, intensities extracted from images	25.10.2010
4.13 (a)	Nr004 - Nr007, Nr011, Nr016 - Nr019	27.08.2009
4.13 (b)	Nr004 - Nr007, Nr011, Nr016 - Nr019	27.08.2009
	Nr005, Nr007	18.04.2011
	Nr006, Nr008, Nr010, Nr012	16.06.2011
	Nr007, Nr009, Nr013, Nr015, Nr017, Nr021, Nr023	02.07.2011
4.14 (a), (b)	165_0210.mps (images 0038 and 0060)	08.07.2011
4.14 (c)	165_0220.mps	09.07.2011
4.15	Nr022	21.09.2010
4.16 (a)	Nr003	29.10.2010
4.16 (b)	Nr012	14.12.2010
4.16 (c)	Nr008	15.04.2011
4.17	165_0011.mps - 165_0013.mps	16.09.2010
4.17	MWOX_041.mps (images 0006, 0010, 0014, 0018, 0022)	29.10.2010
4.19	MWOX_041.mps (images 0013 - 0020)	29.10.2010
	165_0049.mps (images 0015 - 0019)	30.04.2011
4.20	MWOX_040.mps (images 0003, 0004, 0005, 0014)	29.10.2010
4.21	Nr015 - Nr030	15.04.2011
4.22	Nr021, Nr022	04.07.2011
4.23	165_0185.mps (images 0005, 0008, 0015 and 0022)	15.04.2011
4.24	165_0113.mps (images 0000, 0002, and 0006)	28.06.2011
4.25	165_0091.mps	21.06.2011
4.26 (a), (b)	Nr006, - Nr011	06.07.2010
4.26 (c)	MWOY1047.mps (images 0018, 0025, 0029, 0031)	02.03.2010
5.1	Nr012 - Nr015, Nr032, Nr033, Nr036	16.11.2009
	Nr013, Nr014	17.11.2009
5.2	Nr031	16.11.2009
5.3	CuO_0035.mps	10.11.2009
5.4	20111213_16....hgy	12.12.2011
A.1 (a)-(c)	Nr005, Nr007, Nr008, Nr003, Nr004	15.09.2010
A.2	Nr012 - Nr024	15.09.2010
A.3	Nr001 - Nr009	07.07.2010
A.4	Nr006, Nr007	08.07.2010
B.1 (a)	Nr010, Nr011	04.08.2011
B.1 (b)	Nr011	01.08.2011
B.1 (c)	Nr009	02.08.2011
B.1 (d), (e)	sample heating by pump beam2.opj	04.08.2011
B.3 (a)	Nr003	15.08.2011
B.3 (b)	Nr009, Nr022, Nr024	16.08.2011
C.2 (a)	Nr003, Nr006, Nr007	29.11.2011
	Nr002	30.11.2011
C.2 (b)	Nr014	17.11.2011

Bibliography

- [1] H. Ishiwara, M. Okuyama, and Y. Arimoto. *Ferroelectric Random Access Memories*. Springer, Berlin, 2004.
- [2] J. F. Scott. *Ferroelectric Memories*. Springer, Berlin, 2000.
- [3] URL: <http://www.fujitsu.com/emea/services/microelectronics/fram/>.
- [4] J.G. Bednorz and K.A. Müller. “Possible high T_c superconductivity in the Ba-La-Cu-O system”. In: *Zeitschrift für Physik B: Condensed Matter* 64 (1986), pp. 189–93. DOI: [10.1007/BF01303701](https://doi.org/10.1007/BF01303701).
- [5] M. N. Baibich, J. M. Broto, A. Fert, F. Nguyen Van Dau, F. Petroff, P. Etienne, G. Creuzet, A. Friederich, and J. Chazelas. “Giant Magnetoresistance of (001)Fe/(001)Cr Magnetic Superlattices”. In: *Physical Review Letters* 61 (21 1988), pp. 2472–2475. DOI: [10.1103/PhysRevLett.61.2472](https://doi.org/10.1103/PhysRevLett.61.2472).
- [6] G. Binasch, P. Grünberg, F. Saurenbach, and W. Zinn. “Enhanced magnetoresistance in layered magnetic structures with antiferromagnetic interlayer exchange”. In: *Physical Review B* 39 (7 1989), pp. 4828–4830. DOI: [10.1103/PhysRevB.39.4828](https://doi.org/10.1103/PhysRevB.39.4828).
- [7] K. Chahara, T. Ohno, M. Kasai, and Y. Kozono. “Magnetoresistance in magnetic manganese oxide with intrinsic antiferromagnetic spin structure”. In: *Applied Physics Letters* 63 (1993), pp. 1990–1992. DOI: [10.1063/1.110624](https://doi.org/10.1063/1.110624).
- [8] R. von Helmolt, J. Wecker, B. Holzapfel, L. Schultz, and K. Samwer. “Giant negative magnetoresistance in perovskitelike $\text{La}_{2/3}\text{Ba}_{1/3}\text{MnO}_x$ ferromagnetic films”. In: *Physical Review Letters* 71 (1993), pp. 2331–2333. DOI: [10.1103/PhysRevLett.71.2331](https://doi.org/10.1103/PhysRevLett.71.2331).
- [9] J. Nogues and I. K. Schuller. “Exchange bias”. English. In: *Journal of Magnetism and Magnetic Materials* 192.2 (1999), 203–232. ISSN: 0304-8853. DOI: [10.1016/S0304-8853\(98\)00266-2](https://doi.org/10.1016/S0304-8853(98)00266-2).
- [10] A. E. Berkowitz and K. Takano. “Exchange anisotropy - a review”. English. In: *Journal of Magnetism and Magnetic Materials* 200.1-3 (1999), p. 552. ISSN: 0304-8853. DOI: [10.1016/S0304-8853\(99\)00453-9](https://doi.org/10.1016/S0304-8853(99)00453-9).
- [11] URL: <http://www.semicon.toshiba.co.jp/eng/product/storage/innovation/challenge/index.html>.

- [12] J.G. Zhu, Y.F. Zheng, and G.A. Prinz. “Ultra-high density vertical magnetoresistive random access memory (invited)”. English. In: *Journal of Applied Physics* 87.9, Part 3 (2000). 44th Annual Conference on Magnetism and Magnetic Materials, SAN JOSE, CALIFORNIA, NOV 15-18, 1999, pp. 6668–6673. ISSN: 0021-8979. DOI: [10.1063/1.372805](https://doi.org/10.1063/1.372805).
- [13] S Tehrani, JM Slaughter, E Chen, M Durlam, J Shi, and M DeHerrera. “Progress and outlook for MRAM technology”. English. In: *IEEE Transactions on Magnetics* 35.5, Part 1 (1999). 1999 International Magnetism Conference (INTERMAG 99), KYONGJU, SOUTH KOREA, MAY 18-21, 1999, pp. 2814–2819. ISSN: 0018-9464. DOI: [10.1109/20.800991](https://doi.org/10.1109/20.800991).
- [14] J.S. Moodera, L.R. Kinder, T.M. Wong, and R. Meservey. “Large Magnetoresistance At Room-temperature In Ferromagnetic Thin-film Tunnel-junctions”. English. In: *Physical Review Letters* 74.16 (1995), p. 3273. ISSN: 0031-9007. DOI: [10.1103/PhysRevLett.74.3273](https://doi.org/10.1103/PhysRevLett.74.3273).
- [15] S Tehrani, B Engel, JM Slaughter, E Chen, M DeHerrera, M Durlam, P Naji, R Whig, J Janesky, and J Calder. “Recent developments in Magnetic Tunnel Junction MRAM”. English. In: *IEEE Transactions on Magnetics* 36.5, Part 1 (2000). International Magnetism Conference (INTERMAG 2000), TORONTO, CANADA, APR 09-12, 2000, pp. 2752–2757. ISSN: 0018-9464. DOI: [10.1109/20.908581](https://doi.org/10.1109/20.908581).
- [16] N. Nishimura, T. Hirai, A. Koganei, T. Ikeda, K. Okano, Y. Sekiguchi, and Y. Osada. “Magnetic tunnel junction device with perpendicular magnetization films for high-density magnetic random access memory”. English. In: *Journal of Applied Physics* 91.8 (2002), pp. 5246–5249. ISSN: 0021-8979. DOI: [10.1063/1.1459605](https://doi.org/10.1063/1.1459605).
- [17] S Tehrani, JM Slaughter, M Deherrera, BN Engel, ND Rizzo, J Salter, M Durlam, RW Dave, J Janesky, B Butcher, K Smith, and G Grynkewich. “Magnetoresistive random access memory using magnetic tunnel junctions”. English. In: *PROCEEDINGS OF THE IEEE* 91.5 (2003), pp. 703–714. ISSN: 0018-9219. DOI: [10.1109/JPROC.2003.811804](https://doi.org/10.1109/JPROC.2003.811804).
- [18] M. Fiebig. “Revival of the magnetoelectric effect”. In: *Journal of Physics D: Applied Physics* 38 (2005), R123–R152. DOI: [10.1088/0022-3727/38/8/R01](https://doi.org/10.1088/0022-3727/38/8/R01).
- [19] T. Kimura, T. Goto, H. Shintani, Ishizaka K., T. Arima, and Y. Tokura. “Magnetic control of ferroelectric polarization”. In: *Nature* 426 (2003), pp. 55–58. DOI: [10.1038/nature02018](https://doi.org/10.1038/nature02018).
- [20] N. Hur, S. Park, P. A. Sharma, J. S. Ahn, S. Guha, and S.-W. Cheong. “Electric polarization and memory in a multiferroic material induced by magnetic fields”. In: *Nature* 429 (2004), pp. 392–395. DOI: [10.1038/nature02572](https://doi.org/10.1038/nature02572).
- [21] Th. Lottermoser, Th. Lonkai, U. Amman, D. Hohlwein, J. Ihringer, and M. Fiebig. “Magnetic Phase Control by an Electric Field”. In: *Nature* 430 (2004), pp. 541–545. DOI: [10.1038/nature02728](https://doi.org/10.1038/nature02728).
- [22] T. Goto, T. Kimura, G. Lawes, A. P. Ramirez, and Y. Tokura. “Ferroelectricity and Giant Magnetocapacitance in Perovskite Rare-Earth Manganites”. In: *Physical Review Letters* 92 (2004), p. 257201. DOI: [10.1103/PhysRevLett.92.257201](https://doi.org/10.1103/PhysRevLett.92.257201).

- [23] Y. Yamasaki, S. Miyasaka, Y. Kaneko, J.-P. He, T. Arima, and Y. Tokura. “Magnetic Reversal of the Ferroelectric Polarization in a Multiferroic Spinel Oxide”. In: *Physical Review Letters* 96 (2006), p. 207204. DOI: [10.1103/PhysRevLett.96.207204](https://doi.org/10.1103/PhysRevLett.96.207204).
- [24] Y. Yamasaki, H. Sagayama, T. Goto, M. Matsuura, K. Hirota, T. Arima, and Y. Tokura. “Electric Control of Spin Helicity in a Magnetic Ferroelectric”. In: *Physical Review Letters* 98 (2007), p. 147204. DOI: [10.1103/PhysRevLett.98.147204](https://doi.org/10.1103/PhysRevLett.98.147204).
- [25] T. Kimura, G. Lawes, and A. P. Ramirez. “Electric polarization rotation in a hexaferrite with long-wavelength magnetic structures”. English. In: *Physical Review Letters* 94.13 (2005). ISSN: 0031-9007. DOI: [10.1103/PhysRevLett.94.137201](https://doi.org/10.1103/PhysRevLett.94.137201).
- [26] N. A. Hill. “Why are there do few magnetic ferroelectrics”. In: *Journal of Physical Chemistry B* 104 (2000), pp. 6694–6709. DOI: [10.1021/jp000114x](https://doi.org/10.1021/jp000114x).
- [27] S.-W. Cheong and M. Mostovoy. “Multiferroics: a magnetic twist for ferroelectricity”. In: *Nature Materials* 6 (2007), pp. 13–20. DOI: [10.1038/nmat1804](https://doi.org/10.1038/nmat1804).
- [28] H. Katsura, N. Nagaosa, and A. V. Balatsky. “Spin Current and Magnetoelectric Effect in Noncollinear Magnets”. In: *Physical Review Letters* 95 (2005), p. 057205. DOI: [10.1103/PhysRevLett.95.057205](https://doi.org/10.1103/PhysRevLett.95.057205).
- [29] M. Mostovoy. “Ferroelectricity in Spiral Magnets”. In: *Physical Review Letters* 96 (2006), p. 067601. DOI: [10.1103/PhysRevLett.96.067601](https://doi.org/10.1103/PhysRevLett.96.067601).
- [30] M. Kenzelmann, A. B. Harris, S. Jonas, C. Broholm, J. Schefer, S. B. Kim, C. L. Zhang, S.-W. Cheong, O. P. Vajk, and J. W. Lynn. “Magnetic Inversion Symmetry Breaking and Ferroelectricity in TbMnO_3 ”. In: *Physical Review Letters* 95 (8 2005), p. 087206. DOI: [10.1103/PhysRevLett.95.087206](https://doi.org/10.1103/PhysRevLett.95.087206).
- [31] T. Goto, T. Kimura, G. Lawes, A. P. Ramirez, and Y. Tokura. “Ferroelectricity and Giant Magnetocapacitance in Perovskite Rare-Earth Manganites”. In: *Physical Review Letters* 92 (25 2004), p. 257201. DOI: [10.1103/PhysRevLett.92.257201](https://doi.org/10.1103/PhysRevLett.92.257201).
- [32] T. Kimura, G. Lawes, T. Goto, Y. Tokura, and A. P. Ramirez. “Magnetoelectric phase diagrams of orthorhombic RMnO_3 ($R = \text{Gd}, \text{Tb}, \text{and Dy}$)”. In: *Physical Review B* 71 (22 2005), p. 224425. DOI: [10.1103/PhysRevB.71.224425](https://doi.org/10.1103/PhysRevB.71.224425).
- [33] G. Lawes, A. B. Harris, T. Kimura, N. Rogado, R. J. Cava, A. Aharony, O. Entin-Wohlman, T. Yildirim, M. Kenzelmann, C. Broholm, and A. P. Ramirez. “Magnetically Driven Ferroelectric Order in $\text{Ni}_3\text{V}_2\text{O}_8$ ”. In: *Physical Review Letters* 95 (8 2005), p. 087205. DOI: [10.1103/PhysRevLett.95.087205](https://doi.org/10.1103/PhysRevLett.95.087205).
- [34] M. Fiebig, Thomas Lottermoser, D. Fröhlich, A.V. Goltsev, and R.V. Pisarev. “Observation of coupled magnetic and electric domains”. In: *Nature* 419 (2002), pp. 818–820. DOI: [10.1038/nature01077](https://doi.org/10.1038/nature01077).
- [35] Th. Lottermoser and M. Fiebig. “Magnetoelectric behavior of domain walls in multiferroic HoMnO_3 ”. In: *Physical Review B* 70 (2004), p. 220407. DOI: [10.1103/PhysRevB.70.220407](https://doi.org/10.1103/PhysRevB.70.220407).

- [36] T. Zhao, A. Scholl, K. Zavaliche and Lee, M. Barry, A. Doran, M. P. Cruz, Y. H. Chu, C. Ederer, N. A. Spaldin, R. R. Das, D. M. Kim, S. H. Baek, C. B. Eom, and R. Ramesh. “Electrical control of antiferromagnetic domains in multiferroic BiFeO₃ films at room temperature”. In: *Nature Materials* 5 (2006), pp. 823–829. DOI: [10.1038/nmat1731](https://doi.org/10.1038/nmat1731).
- [37] A. Vasudevarao, A. Kumar, L. Tian, J. H. Haeni, Y. L. Li, C.-J. Eklund, Q. X. Jia, R. Uecker, P. Reiche, K. M. Rabe, L. Q. Chen, D. G. Schlom, and Venkatraman Gopalan. “Multiferroic Domain Dynamics in Strained Strontium Titanate”. In: *Physical Review Letters* 97 (25 2006), p. 257602. DOI: [10.1103/PhysRevLett.97.257602](https://doi.org/10.1103/PhysRevLett.97.257602).
- [38] D. Meier, N. Leo, M. Maringer, Th. Lottermoser, P. Becker, L. Bohatý, and M. Fiebig. “Topology and manipulation of multiferroic domains in MnWO₄”. In: *Physical Review B* 80 (2009), p. 224420. DOI: [10.1103/PhysRevB.80.224420](https://doi.org/10.1103/PhysRevB.80.224420).
- [39] W. Eerenstein, M. Wiora, J. L. Prieto, J. F. Scott, and N. D. Mathur. “Giant sharp and persistent converse magnetoelectric effects in multiferroic epitaxial heterostructures”. In: *Nature Materials* 6 (2006), p. 348. DOI: [10.1038/nmat1886](https://doi.org/10.1038/nmat1886).
- [40] J. J. Yang, Y. G. Zhao, H. F. Tian, L. B. Luo, H. Y. Zhang, Y. J. He, and H. S. Luo. “Electric field manipulation of magnetization at room temperature in multiferroic CoFe₂O₄/Pb(Mg₃Nb_{2/3})_{0.7}Ti_{0.3}O₃ heterostructures”. In: *Applied Physics Letters* 94.21, 212504 (2009), p. 212504. DOI: [10.1063/1.3143622](https://doi.org/10.1063/1.3143622).
- [41] A. Pimenov, A. A. Mukhin, V. Yu. Ivanov, V. D. Travkin, A. M. Balbashov, and A. Loidl. “Possible evidence for electromagnons in multiferroic manganites”. In: *Nature Physics* 2 (2006), p. 97. DOI: [10.1038/nphys212](https://doi.org/10.1038/nphys212).
- [42] A. V. Kimel, R. V. Pisarev, F. Bentivegna, and Th. Rasing. “Time-resolved nonlinear optical spectroscopy of Mn³⁺ ions in rare-earth hexagonal manganites RMnO₃ (R = Sc, Y, Er)”. In: *Physical Review B* 64 (20 2001), p. 201103. DOI: [10.1103/PhysRevB.64.201103](https://doi.org/10.1103/PhysRevB.64.201103).
- [43] M. Matsubara, Y. Kaneko, J.-P. He, H. Okamoto, and Y. Tokura. “Ultrafast polarization and magnetization response of multiferroic GaFeO₃ using time-resolved nonlinear optical techniques”. In: *Physical Review B* 79 (14 2009), p. 140411. DOI: [10.1103/PhysRevB.79.140411](https://doi.org/10.1103/PhysRevB.79.140411).
- [44] S. L. Johnson, R. A. de Souza, U. Staub, P. Beaud, E. Möhr-Vorobeva, G. Ingold, A. Caviezel, V. Scagnoli, W. F. Schlotter, J. J. Turner, O. Krupin, W.-S. Lee, Y.-D. Chuang, L. Patthey, R. G. Moore, D. Lu, M. Yi, P. S. Kirchmann, M. Trigo, P. Denes, D. Doering, Z. Hussain, Z.-X. Shen, D. Prabhakaran, and A. T. Boothroyd. “Femtosecond Dynamics of the Collinear-to-Spiral Antiferromagnetic Phase Transition in CuO”. In: *Physical Review Letters* 108 (3 2012), p. 037203. DOI: [10.1103/PhysRevLett.108.037203](https://doi.org/10.1103/PhysRevLett.108.037203).
- [45] K. Taniguchi, N. Abe, T. Takenobu, Y. Iwasa, and T. Arima. “Ferroelectric Polarization Flop in a Frustrated Magnet MnWO₄ Induced by a Magnetic Field”. In: *Physical Review Letters* 97 (2006), p. 097203. DOI: [10.1103/PhysRevLett.97.097203](https://doi.org/10.1103/PhysRevLett.97.097203).
- [46] T. Kimura, Y. Sekio, H. Nakamura, T. Siegrist, and A. P. Ramirez. “Cupric oxide as an induced-multiferroic with high-T-C”. In: *Nature Materials* 7.4 (Mar. 2008), pp. 291–294. DOI: [10.1038/nmat2125](https://doi.org/10.1038/nmat2125).

- [47] M. Fiebig, V. V. Pavlov, and R. V. Pisarev. “Second-harmonic generation as a tool for studying electronic and magnetic structures of crystals”. In: *Journal of the Optical Society of America B* 22 (2005), pp. 96–118. DOI: [10.1364/JOSAB.22.000096](https://doi.org/10.1364/JOSAB.22.000096).
- [48] K. Aizu. “Possible species of “ferroelastic” crystals and of simultaneously ferroelectric and ferroelastic crystals.” In: *Journal of the Physical Society of Japan* 27 (1969), pp. 387–396. DOI: [10.1143/JPSJ.27.387](https://doi.org/10.1143/JPSJ.27.387).
- [49] K. Aizu. “Possible species of ferromagnetic, ferroelectric, and ferroelastic crystals”. In: *Physical Review B* 2 (1970), pp. 754–772. DOI: [10.1103/PhysRevB.2.754](https://doi.org/10.1103/PhysRevB.2.754).
- [50] V. K. Wadhawan. “Towards a rigorous definition of ferroic phase transitions”. In: *Phase Transitions* 64 (1998), pp. 165–177. DOI: [10.1080/01411599808220645](https://doi.org/10.1080/01411599808220645).
- [51] L. D. Landau. “Theory of phase transformations. I”. In: *Phys. Z. Sovjet*. 11 (1937), p. 26.
- [52] A. F. Devonshire. “THEORY OF BARIUM TITANATE .1.” English. In: *Philosophical Magazine* 40.309 (1949), pp. 1040–1063. ISSN: 0031-8086. DOI: [10.1080/14786444908561372](https://doi.org/10.1080/14786444908561372).
- [53] J. C. Tolédano and P. Tolédano. *The Landau theory of phase transitions*. World Scientific, 1987.
- [54] S. Ducharme, V. M. Fridkin, A. V. Bune, S. P. Palto, L. M. Blinov, N. N. Petukhova, and S. G. Yudin. “Intrinsic Ferroelectric Coercive Field”. In: *Physical Review Letters* 84 (1 2000), pp. 175–178. DOI: [10.1103/PhysRevLett.84.175](https://doi.org/10.1103/PhysRevLett.84.175).
- [55] W. J. Merz. “Domain Formation and Domain Wall Motions in Ferroelectric BaTiO₃ Single Crystals”. In: *Physical Review* 95 (3 1954), pp. 690–698. DOI: [10.1103/PhysRev.95.690](https://doi.org/10.1103/PhysRev.95.690).
- [56] W. J. Merz. “Switching Time in Ferroelectric BaTiO₃ and Its Dependence on Crystal Thickness”. In: *Journal of Applied Physics* 27.8 (1956), pp. 938–943. DOI: [10.1063/1.1722518](https://doi.org/10.1063/1.1722518).
- [57] Y. Ishibashi. “A Model of Polarization Reversal in Ferroelectrics”. In: *Journal of the Physical Society of Japan* 59.11 (1990), pp. 4148–4154. DOI: [10.1143/JPSJ.59.4148](https://doi.org/10.1143/JPSJ.59.4148).
- [58] Dan Ricinchi, Catalin Harnagea, Constantin Papusoi, Liliana Mitoseriu, Vasile Tura, and Masanori Okuyama. “Analysis of ferroelectric switching in finite media as a Landau-type phase transition”. In: *Journal of Physics: Condensed Matter* 10.2 (1998), p. 477. DOI: [10.1088/0953-8984/10/2/026](https://doi.org/10.1088/0953-8984/10/2/026).
- [59] T. K. Song. “Landau-Khalatnikov Simulations for Ferroelectric Switching in Ferroelectric Random Access Memory Application”. In: *J. Korean Phys. Soc.* 46 (2005), p. 5. DOI: [10.3938/jkps.46.5](https://doi.org/10.3938/jkps.46.5).
- [60] B.B. van Aken, J.-P. Rivera, Schmidt. H., and M. Fiebig. “Observation of ferrotoroidic domains”. In: *Nature* 449 (2007), p. 702. DOI: [doi:10.1038/nature06139](https://doi.org/10.1038/nature06139).
- [61] Nicola A. Spaldin, Manfred Fiebig, and Maxim Mostovoy. “The toroidal moment in condensed-matter physics and its relation to the magnetoelectric effect”. English. In: *Journal of Physics: Condensed Matter* 20.43 (2008). ISSN: 0953-8984. DOI: [10.1088/0953-8984/20/43/434203](https://doi.org/10.1088/0953-8984/20/43/434203).

- [62] Stephen Blundell. *Magnetism in Condensed Matter*. Oxford University Press, U.S.A., 2000.
- [63] A. Hubert and R. Schäfer. *Magnetic Domains*. Springer, 1998.
- [64] N. P. Duong, T. Satoh, and M. Fiebig. “Ultrafast Manipulation of Antiferromagnetism of NiO”. In: *Physical Review Letters* 93 (11 2004), p. 117402. DOI: [10.1103/PhysRevLett.93.117402](https://doi.org/10.1103/PhysRevLett.93.117402).
- [65] J. Hérault, R. C. Sousa, C. Ducruet, B. Dieny, Y. Conraux, C. Portemont, K. Mackay, I. L. Prejbeanu, B. Delaët, M. C. Cyrille, and O. Redon. “Nanosecond magnetic switching of ferromagnet-antiferromagnet bilayers in thermally assisted magnetic random access memory”. In: *Journal of Applied Physics* 106 (2009), p. 014505. DOI: [10.1063/1.3158231](https://doi.org/10.1063/1.3158231).
- [66] S. Loth, S. Baumann, C. P. Lutz, D. M. Eigler, and A. J. Heinrich. “Bistability in Atomic-Scale Antiferromagnets”. In: *Science* 335.6065 (2012), pp. 196–199. DOI: [10.1126/science.1214131](https://doi.org/10.1126/science.1214131).
- [67] T. J. Yang, V. Gopalan, P. J. Swart, and U. Mohideen. “Direct Observation of Pinning and Bowing of a Single Ferroelectric Domain Wall”. In: *Physical Review Letters* 82 (20 1999), pp. 4106–4109. DOI: [10.1103/PhysRevLett.82.4106](https://doi.org/10.1103/PhysRevLett.82.4106).
- [68] A. Agronin, Y. Rosenwaks, and G. Rosenman. “Direct observation of pinning centers in ferroelectrics”. In: *Applied Physics Letters* 88.7, 072911 (2006), p. 072911. DOI: [10.1063/1.2172230](https://doi.org/10.1063/1.2172230).
- [69] M. Bode, E. Y. Vedmedenko, K. von Bergmann, A. Kubetzka, P. Ferriani, S. Heinze, and R. Wiesendanger. “Atomic spin structure of antiferromagnetic domain walls”. In: *Nature Materials* 5 (2006), p. 477. DOI: [10.1038/nmat1646](https://doi.org/10.1038/nmat1646).
- [70] Karin M. Rabe, Charles H. Ahn, and Jean-Marc Triscone, eds. *Physics of Ferroelectrics: A Modern Perspective*. Springer Berlin Heidelberg, 2007.
- [71] F. Kagawa, M. Mochizuki, Y. Onose, H. Murakawa, Y. Kaneko, N. Furukawa, and Y. Tokura. “Dynamics of Multiferroic DomainWall in Spin-Cycloidal Ferroelectric DyMnO₃”. In: *Physical Review Letters* 102 (2009), p. 057604. DOI: [10.1103/PhysRevLett.102.057604](https://doi.org/10.1103/PhysRevLett.102.057604).
- [72] M. Dawber, K. M. Rabe, and J. F. Scott. “Physics of thin-film ferroelectric oxides”. In: *Rev. Mod. Phys.* 77 (4 2005), pp. 1083–1130. DOI: [10.1103/RevModPhys.77.1083](https://doi.org/10.1103/RevModPhys.77.1083).
- [73] N. Setter, D. Damjanovic, L. Eng, G. Fox, S. Gevorgian, S. Hong, A. Kingon, H. Kohlstedt, N. Y. Park, G. B. Stephenson, I. Stolitchnov, A. K. Taganstev, D. V. Taylor, T. Yamada, and S. Streiffer. “Ferroelectric thin films: Review of materials, properties, and applications”. In: *Journal of Applied Physics* 100.5, 051606 (2006), p. 051606. DOI: [10.1063/1.2336999](https://doi.org/10.1063/1.2336999).
- [74] Alexander K. Tagantsev, Igor Stolichnov, Nava Setter, Jeffrey S. Cross, and Mineharu Tsukada. “Non-Kolmogorov-Avrami switching kinetics in ferroelectric thin films”. In: *Physical Review B* 66 (21 2002), p. 214109. DOI: [10.1103/PhysRevB.66.214109](https://doi.org/10.1103/PhysRevB.66.214109).

- [75] H. Orihara, S. Hashimoto, and Y. Ishibashi. “A Theory of D-E Hysteresis Loop Based on the Avrami Model”. In: *Journal of the Physical Society of Japan* 63 (1994), p. 1031. DOI: [10.1143/JPSJ.63.1031](https://doi.org/10.1143/JPSJ.63.1031).
- [76] D. Li and D. A. Bonnell. “Controlled Patterning of Ferroelectric Domains: Fundamental Concepts and Applications”. In: *Annual Review of Materials Research* 38.1 (2008), pp. 351–368. DOI: [10.1146/annurev.matsci.37.052506.084303](https://doi.org/10.1146/annurev.matsci.37.052506.084303).
- [77] C. T. Nelson, P. Gao, J. R. Jokisaari, C. Heikes, C. Adamo, A. Melville, S.-H. Baek, C. M. Folkman, B. Winchester, Y. Gu, Y. Liu, K. Zhang, E. Wang, J. Li, L.-Q. Chen, C.-B. Eom, D. G. Schlom, and X. Pan. “Domain Dynamics During Ferroelectric Switching”. In: *Science* 334.6058 (2011), pp. 968–971. DOI: [10.1126/science.1206980](https://doi.org/10.1126/science.1206980).
- [78] H. Schmid. “Multi-ferroic magnetoelectrics”. In: *Ferroelectrics* 162 (1994), pp. 317–338. DOI: [10.1080/00150199408245120](https://doi.org/10.1080/00150199408245120).
- [79] W. Eerenstein, N. D. Mathur, and J. F. Scott. “Multiferroic and magnetoelectric materials”. In: *Nature* 442 (2006), pp. 759–765. DOI: [10.1038/nature05023](https://doi.org/10.1038/nature05023).
- [80] N. A. Spaldin and M. Fiebig. “The Renaissance of Magnetoelectric Multiferroics”. In: *Science* 309 (2005), pp. 391–392. DOI: [10.1126/science.1113357](https://doi.org/10.1126/science.1113357).
- [81] D. Khomskii. “Classifying multiferroics: Mechanisms and effects”. In: *Physics* 2 (2009), p. 20. DOI: [10.1103/Physics.2.20](https://doi.org/10.1103/Physics.2.20).
- [82] Th. Lottermoser, D. Meier, R. V. Pisarev, and M. Fiebig. “Giant coupling of second-harmonic generation to a multiferroic polarization”. In: *Physical Review B* 80 (10 2009), p. 100101. DOI: [10.1103/PhysRevB.80.100101](https://doi.org/10.1103/PhysRevB.80.100101).
- [83] I. Sosnowska, T. P. Neumaier, and E. Steichele. “Spiral magnetic ordering in bismuth ferrite”. In: *Journal of Physics C: Solid State Physics* 15 (1982), pp. 4835–4846. DOI: [10.1088/0022-3719/15/23/020](https://doi.org/10.1088/0022-3719/15/23/020).
- [84] J. Wang, J. B. Neaton, H. Zheng, V. Nagarajan, S. B. Ogale, B. Liu, D. Viehland, V. Vaithyanathan, D. G. Schlom, U. V. Waghmare, N. A. Spaldin, K. M. Rabe, M. Wuttig, and R. Ramesh. “Epitaxial BiFeO₃ Multiferroic Thin Film Heterostructures”. In: *Science* 299 (2003), pp. 1719–1722. DOI: [10.1126/science.1080615](https://doi.org/10.1126/science.1080615).
- [85] B.B. van Aken, T.T.M. Palstra, A. Filippetti, and N.A. Spaldin. “Origin of ferroelectricity in magnetoelectric YMnO₃”. In: *Nature Materials* 3 (2004), pp. 164–170. DOI: [10.1038/nmat1080](https://doi.org/10.1038/nmat1080).
- [86] T. Lonkai, D. G. Tomuta, U. Amann, J. Ihringer, R. W. A. Hendriks, D. M. Többsen, and J. A. Mydosh. “Development of the high-temperature phase of hexagonal manganites”. In: *Physical Review B* 69 (2004), p. 134108. DOI: [10.1103/PhysRevB.69.134108](https://doi.org/10.1103/PhysRevB.69.134108).
- [87] S. Picozzi, K. Yamauchi, B. Sanyal, I. A. Sergienko, and E. Dagotto. “Dual Nature of Improper Ferroelectricity in a Magnetoelectric Multiferroic”. In: *Physical Review Letters* 99 (2007), p. 227201. DOI: [10.1103/PhysRevLett.99.227201](https://doi.org/10.1103/PhysRevLett.99.227201).
- [88] P. G. Radaelli, L. C. Chapon, A. Daoud-Aladine, C. Vecchini, P. J. Brown, T. Chatterji, S. Park, and S.-W. Cheong. “Electric Field Switching of Antiferromagnetic Domains in YMn₂O₅: A Probe of the Multiferroic Mechanism”. In: *Physical Review Letters* 101 (2008), p. 067205. DOI: [10.1103/PhysRevLett.101.067205](https://doi.org/10.1103/PhysRevLett.101.067205).

- [89] L. C. Chapon, G. R. Blake, M. J. Gutmann, S. Park, N. Hur, P. G. Radaelli, and S.-W. Cheong. “Structural Anomalies and Multiferroic Behavior in Magnetically Frustrated TbMn_2O_5 ”. In: *Physical Review Letters* 93 (2004), p. 177402. DOI: [10.1103/PhysRevLett.93.177402](https://doi.org/10.1103/PhysRevLett.93.177402).
- [90] V. K. Wadhawan. *Introduction to ferroic materials*. Gordon and Breach Science Publishers, 2000.
- [91] Pierre Tolédano. “Pseudo-proper ferroelectricity and magnetoelectric effects in TbMnO_3 ”. In: *Physical Review B* 79 (9 2009), p. 094416. DOI: [10.1103/PhysRevB.79.094416](https://doi.org/10.1103/PhysRevB.79.094416).
- [92] P. Tolédano, B. Mettout, W. Schranz, and G. Krexner. “Directional magnetoelectric effects in MnWO_4 : magnetic sources of the electric polarization”. In: *Journal of Physics: Condensed Matter* 22 (2010), p. 065901. DOI: [10.1088/0953-8984/22/6/065901](https://doi.org/10.1088/0953-8984/22/6/065901).
- [93] W. F. Brown Jr., R. M. Hornreich, and S. Shtrikman. “Upper bound on the magnetoelectric susceptibility”. In: *Physical Review* 168.2 (1968), pp. 574–577. DOI: [10.1103/PhysRev.168.574](https://doi.org/10.1103/PhysRev.168.574).
- [94] T. Moriya. “Anisotropic Superexchange Interaction and Weak Ferromagnetism”. In: *Physical Review* 120 (1960), pp. 91–98. DOI: [10.1103/PhysRev.120.91](https://doi.org/10.1103/PhysRev.120.91).
- [95] J. B. Goodenough. *Magnetism and the Chemical Bond*. Ed. by F. A. Cotton, G. A. Olah, and I. Prigogine. John Wiley and Sons, New York-London, 1963.
- [96] I. A. Sergienko and E. Dagotto. “Role of the Dzyaloshinskii-Moriya interaction in multiferroic perovskites”. In: *Physical Review B* 73 (2006), p. 094434. DOI: [10.1103/PhysRevB.73.094434](https://doi.org/10.1103/PhysRevB.73.094434).
- [97] T. Kimura. “Spiral Magnets as Magnetoelectrics”. In: *Annual Review of Material Research* 37 (2007), pp. 387–413. DOI: [10.1146/annurev.matsci.37.052506.084259](https://doi.org/10.1146/annurev.matsci.37.052506.084259).
- [98] P. Bruno and V. K. Dugaev. “Equilibrium spin currents and the magnetoelectric effect in magnetic nanostructures”. In: *Physical Review B* 72 (2005), p. 241302. DOI: [10.1103/PhysRevB.72.241302](https://doi.org/10.1103/PhysRevB.72.241302).
- [99] L. C. Chapon, P. G. Radaelli, G. R. Blake, S. Park, and S.-W. Cheong. “Ferroelectricity Induced by Acentric Spin-Density Waves in YMn_2O_5 ”. In: *Physical Review Letters* 96 (2006), p. 097601. DOI: [10.1103/PhysRevLett.96.097601](https://doi.org/10.1103/PhysRevLett.96.097601).
- [100] G. R. Blake, L. C. Chapon, P. G. Radaelli, S. Park, N. Hur, S.-W. Cheong, and J. Rodríguez-Carvajal. “Spin structure and magnetic frustration in multiferroic RMn_2O_5 (R=Tb, Ho, Dy)”. In: *Physical Review B* 71 (2005), p. 214402. DOI: [10.1103/PhysRevB.71.214402](https://doi.org/10.1103/PhysRevB.71.214402).
- [101] G. Giovannetti and J. van den Brink. “Electronic Correlations Decimate the Ferroelectric Polarization of Multiferroic HoMn_2O_5 ”. In: *Physical Review Letters* 100 (2008), p. 227603. DOI: [10.1103/PhysRevLett.100.227603](https://doi.org/10.1103/PhysRevLett.100.227603).
- [102] X. Chen, A. Hochstrat, P. Borisov, and Kleemann W. “Magnetoelectric exchange bias systems in spintronics”. In: *Applied Physics Letters* 89.20, 202508 (2006), p. 202508. DOI: [10.1063/1.2388149](https://doi.org/10.1063/1.2388149).
- [103] M. Göppert-Mayer. “Über Elementarakte mit zwei Quantensprüngen”. In: *Annalen der Physik* 401.3 (1931), pp. 273–294. ISSN: 1521-3889. DOI: [10.1002/andp.19314010303](https://doi.org/10.1002/andp.19314010303).

- [104] T.H. Maiman. “Stimulated Optical Radiation in Ruby”. In: *Nature* 187 (1960), p. 493. DOI: [10.1038/187493a0](https://doi.org/10.1038/187493a0).
- [105] P. A. Franken, A. E. Hill, C. W. Peters, and G. Weinreich. “Generation of Optical Harmonics”. In: *Physical Review Letters* 7 (1961), p. 118. DOI: [10.1103/PhysRevLett.7.118](https://doi.org/10.1103/PhysRevLett.7.118).
- [106] Y. R. Shen. “Surface properties probed by second-harmonic and sum-frequency generation”. In: *Nature* 337 (1989), p. 619. DOI: [10.1038/337519a0](https://doi.org/10.1038/337519a0).
- [107] F. M. Geiger. “Second Harmonic Generation, Sum Frequency Generation, and $\chi(3)$: Dissecting Environmental Interfaces with a Nonlinear Optical Swiss Army Knife”. In: *Annual Review of Physical Chemistry* 60.1 (2009). PMID: 18851705, pp. 61–83. DOI: [10.1146/annurev.physchem.59.032607.093651](https://doi.org/10.1146/annurev.physchem.59.032607.093651).
- [108] P.J. Campagnola and C.-Y. Dong. “Second harmonic generation microscopy: principles and applications to disease diagnosis”. In: *Laser & Photonics Reviews* 5.1 (2011), pp. 13–26. ISSN: 1863-8899. DOI: [10.1002/lpor.200910024](https://doi.org/10.1002/lpor.200910024).
- [109] Y. Tanabe, M. Muto, M. Fiebig, and E. Hanamura. “Interference of second harmonics due to electric and magnetic dipoles in antiferromagnetic Cr_2O_3 ”. In: *Physical Review B* 58 (1998), pp. 8654–8666. DOI: [10.1103/PhysRevB.58.8654](https://doi.org/10.1103/PhysRevB.58.8654).
- [110] T. Iizuka-Sakano, E. Hanamura, and Y. Tanabe. “Second-harmonic-generation spectra of the hexagonal manganites RMnO_3 ”. In: *Journal of Physics: Condensed Matter* 13 (2001), pp. 3031–3055. DOI: [10.1088/0953-8984/13/13/316](https://doi.org/10.1088/0953-8984/13/13/316).
- [111] F. E. Neumann. *Vorlesungen über die Theorie der Elastizität der festen Körper und des Lichtäthers*. B. G. Teubner-Verlag, Leipzig, 1885.
- [112] R. R. Birss. *Symmetry and Magnetism*. Ed. by E. P. Wohlfarth. North-Holland Publishing Company, 1964.
- [113] D. Sa, R. Valenti, and C. Gros. “A generalized Ginzburg-Landau approach to second harmonic generation”. In: *European Physical Journal B - Condensed Matter and Complex Systems* 14 (2000), pp. 301–305. DOI: [10.1007/s100510050133](https://doi.org/10.1007/s100510050133).
- [114] D. Meier, M. Maringer, Th. Lottermoser, P. Becker, L. Bohatý, and M. Fiebig. “Observation and coupling of domains in a spin-spiral multiferroic”. In: *Physical Review Letters* 102 (2009), p. 107202. DOI: [10.1103/PhysRevLett.102.107202](https://doi.org/10.1103/PhysRevLett.102.107202).
- [115] D. Meier. “Order Parameters and Domain Topology in Magnetically Induced Ferroelectrics”. PhD thesis. University Bonn, 2010.
- [116] M. Fiebig, D. Fröhlich, St. Leute, and R. V. Pisarev. “Topography of antiferromagnetic domains using second harmonic generation with an external reference”. In: *Applied Physics B: Laser and Optics* 66 (1998), pp. 265–270. DOI: [10.1007/s003400050387](https://doi.org/10.1007/s003400050387).
- [117] D. Meier, N. Leo, Th. Lottermoser, P. Becker, L. Bohatý, and M. Fiebig. “Imaging of Hybrid-Multiferroic and Translation Domains in a Spin-Spiral Ferroelectric”. In: *Proceedings of the MRS Fall Meeting 2009*. 2009. DOI: [10.1557/PROC-1199-F02-07](https://doi.org/10.1557/PROC-1199-F02-07).
- [118] Y. R. Shen. *The Principles of Nonlinear Optics*. Wiley-Interscience, 2002.
- [119] Robert W. Boyd. *Nonlinear Optics*. Academic Press, 2008.

- [120] G. He and S. H. Liu. *Physics of Nonlinear Optics*. World Scientific, 2000.
- [121] P. Thielen. “Time Resolved Magnetolectric Reversal of Spin-Spiral Domains in Multi-ferroic MnWO₄”. MA thesis. Rheinischen Friedrich-Wilhelms-Universität Bonn, 2011.
- [122] R. Villarreal, G. Quirion, M. L. Plumer, M. Poirier, T. Usui, and T. Kimura. “Magnetic Phase Diagram of CuO”. In: *ArXiv e-prints* (2012). arXiv: 1205.5229 [cond-mat.mtrl-sci]. URL: <http://arxiv.org/abs/1205.5229v1>.
- [123] G. Lautenschläger, H. Weitzel, T. Vogt, R. Hock, A. Böhm, M. Bonnet, and H. Fuess. “Magnetic phase transitions of MnWO₄ studied by the use of neutron diffraction”. In: *Physical Review B* 48 (1993), pp. 6087–6098. DOI: 10.1103/PhysRevB.48.6087.
- [124] C. Tian, C. Lee, H. Xiang, Y. Zhang, S. Payen C. and Jobic, and M.-H. Whangbo. “Magnetic structure and ferroelectric polarization of MnWO₄ investigated by density functional calculations and classical spin analysis”. In: *Physical Review B* 80 (2009), p. 104426. DOI: 10.1103/PhysRevB.80.104426.
- [125] N. Hollmann, Z. Hu, T. Willers, L. Bohatý, P. Becker, A. Tanaka, H. H. Hsieh, H.-J. Lin, C. T. Chen, and L. H. Tjeng. “Local symmetry and magnetic anisotropy in multiferroic MnWO₄ and antiferromagnetic CoWO₄ studied by soft x-ray absorption spectroscopy”. In: *Physical Review B* 82 (18 2010), p. 184429. DOI: 10.1103/PhysRevB.82.184429.
- [126] A. H. Arkenbout, T. T. M. Palstra, T. Siegrist, and T. Kimura. “Ferroelectricity in the cycloidal spiral magnetic phase of MnWO₄”. In: *Physical Review B* 74 (2006), p. 184431. DOI: 10.1103/PhysRevB.74.184431.
- [127] H. Mitamura, H. Nakamura, T. Kimura, T. Sakakibara, and K. Kindo. “Sign Reversal of the Dielectric Polarization of MnWO₄ in Very High Magnetic Fields”. In: *Journal of Physics: Conference Series* 150 (2009), p. 042126. DOI: 10.1088/1742-6596/150/4/042126.
- [128] K. Taniguchi, N. Abe, H. Sagayama, S. Ohtani, T. Takenobu, Y. Iwasa, and T. Arima. “Magnetic-field dependence of the ferroelectric polarization and spin-lattice coupling in multiferroic MnWO₄”. In: *Physical Review B* 77 (2008), p. 064408. DOI: 10.1103/PhysRevB.77.064408.
- [129] K. Taniguchi, N. Abe, H. Umetsu, H. Aruga Katori, and T. Arima. “Control of the Magnetolectric Domain-Wall Stability by a Magnetic Field in a Multiferroic MnWO₄”. In: *Physical Review Letters* 101 (2008), p. 207205. DOI: 10.1103/PhysRevLett.101.207205.
- [130] B. Kundys, C. Simon, and C. Martin. “Effect of magnetic field and temperature on the ferroelectric loop in MnWO₄”. In: *Physical Review B* 77 (2008), p. 172402. DOI: 10.1103/PhysRevB.77.172402.
- [131] H. Mitamura, T. Sakakibara, H. Nakamura, T. Kimura, and K. Kindo. “Multiferroicity on the Zigzag-Chain Antiferromagnet MnWO₄ in High Magnetic Fields”. In: *Journal of the Physical Society of Japan* 81 (2012). DOI: 10.1143/JPSJ.81.054705.
- [132] A Poole, P. J. Brown, and A. S. Wills. “Spherical neutron polarimetry (SNP) study of magneto-electric coupling in the multiferroic MnWO₄”. In: *J. Phys.: Conference Series* 145 (2009), p. 012074. DOI: 10.1088/1742-6596/145/1/012074.

- [133] T. Finger, D. Senff, K. Schmalzl, W. Schmidt, L. P. Regnault, P. Becker, L. Bohatý, and M. Braden. “Electric-field control of the chiral magnetism of multiferroic MnWO_4 as seen via polarized neutron diffraction”. In: *Physical Review B* 81 (2010), p. 054430. DOI: [10.1103/PhysRevB.81.054430](https://doi.org/10.1103/PhysRevB.81.054430).
- [134] M. Maringer. “Spektroskopie und Domänentopographie an multiferroischem MnWO_4 mittels nichtlinearer Optik”. MA thesis. Universität Bonn, 2008.
- [135] D. Meier, N. Leo, G. Yuan, Th. Lottermoser, M. Fiebig, P. Becker, and L. Bohaty. “Second harmonic generation on incommensurate structures: The case of multiferroic MnWO_4 ”. In: *Physical Review B* 82 (2010), p. 155112. DOI: [10.1103/PhysRevB.82.155112](https://doi.org/10.1103/PhysRevB.82.155112).
- [136] K. Momma and F. Izumi. “VESTA3 for three-dimensional visualization of crystal, volumetric and morphology data”. In: *Journal of Applied Crystallography* 44.6 (2011), pp. 1272–1276. DOI: [10.1107/S0021889811038970](https://doi.org/10.1107/S0021889811038970).
- [137] Collaboration: Authors and editors of the volumes III/17E-17F-41C. “Landolt-Börnstein - Group III Condensed Matter”. In: ed. by O. Madelung, U. Rössler, and M. Schulz. Vol. 41C. SpringerMaterials - The Landolt-Börnstein Database. Chap. Cupric oxide (CuO) lattice properties, p. 6. DOI: [10.1007/10681727_53](https://doi.org/10.1007/10681727_53).
- [138] J. B. Forsyth, P. J. Brown, and B. M. Wanklyn. “Magnetism in Cupric Oxide”. In: *Journal of Physics C: Solid State Physics* 21.15 (1988), p. 2917. DOI: [10.1088/0022-3719/21/15/023](https://doi.org/10.1088/0022-3719/21/15/023).
- [139] B. X. Yang, T. R. Thurston, J. M. Tranquada, and G. Shirane. “Magnetic neutron scattering study of single-crystal cupric oxide”. In: *Physical Review B* 39 (7 1989), pp. 4343–4349. DOI: [10.1103/PhysRevB.39.4343](https://doi.org/10.1103/PhysRevB.39.4343).
- [140] Collaboration: Authors and editors of the volumes III/17E-17F-41C. “Landolt-Börnstein - Group III Condensed Matter”. In: ed. by O. Madelung, U. Rössler, and M. Schulz. Vol. 41C. SpringerMaterials - The Landolt-Börnstein Database. Chap. Cupric oxide (CuO) magnetic properties, heat capacity, density, p. 9. DOI: [10.1007/10681727_55](https://doi.org/10.1007/10681727_55).
- [141] M. Ain, A. Menelle, B. M. Wanklyn, and E. F. Bertaut. “Magnetic-structure of CuO By Neutron-diffraction With Polarization Analysis”. In: *Journal of Physics: Condensed Matter* 4.23 (June 1992), pp. 5327–5337. DOI: [10.1088/0953-8984/4/23/009](https://doi.org/10.1088/0953-8984/4/23/009).
- [142] Tadashi Shimizu, Takehiko Matsumoto, Atsushi Goto, Kazuyoshi Yoshimura, and Koji Kosuge. “Magnetic Dimensionality of the Antiferromagnet CuO ”. In: *Journal of the Physical Society of Japan* 72.9 (2003), pp. 2165–2168. DOI: [10.1143/JPSJ.72.2165](https://doi.org/10.1143/JPSJ.72.2165).
- [143] Pierre Tolédano, Naëmi Leo, Dmitry D. Khalyavin, Laurent C. Chapon, Tim Hoffmann, Dennis Meier, and Manfred Fiebig. “Theory of High-Temperature Multiferroicity in Cupric Oxide”. In: *Physical Review Letters* 106 (25 2011), p. 257601. DOI: [10.1103/PhysRevLett.106.257601](https://doi.org/10.1103/PhysRevLett.106.257601).
- [144] G. Giovannetti, S. Kumar, A. Stroppa, J. van den Brink, S. Picozzi, and J. Lorenzana. “High- T_c Ferroelectricity Emerging from Magnetic Degeneracy in Cupric Oxide”. In: *Physical Review Letters* 106 (2 2011), p. 026401. DOI: [10.1103/PhysRevLett.106.026401](https://doi.org/10.1103/PhysRevLett.106.026401).

- [145] G. Jin, K. Cao, G.-C. Guo, and L. He. “Origin of Ferroelectricity in High- T_c Magnetic Ferroelectric CuO”. In: *Physical Review Letters* 108 (18 2012), p. 187205. DOI: [10.1103/PhysRevLett.108.187205](https://doi.org/10.1103/PhysRevLett.108.187205).
- [146] J. Holakovský. “A New Type of the Ferroelectric Phase Transition”. In: *Physica Status Solidi B* 56.2 (1973), pp. 615–619. ISSN: 1521-3951. DOI: [10.1002/pssb.2220560224](https://doi.org/10.1002/pssb.2220560224).
- [147] X. G. Zheng, Y. Sakurai, Y. Okayama, T. Q. Yang, L. Y. Zhang, X. Yao, K. Nonaka, and C. N. Xu. “Dielectric measurement to probe electron ordering and electron-spin interaction”. In: *Journal of Applied Physics* 92.5 (2002), pp. 2703–2708. DOI: [10.1063/1.1498876](https://doi.org/10.1063/1.1498876).
- [148] F. Wang, T. Zou, Y. Liu, L.-Q. Yan, and Y. Sun. “Persistent multiferroicity without magnetoelectric effects in CuO”. In: *Journal of Applied Physics* 110.5, 054106 (2011), p. 054106. DOI: [10.1063/1.3636106](https://doi.org/10.1063/1.3636106).
- [149] P. Babkevich, A. Poole, R. D. Johnson, B. Roessli, D. Prabhakaran, and A. T. Boothroyd. “Electric field control of chiral magnetic domains in the high-temperature multiferroic CuO”. In: *Physical Review B* 85 (13 2012), p. 134428. DOI: [10.1103/PhysRevB.85.134428](https://doi.org/10.1103/PhysRevB.85.134428).
- [150] K. Taniguchi, N. Abe, S. Ohtani, and T. Arima. “Magnetoelectric Memory Effect of the Nonpolar Phase with Collinear Spin Structure in Multiferroic MnWO_4 ”. In: *Physical Review Letters* 102 (2009), p. 147201. DOI: [10.1103/PhysRevLett.102.147201](https://doi.org/10.1103/PhysRevLett.102.147201).
- [151] L. Landau and E. Lifshits. “On the Theory of the Dispersion of Magnetic Permeability In Ferromagnetic Bodies”. In: *Phys. Zeitsch. der Sow.* 8 (1935), pp. 153–169.
- [152] C. Kittel. “Theory of the Structure of Ferromagnetic Domains in Films and Small Particles”. In: *Physical Review* 70 (11-12 1946), pp. 965–971. DOI: [10.1103/PhysRev.70.965](https://doi.org/10.1103/PhysRev.70.965).
- [153] T. Mitsui and J. Furuichi. “Domain Structure of Rochelle Salt and KH_2PO_4 ”. In: *Physical Review* 90 (2 1953), pp. 193–202. DOI: [10.1103/PhysRev.90.193](https://doi.org/10.1103/PhysRev.90.193).
- [154] J F Scott. “Nanoferroelectrics: statics and dynamics”. In: *Journal of Physics: Condensed Matter* 18.17 (2006), R361. DOI: [10.1088/0953-8984/18/17/R02](https://doi.org/10.1088/0953-8984/18/17/R02).
- [155] A. Schilling, T. B. Adams, R. M. Bowman, J. M. Gregg, G. Catalan, and J. F. Scott. “Scaling of domain periodicity with thickness measured in BaTiO_3 single crystal lamellae and comparison with other ferroics”. In: *Physical Review B* 74 (2 2006), p. 024115. DOI: [10.1103/PhysRevB.74.024115](https://doi.org/10.1103/PhysRevB.74.024115).
- [156] G. Catalan, J. F. Scott, A. Schilling, and J. M. Gregg. “Wall thickness dependence of the scaling law for ferroic stripe domains”. In: *Journal of Physics: Condensed Matter* 19.2 (2007), p. 022201. DOI: [10.1088/0953-8984/19/2/022201](https://doi.org/10.1088/0953-8984/19/2/022201).
- [157] M. Mochizuki and N. Nagaosa. “Theoretically Predicted Picosecond Optical Switching of Spin Chirality in Multiferroics”. In: *Physical Review Letters* 105 (14 2010), p. 147202. DOI: [10.1103/PhysRevLett.105.147202](https://doi.org/10.1103/PhysRevLett.105.147202).

- [158] S. Jesse, B. J. Rodriguez, S. Choudhury, A. P. Baddorf, I. Vrejoiu, D. Hesse, M. Alexe, E. A. Eliseev, A. N. Morozovska, J. Zhang, L.-Q. Chen, and S. V. Kalinin. “Direct imaging of the spatial and energy distribution of nucleation centres in ferroelectric materials”. In: *Nature Materials* 7.3 (Mar. 2008), pp. 209–215. ISSN: 1476-1122. DOI: [10.1038/nmat2114](https://doi.org/10.1038/nmat2114).
- [159] A. Nogami, T. Suzuki, and T. Katsufuji. “Second Harmonic Generation from Multiferroic MnWO_4 ”. In: *Journal of the Physical Society of Japan* 77.11 (2008), p. 115001. DOI: [10.1143/JPSJ.77.115001](https://doi.org/10.1143/JPSJ.77.115001).
- [160] H. L. Stadler. “Ferroelectric Switching Time of BaTiO_3 Crystals at High Voltages”. In: *Journal of Applied Physics* 29 (1958), p. 1485. DOI: [10.1063/1.1722973](https://doi.org/10.1063/1.1722973).
- [161] Tim Günter. “Aufbau und Charakterisierung eines Femtosekunden-Lasersystems”. MA thesis. Helmholtz - Institut für Strahlen- und Kernphysik, Universität Bonn, 2008.
- [162] George T. Rado. “On the Inertia of Oscillating Ferromagnetic Domain Walls”. In: *Physical Review* 83 (4 1951), pp. 821–826. DOI: [10.1103/PhysRev.83.821](https://doi.org/10.1103/PhysRev.83.821).
- [163] E. Feldtkeller. “Magnetic Domain Wall Dynamics”. In: *Physica Status Solidi B* 27.1 (1968), pp. 161–170. ISSN: 1521-3951. DOI: [10.1002/pssb.19680270117](https://doi.org/10.1002/pssb.19680270117).
- [164] X. J. Lou. “Polarization fatigue in ferroelectric thin films and related materials”. In: *Journal of Applied Physics* 105.2, 024101 (2009), p. 024101. DOI: [10.1063/1.3056603](https://doi.org/10.1063/1.3056603).
- [165] D. Lebeugle, D. Colson, A. Forget, and M. Viret. “Very large spontaneous electric polarization in BiFeO_3 single crystals at room temperature and its evolution under cycling fields”. In: *Applied Physics Letters* 91.2, 022907 (2007), p. 022907. DOI: [10.1063/1.2753390](https://doi.org/10.1063/1.2753390).
- [166] C.-C. Lee, L.J. Wu, and J.-M. Wu. “Studies on forming gas annealing treated BiFeO_3 thin films and capacitors”. In: *Applied Physics Letters* 91.20, 202902 (2007), p. 202902. DOI: [10.1063/1.2806191](https://doi.org/10.1063/1.2806191).
- [167] Y.-H. Lee, J. M. Wu, and C.-H. Lai. “Influence of La doping in multiferroic properties of BiFeO_3 thin films”. In: *Applied Physics Letters* 88.4, 042903 (2006), p. 042903. DOI: [10.1063/1.2167793](https://doi.org/10.1063/1.2167793).
- [168] R. Y. Zheng, X. S. Gao, Z. H. Zhou, and J. Wang. “Multiferroic BiFeO_3 thin films deposited on SrRuO_3 buffer layer by rf sputtering”. In: *Journal of Applied Physics* 101.5, 054104 (2007), p. 054104. DOI: [10.1063/1.2437163](https://doi.org/10.1063/1.2437163).
- [169] A. V. Kimel, B.A. Ivanov, R. V. Pisarev, P. A. Usachev, A. Kirilyuk, and Th. Rasing. “Inertia-driven spin switching in antiferromagnets”. In: *Nature Physics* 5 (2009), p. 727. DOI: [10.1038/nphys1369](https://doi.org/10.1038/nphys1369).
- [170] Collaboration: Authors and editors of the volumes III/17E-17F-41C. “Landolt-Börnstein - Group III Condensed Matter”. In: ed. by O. Madelung, U. Rössler, and M. Schulz. Vol. 41C. SpringerMaterials - The Landolt-Börnstein Database. Chap. Cupric oxide (CuO) electronic properties, p. 2. DOI: [10.1007/10681727_52](https://doi.org/10.1007/10681727_52).
- [171] T. Satoh, Th. Lottermoser, and M. Fiebig. “Resonance-enhanced two-photon sum-frequency generation in NiO and KNiF_3 ”. In: *Applied Physics B: Laser and Optics* 79 (2004), pp. 701–706. DOI: [10.1007/s00340-004-1615-2](https://doi.org/10.1007/s00340-004-1615-2).

- [172] A.B. Van Oosten, R. Broer, B. Th. Thole, and W. C. Nieuwpoort. "Cluster calculations on localized holes in La₂CuO₄". In: *Journal of the Less Common Metals* 164-165, Part 2.0 (1990), p. 1514. ISSN: 0022-5088. DOI: [10.1016/0022-5088\(90\)90575-5](https://doi.org/10.1016/0022-5088(90)90575-5).
- [173] R.V. Pisarev, I. Sanger, G.A. Petrakovskii, and M. Fiebig. "Magnetic-Field Induced Second Harmonic Generation in CuB₂O₄". In: *Physical Review Letters* 93 (2004), p. 37204. DOI: [10.1103/PhysRevLett.93.037204](https://doi.org/10.1103/PhysRevLett.93.037204).
- [174] S. Maekawa, T. Tohyama, S. E. Barnes, S. Ishihara, W. Koshibae, and G. Khaliullin. *Physics of Transition Metal Oxides*. Springer Berlin Heidelberg, 2004.
- [175] N. Leo, D. Meier, R. V. Pisarev, N. Lee, S.-W. Cheong, and M. Fiebig. "Independent ferroelectric contributions and rare-earth-induced polarization reversal in multiferroic TbMn₂O₅". In: *Physical Review B* 85 (9 2012), p. 094408. DOI: [10.1103/PhysRevB.85.094408](https://doi.org/10.1103/PhysRevB.85.094408).
- [176] W. B. Wu, D. J. Huang, J. Okamoto, S. W. Huang, Y. Sekio, T. Kimura, and C. T. Chen. "Multiferroic nanoregions and a memory effect in cupric oxide". In: *Physical Review B* 81.17 (May 2010), p. 172409. DOI: [10.1103/PhysRevB.81.172409](https://doi.org/10.1103/PhysRevB.81.172409).
- [177] R. D. Johnson, L. C. Chapon, D. D. Khalyavin, P. Manuel, P. G. Radaelli, and C. Martin. "Giant Improper Ferroelectricity in the Ferroaxial Magnet CaMn₇O₁₂". In: *Physical Review Letters* 108 (6 2012), p. 067201. DOI: [10.1103/PhysRevLett.108.067201](https://doi.org/10.1103/PhysRevLett.108.067201).
- [178] M. Mostovoy. "Multiferroic Propellers". In: *Physics* 5 (2012), p. 16. DOI: [10.1103/Physics.5.16](https://doi.org/10.1103/Physics.5.16).
- [179] S. Valencia, A. Crassous, L. Bocher, V. Garcia, X. Moya, R. O. Cherifi, C. Deranlot, K. Bouzehouane, S. Fusil, A. Zobelli, A. Gloter, N. D. Mathur, A. Gaupp, R. Abrudan, F. Radu, A. Barthélémy, and M. Bibes. "Interface-induced room-temperature multiferroicity in BaTiO₃". In: *Nature Materials* 10 (2011), p. 753. DOI: [10.1038/nmat3098](https://doi.org/10.1038/nmat3098).
- [180] G. Srinivasan. "Magnetoelectric Composites". In: *Annual Review of Material Research* 40 (2010), p. 153. DOI: [10.1146/annurev-matsci-070909-104459](https://doi.org/10.1146/annurev-matsci-070909-104459).
- [181] J. Ma, J. Hu, Z. Li, and C.-W. Nan. "Recent Progress in Multiferroic Magnetoelectric Composites: from Bulk to Thin Films". In: *Advanced Materials* 23 (2011), p. 1062. DOI: [10.1002/adma.201003636](https://doi.org/10.1002/adma.201003636).
- [182] Y. Wang, J. Hu, Y. Lin, and C.-W. Nan. "Multiferroic magnetoelectric composite nanostructures". In: *NPG Asia Mater* 2 (2010), p. 68. DOI: [10.1038/asiamat.2010.32](https://doi.org/10.1038/asiamat.2010.32).
- [183] T. Hoffmann. "Ultraschnelle Spin- und Gitterdynamik in HoMnO₃". MA thesis. Helmholtz - Institut für Strahlen- und Kernphysik, Universität Bonn, 2008.
- [184] B. Koopmans. "Laser-induced magnetisation Dynamics". In: *Spin Dynamics in Confined Magnetic Structures II*. Hillebrands, B. and Ounadjela, K., 2003.
- [185] Th. Rasing, H van den Berg, Th Gerrits, and J Hohlfeld. "Ultrafast Magnetisation and switching dynamics". In: *Spin Dynamics in Confined Magnetic Structures II*. Hillebrands, B. and Ounadjela, K., 2003.
- [186] G. Zhang, W. Hübner, E. Beaurepaire, and J.-Y. Bigot. "Laser-induced ultrafast demagnetisation: femtomagnetism, a new Frontier?" In: *Spin Dynamics in Confined Magnetic Structures I*. Hillebrands, B. and Ounadjela, K., 2002.

- [187] A. V. Kimel, Kirilyuk A., F. Hansteen, R. V. Pisarev, and Th. Rasing. “Nonthermal optical control of magnetism and ultrafast laser-induced spin dynamics in solids”. In: *Journal of Physics: Condensed Matter* 19 (2007), p. 043201. DOI: [10.1088/0953-8984/19/4/043201](https://doi.org/10.1088/0953-8984/19/4/043201).
- [188] P. Becker, L. Bohatý, H. J. Eichler, H. Rhee, and A. A. Kaminskii. “High-gain Raman induced multiple Stokes and anti-Stokes generation in monoclinic multiferroic MnWO₄ single crystals”. In: *Laser Physics Letters* 4 (2007), pp. 884–889. DOI: [10.1002/lap1.200710075](https://doi.org/10.1002/lap1.200710075).
- [189] E. Beaurepaire, J.-C. Merle, A. Daunois, and J.-Y. Bigot. “Ultrafast spin dynamics in ferromagnetic nickel”. In: *Physical Review Letters* 76 (1996), pp. 4250–4253. DOI: [10.1103/PhysRevLett.76.4250](https://doi.org/10.1103/PhysRevLett.76.4250).
- [190] T. Ogasawara, K. Ohgushi, Y. Tomioka, K. S. Takahashi, H. Okamoto, M. Kawasaki, and Y. Tokura. “General Features of Photoinduced Spin Dynamics in Ferromagnetic and Ferrimagnetic Compounds”. In: *Physical Review Letters* 94 (8 2005), p. 087202. DOI: [10.1103/PhysRevLett.94.087202](https://doi.org/10.1103/PhysRevLett.94.087202).
- [191] M. Gentile. “PhD Thesis (unpublished), University Bonn”.
- [192] *MAPS Software, Photometrics Ltd. (today: Roper Scientific)*.
- [193] *Python Image Library v. 1.1.7 for Python 2.7*. URL: <http://www.pythonware.com/products/pil/>.
- [194] *py2exe – A tool, which converts Python scripts into executable Windows programs, so they can be run without requiring a Python installation*. URL: <http://www.py2exe.org/>.
- [195] *Qt application and GUI framework (version 4.8.0)*. URL: <http://qt.nokia.com/products/>.
- [196] *OpenCV – Open Source Computer Vision Library*. URL: <http://opencv.willowgarage.com/wiki/>.

Publications and presentations

Publications

- (3) T. Hoffmann, K. Kimura, T. Kimura and M. Fiebig: *Second Harmonic Generation Spectroscopy and Domain Imaging of the High-Temperature Multiferroic CuO*, J. Phys. Soc. Jpn. **81**, 124714 (2012), doi: [10.1143/JPSJ.81.124714](https://doi.org/10.1143/JPSJ.81.124714)
- (2) P. Tolédano, N. Leo, D. D. Khalyavin, L. C. Chapon, T. Hoffmann, D. Meier and M. Fiebig: *Theory of High-Temperature Multiferroicity in Cupric Oxide*, Phys. Rev. Lett. **106**, 257601 (2011), doi: [10.1103/PhysRevLett.106.257601](https://doi.org/10.1103/PhysRevLett.106.257601)
- (1) T. Hoffmann, P. Thielen, P. Becker, L. Bohatý and M. Fiebig: *Time-resolved imaging of magnetoelectric switching in multiferroic MnWO₄*, Phys. Rev. B, **84**, 184404 (2011), *Editor's suggestion*, doi: [10.1103/PhysRevB.84.184404](https://doi.org/10.1103/PhysRevB.84.184404)

Conference contributions

- (15) Group Seminar IPCMS, Strasburg (France), April 12 2012: *Time-resolved imaging of magnetoelectric switching using Optical Second Harmonic Generation*, T. Hoffmann, P. Thielen, P. Becker, L. Bohatý and M. Fiebig (Talk)
- (14) APS Meeting, Boston (USA), February 27 - March 2 2012: *Time-resolved imaging of magnetoelectric switching in MnWO₄*, T. Hoffmann, P. Thielen, P. Becker, L. Bohatý and M. Fiebig (Talk)
- (13) European School on Multiferroics 5, Ascona (Switzerland), Januar 29 - Februar 3 2012: *Time-resolved magnetoelectric switching of spin-spiral domains in MnWO₄*, T. Hoffmann, P. Thielen, P. Becker, L. Bohatý and M. Fiebig (Poster)
- (12) Tokyo-Cologne Workshop on Strongly Correlated Transition-Metal Compounds (SFB 608), Cologne (Germany), September 7-10 2011: *Time-resolved magnetoelectric switching of spin-spiral domains in MnWO₄*, T. Hoffmann, P. Thielen, P. Becker, L. Bohatý and M. Fiebig (Poster)
- (11) DPG conference, Dresden (Germany), March 13-18 2011: *Nonlinear Spectroscopy and Domain Imaging in the High-temperature Multiferroic CuO*, T. Hoffmann, K. Kimura, T. Kimura and M. Fiebig (Poster)

- (10) DPG conference, Dresden (Germany), March 13-18 2011: *Time resolved reversal of spin-spiral domains by an electric field*, T. Hoffmann, P. Thielen, P. Becker, L. Bohatý and M. Fiebig (Talk)
- (9) European School on Multiferroics, L'Aquila (Italy), September 26 - October 1 2010: *Switching dynamics of the magnetically induced ferroelectric MnWO₄*, T. Hoffmann, P. Thielen, P. Becker, L. Bohatý and M. Fiebig (Poster)
- (8) Strongly Correlated Transition Metal Compounds III (SFB 608 Workshop), Bergisch Gladbach (Germany), September 8-10 2010: *Novel types of domains in multiferroics*, T. Hoffmann, D. Meier, N. Leo, Th. Lottermoser, P. Becker, L. Bohatý and M. Fiebig (Poster)
- (7) DPG conference, Regensburg (Germany), March 21-26 2010: *Switching of a spin-spiral induced polarization in multiferroic MnWO₄*, T. Hoffmann, D. Meier, P. Becker, L. Bohatý and M. Fiebig (Talk)
- (6) SFB 608 Regional Workshop on Correlated Systems, Kerkrade (The Netherlands), September 30 - October 2 2009: *Switching behavior of multiferroic domains in MnWO₄*, T. Hoffmann, M. Maringer, D. Meier, Th. Lottermoser, P. Becker, L. Bohatý and M. Fiebig (Poster)
- (5) European School on Multiferroics, Groningen (The Netherlands), September 6-11 2009: *Switching behavior of multiferroic domains in MnWO₄*, T. Hoffmann, M. Maringer, D. Meier, Th. Lottermoser, P. Becker, L. Bohatý and M. Fiebig (Poster)
- (4) PhD Colloquium, Cologne (Germany), July 16 2008: *Ultrafast nonlinear optics as a probe for magnetisation dynamics* T. Hoffmann, T. Günter, T. Satoh, T. Lottermoser and M. Fiebig (Talk)
- (3) DPG Conference, Berlin (Germany), February 25-29 2008: *Spin dynamics of multiferroic HoMnO₃* T. Günter, T. Hoffmann, T. Satoh, T. Lottermoser and M. Fiebig (Talk)
- (2) SPP1133 Concluding Colloquium, Bad Irsee (Germany), September 15-19 2008: *Magnetization dynamics of antiferromagnetic compounds by nonlinear optical spectroscopy* M. Fiebig, B.B. van Aken, N.P. Duong, T. Hoffmann, T. Lottermoser, A. Rubano, T. Satoh (Poster)
- (1) SPP1133 Workshop "Fast magnetic imaging", Kaiserslautern (Germany), October 10-12, 2007: *Spin dynamics of HoMnO₃*, T. Günter, T. Hoffmann, T. Satoh, Th. Lottermoser, M. Fiebig (Poster)